

Laser Spectroscopy of Hydrocarbons for Applications in Atmospheric and Space Science

Thesis by
Douglas Clifford Ober

In Partial Fulfillment of the Requirements for
the degree of
Doctor of Philosophy

The Caltech logo, featuring the word "Caltech" in a bold, orange, sans-serif font, centered within a light orange rectangular background.

CALIFORNIA INSTITUTE OF TECHNOLOGY
Pasadena, California

2023
(Defended June 1, 2023)

© 2023

Douglas Clifford Ober
ORCID: 0009-0005-2257-5029

ACKNOWLEDGEMENTS

I would have never been able to complete this dissertation without the support of countless people over the years. First, I would like to first acknowledge my advisor, professor Mitchio Okumura at Caltech. His guidance and support have profoundly shaped my adult life, both as a scientist and a person. I have enjoyed our countless discussions, and his insistence on pushing me to be the best scientist I can be. I also enjoyed my time being his teaching assistant. I would like to thank committee members professor Jack Beauchamp at Caltech and Dr. Rob Hodyss at JPL for their mentorship and guidance on the multiple mass spectrometry projects, and for their patience when results did not always go as planned. I would like to thank Dr. Mahmood Bagheri at JPL for guidance and funding in frequency comb work. I would also like to thank my other committee members, professors Geoff Blake and Scott Cushing, for their insights and guidance on an unusually challenging thesis committee assignment.

I have had the opportunity to work with many other invaluable staff members at Caltech. Mass spectrometry facility manager Dr. Mona Shahgholi was very generous with her expertise and facilities, providing essential guidance for multiple project's success. Without her many projects would likely never have come to fruition. I would like to thank Dr. Nathan Dalleska for his teaching mentorship and insightful discussions. Machinist Ricardo Zarazua was responsible for machining essential experiment components. Glassblower Nathan Hart was responsible for repairing many glass/quartz pieces, without which experiments could not have happened. I thank Joe Drew and Dr. Nate Siladke for keeping everyone safe in lab, and the many facilities personnel who allowed science to be carried out.

I would like to thank my undergraduate advisor Dr. Tom Tullius at Boston University, whose guidance was instrumental for my development as a scientist. I would like to thank the countless synchronized skating teammates of mine over the years for being great friends of mine, especially Alex Wright, Amira Miyaji, and Dana Manson, for the wonderful memories doing a hobby I enjoy.

I also would like to acknowledge the help and guidance from JPL scientists and staff I have worked with directly during my time both at JPL and in continued projects, specifically Professor Lukasz Sterczewski, Dr. Paul Johnson, Dr. Deacon Nemchick, Dr. Pin Chen, Dr. Frank Maiwald, Dr. Andrew Sappey, Spencer Satz, Dr. Xu Zhang, and Tim Crawford. I would also like to thank Dr. Stan Sander, Dr. Brian Drouin, Dr. Keeyoon Sung, Dr. Fred Winiberg, and Dr. Carl Percival for their insights and guidance.

Other people at Caltech I would like to thank are Professor Doug Rees and his student Dr. Siobhán MacArdle for their collaboration on the nitrogenase project, and Professor Yuk Yung and his students Dr. Mike Wong and Dr. Danica Adams for our weekly planetary modeling meetings.

Finally, I would like to thank my peers, both graduate and undergraduate, who have worked with me or guided me over these years. I have worked with one undergraduate, Kyla Hudson from Georgia Tech, and have had the pleasure of getting to know many others: Michael Lissano, Jamie Vinson, Katerina Gorou, Sylvia Meng, and high schooler Xochitl Loza. In the Okumura group, I have enjoyed working with many graduate students and post-docs: Dr. Linhan Shen, Dr. Matt Smarte, Dr. Aileen Hui, Dr. Elizabeth Lunny, Dr. Gautam Stroschio, Dr. Joey Messinger, Wen Chao, Leah Stevenson, Dr. Charlie Markus, Tyler Nguyen, Termeh Bashiri, and Megan Woods. At Caltech, I also enjoyed working with visiting scientists Dr. Ofir Shoshanim on his sabbatical, both Dr. Carlos Abad and his student Dalia Morcillo from Bundesanstalt für Materialforschung und-prüfung, and Robin Miri from École Normale Supérieure de Cachan and Université de Sorbonne.

In particular, I want to recognize three Okumura group members who really made my time at Caltech enjoyable, both scientifically as well as friends outside of work: Greg Jones, Professor Tzu-Ling Chen, and Hannah Szentkuti. Greg has been a great scientist who is always thinking carefully and exactly about all details, and has been a great friend. It was great getting to know Tzu-Ling and her family; I cherish the memories of taking Moana trick-or-treating or hanging out on group outings, and she really was formative in pushing me to strive to work hard and be the best I can be. Hannah has always been a great friend who's always had my back through fun or hard times, whether it's commiserating about life or playing with Jax the guinea pig. I will always look back fondly on our time together, and know my life would be profoundly different had I not met her.

This thesis is for my family and friends, who made this all possible.

ABSTRACT

This thesis describes applications of spectroscopy and mass spectrometry towards applications of *in situ* sensing, chemical kinetics, and photodissociation processes of hydrocarbon species. Both mass spectrometry and cavity ring-down spectroscopy are used in this work. Irradiation of protonated coronene was used to study photodissociation process of polycyclic aromatic hydrocarbons (PAHs), with the power, irradiation time, and fragmentation studied to elucidate a photofragmentation mechanism. Biomolecules were ionized *via* Direct Analysis in Real Time (DART) to explore the feasibility and sensitivity of the ionization technique for different chemical species for *in situ* measurement in simulated extraterrestrial conditions. Photofragmentation and DART ionization were combined to quantify mixtures of isobaric PAHs, providing a tunable and complimentary technique for *in situ* analysis of mixtures. Finally, frequency-stabilized cavity ring-down spectroscopy was used to analyze precise $^{13}\text{CH}_4$, CH_3D , and CH_2D_2 to CH_4 isotologue ratios using optically-switched dual-wavelengths, allowing for sensitive measurement of the kinetic isotope effect of methane oxidation with $\text{O}(^1\text{D})$.

PUBLISHED CONTENT AND CONTRIBUTIONS

Chen, T. L., Ober, D. C., Miri, R., Bui, T. Q., Shen, L., Okumura, M.; “Optically Switched Dual-Wavelength Cavity Ring-Down Spectrometer for High-Precision Isotope Ratio Measurements of Methane δD in the Near Infrared”, *Anal. Chem.*, 93(16), Apr 12, 2021, 6375-84. DOI: 10.1021/acs.analchem.0c05090.

D. C. Ober participated in the determining the experimental conditions, data collection, verifying data analysis accuracy, and participated in the writing of the manuscript.

TABLE OF CONTENTS

Acknowledgements	iii
Abstract	v
Published Content and Contributions	vi
Table of Contents	vii
List of Figures	ix
List of Tables	xiv
Summary	xv
 Chapter 1: Photodissociation Dynamics of Coronene at 532 nm	 1-1
Abstract	1-1
Introduction	1-2
Experimental	1-7
Results: General	1-20
Coronene 5 ms Irradiation	1-22
Coronene 10 ms Irradiation	1-34
Coronene Varying Irradiation Time	1-40
Perdeuterated Coronene 5 ms Irradiation	1-57
Perdeuterated Coronene 10 ms Irradiation	1-80
Perdeuterated Coronene Varying Irradiation Time	1-82
Discussion	1-93
Conclusion	1-98
Acknowledgments	1-101
References	1-102
Appendix	1-103
 Chapter 2: Feasibility of DART-MS for Remote Detection of Biomolecules	 2-1
Abstract	2-1
Introduction	2-2
Experimental	2-2
Results: General	2-6
Ibuprofen	2-9
Glycine	2-14
Arginine	2-16
Phenylalanine methyl ester	2-18
Bradykinin	2-20
Stearic Acid	2-23
DMPC	2-28
Cholesterol	2-31
Hopane Mixture	2-33
Discussion	2-39
Conclusion	2-40

Acknowledgments	2-41
References	2-42
Chapter 3: Visible Photodissociation DART Quantification of Isomeric Naphthalene/Azulene Mixtures	
Abstract	3-1
Introduction	3-2
Experimental	3-4
Results	3-8
Discussion	3-17
Conclusion.....	3-19
Acknowledgments	3-20
References	3-21
Chapter 4: Kinetic Isotope Effect of O(¹ D) and Methane	
Abstract	4-1
Introduction	4-2
Experimental	4-3
Reaction.....	4-8
Data Processing	4-13
Results	4-19
Conclusion.....	4-21
Acknowledgments	4-22
References	4-23
Appendix	4-30

LIST OF FIGURES

Figure	Page
Figure 1.1: Allan deviation of $m/z = 301$ ion count uncertainty versus number of samples averaged.	1-11
Figure 1.2 Schematic of laser set-up. (PD) photodiode, (LP) low-pass. Made in Inkscape using optics package by Alexander Franzen. ²⁹	1-12
Figure 1.3: Screenshot of the unfiltered DC-coupled gate lens voltage as a function of time during a MS^n spectrum of $m/z = 301$	1-14
Figure 1.4: Screenshot of the AC-coupled gate lens pulse sequence during an MS^n trapping at $m/z = 301$	1-15
Figure 1.5: Low-pass circuit for filtering the LTQ gate lens signal. Frequency -3 dB cutoff is 38 Hz.	1-16
Figure 1.6: Screenshot of the AC-coupled gate lens signal (blue), filtered gate lens signal (yellow), and shuttering photodiode signal (pink).	1-17
Figure 1.7: Voltage vs time for gate lens, shutters, and laser during pulse sequence.	1-18
Figure 1.8: Example plot of data vs modeled fit.	1-20
Figure 1.9: Laser power and irradiation time combinations measured.	1-21
Figure 1.10: Spectrum of $CorH^+$ sample prior to mass selection.	1-22
Figure 1.11: Spectrum of $CorH^+$ sample prior to mass selection, narrower mass range.	1-22
Figure 1.12: CID Spectrum of $CorH^+$ at CID = 50 and 200 ms trapping.	1-24
Figure 1.13: Photodissociation yield vs laser power at 5 ms irradiation time.	1-25
Figure 1.14: $CorH^+$ vs Cor^+ peaks at 10 ms irradiation.	1-26
Figure 1.15: Ion counts vs laser power at 5 ms irradiation time for H-loss region peaks.	1-27
Figure 1.16: Ion counts vs laser power at 5 ms irradiation time for C-loss region peaks.	1-27
Figure 1.17: Odd/Even ratio vs laser power at 5 ms irradiation.	1-29
Figure 1.18. $CorH^+$ spectrum 500 mW 100 ms irradiation without A-delay.	1-30
Figure 1.19: Max counts and power for C-loss region, 5 ms irradiation time.	1-32
Figure 1.20. C_n^+/C_nH^+ ratio in C-loss region, 5 ms irradiation time.	1-33
Figure 1.21: Mass spectrum vs laser power at 10 ms irradiation.	1-34
Figure 1.22: $CorH^+$ vs Cor^+ peaks at 10 ms irradiation.	1-35
Figure 1.23: H-loss peaks vs power at 10 ms irradiation.	1-36
Figure 1.24: C-loss peaks vs power at 10 ms irradiation.	1-37
Figure 1.25: Odd/even ratio vs laser power at 10 ms irradiation.	1-38
Figure 1.26: C_n^+/C_n^+ Ratio vs Laser Power at 10 ms Irradiation.	1-39
Figure 1.27: PD Yield of $CorH^+$ vs Irradiation Time and Laser Power. Total counts are either from the same scan or from the total counts at 5 ms.	1-40
Figure 1.28: $CorH^+$ and Cor^+ vs irradiation time and laser power.	1-41
Figure 1.29: Cor^+ to $CorH^+$ ratio vs irradiation time and laser power.	1-41

Figure 1.30: CorH ⁺ mass spectrum vs irradiation time, 160 mW laser power.....	1-43
Figure 1.31: CorH ⁺ H-loss region mass spectrum vs irradiation time, 160 mW laser power	1-43
Figure 1.32: CorH ⁺ mass spectrum vs irradiation time at 320 mW laser power.....	1-44
Figure 1.33: CorH ⁺ mass spectrum in H-loss region vs irradiation time at 320 mW laser power.....	1-44
Figure 1.34: CorH ⁺ H-loss region mass spectrum peaks vs irradiation time at 160 mW laser power.....	1-45
Figure 1.35: CorH ⁺ C-loss region mass spectrum peaks vs irradiation time at 160 mW laser power.....	1-45
Figure 1.36: CorH ⁺ H-loss region mass spectrum peaks vs irradiation time at 320 mW laser power.....	1-46
Figure 1.37: CorH ⁺ H-loss region mass spectrum peaks vs irradiation time at 320 mW laser power.....	1-47
Figure 1.38: CorH ⁺ H-loss region peaks odd/even ratio vs irradiation time at 160 mW laser power.....	1-48
Figure 1.39: CorH ⁺ H-loss region peaks odd/even ratio vs irradiation time at 320 mW laser power.....	1-49
Figure 1.40: CorH ⁺ C-loss region peaks C _n ⁺ /C _n H ⁺ ratio vs irradiation time at 160 mW laser power.....	1-50
Figure 1.41: CorH ⁺ C-loss region peaks C _n ⁺ /C _n H ⁺ ratio vs irradiation time at 320 mW laser power.....	1-50
Figure 1.42: CorH ⁺ C-loss region 500 mW 100 ms irradiation, no A-delay.	1-51
Figure 1.43: Predicted vs experimental C _n ⁺ / C _n H ⁺ ratio in C-loss region of CorH ⁺ for 500 mW 100 ms no A-delay	1-53
Figure 1.44: Mass spectra of CorH ⁺ with same laser power × irradiation time product	1-54
Figure 1.45: Mass spectra of CorH ⁺ with same (laser power) ² × irradiation time product	1-55
Figure 1.46: d ₁₂ -CorH ⁺ and one-hydrogen loss products vs laser power.....	1-58
Figure 1.47: d ₁₂ -CorH ⁺ and H vs D loss ratio.	1-58
Figure 1.48: Mass spectrum of d ₁₂ -CorH ⁺ at 560 mW laser power 5 ms irradiation	1-60
Figure 1.49: Mass spectrum of d ₁₂ -CorH ⁺ at 4000 mW laser power 5 ms irradiation	1-60
Figure 1.50: Counts vs laser power for d ₁₂ -CorH ⁺ 4k peaks 5 ms irradiation.....	1-61
Figure 1.51: Counts vs laser power for d ₁₂ -CorH ⁺ 4k + 1 peaks 5 ms irradiation.....	1-62
Figure 1.52: Counts vs laser power for d ₁₂ -CorH ⁺ 4k + 2 peaks 5 ms irradiation.....	1-62
Figure 1.53 Counts vs laser power for d ₁₂ -CorH ⁺ 4k + 3 peaks 5 ms irradiation.....	1-63
Figure 1.54: Max counts of each H-loss peak of d ₁₂ -CorH ⁺ by type.	1-64
Figure 1.55: Power at which max counts of each H-loss peak of d ₁₂ -CorH ⁺ are reached.....	1-65
Figure 1.56: d ₁₂ -CorH ⁺ reactant to product ratios of H-loss peaks losing H vs laser power 1-68	
Figure 1.57: d ₁₂ -CorH ⁺ even reactant to product ratios of H-loss peaks losing D vs laser power.....	1-68

Figure 1.58: d_{12} -CorH ⁺ odd reactant to product ratios of H-loss peaks losing D vs laser power	1-69
Figure 1.59: d_{12} -CorH ⁺ reactant to product ratios of H-loss peaks losing HD vs laser power	1-70
Figure 1.60: d_{12} -CorH ⁺ reactant to product ratios of H-loss peaks losing D ₂ vs laser power	1-71
Figure 1.61: d_{12} -CorH ⁺ reactant to product ratios of H-loss peaks losing D ₂ vs laser power	1-71
Figure 1.62: d_{12} -CorH ⁺ reactant to product ratios of H-loss peaks losing H at each laser power vs m/z	1-72
Figure 1.63: d_{12} -CorH ⁺ odd reactant to product ratios of H-loss peaks losing H at each laser power vs m/z	1-73
Figure 1.64: d_{12} -CorH ⁺ even reactant to product ratios of H-loss peaks losing D at each laser power vs m/z	1-73
Figure 1.65: d_{12} -CorH ⁺ 4k+2 reactant to product ratios of H-loss peaks losing D at each laser power vs m/z	1-74
Figure 1.66: d_{12} -CorH ⁺ odd reactant to product ratios of H-loss peaks losing D at each laser power vs m/z	1-74
Figure 1.67: d_{12} -CorH ⁺ reactant to product ratios of H-loss peaks losing HD at each laser power vs m/z	1-75
Figure 1.68: d_{12} -CorH ⁺ even reactant to product ratios of H-loss peaks losing D ₂ at each laser power vs m/z	1-75
Figure 1.69: d_{12} -CorH ⁺ odd reactant to product ratios of H-loss peaks losing D ₂ at each laser power vs m/z	1-76
Figure 1.70: d_{12} -CorH ⁺ all reactant peaks to specific even product peak ratios of H-loss peaks at each laser power vs m/z	1-77
Figure 1.71: d_{12} -CorH ⁺ all reactant peaks to specific even product peak ratios of H-loss peaks at each laser power vs m/z zoomed in	1-78
Figure 1.72: d_{12} -CorH ⁺ all reactant peaks to specific odd product peak ratios of H-loss peaks at each laser power vs m/z	1-78
Figure 1.73: d_{12} -CorH ⁺ all reactant peaks to specific odd product peak ratios of H-loss peaks at each laser power vs m/z zoomed in	1-79
Figure 1.74: d_{12} -CorH ⁺ mass spectrum vs laser power, 10 ms irradiation	1-81
Figure 1.75: d_{12} -CorH ⁺ and single H or D loss product counts vs irradiation time at 9 mW	1-82
Figure 1.76: d_{12} -CorH ⁺ and single H or D loss product counts vs irradiation time at 160 mW	1-83
Figure 1.77: d_{12} -CorH ⁺ and single H or D loss product counts vs irradiation time at 320 mW	1-84
Figure 1.78: d_{12} -CorH ⁺ H-loss region peaks vs irradiation time at 160 mW	1-85
Figure 1.79: d_{12} -CorH ⁺ H-loss region peaks vs irradiation time at 160 mW	1-86
Figure 1.80: d_{12} -CorH ⁺ H-loss region odd/even ratio vs irradiation time at 160 mW	1-87
Figure 1.81: d_{12} -CorH ⁺ H-loss region odd/even ratio vs irradiation time at 320 mW	1-87
Figure 1.82: d_{12} -CorH ⁺ C-loss region mass spectrum vs laser power at constant total energy	1-89

Figure 1.83: d_{12} -CorH ⁺ H-loss region mass spectrum vs laser power at constant total energy	1-89
Figure 1.84: d_{12} -CorH ⁺ and first H or D counts vs laser power at constant total energy	1-90
Figure 1.85: d_{12} -CorH ⁺ first H or D loss ratio vs laser power at constant total energy	1-90
Figure 1.86: d_{12} -CorH ⁺ H-loss region odd/even ratio vs laser power at constant total energy	1-91
Figure 1.87: CorH ⁺ mass spectrum vs laser power	1-105
Figure 1.88: CorH ⁺ mass spectrum vs laser power zoomed in	1-105
Figure 1.89: CorH ⁺ H-loss region mass spectrum vs laser power	1-106
Figure 1.90: CorH ⁺ mass spectrum 5 ms irradiation C-loss region C_n^+ / C_nH^+ ratio vs laser power.....	1-107
Figure 1.91: CorH ⁺ mass spectrum 5 ms irradiation C-loss region C_n^+ / C_nH^+ ratio vs carbon number n.....	1-107
Figure 1.92: CorH ⁺ 5 ms irradiation $C_{24}^+ / C_{24}H^+$ ratio.....	1-108
Figure 1.93: CorH ⁺ mass spectrum 5 ms irradiation C-loss region C_n^+ / C_nH^+ ratio fit residuals vs carbon number n	1-109
Figure 1.94: CorH ⁺ mass spectrum 10 ms irradiation vs laser power.....	1-110
Figure 1.95: CorH ⁺ mass spectrum H-loss region 10 ms irradiation vs laser power	1-110
Figure 1.96: CorH ⁺ mass spectrum 10 ms irradiation C-loss region C_n^+ / C_nH^+ vs carbon number n.....	1-111
Figure 1.97: CorH ⁺ mass spectrum 10 ms irradiation C-loss region C_n^+ / C_nH^+ ratio vs carbon number n.....	1-111
Figure 1.98: CorH ⁺ mass spectrum 10 ms irradiation C-loss region C_n^+ / C_nH^+ ratio fit residuals vs carbon number n.....	1-112
Figure 1.99: d_{12} -CorH ⁺ H-loss region mass spectrum 5 ms irradiation vs laser power zoomed in.....	1-113
Figure 2.1: Exterior of plastic shroud covering DART inlet.	2-4
Figure 2.2: DART inlet beneath shroud.	2-4
Figure 2.3: Close-up of DART ionization source.	2-4
Figure 2.4: Mass spectrum without a bag covering the source apparatus, in positive and negative mode.....	2-5
Figure 2.5: Photograph of stainless steel DART inlet.	2-5
Figure 2.6: Structure of ibuprofen.....	2-9
Figure 2.7: Neat Ibuprofen at 20 °C in positive mode.....	2-9
Figure 2.8: Neat ibuprofen mass spectrum at –180 °C positive mode.....	2-11
Figure 2.9: Neat ibuprofen mass spectrum at –180 °C negative mode.....	2-12
Figure 2.10: Structure of glycine.	2-14
Figure 2.11: 1 M glycine in the simulated Enceladus solution in positive mode at room temperature.....	2-15
Figure 2.12: Structure of arginine.	2-16
Figure 2.13: Neat arginine at room temperature, positive mode.....	2-16
Figure 2.14: Phenylalanine methyl ester structure.	2-18

Figure 2.15: Phenylalanine methyl ester room temperature positive mode mass spectrum.	18
Figure 2.16: Bradykinin structure	2-20
Figure 2.17: Plot of mass spectrum vs bradykinin concentration at room temperature in positive mode.	2-22
Figure 2.18: Stearic acid structure.	2-23
Figure 2.19: Neat stearic acid room temperature positive mode mass spectrum.	2-23
Figure 2.20: Mass spectrum of neat stearic acid positive mode in modeled Enceladus solution at -180°C	2-25
Figure 2.21: Mass spectrum of room temperature neat stearic acid positive mode at CID = 10.	2-27
Figure 2.22: DMPC structure.	2-28
Figure 2.23: Neat DMPC mass spectrum at room temperature positive mode.	2-28
Figure 2.24: Structure of Cholesterol.	2-31
Figure 2.25: Neat cholesterol mass spectrum -180°C positive mode.	2-32
Figure 2.26: Mass Spectrum of hopane mixture at room temperature positive mode.	2-36
Figure 2.27: Mass Spectrum of hopane mixture at room temperature positive mode.	2-37
Figure 3.1: Laser power at 450 nm vs laser diode current.	3-7
Figure 3.2: Laser power at 402 nm vs laser diode current.	3-7
Figure 3.3: Mass spectra of pure naphthalene and azulene in scan mode.	3-8
Figure 3.4: PD yield of azulene vs laser power at 450 nm vs different laser powers and trapping times.	3-10
Figure 3.5: Plot of photodissociation yield vs CID % for different trapping times.	3-10
Figure 3.6: Mass spectrum vs different irradiation times to 450 nm 650 mW light.	3-11
Figure 3.7: Mass spectrum vs varying laser power at 1000 ms trapping time for Azu^+ and Nap^+	3-12
Figure 3.8: Mass spectrum vs CID percentage and molecule.	3-13
Figure 3.9: Azu^+ and Nap^+ overlaid at scaling value to minimize sum of squares.	3-14
Figure 3.10: Plot of naphthalene concentration derived from spectrum vs naphthalene concentration in the prepared sample.	3-16
Figure 4.1: Kintecus plot of key species concentration vs time for $\text{CH}_4 + \text{O}(^1\text{D})$ reaction.	4-6
Figure 4.2: The FS-CRDS alignment set-up.	4-10
Figure 4.3: Diagram of the I_2 stabilized DFB laser	4-11
Figure 4.4: Frequency-stabilized 633 nm light in red, near-IR light in grey.	4-12
Figure 4.5: Frequency vs laser diode temperature for DFB1	4-12
Figure 4.6: Frequency vs laser diode temperature for DFB1 and DFB2.	4-13
Figure 4.7: CH_4 peak used to fit the $\text{CH}_2\text{D}_2 + \text{O}(^1\text{D})$ data.	4-15
Figure 4.8: CH_2D_2 peak used to fit the $\text{CH}_2\text{D}_2 + \text{O}(^1\text{D})$ KIE	4-15
Figure 4.9: Change in the CH_2D_2 peak width at 5993.83 cm^{-1} vs pressure.	4-17
Figure 4.10: Change in the CH_2D_2 peak center frequency at 5993.83 cm^{-1} vs pressure.	4-18
Figure 4.11: Spectrum of CH_2D_2 loss vs frequency $5989.75 - 6000\text{ cm}^{-1}$	4-42
Figure 4.12: Spectrum of CH_2D_2 loss vs frequency $6000 - 6012\text{ cm}^{-1}$	4-42
Figure 4.13: Spectrum of CH_2D_2 loss vs frequency $6450.8 - 6468\text{ cm}^{-1}$	4-43

LIST OF TABLES

Table	Page
Table 1.1: Optimized Finnegan LTQ parameters for $m/z = 301$ and 311	1-9
Table 1.2: SRS 535 delay times for each channel.	1-19
Table 1.3: List of laser power and irradiation times measured.	1-21
Table 1.4: Prominent masses in coronene mass spectrum scan mode.	1-23
Table 1.5: Table of laser power and irradiation time conditions with same total energy delivered.....	1-52
Table 2.1: Neat ibuprofen peaks at room temperature	2-10
Table 2.2: Neat ibuprofen peaks at room temperature under shroud.....	2-10
Table 2.3: Table of neat ibuprofen mass spectrum peaks at $-180\text{ }^{\circ}\text{C}$ positive mode.....	2-11
Table 2.4: Table of neat ibuprofen mass spectrum peaks at $-180\text{ }^{\circ}\text{C}$ negative mode.....	2-12
Table 2.5: Phenylalanine methyl ester room temperature positive mode mass peaks.	2-19
Table 2.6: Bradykinin CID fragment ions at $\text{CID} = 10$	2-21
Table 2.7: List of stearic acid neat room temperature positive mode mass spectrum peaks... ..	2-24
Table 2.8: Isotopic Ratios of protonated neat stearic acid at room temperature.	2-24
Table 2.9: Mass spectrum peaks of neat stearic acid positive mode in modeled Enceladus solution at $-180\text{ }^{\circ}\text{C}$	2-25
Table 2.10: DMPC neat positive mode room temperature peaks seen.	2-29
Table 2.11: DMPC peaks at $-180\text{ }^{\circ}\text{C}$ for neat and $100\text{ }\mu\text{M}$ Enceladus sample.	2-29
Table 2.12: Hopane mixture composition.....	2-33
Table 2.13: Hopane mixture expected ion peaks.....	2-33
Table 2.14. Hopane mixture chemical structures.	2-34
Table 2.15: Observed peaks in mass spectrum of hopane at room temperature positive mode.	2-37
Table 3.1: Optimized Finnegan LTQ Parameters at $m/z = 128$	3-6
Table 3.2: Masses and potential identities in scan mode spectra.	3-9
Table 3.3: Fitting constants for exponential fit at both wavelengths.	3-17
Table 4.1: Conditions for $\text{CH}_3\text{D} + \text{O}(^1\text{D})$ experiment	4-5
Table 4.2: Line center and line strength of KIE absorption transitions	4-14
Table 4.3: KIE Results.....	4-19

SUMMARY

The work outlined in this thesis covers broad subjects in photodissociation, mass spectrometry sources, high-resolution spectroscopy, and chemical kinetics. Chapter 1 introduces the photodissociation instrumentation used in both chapters 1 and 3, and details the laser-induced photodissociation of coronene and per-deuterated coronene at 532 nm. This experiment was motivated by desire to better understand the photodissociation of polycyclic aromatic hydrocarbons (PAHs), an important source of interstellar carbon. The mechanism of synthesis of larger PAHs or fullerene molecules however is not well-detailed. Scanning the laser power and irradiation time between 0 – 4000 mW and 0 – 1000 ms revealed several unexplored phenomena. Photodissociation showed several sequential steps: first creation of the coronene cation, then hydrogen loss through molecular hydrogen, and finally carbon cluster fragments produced from shrinking aromatic cations. The mass spectrum's dependence on laser power and irradiation time was explored and not found to be dependent on the total energy delivered. Finally, several unexpected spectroscopic states and potential isomerization were discovered in the photodissociation process.

Chapter 2 discusses the feasibility of direct analysis in real time (DART) ionization for biomolecule detection. With NASA prioritizing the search for extraterrestrial life, new instrumentation capable of detecting potential trace biomolecular signatures in extraterrestrial environments is needed. The biomolecules of greatest interest included lipids, amino acids, and nucleotides, as these molecules comprise membranes, proteins, and nucleic acids. These molecules were tested both at room and cryogenic temperatures on neat samples and simulated ocean world solutions. DART ionization was found to work for

non-zwitterionic compounds and especially well for compounds with aliphatic functionalization, though the technique was also found to be sensitive to inlet geometry.

Chapter 3 details a combination of techniques in chapters 1 and 2 to quantitatively measure mixtures of isobaric PAHs ionized via DART and quantified *via* photodissociation at multiple wavelengths. Standard curves of the pure PAH species allowed the detection of low levels of azulene in naphthalene. Using photodissociation at different wavelengths quantitatively for isobaric sample quantification has only recently been performed, and has never been combined with DART ionization. This finding should greatly expand the potential application of DART, both for NASA and for terrestrial uses such as quality control.

Chapter 4 details upgrades to an existing near-IR cavity ring-down spectroscopic instrument and the remeasurement of the kinetic isotope effect (KIE) of methane isotopologues. The KIE of methane isotopologues are important for modelers determining how methane samples age during atmospheric transport and the effect on the observed isotope signature. The KIE of CH_2D_2 was measured for the first time to be 1.102 ± 0.022 via flash photolysis, as well as the remeasurement of $^{13}\text{CH}_4$ and $\text{CH}_3\text{D} + \text{O}(^1\text{D})$ values to be 1.069 ± 0.028 and 1.09 ± 0.03 , respectively. Spectroscopic parameters of unlisted molecules to improve line shape fitting could be determined, as well as absorption profiles for molecules not recorded as having transitions in the $5996 - 6014 \text{ cm}^{-1}$ and $6450 - 6248 \text{ cm}^{-1}$ regions.

Photodissociation Dynamics of Coronene at 532 Nm

Abstract:

A custom mass spectrometer has been built for measuring the visible laser-induced photodissociation of coronene and per-deuterated coronene at 532 nm. The electrical and optical properties of a commercial linear ion trap MS have been augmented, and the resulting instrument characterized. Trapped protonated coronene and perdeuterated coronene were irradiated systematically between 0 – 4000 mW and 0 – 1000 ms to discover trends in the photodissociation process. Our results showed several sequential steps to photodissociation: first creation of the coronene cation, then hydrogen loss through molecular hydrogen, and finally carbon cluster fragmentation to produce shrinking aromatic cations. The mass spectrum's dependence on laser power and irradiation time were different, with the spectrum's evolution second order with respect to laser power but first order with respect to irradiation time. Lastly, several unexpected spectroscopic states and potential isomerization were discovered in the photodissociation process.

Introduction:

Polycyclic aromatic hydrocarbons (PAHs) are a class of all-carbon molecules which are suspected to be the origin of several unidentified diffuse interstellar bands (DIBs) of molecules in outer space.¹ In particular, PAHs are believed to be the origin of the 3 – 15 μm emission range of the interstellar medium (ISM), and absorption bands in our galaxy between 0.38 – 1.3 μm . Besides being a reservoir of potentially 20% of the carbon in the ISM,² polycyclic aromatic hydrocarbons are likely to play a chemical role in the ISM. A hypothesized role of PAHs are acting as catalysts, for example for the important reaction $\text{H} + \text{H} \rightarrow \text{H}_2$,³ which despite being the most abundant molecule in the ISM, requires a third body to remove energy for bond formation. Another important role is the precursors to fullerenes formed through photodissociation,⁴ which have been positively detected in the ISM as neutrals and cations.⁵ Therefore, processes related to the formation, reactivity, and degradation of PAHs have motivated numerous studies. After irradiation by visible and UV photons, four channels compete to dispel the internal energy: ionization, radiative relaxation of IR photons, electronic transitions, and unimolecular reactions ejecting small fragments such as C_2H_2 , H , H_2 .⁶

Coronene ($\text{C}_{24}\text{H}_{12}$, abbreviated Cor) is the smallest planar polycyclic aromatic hydrocarbon containing a ring completely surrounded by other carbon rings, therefore forms an important graphene-like carbon surface. While cations of smaller PAH molecules such as naphthalene,^{7–9} anthracene,^{7,10,11} and pyrene^{7,12,13} have been studied in detail, the coronene cation has mostly been studied with a wide variety of other PAH cations to observe trends with size or cation structure.^{7,12,14,15} Experimental studies of the coronene cation ($\text{C}_{24}\text{H}_{12}^+$, abbreviated Cor^+) have been performed by Jochims 1994,⁷

Ekern 1997 and 1998.^{12,16} Later investigations include theoretical studies by Paris 2014¹⁷, experimental studies at 8 – 40 eV by Zhen 2015,¹⁸ and experimental and theoretical studies by Castellanos 2018.¹⁵ All of these studies differ from our experimental study because these studies are theoretical,^{15,17} in noble gas matrices,^{19,20} use broadband light sources,^{12,16} or high photon energies.^{18,21} No study has used isotopic substitution to study the coronene cation to date, nor have any looked at unimolecular dissociation beyond the first few H atoms.^{14,15}

The earliest study of unimolecular photofragmentation of Cor^+ by Jochims *et al.* revealed via photoionization mass spectrometry at 400 K in the gas phase that Cor^+ has an appearance potential = 7.27 ± 0.02 eV.⁷ The appearance energies of unimolecular decomposition are 18.70 ± 0.15 and 20.12 ± 0.15 eV when the first H and H₂ fragmentation begins. On fragmentation, the remaining cation has $E_{\text{int}} = 12.05$ or 13.43 eV, respective, at the first H and H₂ fragmentation appearance, removing 6.65 and 6.69 eV of energy with the neutral fragment.¹⁴ The subsequent reaction $\text{Cor}^+ \rightarrow \text{C}_{24}\text{H}_{11}^+ + \text{H}$ has an appearance energy of 4.64 eV.²² No C₂H₂ production was observed for Cor^+ , but for smaller PAH cations C₂H₂ formation was observed..⁷ Jochims also discovered the remaining E_{int} when H loss occurred scaled linearly with the number of total atoms, carbon number, and degrees of vibrational degrees of freedom – 1, and E_{int} when H₂ loss occurred scaled linearly with the degrees of vibrational freedom – 1.⁷

Ekern used a Fourier transform ion cyclotron resonance mass spectrometer to trap resistively heated coronene ionized via electron impact just above appearance potential.¹² Exposing the trapped Cor^+ ions to a broadband Xe lamp induced dehydrogenation, producing various $\text{C}_{24}\text{H}_m^+$ ($m = 0 \dots 11$) product ions. The product distribution shifted

towards lower m with increasing photon intensity, and ions with even values of m were more abundant than odd m peaks, implying the dissociation of H_2 as well as H .^{12,16} Ekern did not see any C_2H_2 formation, consistent with Jochims, but also did not observe fragmentation of the bare C_{24}^+ ion into smaller carbon fragments.

Paris described theoretically the mechanism and energetics behind dissociation of H , H_2 , H^+ , and H_2^+ from variously charged Cor^{q+} ($q = 1 \dots 5$) species.¹⁷ The energy to remove H^+ and H_2^+ from Cor^+ is significantly higher than removing H and H_2 . There are two competing processes for dehydrogenation of coronene,¹⁷ one where hydrogen atoms are sequentially removed from adjacent carbons, and a concerted mechanism for H_2 removal is an H atom shifts from one edge carbon to an adjacent edge carbon, creating an empty site and a non-aliphatic CH_2 site. The aliphatic hydrogens then rearrange linearly, forming a $C - H - H$ group, which dissociates to $C + H_2$.

Castellanos investigated the work of Paris experimentally by building a larger model of H loss. Castellanos irradiated gas phase Cor^+ ions with 3 pulses of 656 nm laser light with power varying from 0 – 12 mJ/pulse and allowed the ions to react for 0.1 sec between laser pulses. Castellanos found the fragmentation of PAH cations were a function of size and arrangement of H atoms on the PAH's structure's edge. For coronene, because the edge consists of six pairs of H atoms on adjacent C atoms, the first H of a pair to be removed requires 4.8 eV energy, while the second, now-unpaired H requires 3.8 eV. A processes Castellanos explores theoretically is H hopping and isomerization, both of which are efficient below the E_{int} necessary for dissociation. For the concerted removal of H_2 , two H atoms can form a bond from one pair to the next, one H can hop to a tertiary carbon and form a bond with an H from an adjacent pair, or one H

atom can hop onto the adjacent H atom's carbon forming an sp^3 CH_2 site and an empty C, similar to Paris's findings but without the added C – H – H rearrangement.

Castellanos notes at low laser pulse powers ≤ 1 mJ/pulse, the H and H_2 channels are of similar intensity. Between 1 mJ/pulse \leq laser pulse power ≤ 3 mJ, $2H$ loss dominates, then at laser pulse powers ≥ 3 mJ/pulse $4H$ loss is greater than H loss. Castellanos also observes the odd/even ratio increases for $M-3H/M-4H$ vs $M-H/M-2H$, and that the ratio first increases then stabilizes at ≥ 3 mJ/pulse. The molecular size is important for these odd/even ratios; for PAHs with >32 C atoms the ratio changes less with increasing laser pulse power. Further, with larger number of C atoms H loss, the H loss channel is nearly non-existent; only the even $2H$ and $4H$ loss channels exist.

The protonated forms of PAHs have been sparsely studied too, but are also of interest as contributing to DIBs and astrochemistry (though protonated coronene $C_{24}H_{13}^+$ itself has been ruled out contributing to DIBs in the mid-IR²⁰). The mechanism of protonated PAH photodissociation and reaction could elucidate the formation mechanisms for producing larger PAHs. Experimentally, the gas-phase absorption spectrum of protonated coronene $C_{24}H_{13}^+$ (abbreviated $CorH^+$) and photodissociation products are relatively unexplored in the visible spectrum (400 – 700 nm). The spectrum of protonated coronene in this region has been studied by Garkusha *et al.* via matrix experiments in Ne at 6 K,¹⁹ revealing a $S_2 (^1A') \leftarrow S_0 (^1A')$ transition at 532 – 560 nm. A subsequent paper detailed the high resolution 15 K gas-phase spectrum at the $S_1 (^1A') \leftarrow S_0 (^1A')$ transition using a $1 + 1'$ multiphoton excitation with a 14,340 – 17,700 cm^{-1} (677 – 697 nm) dye laser pulse and a 1064 nm Nd:YAG pulse.²⁰ Matrix experiments however can shift frequency positions and intensities of absorption peaks due to interactions

between absorbing ions and the matrix. The gas phase absorption experiment used a multiphoton absorption, but the laser power correction assumed peak intensities scaled linearly with power, and only measured the dissociation of the first H atom.

Theoretical determination of the absorption cross-section also shows discrepancies with the measured matrix CorH^+ spectrum. In particular, the oscillator strength, which is proportional to the absorption cross-section, has been computed by Hammonds *et al.* via time-dependent density functional theory (TD-DFT) calculations.²³ The oscillator strength is large around 532 nm, while the experimental spectrum measure by Garkusha *et al.* shows a minimum near this wavelength. The calculations were performed using Q-Chem V3.0, with a 6-31G* basis. B3LYP was chosen to optimize geometries, and excitation energies calculated with BLYP functionals. The low levels of theory give stated accuracies of 0.3 eV, or which is the range 471 – 611 nm. Larger PAHs such as ovalene, circumpyrene, and more heavily hydrogenated ions derived from the coronene C_{24} framework, are expected to show prominent visible absorption in this region too. The Hammonds TD-DFT calculations compliment and agree with the lower frequency range of the TD-DFT calculations independently performed by Mallocci *et al* on neutral coronene.²⁴

However, little theoretical work has been performed looking at dehydrogenated cationic forms of coronene, which were seen as the main photodissociation products in Ekern's experiments. Castellanos restricted their study to the first 4 H atoms removed from Cor^+ to avoid complications with carbon atom loss.

Our experiment differs from those of Castellanos and others by using monochromatic continuous 532 nm light which is chopped and focused, and we are using

CorH⁺ instead of Cor⁺ as the parent ion. What we expect to see is CorH⁺ absorption by at least one photon. Based on the neutral coronene absorption spectrum with a 150 Mb cross-section at 330 nm (3.76 eV) corresponding to an oscillator strength of 0.46 from Hammond *et al.*,^{23,24} the oscillator strength of CorH⁺ at 532 nm (2.33 eV) is predicted to give a cross-section of $5.5 \times 10^{-17} \text{ cm}^2$. Assuming this cross-section, then with 200 mW irradiation at 532 nm, the total rate of photons delivered per second is the power divided by energy per photon.

$$P \left(\frac{hc}{\lambda} \right)^{-1} = 5.4 \times 10^{17} \text{ photons/sec}$$

With f being the focal length of the focusing lens, λ the wavelength in μm , M being the being propagation ratio, and D being the beam diameter at the lens, the formula for the spot size is given below. With a focused spot size diameter of $\sim 91 \mu\text{m}$ in the center of the trap and $M^2 = 1.1$, the rate of photon absorption is

$$\text{Spot size } (\mu\text{m}) = \frac{4 \times f \times \lambda \times M^2}{\pi \times \text{Beam diam}} = 4.5 \times 10^5 \text{ photons/sec}$$

Using Mallocci *et al.*'s gas phase cross-sections for Cor and Cor⁺, the cross-section is $2 \times 10^{-18} \text{ cm}^2$ for a ground state Cor⁺, corresponding to a rate of photon absorption of $1.13 \times 10^5 \text{ photons/sec}$.²⁴

Experimental:

Coronene C₂₄H₁₂ (Sigma-Aldrich 97% pure) or per-deuterated d₁₂-coronene C₂₄D₁₂ (CDN Isotopes 97% D, abbreviated d₁₂-Cor) was serially diluted to 10 μM with 100% methanol (Sigma MS Grade), and 1 drop/mL (final concentration $\sim 20 \text{ mM}$) of 1 M aqueous ammonium acetate (Fischer) were added to increase coronene protonation efficiency.²⁵ Expected contamination of d₁₂-Cor by isobaric ¹³C¹²C₂₃D₁₁H is

approximately 5.3%. The proton affinity of coronene is 205.9 kcal/mol,²⁶ while the gas-phase proton affinity for NH₃(g) is nearly the same at 204.0 kcal/mol,²⁶ ensuring good protonation of the precursor. Coronene was then flowed into the electrospray source at 10 μ L/min from a 250 or 500 μ L Hamilton syringe into a calibrated Thermo-Fischer Finnigan LTQ to produced protonated coronene (CorH⁺) at m/z = 301.1 and protonated per-deuterated d₁₂-coronene (d¹²-CorH⁺) at m/z = 313.2. The ionization potential for coronene is 7.29 eV.²⁷

The electrospray parameters were optimized iteratively for the collection of m/z = 301 and 313 via the internal LTQ Tune method. Briefly, the order of ion optics is as follows: the ion sweep cone and ion transfer capillary pass from the atmospheric pressure electrospray head to the first differential pumping region. The ions pass through the tube lens, skimmer, Q00 quadrupole, and Lens 0 into the second differential pumping region. The ions then pass through the Q0 quadrupole and lens 1 into the high vacuum region. The ions then pass through a gate lens to shutter the ion current, the Q1 octapole, and the front lens into the 6.5 cm segmented linear quadrupole ion trap. After mass analysis, the ions are ejected in increasing m/z longitudinally from the trap, accelerated into a 15 kV conversion dynode, and the resulting fragments counted.²⁸ The optimized parameters are shown in table 1.

Table 1.1: Optimized Finnegan LTQ parameters for $m/z = 301$ and 311 .

Parameter	Value $m/z = 301$	Value $m/z = 313$
Capillary voltage (V)	36.5	65.5
Tube lens voltage (V)	79	12
Sheath gas flow (arb)	13	7
Auxiliary gas flow (arb)	11	19
Sweep gas flow (arb)	44	6
Multiple RF DAC (V)	750	650
Multipole 00 offset (V)	-5.3	-5.0
Lens 0 (V)	-6.6	-5.6
Multipole 0 offset (V)	-10.7	-8.6
Lens 1 (V)	-133	-48.0
Multipole 1 offset (V)	-22.0	-16.0
Gate lens (V)	-18.0	-10.0
Front lens (V)	-14.0	-9.0

In general, the ion current was relatively insensitive to atmospheric pressure parameters and capillary voltage, very sensitive to the tube lens voltage and lens 0, moderately sensitive to the ion lenses, and moderately sensitive to the gate lens and front lens voltage.

The ions were introduced into ion trap either for 100 ms or until the trap had collected 10,000 ions in either scan or MS^n mode, which allowed for a particular mass to be selected while preventing mass peak saturation. Shorter trap times than 10 – 20 ms did not produce consistent ion starting ion counts. The ion trap was filled with 1 mtorr He to improve mass resolution by translationally cooling incoming ions and removing internal energy formed during ionization and sample introduction. The ions were then held for a specified trapping time before sequential ejection and detection on a dynode and electron multiplier. The trap Q factor of 0.25 resulted in a low-mass cutoff of 27% the parent mass, or $m/z = 81$ for $CorH^+$ and $m/z = 85$ for $d_{12}-CorH^+$, and the iso-width of the trapped ions were 0.5 m/z , corresponding to a FWHM = 0.40 at $m/z = 301$.

While trapped, the mass-selected ions could undergo collision-induced dissociation (CID), whereby RF voltage was applied to accelerate trapped ions into dissociating collisions with the He buffer gas. The resulting molecular fragments were mass analyzed and could provide insight to the chemical composition of the parent and product masses. The stated CID percentage is the percentage of the RF voltage amplitude needed to 100% dissociate the mass calibration standard, which for this mass region is caffeine, with typical values of 35 – 40 V.

With $N = 300$ individual scans averaged together, an average ion count \bar{I} was produced with an uncertainty of $4.1\% \times \bar{I}^{0.44}$ at each m/z . Due to fluctuations in the electrospray source, the relative uncertainty of the average count intensity \bar{I} was not proportional to $1/\sqrt{N}$, as is common in Poisson counting statistics. Instead, the uncertainty was described better by the following formula:

$$\Delta I = \frac{(N \cdot \bar{I})^{0.44}}{N} = 4.1\%(\bar{I}^{0.44})$$

The determination of the exponent 0.44 is the slope of the green trendline in the Allan deviation of the ion signal intensity. As can be seen from the Allan deviation of the ion count uncertainty, the default LTQ data collection method averaging $N = 50$ scans yields $10.8\% \times \bar{I}^{0.44}$, but either $N = 10$ or $N = 300$ yield a much better uncertainty reduction for the sample measurement time.

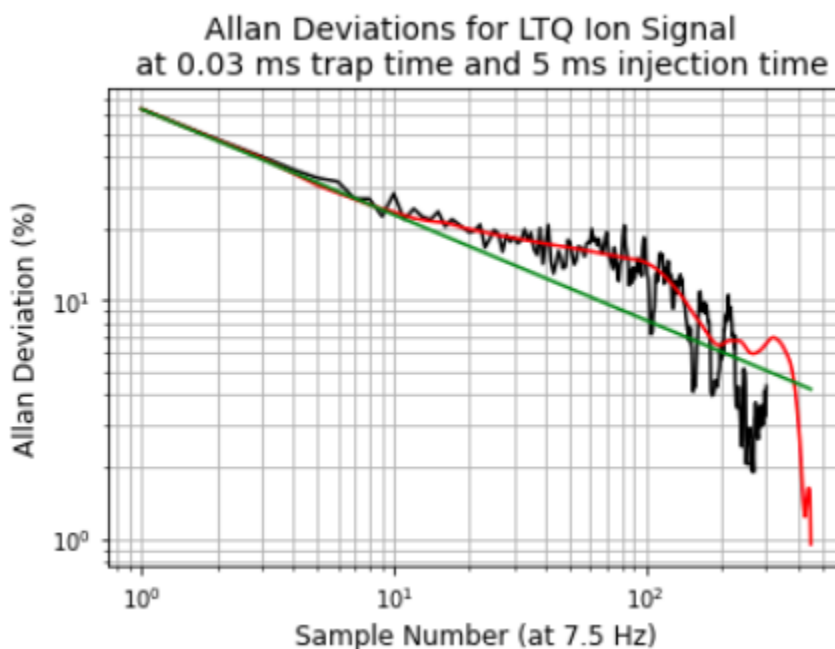


Figure 1.1: Allan deviation of $m/z = 301$ ion count uncertainty versus number of samples averaged. Black trace is the Allan deviation, red is the modified Allan deviation, green is the trendline from first 10 samples with slope -0.44 . Sampling rate is 7.5 Hz, 30 μ s trapping time, and a 5 ms injection time.

To photodissociate the trapped Cor^+ and $\text{d}_{12}\text{-CorH}^+$ ions, a custom optical set-up was constructed in which the ions were irradiated by a high power shuttered continuous-wave (cw) laser. A frequency-doubled Nd:YAG Coherent Verdi-5W laser (Model 0174-525-52) was used to generate 532 nm light from 0 to 5 W (power stability $< 1\%$) with 10 mW resolution. After reflecting through a periscope, two flip mirrors to allow for other co-aligned laser beams to be selected, an iris, and two alignment mirrors, the beam passed through shutter 1. The shutters were used to control photolysis were Thorlabs SH05 shutters with Thorlabs SC10 shutter controllers, with a measured 10% to 90% opening time of 1 ms for the 2.25 mm diameter beam. The SH05 has a minimum open time of 10 ms, and a maximum repetition rate of 25 Hz under optimal conditions. The beam was then reflected off another alignment mirror, through a second shutter to allow

consistent shuttering of the beam faster than 40 ms, through a second iris, and through a microscope slide. The slide provides a 4% reflection to a Thorlabs Si PDA015A photodetector to visualize the shutter synchronization with the mass spectrometer. The beam was then focused through a 250 mm N-BK7 lens and through a borosilicate vacuum window onto the longitudinal axis of the linear ion trap with the focal point of the beam in the center of the trap. A schematic is shown below.

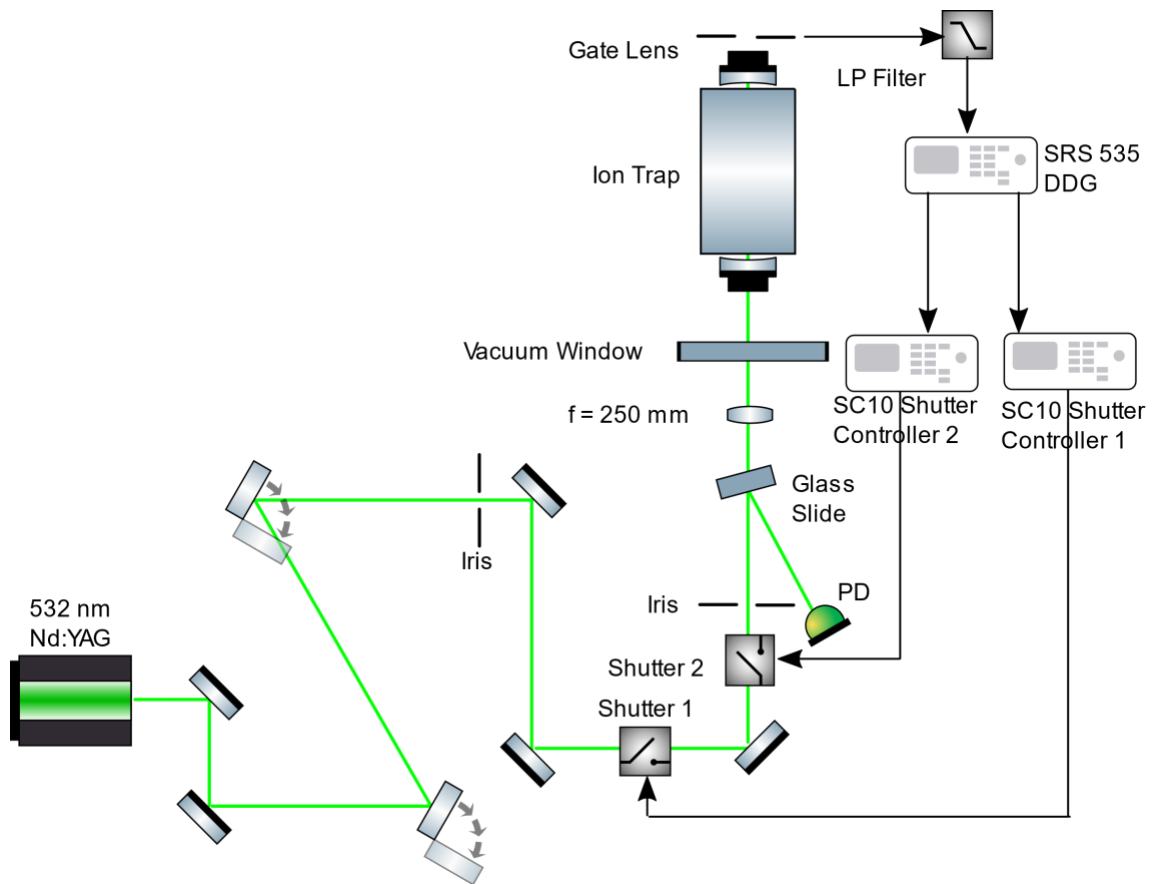


Figure 1.2 Schematic of laser set-up. (PD) photodiode, (LP) low-pass. Made in Inkscape using optics package by Alexander Franzen.²⁹

The power reaching the ion trap window was measured via a Thorlabs PM100USB power meter to account for reflection losses, which were found to reduce the laser power by 21%. The addition of a 250 mm focusing lens noticeably improved the

photodissociation yield, with unfocused yields at 4000 mW laser light qualitatively matching focused 100 mW focused laser light. The spot size of the focused laser was determined by the following formula with the 2.25 mm diameter beam and $M^2 = 1.1$.

$$\text{Spot size} = \frac{4 \times f \times \lambda \times M^2}{\pi \times \text{Beam diameter at lens}} = 91 \mu\text{m}$$

To synchronize the laser and shutter to the trapping cycle, feedback from the voltages on the gate lens of the ion trap was needed. The laser needed to be shuttered when the ion trap is filling, but once filled, the laser should unshutter to irradiate the trapped ions. To allow for ion filling in the LTQ, the gate lens has two DC levels: one at the user-defined value (here optimized to -11.0 V), and a lower value around -55 V when trapping or mass analyzing. During a scan, the ion trap is alternately filled in first a “pre-scan”, where the ion signal is measured to ensure on the subsequent measurement scan that the ion signal is not grossly saturated. A wire connected to the gate lens was used to monitor the fill state of the ion trap, though using the front lens and the ion trap itself were also tested for this purpose. The signal and ground wires were passed through blank pins on an 8-pin vacuum feedthrough and connected to a Tektronix 3052 oscilloscope. A plot of the gate lens voltage vs time is shown below for a scan.

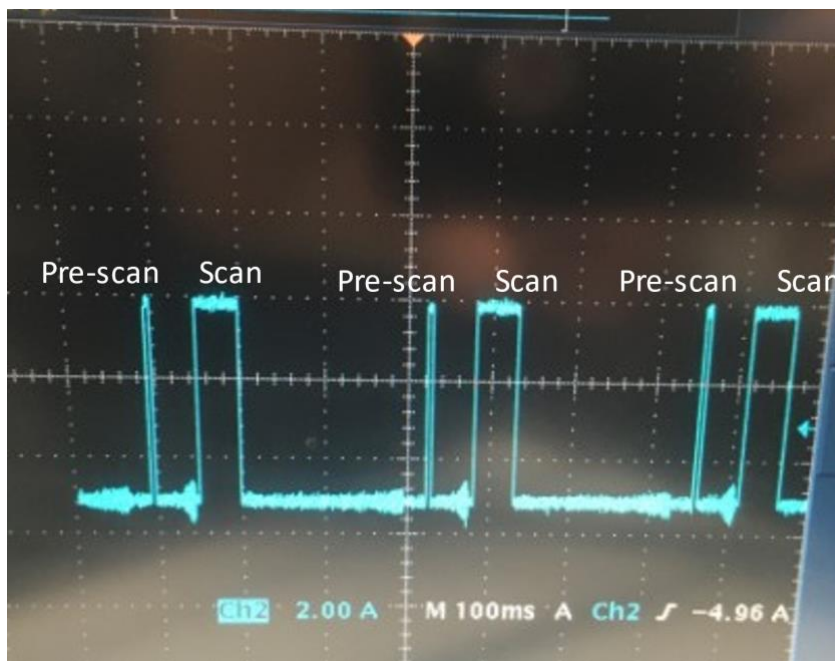


Figure 1.3: Screenshot of the unfiltered DC-coupled gate lens voltage as a function of time during a MS^n spectrum of $m/z = 301$.

A pulse sequence consists of multiple voltage changes for the gate lens. Injection is 500 ms at -11 V, followed by 1000 ms trapping at -55 V, with the triangular area representing analysis, the length of time and variation in amplitude growing as mass range analyzed grows. The short pre-scan, pre-scan trap, and mass analysis are visible to the left of the normal mass analysis in the AC-coupled screenshot. Below are the DC and AC-coupled MS^n mass spectra of $m/z = 301$ at 5% full voltage scale.

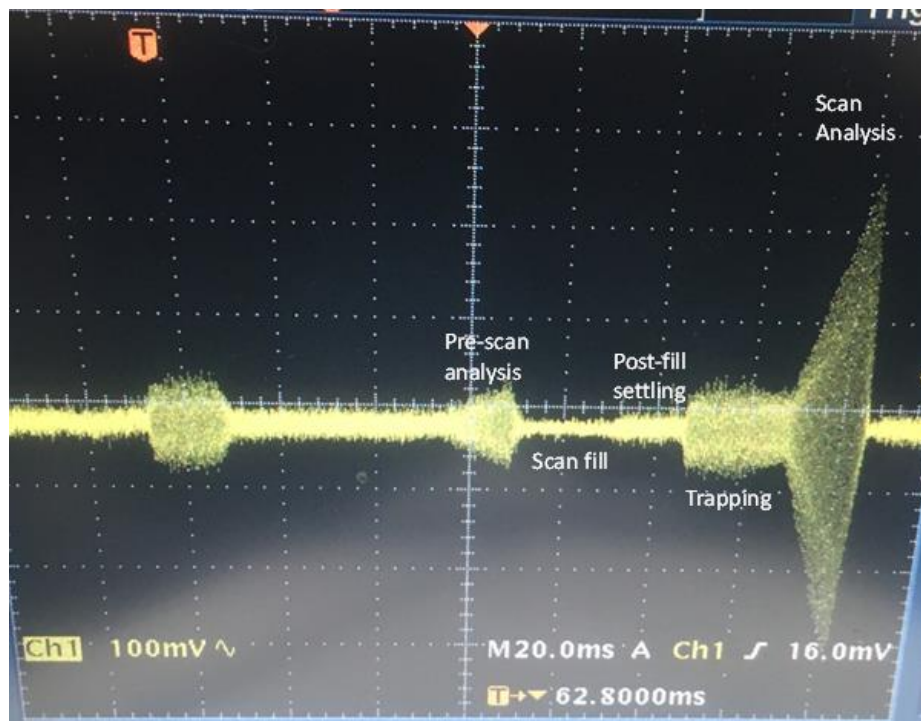


Figure 1.4: Screenshot of the AC-coupled gate lens pulse sequence during an MS^n trapping at $m/z = 301$.

The DC oscilloscope screenshot shows the gate lens is only at the higher -11 V level when the trap is filling. After the scan fill is a 29.8 ms settling period when the injected ions are collisionally-stabilized before trapping for a user-set length of time (which may include CID) and sequential mass ejection. The importance of this 29.8 ms period will be discussed later.

Because the pre-scan filling signal has a shorter duration than the real scan's signal, this difference can be exploited to trigger the laser. To convert this difference in time-duration to a difference in voltage for triggering, a low-pass RC filter was built, with the circuit diagram below:

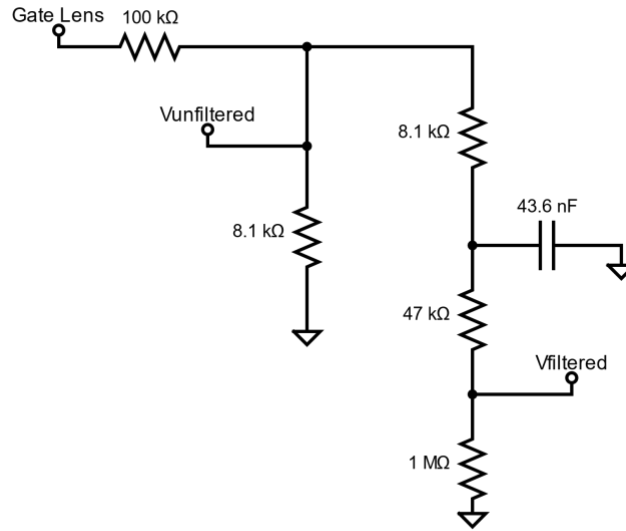


Figure 1.5: Low-pass circuit for filtering the LTQ gate lens signal. Frequency -3 dB cutoff is 38 Hz.

The $100\text{ k}\Omega$ resistor provided sufficient impedance to avoid disrupting the gate lens voltage in the vacuum region of the mass spectrometer, without which the mass spectrometer was found not to transmit any ion current. The $V_{\text{unfiltered}}$ connection provides visualization of the AC-coupled signal, while the 43.6 nF capacitor provides the RC filtering with the $47\text{ k}\Omega$ and $1\text{ M}\Omega$ resistors. The V_{filtered} signal is 4.7% the voltage without the voltage divider, to ensure the filtered signal remains $\pm 2.5\text{ V}$ for the upcoming digital delay generator (DDG). Consideration was given to the RC circuit's -3 dB cutoff, occurring at:

$$f_c = \frac{(R_1 + R_2)\sqrt{10^{\frac{3}{10}} - 1}}{2\pi R_1 R_2 C} = \frac{0.995(104.05\text{ k}\Omega + 1.047\text{ m}\Omega)}{2\pi(1.047\text{ M}\Omega)(104.05\text{ k}\Omega)(43.6\text{ nF})} = 38\text{ Hz}$$

A plot of the AC-coupled gate lens signal, the filtered gate lens signal (as compared to the unfiltered AC-coupled signal above), and a photodiode watching the shuttered reflected laser light can be seen below.

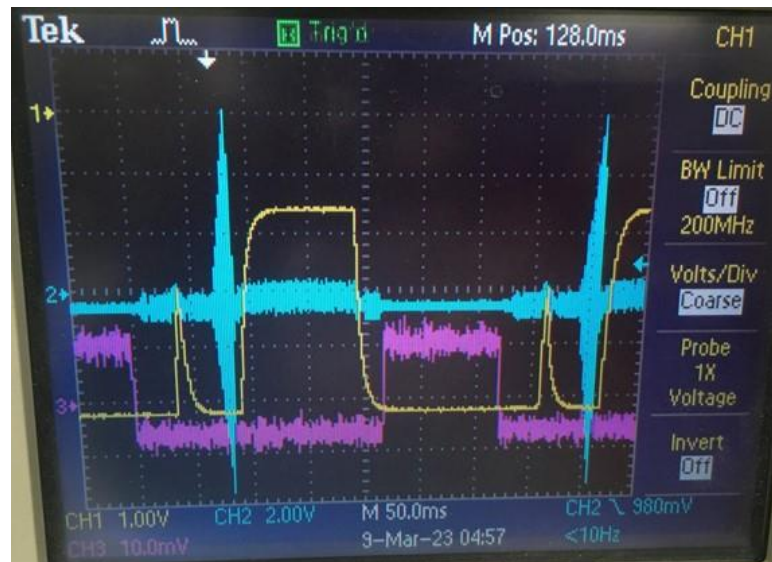


Figure 1.6: Screenshot of the AC-coupled gate lens signal (blue), filtered gate lens signal (yellow), and shuttering photodiode signal (pink).

The filtered signal could then be used as the input trigger into an SRS 535 DDG / pulse generator to gate the shutters with simple digital logic. A diagram of voltage vs time in a pulse sequence is shown below.

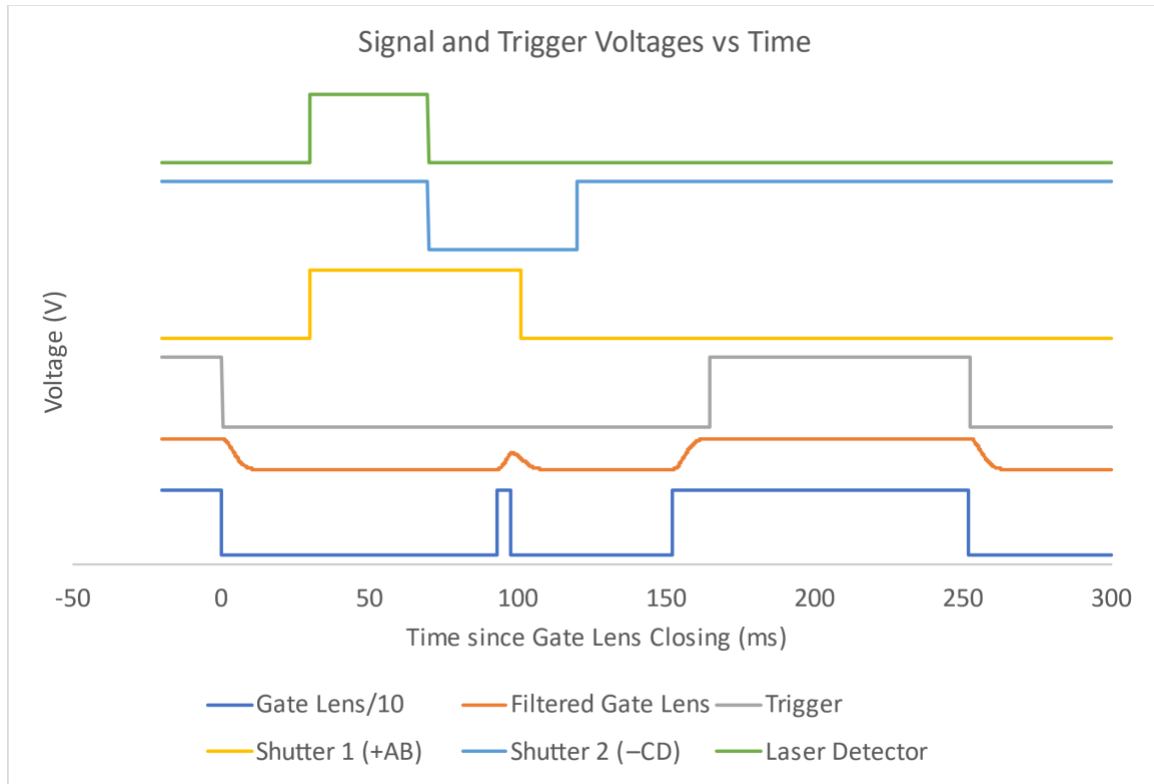


Figure 1.7: Voltage vs time for gate lens, shutters, and laser during pulse sequence. Two shutters were needed because a single shutter could not the laser fast enough to provide a consistent <25 ms chopped beam. In our configuration, after the ion trap had been filled, the DDG trigger was set to the falling edge of the processed gate lens signal. The trigger threshold was set high enough to trigger off the real scan fill and not the pre-scan fill, with resolution around 1 ms opened (with an opening time of 7 ms) to pass the beam, then shutter 2 closed to block the beam, allowing for a consistent open time as short as 1 ms. The two shutters then reset to the starting positions while continuously blocking the beam.

The delay between the trigger and the signal sent to open shutter 1 (A-delay) was set to 22.4 ms to account for the delay between the closing of the gate lens and the trigger starting (0.4 ms) and the shutter opening (7 ms), resulting in the laser irradiating the

trapped ions 29.8 ms after the ion trap gate lens closing. The delay to close shutter 2 (C-delay) was set to the desired laser irradiation time. The delay to close shutter 1 (B-delay) was set to $C + 10$ ms, and the delay to open shutter 2 (D-delay) was set to $B + 10$ ms. The trigger was set to the falling edge of the filtered gate lens output, and the trigger height of -2.00 V. The output pulses were TTL pulses, and the output fed to the Tektronix oscilloscope and the shutter controller, which would open with a high voltage TTL state. A summary table can be found below.

Table 1.2: SRS 535 delay times for each channel.

SRS 535 Delay	Value (ms)
Trigger ($t = 0$)	Falling edge of filtered gate lens signal, -2.00 V
A	Trigger + 22.4
B	$C + 10$
C	A + desired irradiation time
D	$B + 10$

The resulting mass spectra were processed by fitting a series of peaks to a sum of Gaussian peaks, because the tails of each peak were overlapping. This resulted in a computationally challenging model to optimize, with each Gaussian peak requiring fitting of the peak height, center, and width. Below is an example plot of a Gaussian fit requiring 15 peaks (45 independent parameters) to be optimized. Because the residuals all exhibit the same trend across peaks, the peak-fitting model could be changed to include a peak-asymmetry parameter. This upgrade was employed by Castellanos, who used a Pearson IV fit to reduce fitting error at the cost of an extra fitting parameter.¹⁵ However, even using the simplest model—using the maximum experimental counts within ± 0.5 amu of a peak—yields maximum ion counts that are at most only 10% lower than the Gaussian fit maximum ion counts.

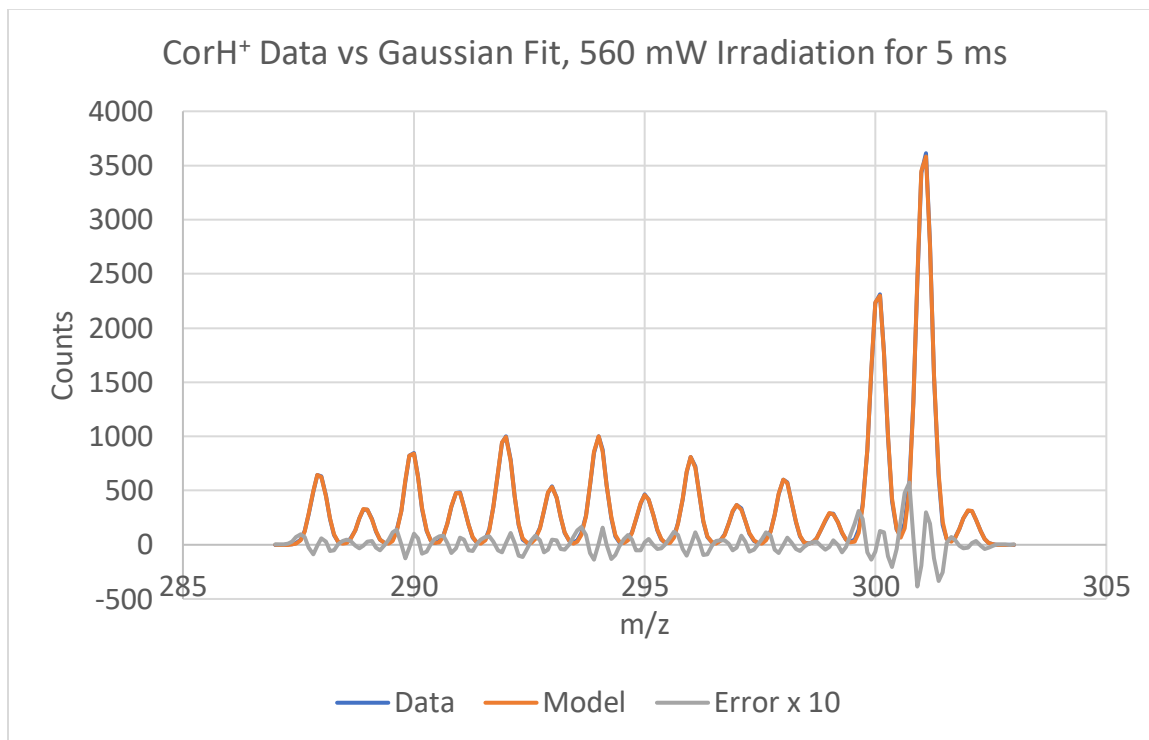


Figure 1.8: Example plot of data (blue) vs modeled fit of sum of 15 Gaussian peaks (orange) with residuals (grey).

Results:

The mass spectrum's dependence on trap time and laser power was investigated, with the following combinations of trap time and laser power explored. The conditions used were:

Table 1.3: List of laser power and irradiation times measured.

Laser Power at 532 nm (mW)	Laser Irradiation Time (ms)
0	5
9	10
16	20
40	50
80	100
160	250
240	500
320	1000
400	
560	
800	
1600	
2400	
3200	
4000	

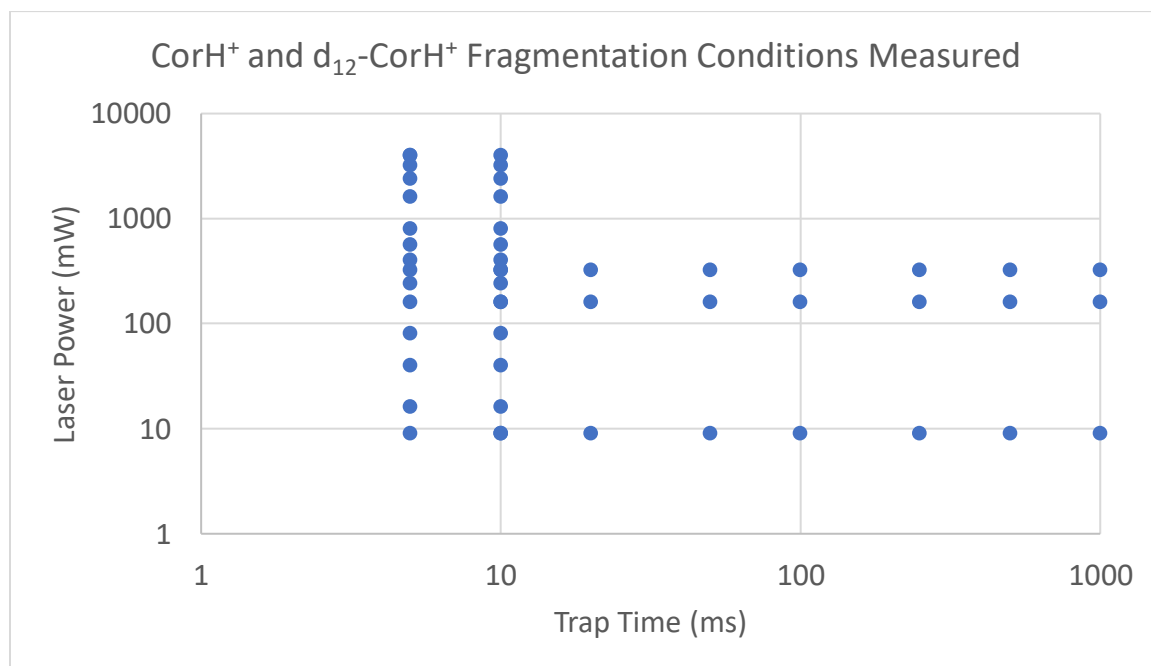


Figure 1.9: Laser power and irradiation time combinations measured.

Coronene

Because of coronene's high C:H ratio, any coronene fragment in a coronene-only MSⁿ scan can be unambiguously assigned as C_nH_m⁺, with $n \leq 24$ and $m \leq 12$. The overall mass spectrum of the coronene solution without laser irradiation looks as such:

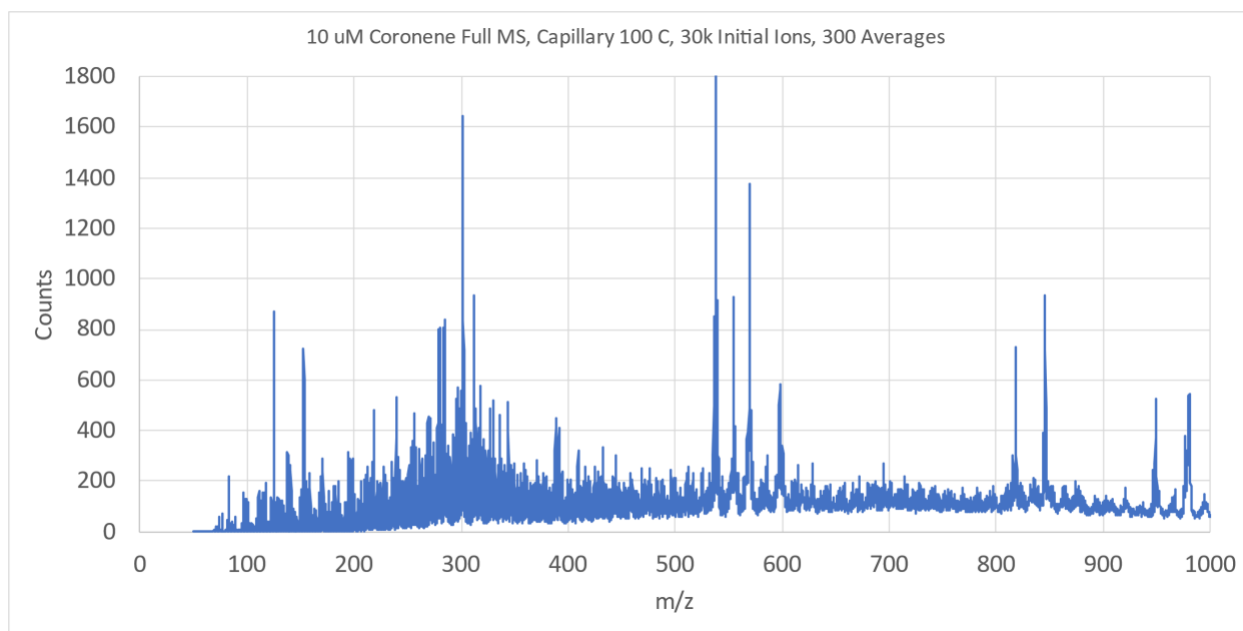


Figure 1.10: Spectrum of CorH⁺ sample prior to mass selection.

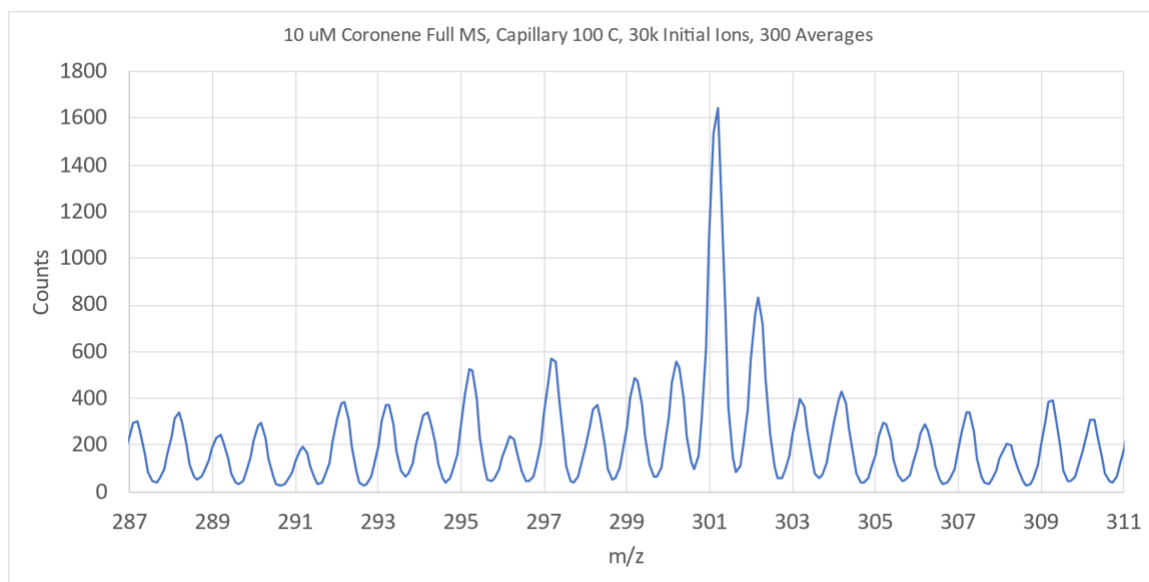


Figure 1.11: Spectrum of CorH⁺ sample prior to mass selection, narrower mass range.

A table of some prominent masses can be seen below:

Table 1.4: Prominent masses in coronene mass spectrum scan mode.

m/z	Intensity (blue)	Uncertainty	Proposed Identity
125.0	873	26	
153.1	725	22	
301.2	1645	49	Coronene-H ⁺
302.2	830	25	¹³ C-Coronene-H ⁺
312.3	936	28	
318.2	936	28	Coronene-NH ₄ ⁺
537.9	4165	125	Likely is 554.6 peak without OH
554.6	872	26	Likely is 569.4 peak without CH ₃
569.4	1327	40	
597.4	548	16	Dicoronylene-H ⁺
817.7	729	22	
845.8	891	27	
948.7	500	15	
980.3	484	15	

Several peaks associated with coronene were seen, confirmed by a CID spectrum, indicating the procedure for producing CorH⁺ was successful. The higher m/z peaks likely come from contaminant PAHs in the sample. The CID spectra of these molecules do not give meaningful clues to these molecules' identities. The d₁₂-CorH⁺ sample spectrum was similar, just with peaks shifted by expected per-deuteration.

The CID spectrum at CID = 50 is shown below.

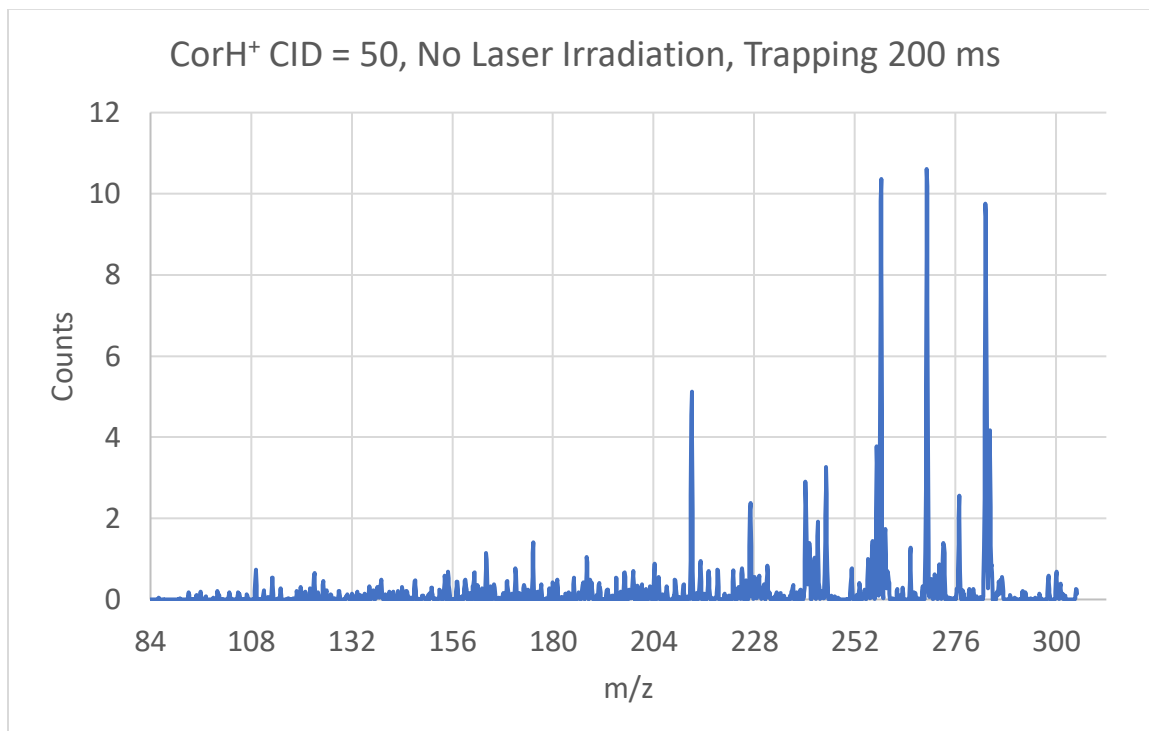


Figure 1.12: CID Spectrum of CorH⁺ at CID = 50 and 200 ms trapping.

The photodissociation (PD) yield of the CorH⁺ is shown as a function of laser power for both a 5 and 10 ms irradiation time. The full mass spectra are seen in the appendix.

These short irradiation times were chosen to highlight CorH⁺ evolution on short timescales. Photodissociation yield was calculated using the relationships:

$$\text{PD Yield} = 1 - I_{301}/I_{\text{totalF}}$$

$$\text{PD Yield} = 1 - I_{301}/I_{\text{total0mW}}$$

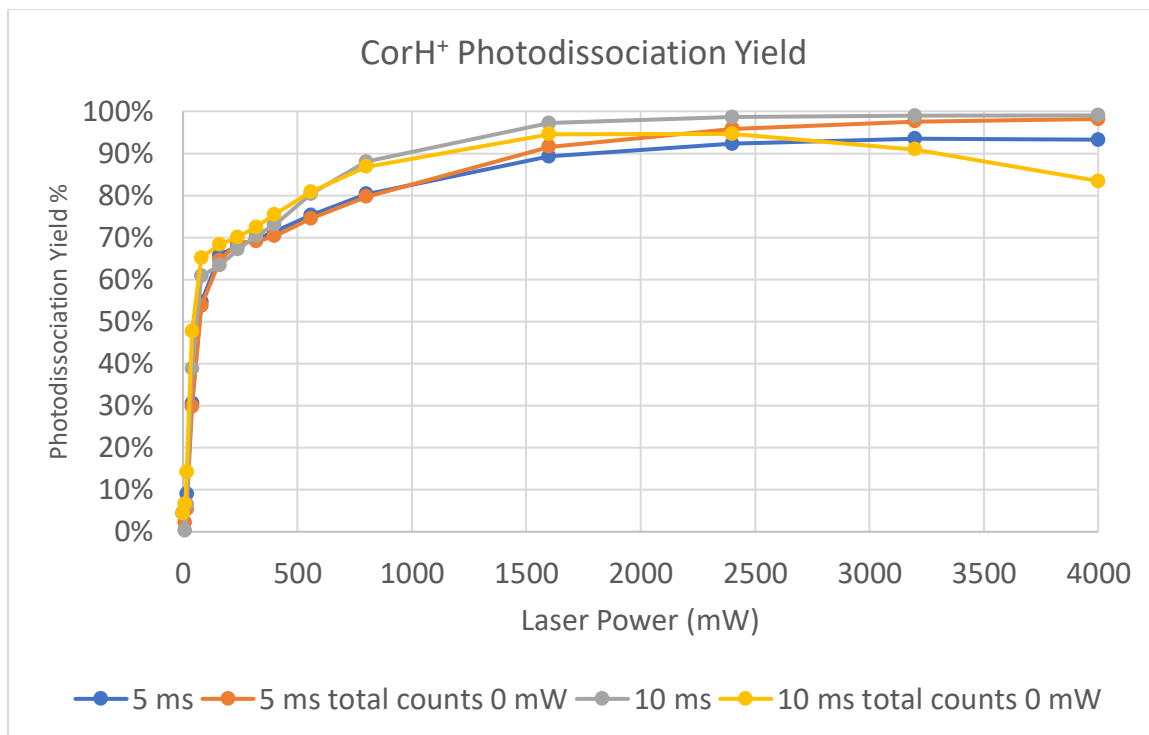


Figure 1.13: Photodissociation yield vs laser power at 5 ms irradiation time. The orange and yellow traces use the total counts seen at 0 mW irradiation as the reference, while the blue and grey curves use the total counts of the irradiated spectrum.

Scanning the laser power with a 5 ms irradiation yields the following product $m/z = 300$ curve.

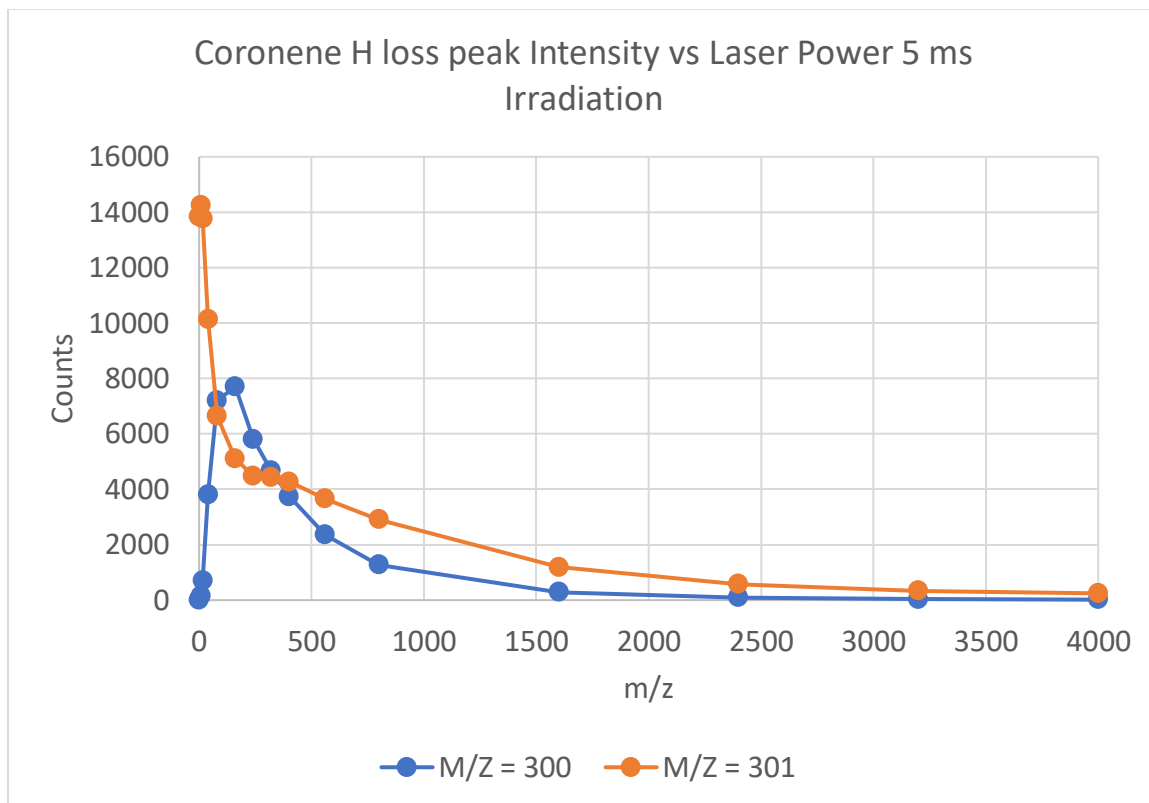


Figure 1.14: CorH^+ vs Cor^+ peaks at 10 ms irradiation.

These plots highlight different areas of the same data set, namely the dependence of the mass spectrum with laser power at a constant 5 ms irradiation time. The following plots present the same ion count data as a function of power instead of m/z.

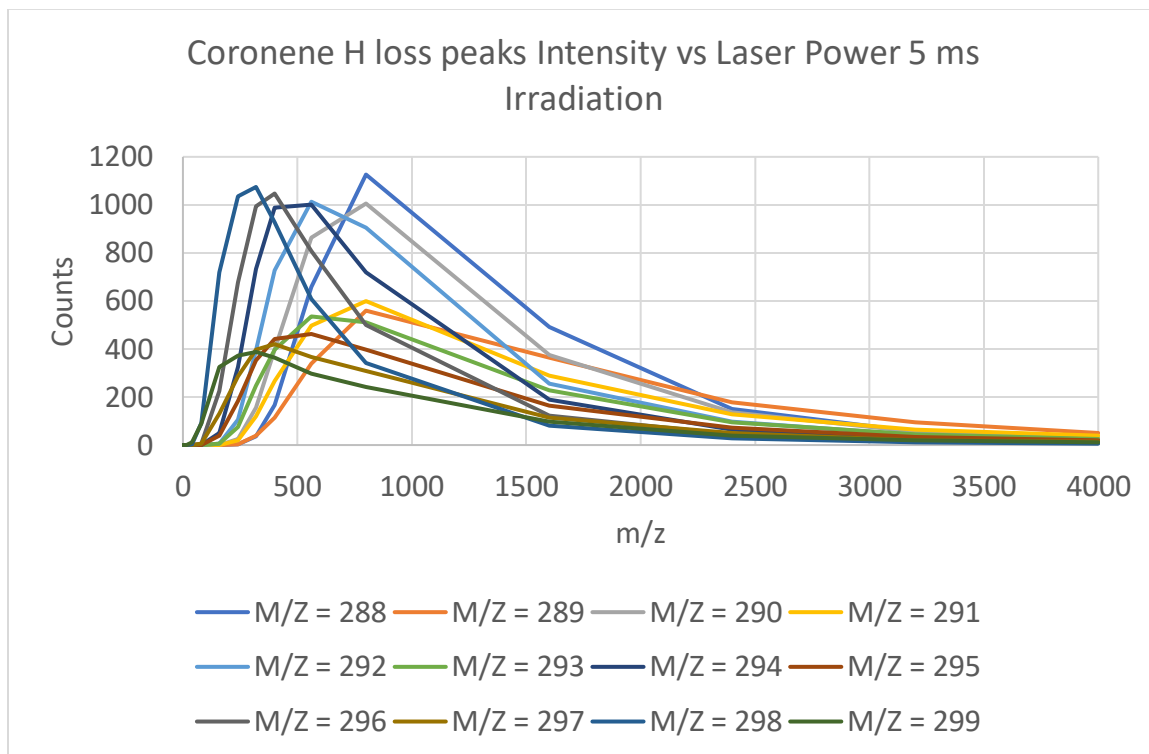


Figure 1.15: Ion counts vs laser power at 5 ms irradiation time for H-loss region peaks

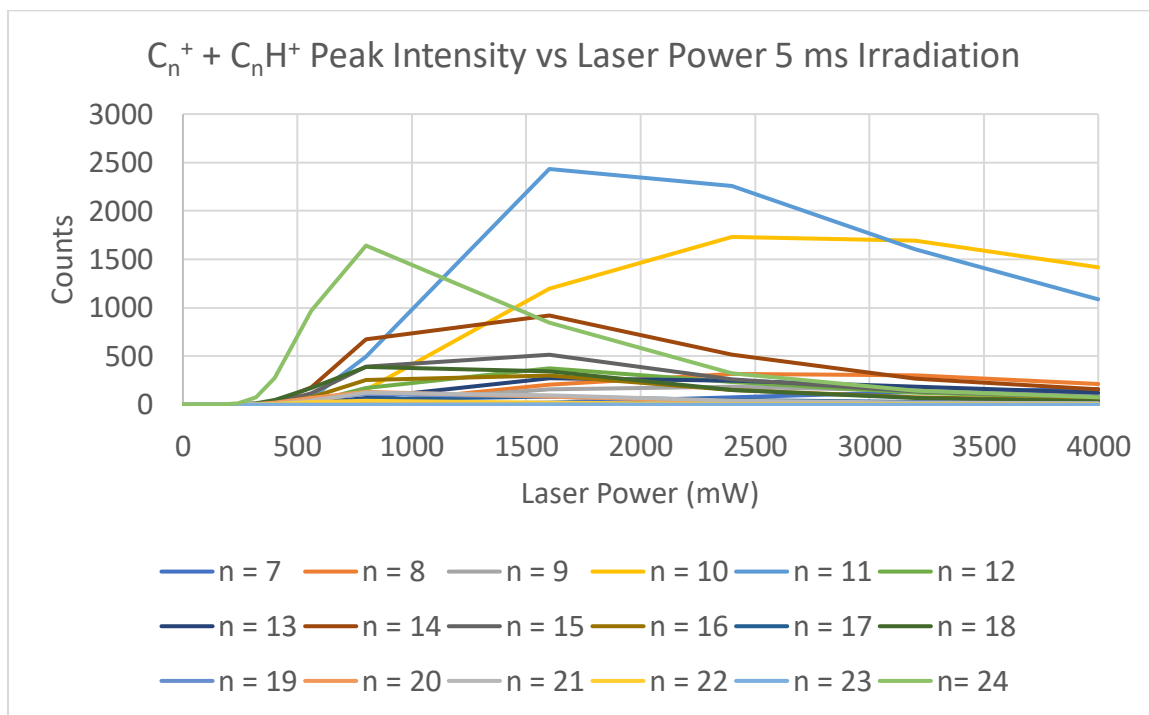


Figure 1.16: Ion counts vs laser power at 5 ms irradiation time for C-loss region peaks

A great deal can be gleaned from the mechanism of photofragmentation through these plots. One conclusion is the existence of three different photofragmentation regimes based on laser power, which will be termed low (<80 mW), middle (80 – 560 mW), and high (>560 mW).

In the low photofragmentation regime, the PD yield shows a rapid increase with increasing laser power. In the plot of $m/z = 300$ and 301, the low regime corresponds to dehydrogenation of CorH^+ forming Cor^+ , but little fragmentation is seen in the plots of $m/z = 299$ or 298 ion counts vs laser power. Since protonating coronene creates an aliphatic sp^3 carbon atom while removing an aliphatic H would restore coronene's aromaticity, one of these two H atoms are likely lost creating $m/z = 300$. For the $m/z = 299$ and 298 counts that can be seen, the counts for $m/z = 299$ are great than $m/z = 298$, indicating either single-H atom removal process from $m/z = 300$ dominates, or photon intensities are low enough to allow a small fraction of CorH^+ to dehydrogenate H_2 to become $m/z = 299$.

In the middle photofragmentation regime, the PD yield vs laser power shows a decrease in slope, but the PD yield remains linear to laser power. This regime sees Cor^+ undergo multiple dehydrogenation events, resulting in a bare C_{24}^+ ion at $m/z = 288$. An aromatic C–C bond dissociation energy (BDE) is approximately 124 kcal/mol (5.38 eV), while the predicted C–H BDE of neutral coronene is 26.6 kcal/mol (1.15 eV).³⁰ As laser power increases, the distribution of the peaks between $m/z = 288$ to 300 shifts towards C_{24}^+ , as exhibited in the plot of each peak's counts vs laser power. Another feature of this photofragmentation regime is the appearance of an alternation in peak intensities, with even m/z peaks at significantly higher intensity than odd m/z peaks. This

pattern indicates dehydrogenation occurs mainly through loss of H_2 rather than H , and because both the reactant and product cations are both large (24 – 36 atoms) and of similar structure, the cause is likely the stability of the product H_2 vs H . The predicted C–H BDE of neutral coronene is 26.6 kcal/mol (1.15 eV),³⁰ but when H_2 is a product, the energy is –104 kcal/mol (4.51 eV), making the loss of the H_2 favorable over the sequential losses of H then H , if energy is constrained like in the middle photofragmentation regime. A plot of the odd/even ratio of the peaks is shown below, which shows the ratio decrease throughout the middle photofragmentation regime. Because the even m/z peaks are larger, this indicates the H_2 loss started with $m/z = 300$, and that the odd peaks are due to a less common H loss transforming an even into an odd peak.

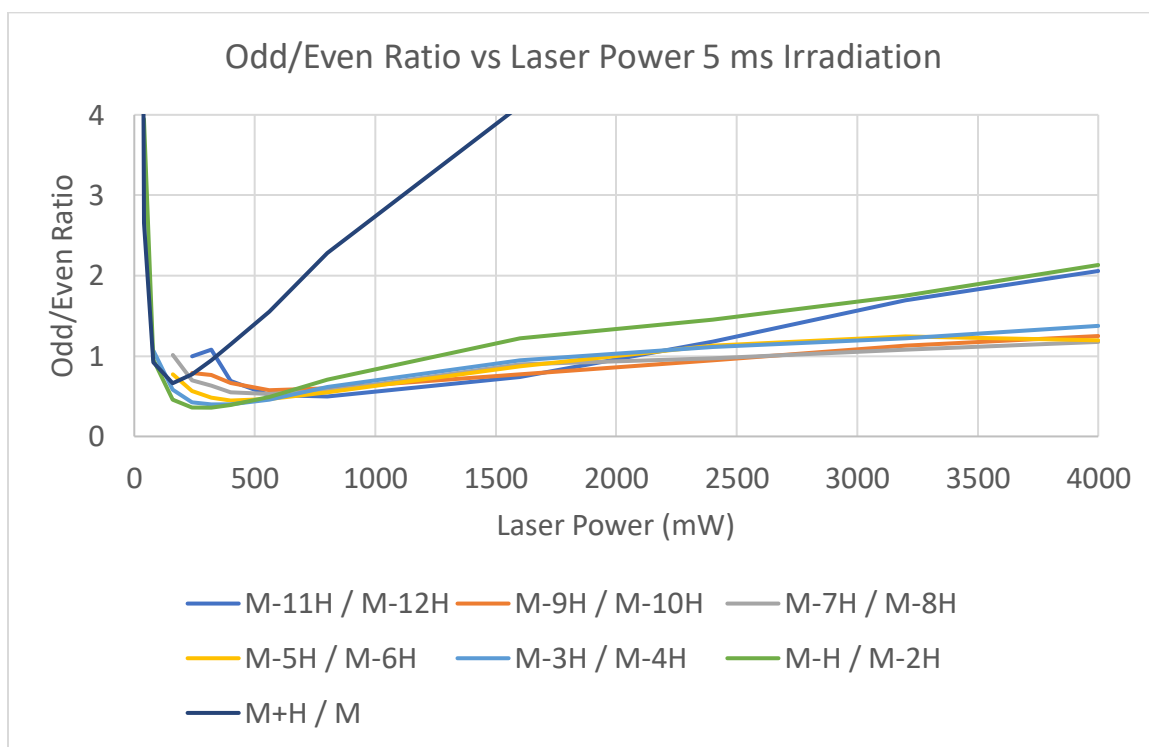


Figure 1.17: Odd/Even ratio vs laser power at 5 ms irradiation.

However, this odd/even ratio result is completely reversed if the 29.8 ms A-delay on the mass spectrometer shutter is changed to 0 ms. This allows irradiation to begin as soon as the ions have entered the trap, without time to collisionally de-excite. While all spectra which are in the middle photofragmentation regime for laser power demonstrate the odd peak enhancement, the selected example below has a high odd/even ratio.

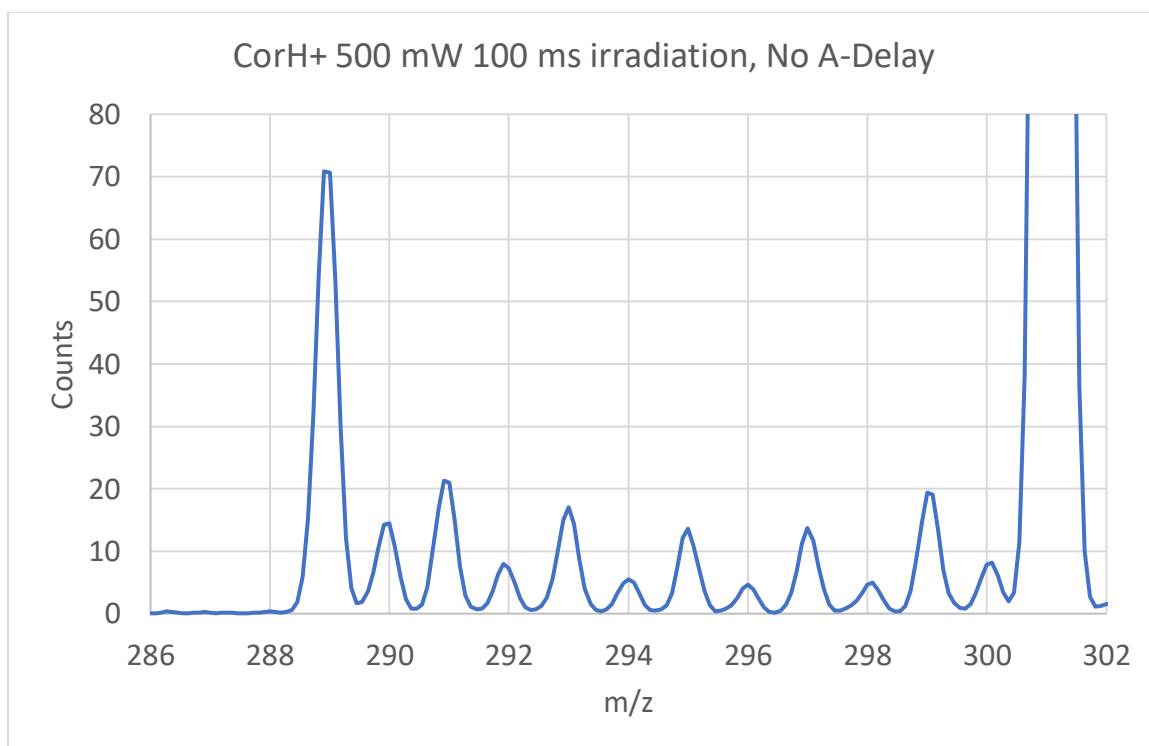


Figure 1.18. CorH⁺ spectrum 500 mW 100 ms irradiation without A-delay

A nearly-universal feature of spectra taken without an A-delay is $m/z = 289$ C₂₄H⁺ is the end product of the H-loss region. Almost no C₂₄⁺ is created without an A-delay, and because H₂ is the primary loss process for Cor⁺, H loss to form C₂₄⁺ is unlikely, especially with the strong binding of H to C₂₄⁺ discussed later. This pattern suggests without an A-delay, CorH⁺ actually dissociates to C₂₄H₁₁⁺ in a sequential manner at moderate laser powers, despite Cor⁺ being the first fragment seen from CorH⁺ without an A-delay at low laser powers. The extra E_{int} available without collisional stabilization

likely allows CorH^+ to have two H atoms sequentially dissociate via a higher energy mechanism that does not need the energy released from H_2 formation.

The third regime is the high photofragmentation regime, where C atoms are lost from the dehydrogenated cation. In the $m/z = 288 - 300$ range, the odd/even ratio starts to increase again, which could be due to differences in the absorption cross-section of the $\text{C}_{24}\text{H}_m^+$ ions. The ions in the $m/z < 288$ region are all C_n^+ or C_nH^+ products of fragmentation of either C_{24}^+ or C_{24}H^+ , since had C fragmentation occurred from other reactant ions, masses with more than one H would be visible. The C_{24}H^+ ion would give rise to C_nH^+ products, because losing a single H to form C_n^+ would be thermodynamically unfavorable, and the H serves as an identifier for C_nH^+ products.

The PD yield of the high photofragmentation regime exhibits an exponentially-decreasing growth of the PD yield towards 100% with laser power, however, the two metrics for PD yield start to diverge. This is because the metric using a scan's summed ion count as the total number of starting $m/z = 301$ ions is missing ions, as some have likely dissociated to ions smaller than the low-mass cut off of $m/z = 81$ and are no longer observed, reducing the total ion count. With the CorH^+ ion count = 236 even at 4000 mW, the total number of observable is decreasing faster than the number of CorH^+ dehydrogenating.

The distribution of products shifts towards smaller n with increasing laser powers, and for a given n value for C_n^+ and C_nH^+ , smaller n value ions reach that those ions' maximum ion counts at a higher laser power. However, there is not a smooth trend in the value of the maximum ion counts with n, because of the chemical identity of that ion. Values for $n = 10, 11, 14,$ and 18 are particularly abundant.

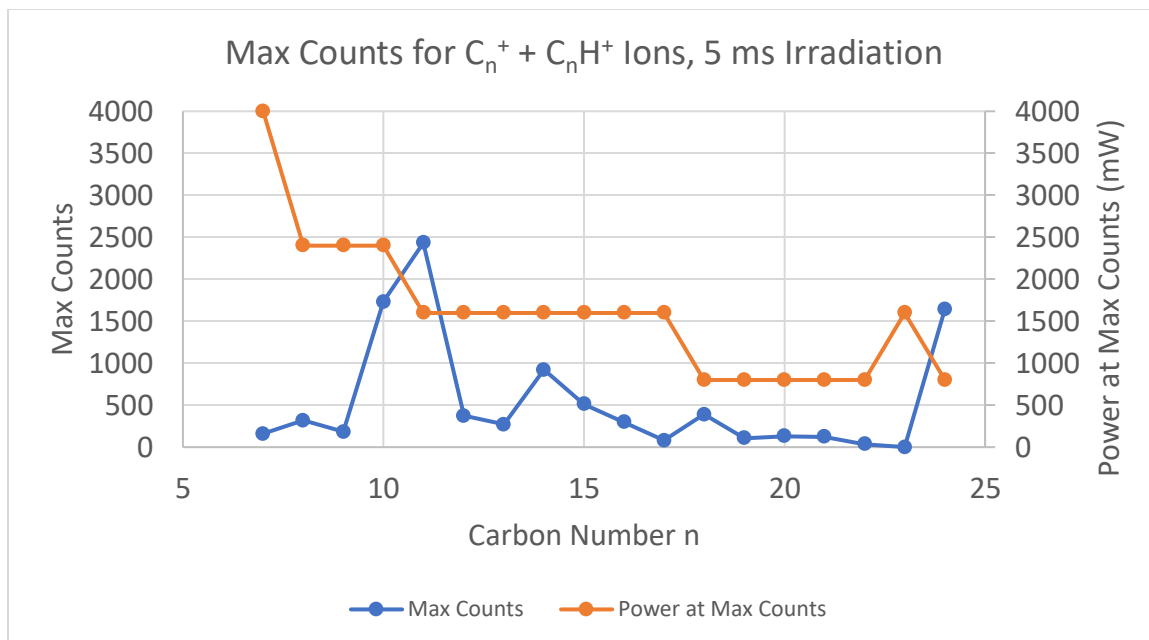


Figure 1.19: Max counts and power for C-loss region, 5 ms irradiation time

Another result to the high photofragmentation regime is the C_n^+/C_nH^+ peak ratio and how this ratio changes with laser power. Below is a plot of this ratio with respect to laser power and to carbon number n (full-scale versions of this plot can be seen in the appendix).

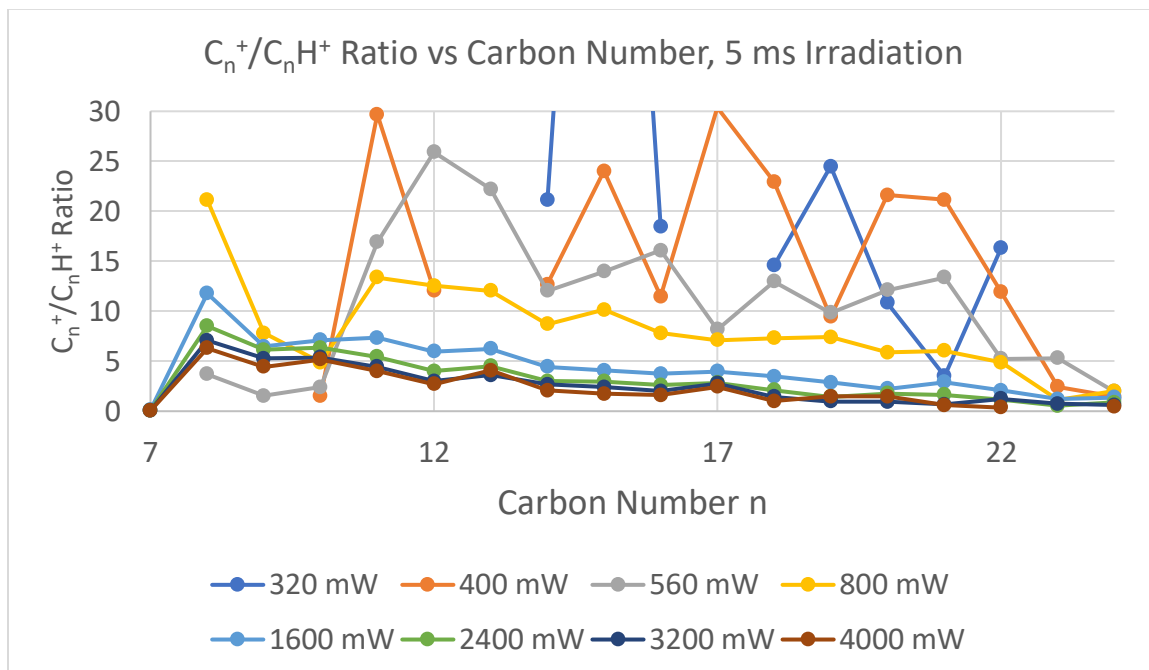


Figure 1.20. C_n^+/C_nH^+ ratio in C-loss region, 5 ms irradiation time

Much of the variance in the C_n^+/C_nH^+ ratio comes at lower laser powers, with the ratio curves for 1600 – 4000 mW laser irradiation following a similar trend with respect to carbon number and power. At high power, a general trend could be seen, and parameters A, B, C, D, and E were fit as a function of carbon number n , the $m/z = 288/289$ ratio R at laser power P , and the trapping time T :

$$\frac{C_n^+}{C_nH^+} = A \left(\frac{1 - \frac{n}{24}}{\frac{n}{24}} \right) - BR - C(P - D) - ET$$

The A term is a simple model assuming the H on a $C_{24}H^+$ ion stays attached to a random carbon, and the odds of that carbon remaining on the cation fragment if the cation and neutral fragment formation is chemically unaffected by the H atom's presence. The plot of the 288/289 ratio (the inverse of the odd/even ratio curve) is in the appendix.

The optimized fitting parameters were $A = 3.3$, $B = 0$, $C = 8.6 \times 10^{-4} \text{ mW}^{-1}$, $D = 3900 \text{ mW}$, $E = 2.3 \times 10^{-3} \text{ ms}^{-1}$. A least-squares fit of the model was found to stay nearly within an error of ± 1 for the experimental $\text{C}_n^+/\text{C}_n\text{H}^+$ ratio (residuals seen in appendix).

Next, the same data was taken, except the laser irradiation time was increased to 10 ms. The following plots are similar to the 5 ms CorH^+ plots.

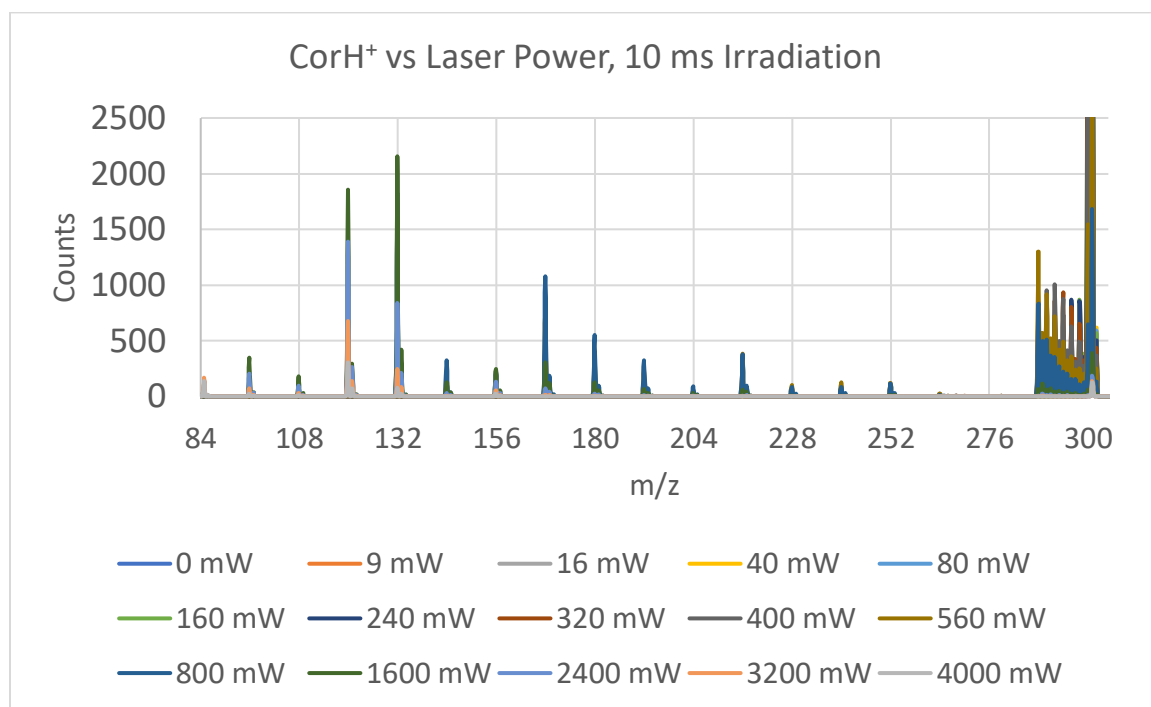


Figure 1.21: Mass spectrum vs laser power at 10 ms irradiation

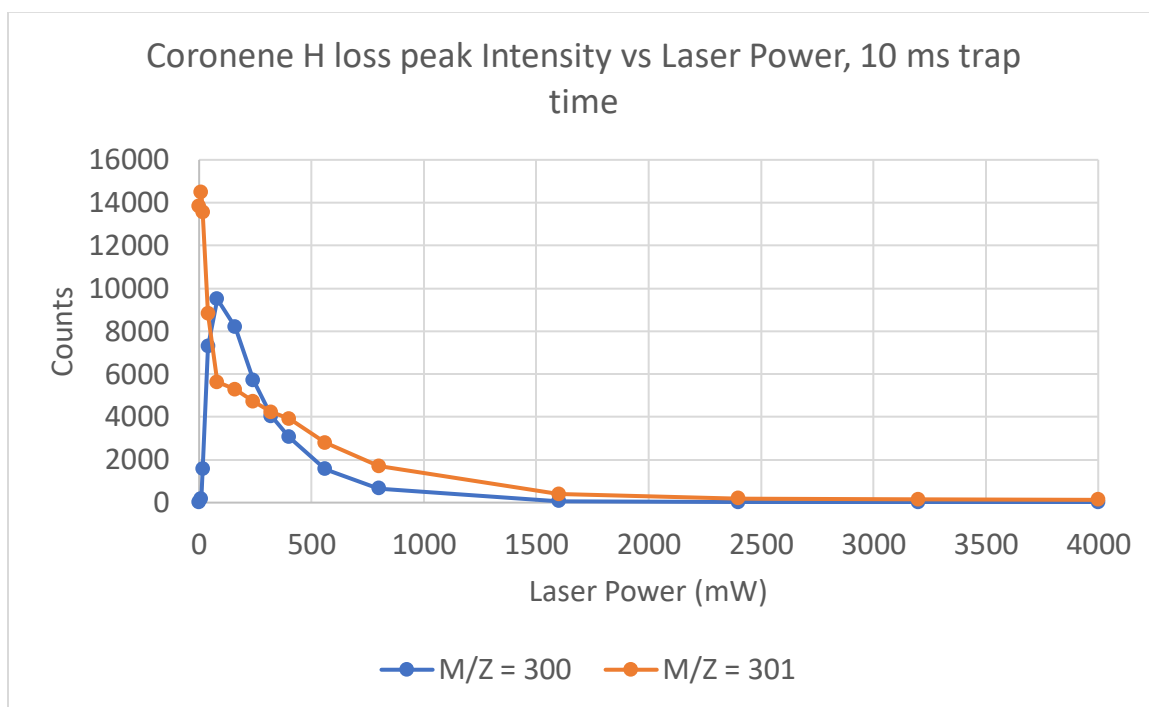


Figure 1.22: CorH⁺ vs Cor⁺ peaks at 10 ms irradiation.

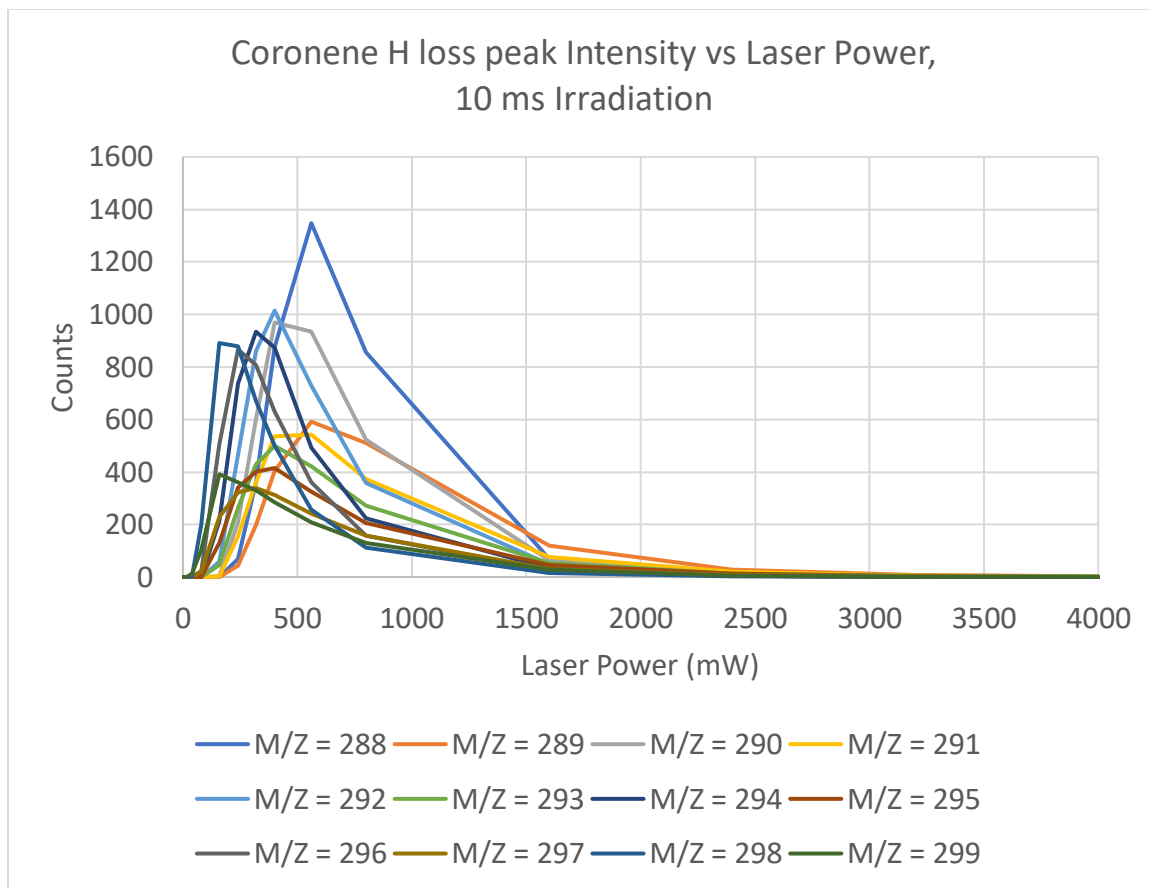


Figure 1.23: H-loss peaks vs power at 10 ms irradiation

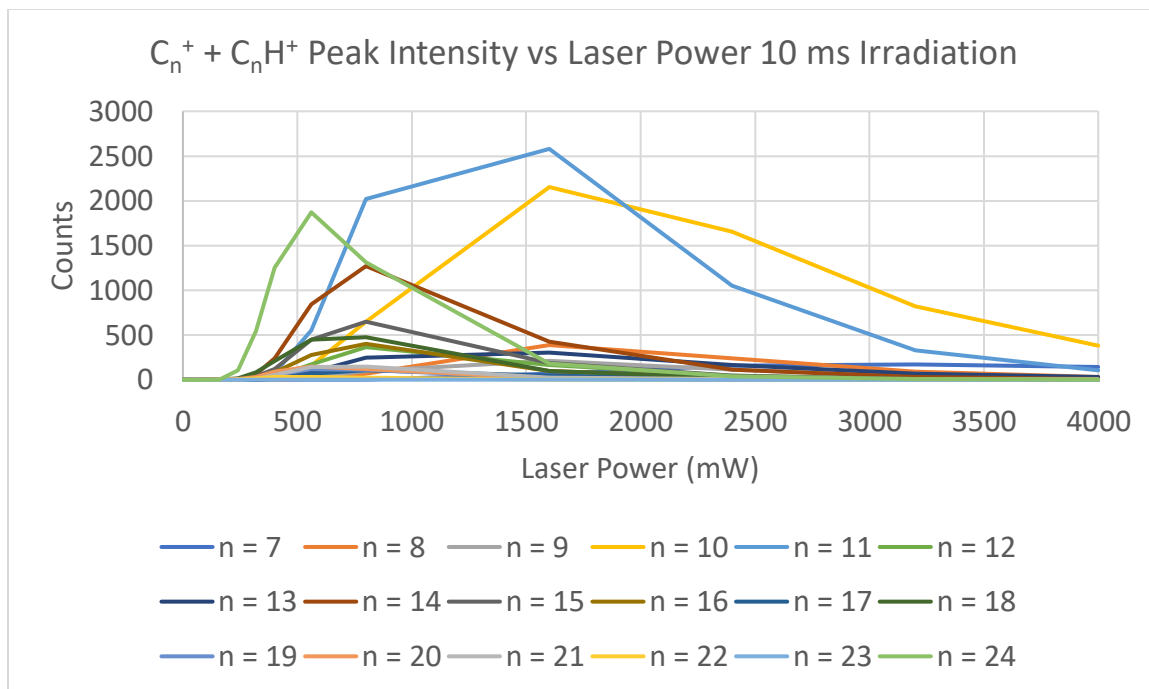


Figure 1.24: C-loss peaks vs power at 10 ms irradiation

At 10 ms, the same trends with respect to power were seen. The PD yield (shown above with the 5 ms irradiation time data) exhibits the same trend in all three photofragmentation regimes, except in the high photofragmentation regime where the difference between the using the sum of the ions in a scan or the sum of the ions in the 0 mW scan is 16% instead of 5%.

In the H-loss region from $m/z = 288 - 301$, in the low photofragmentation regime, the behavior of the 5 and 10 ms irradiation length scans is the same: only $m/z = 300$ Cor^+ is created. In the middle photofragmentation regime, the odd/even ratio was lower, but in the high regime, the odd/even ratio was higher than for the 5 ms irradiation, indicating longer irradiation likely is transforming C_{24}^+ into C_n^+ ($n < 24$) more efficiently than $C_{24}H^+$ into C_nH^+ , again likely due to the larger C_{24}^+ cross-section.

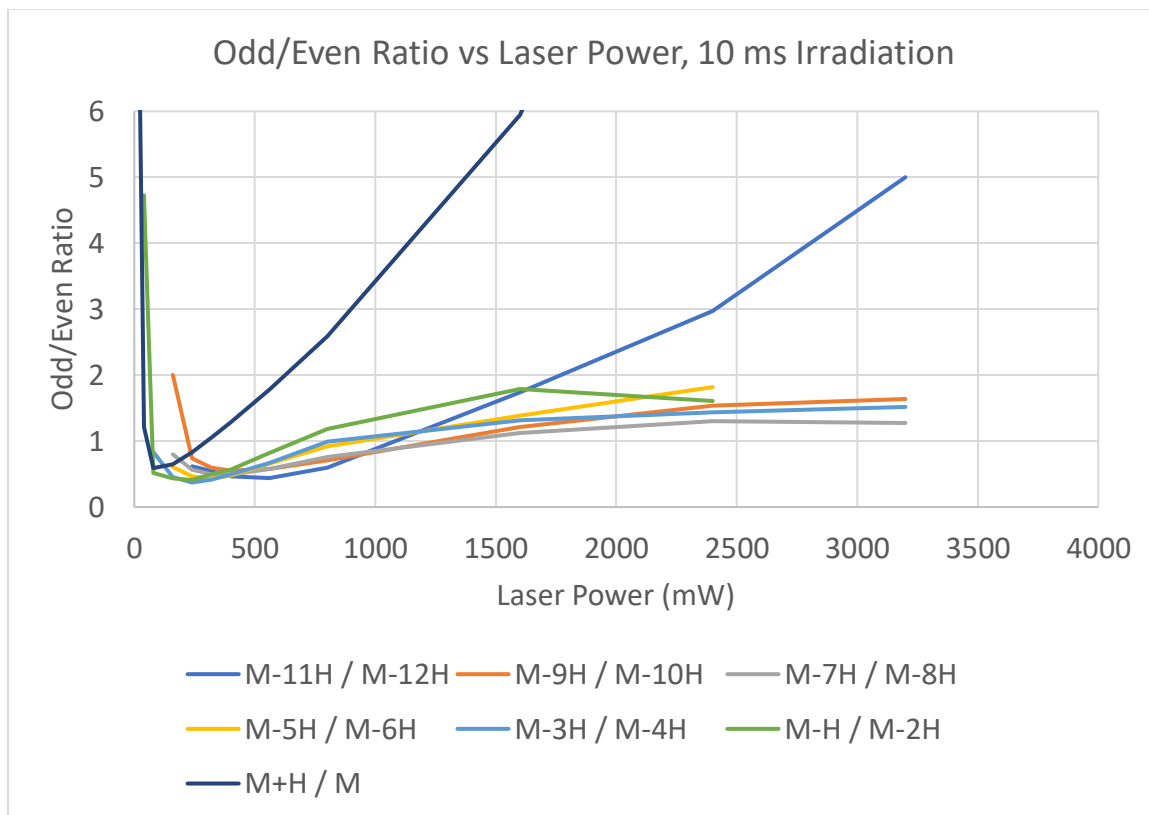


Figure 1.25: Odd/even ratio vs laser power at 10 ms irradiation

In the C-loss region from $m/z = 80 - 288$, the C_n^+/C_nH^+ ratio showed the identical pattern for 10 ms as for 5 ms, but the common ions for 5 ms were an even larger percentage of the total $m/z = 80 - 288$ ions.

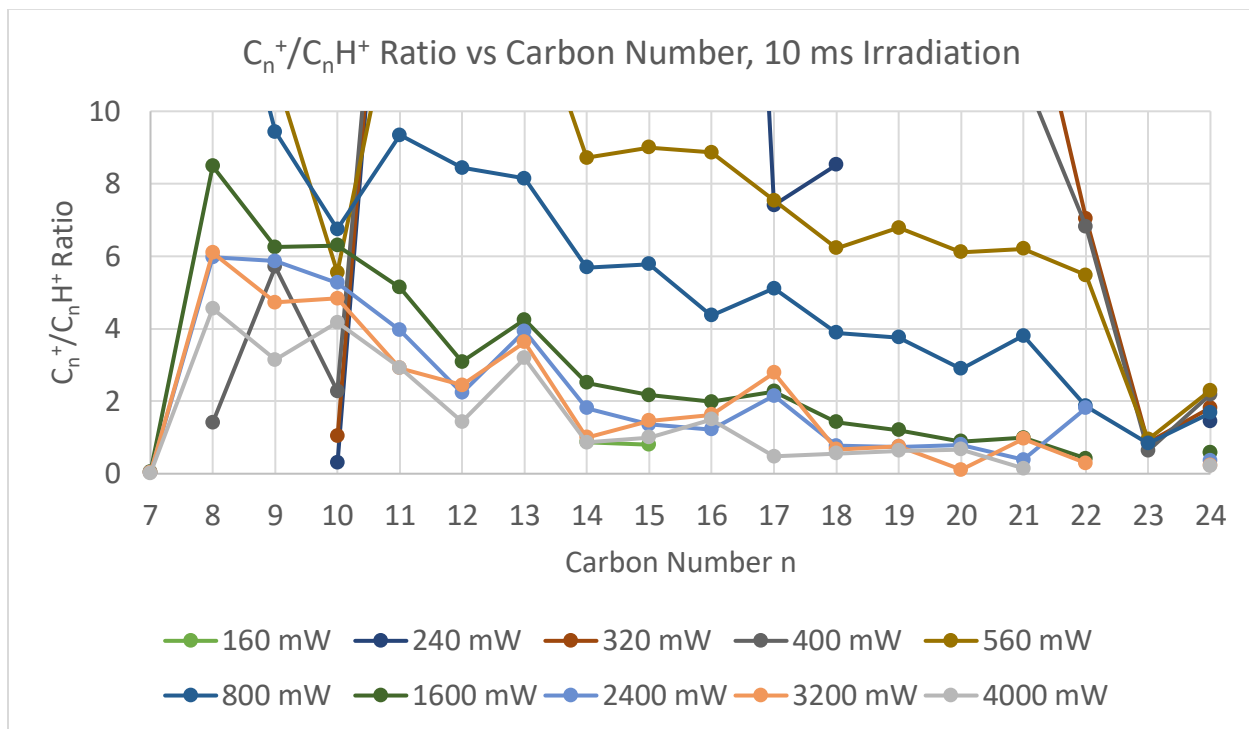


Figure 1.26: C_n⁺/C_nH⁺ Ratio vs Laser Power at 10 ms Irradiation

Performing a fit of the 10 ms C_n⁺/C_nH⁺ ratio with the model used for the 5 ms

C_n⁺/C_nH⁺ ratio (full plot view in appendix), the fit parameters were $A = 2.61$, $B = 0.17$, $C = 6.2 \times 10^{-4} \text{ mW}^{-1}$, $D = 3000 \text{ mW}$, and $E = 2.3 \times 10^{-3} \text{ ms}^{-1}$. The value of E has fit well between these two irradiation time scans, providing evidence that the counts in the C-loss region are proportional to trap time. A plot of the residual fit is in the appendix.

Interesting to note is the ratio of C₁₃⁺/C₁₃H⁺ is consistently underfit by 1 for all 4 high photofragmentation scans used. The value $n = 13$ is not an abundant peak because $n = 13$ is expected to be anti-aromatic for a cation. The additional H may help stabilize the cation, but the structure cannot be determined further with the mass spectrum alone.

Irradiation Time:

After varying the laser power at short irradiation times, next the dependence of irradiation time on the mass spectrum was investigated.

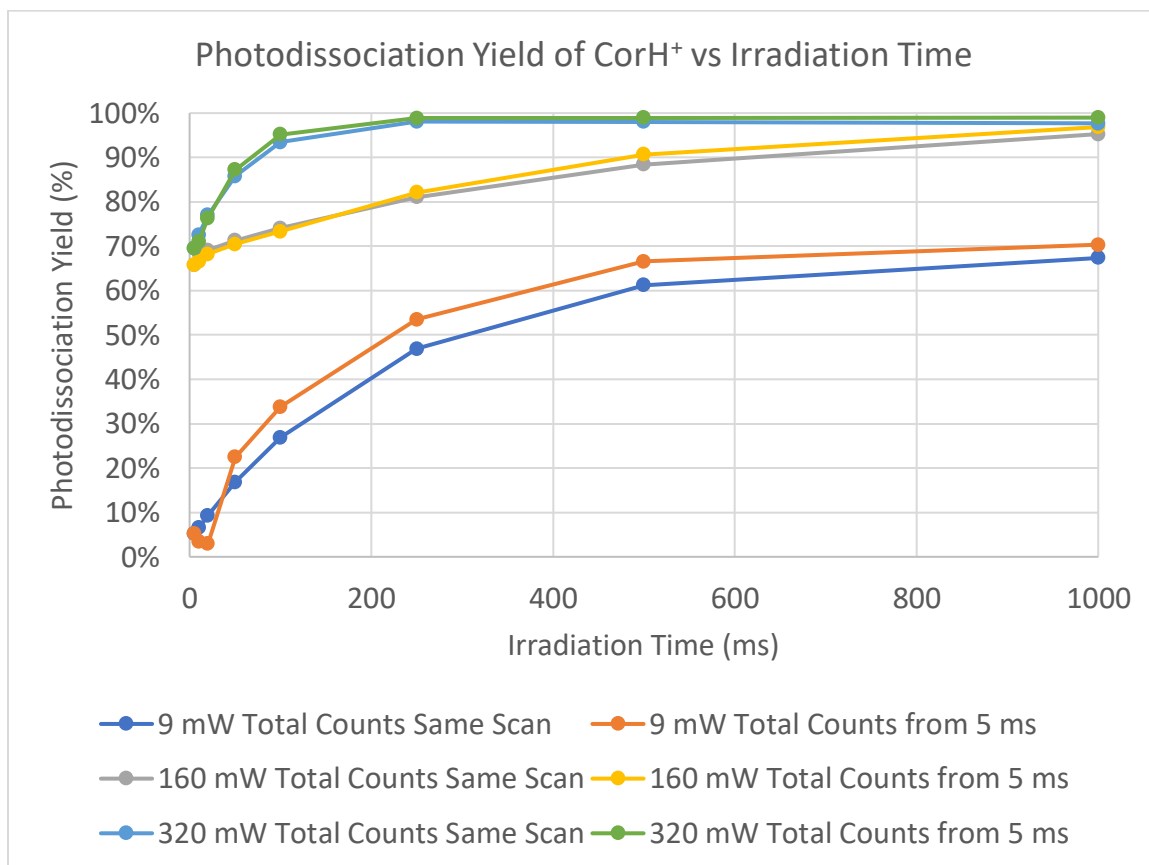


Figure 1.27: PD Yield of CorH⁺ vs Irradiation Time and Laser Power. Total counts are either from the same scan or from the total counts at 5 ms.

The values of 9, 160, and 320 mW correspond to the low and middle photofragmentation regimes. High photofragmentation regime laser powers resulted in weak ion signal, because most of the ions were fully photofragmented to below $m/z = 80$.

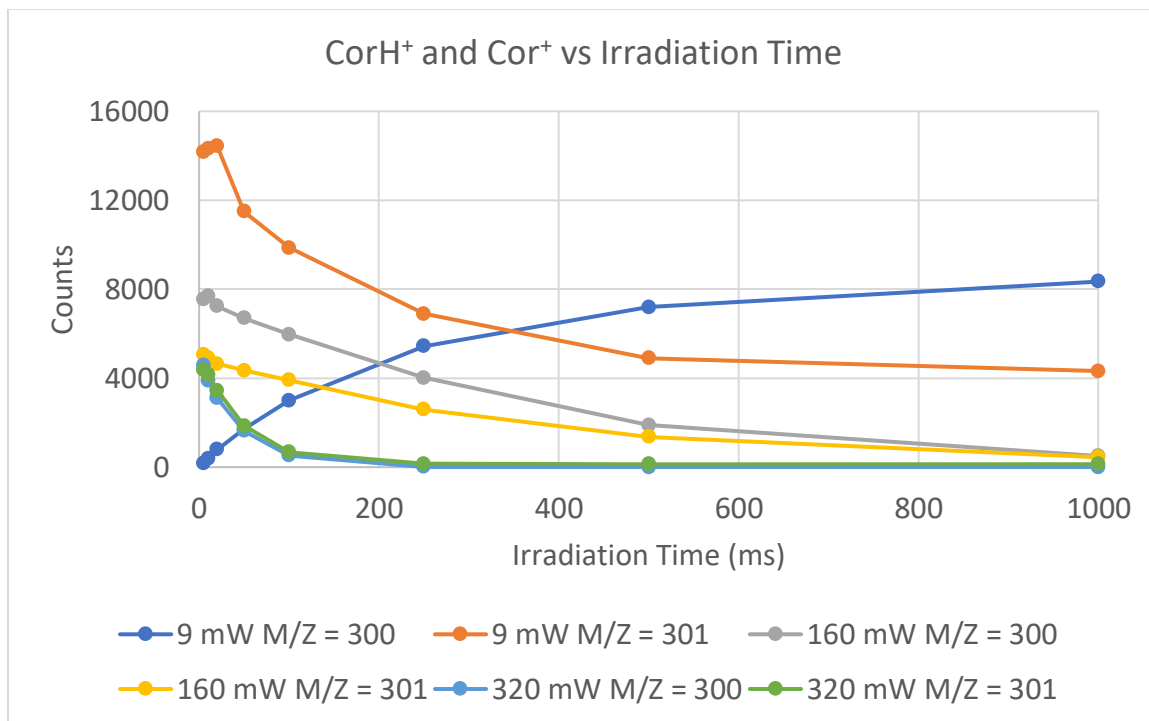


Figure 1.28: CorH⁺ and Cor⁺ vs irradiation time and laser power

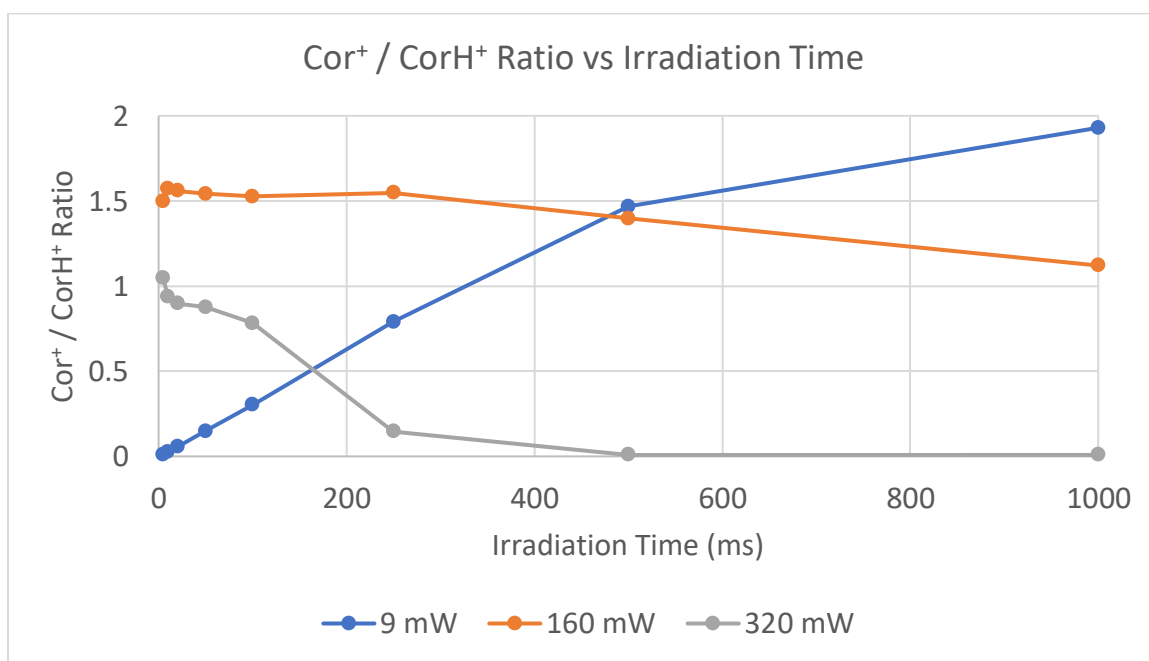


Figure 1.29: Cor⁺ to CorH⁺ ratio vs irradiation time and laser power

In the low photofragmentation regime at 9 mW, the Cor⁺ signal increased while the CorH⁺ signal decreased in 1:1 correspondence, with the ratio of the two ions

increasing linearly. The growth of Cor^+ with 9 mW light is well-described by an exponentially-decreasing growth to a constant, with a fit function of:

$$\frac{I_m}{z}=300(t) = 8250 \left(1 - \exp \left(-\frac{t}{223} \right) \right)$$

In the mid photofragmentation regime, the populations of both CorH^+ and Cor^+ decay towards a constant, with a faster decay seen at higher power. While 160 mW cannot fully deplete either population in 1000 ms, 320 mW light causes both populations to become constant in 250 ms. The Cor^+ population decays to 0 counts with increasing time, but the population of CorH^+ never reaches 0 counts, but is a constant value of 132 counts. This implies there is either re-generation of CorH^+ (unlikely), or there is a 2.9% population of CorH^+ which has negligible cross-section to 532 nm light. Either the light causes isomerization to a non-absorbing structure, or CorH^+ is photo-excited and has a small probability transition into a long-lived dark state. An excited dark state could be significant however, as this would provide a photo-stable large graphene surface on which chemistry of other molecules could occur.

The following spectra were taken of the 160 mW and 320 mW CorH^+ counts vs irradiation time.

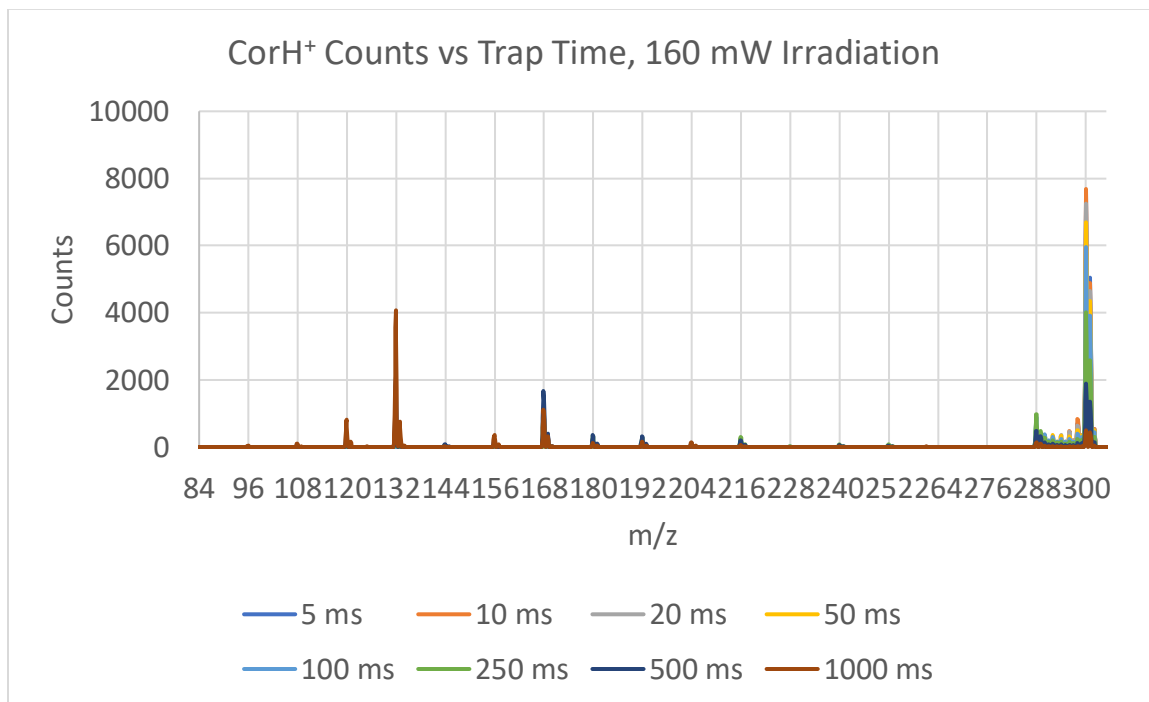


Figure 1.30: CorH⁺ mass spectrum vs irradiation time, 160 mW laser power

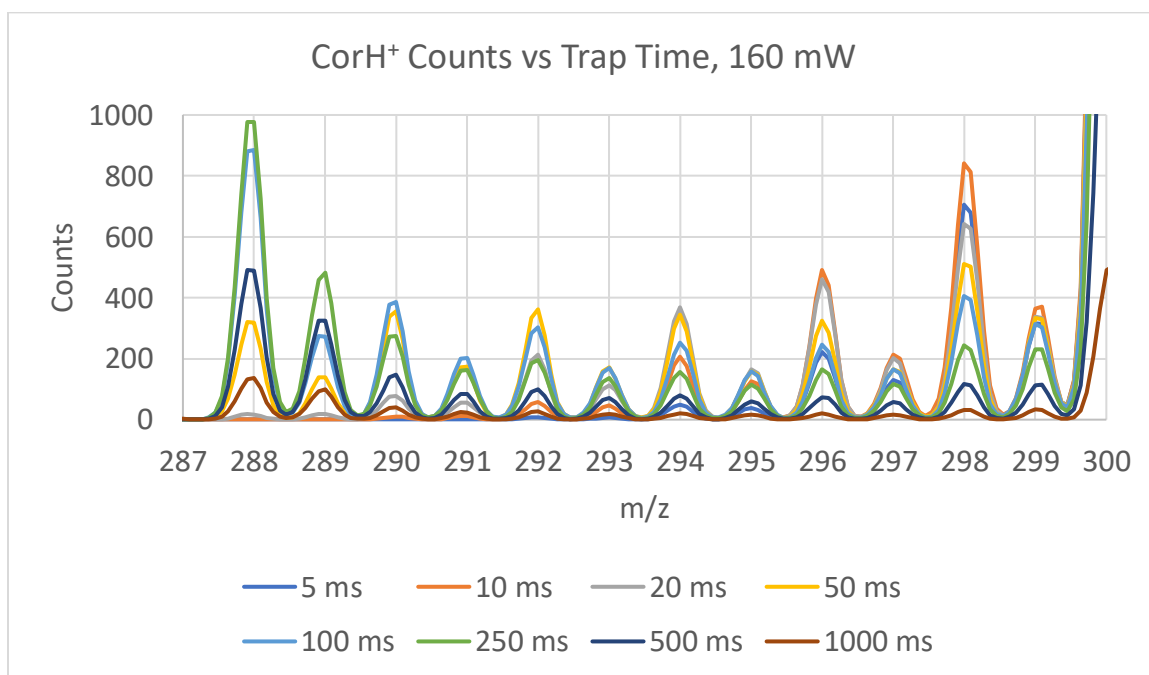


Figure 1.31: CorH⁺ H-loss region mass spectrum vs irradiation time, 160 mW laser power

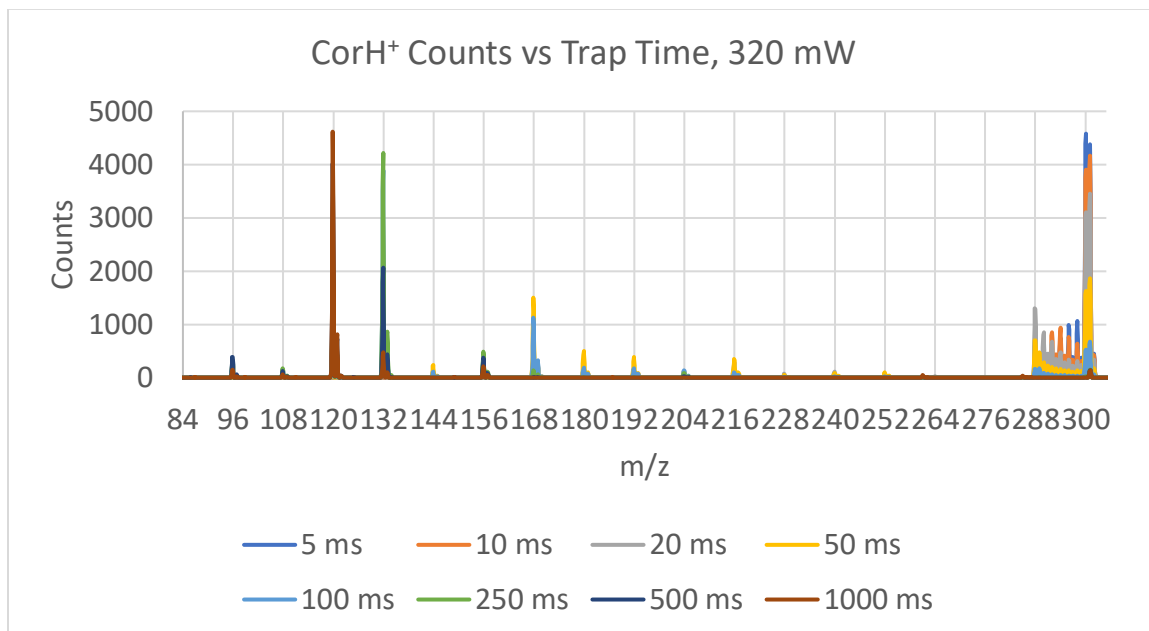


Figure 1.32: CorH⁺ mass spectrum vs irradiation time at 320 mW laser power

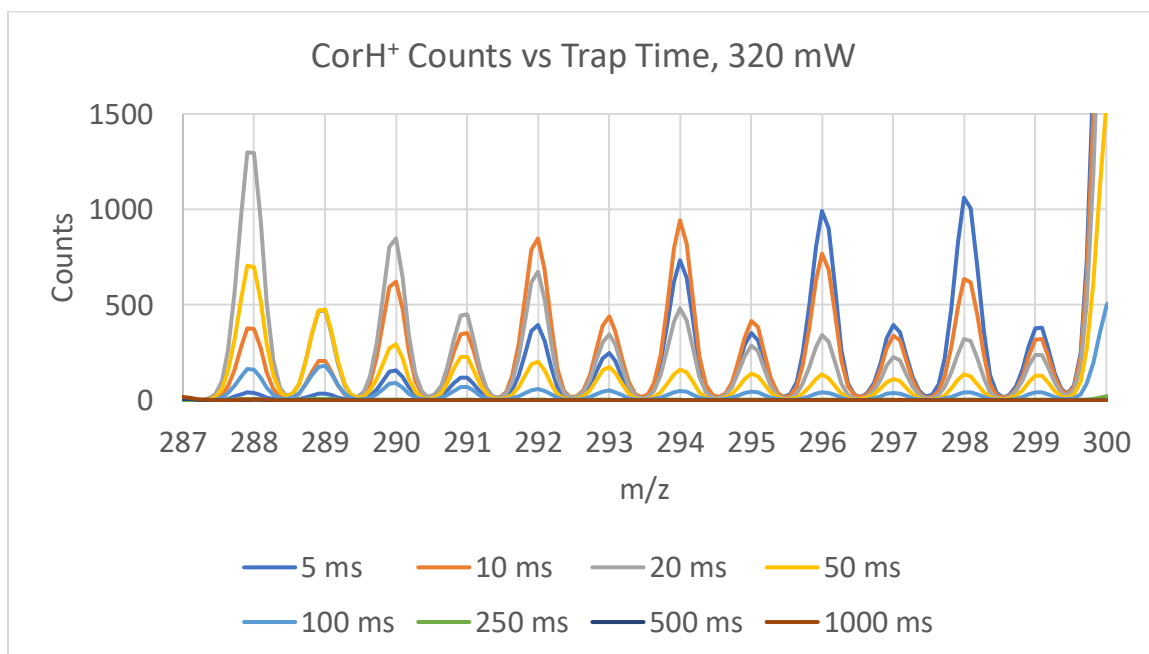


Figure 1.33: CorH⁺ mass spectrum in H-loss region vs irradiation time at 320 mW laser power

Replotting each m/z as a function of trapping time, the following plots are created:

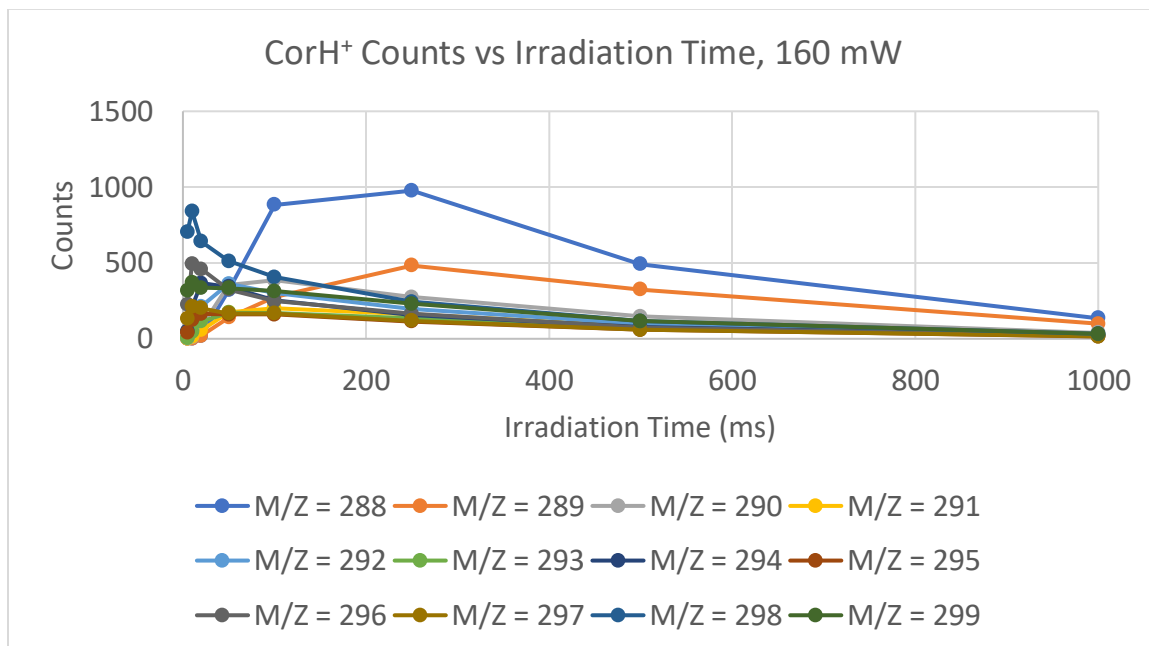


Figure 1.34: CorH⁺ H-loss region mass spectrum peaks vs irradiation time at 160 mW laser power

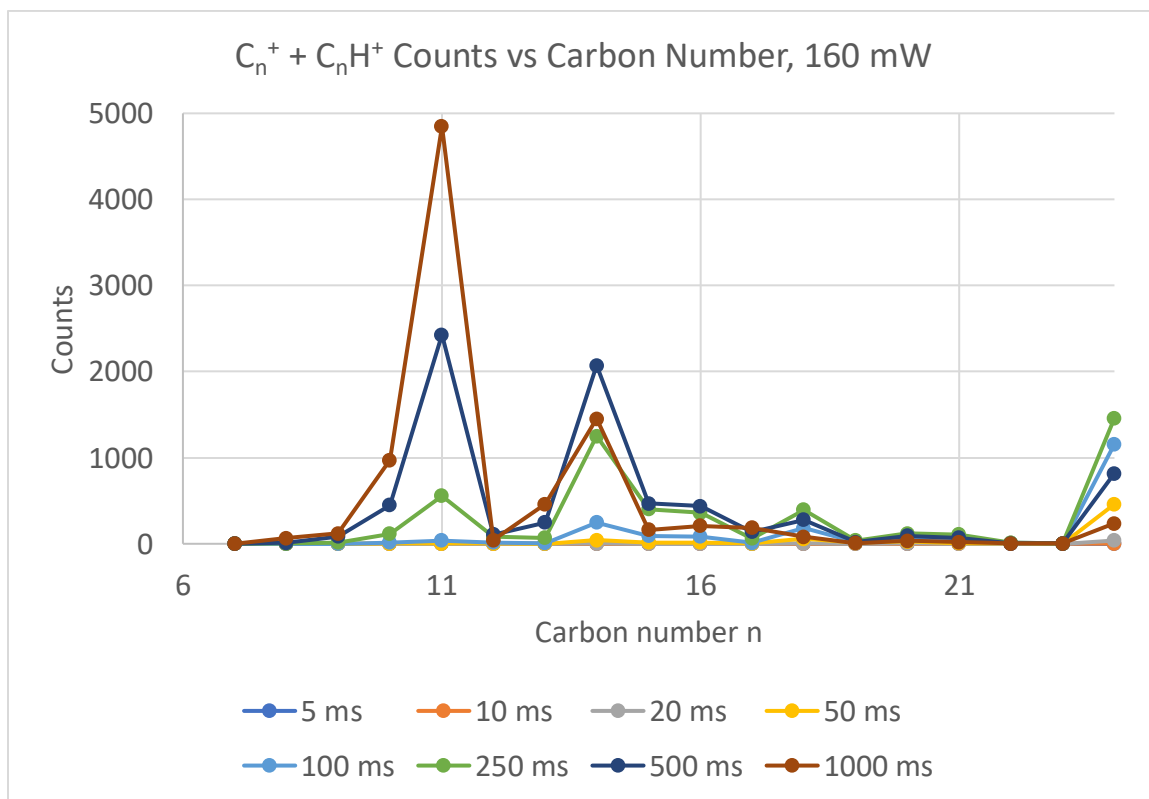


Figure 1.35: CorH⁺ C-loss region mass spectrum peaks vs irradiation time at 160 mW laser power

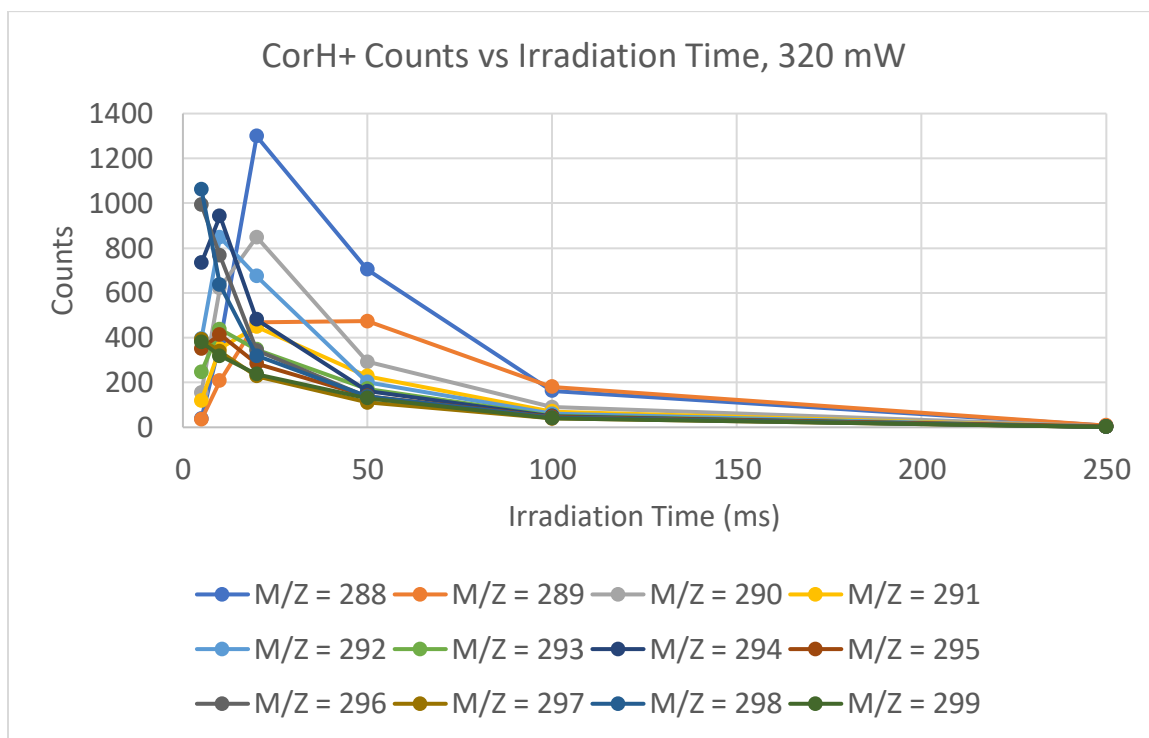


Figure 1.36: CorH⁺ H-loss region mass spectrum peaks vs irradiation time at 320 mW laser power

For times longer than 250 ms at 320 ms irradiation, the ion counts are almost 0 for all masses in the $m/z = 288 - 299$ range.

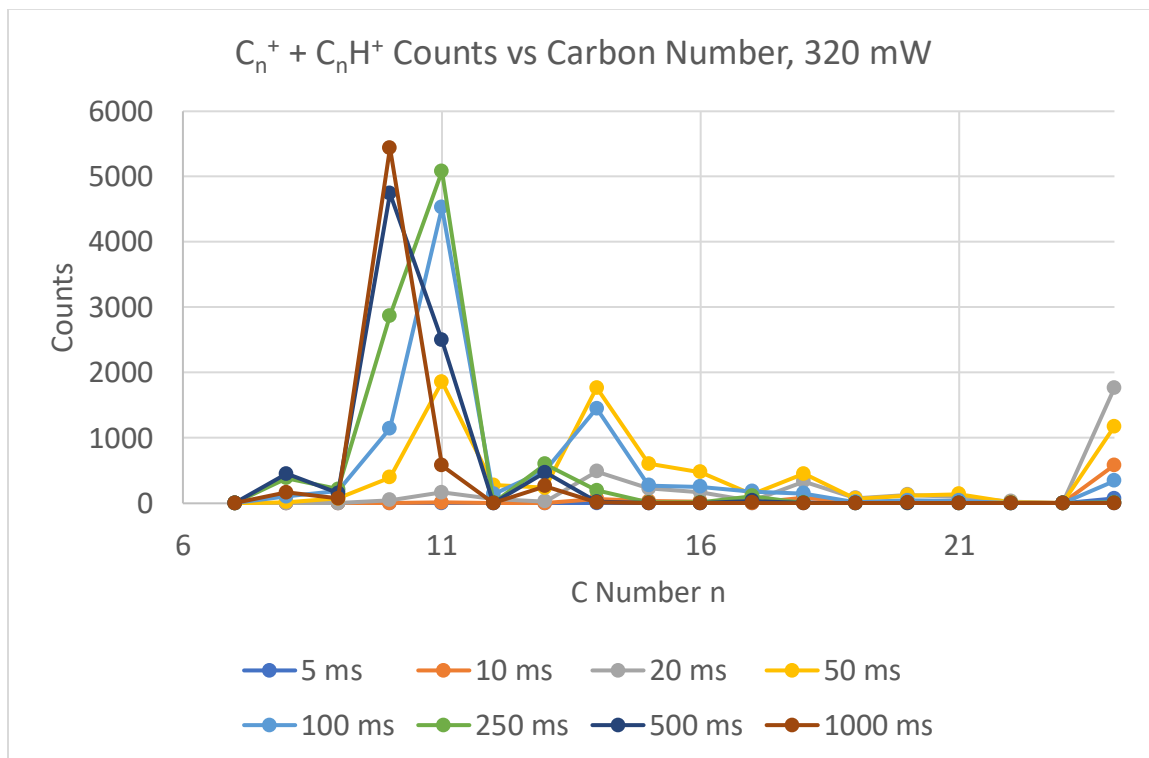


Figure 1.37: $CorH^+$ H-loss region mass spectrum peaks vs irradiation time at 320 mW laser power

The spectra for the most abundant C_n^+ species changes with irradiation time, with shorter irradiation times favoring the larger common n values for C_n^+ species, despite these laser powers being in the middle photofragmentation regime. The increased irradiation time at moderate laser powers has resulted in photofragmentation of the C_{24}^+ cation, but unlike at high laser powers for short irradiation times, the progression of lower n peaks in the $m/z = 80 - 288$ region could be seen as the irradiation time grew. As irradiation time progresses from 50 to 1000 ms, the n value favored progresses from 18 to 14 to 11 to 10 for a constant laser power. This finding suggests sequential loss of first C_4 , then C_3 , then C to form stable C_n^+ species, which was unobservable in the scan of the power at short irradiation times. Most of the product ions from the initial $CorH^+$ trapped

ions remained within the ion trap because the two different PD yield metrics were similar, indicating insignificant reduction in total ion count with time.

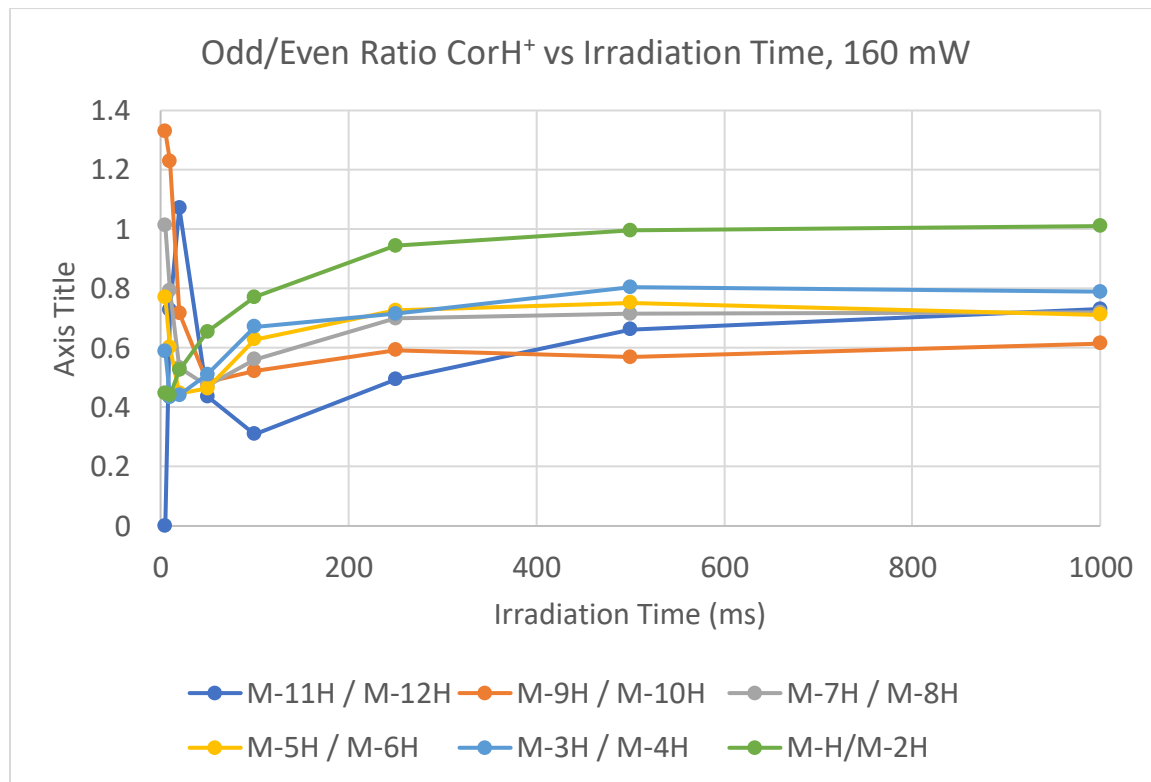


Figure 1.38: CorH⁺ H-loss region peaks odd/even ratio vs irradiation time at 160 mW laser power

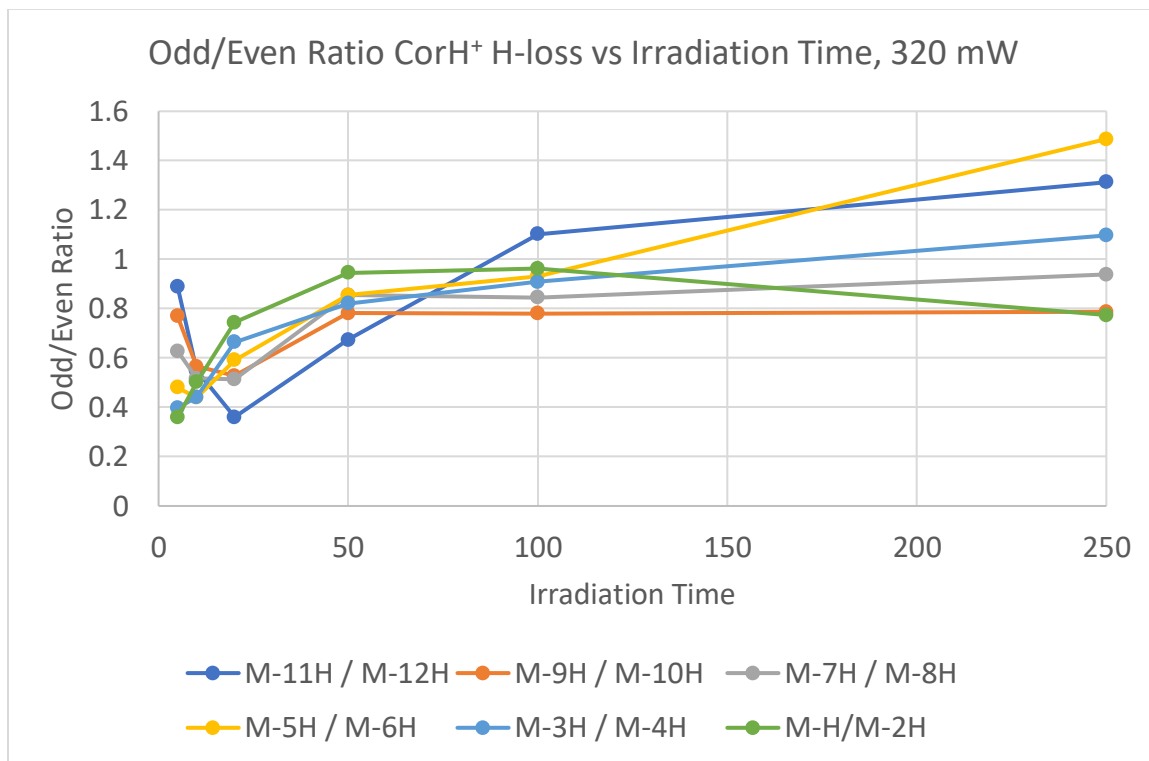


Figure 1.39: CorH⁺ H-loss region peaks odd/even ratio vs irradiation time at 320 mW laser power

The odd/even ratios in the H-loss region for 160 mW became a constant after approximately 250 ms, while the odd/even ratio at 320 ms continued to change. The ion counts at 160 mW still possessed good signal-to-noise at 1000 ms, but ion levels had fallen to <1 count at >250 ms at 320 mW. This could be from the appreciable concentration of CorH⁺ still available for photofragmentation at 1000 ms at 160 mW, while the population of CorH⁺ is near 0 for 320 mW, so without a new supply of H-rich Cor⁺ ions, the odd/even ratio is subject to changes based on the different cross-sections of the various C₂₄H_m⁺ species. For both laser powers there is no obvious trend in the C-H ratio with H-number, but the relative ordering of odd/even ratio vs H-number remains similar, with m = 0 vs 1 showing the lowest odd/even ratio between 50 – 100 ms.

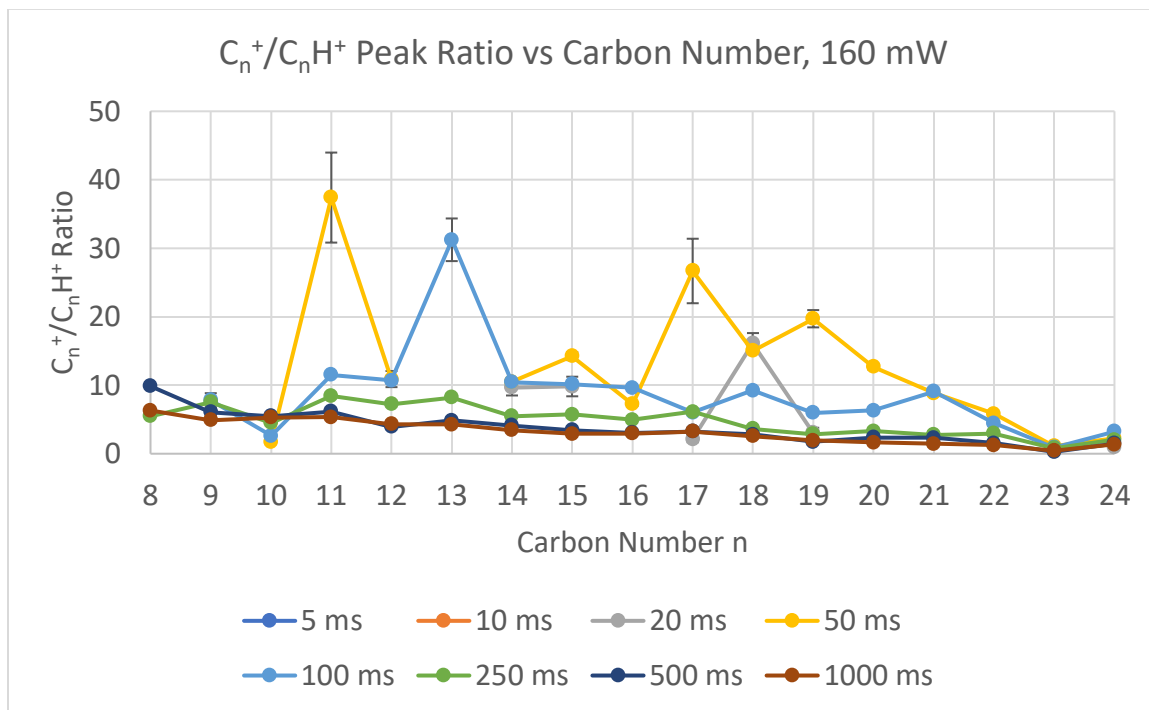


Figure 1.40: CorH⁺ C-loss region peaks C_n^+/C_nH^+ ratio vs irradiation time at 160 mW laser power

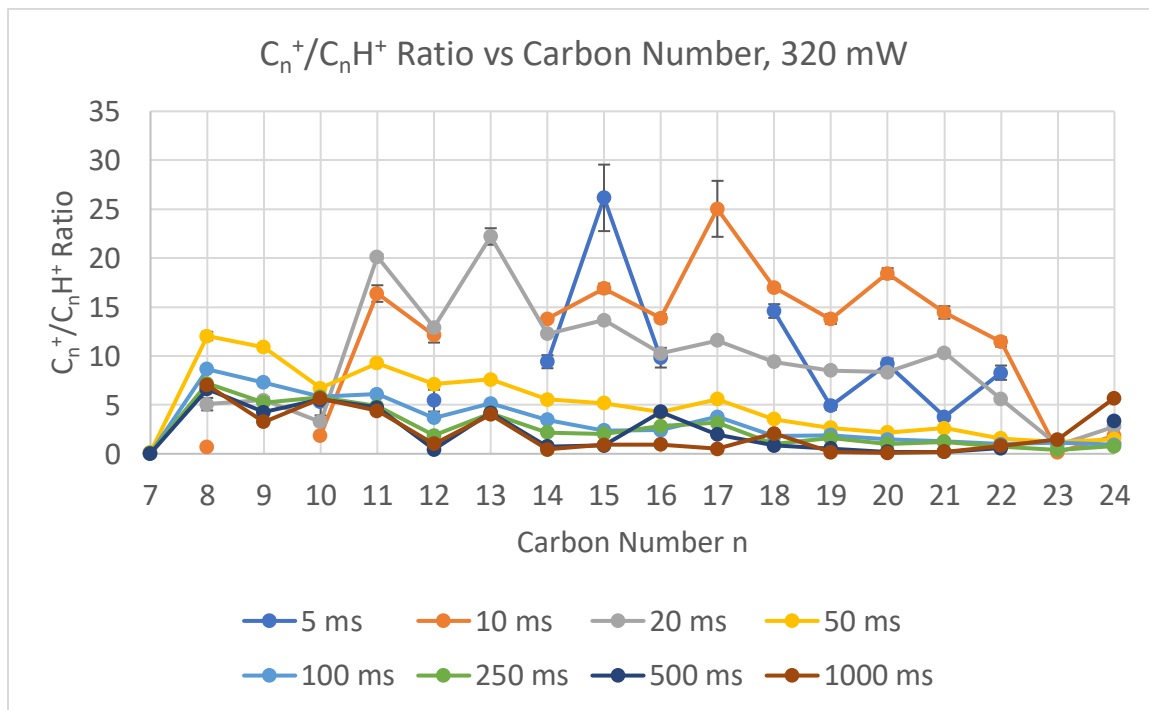


Figure 1.41: CorH⁺ C-loss region peaks C_n^+/C_nH^+ ratio vs irradiation time at 320 mW laser power

For both 160 and 320 mW laser powers, there exists a general trend of a lower C_n^+/C_nH^+ ratio with increasing trap time, which is expected based on the power-series measurements. There exists a threshold for good C_n^+/C_nH^+ vs carbon number plots, which is about 250 ms for 160 mW and 50 ms for 320 mW. While there are only 8 different time scans, the threshold for smooth C_n^+/C_nH^+ vs carbon number scans is not a simple function of total energy, which is the product of power \times irradiation time.

Without the 29.8 ms A-delay on the SRS 353 DDG however, the predominant C-loss starting ion was $C_{24}H^+$ instead of C_{24}^+ (see 500 mW 100 ms spectrum above in Figure 1.17), therefore the C_n^+/C_nH^+ C-loss ratio model is different than without the A-delay than above. A plot of the C-loss region is shown below.

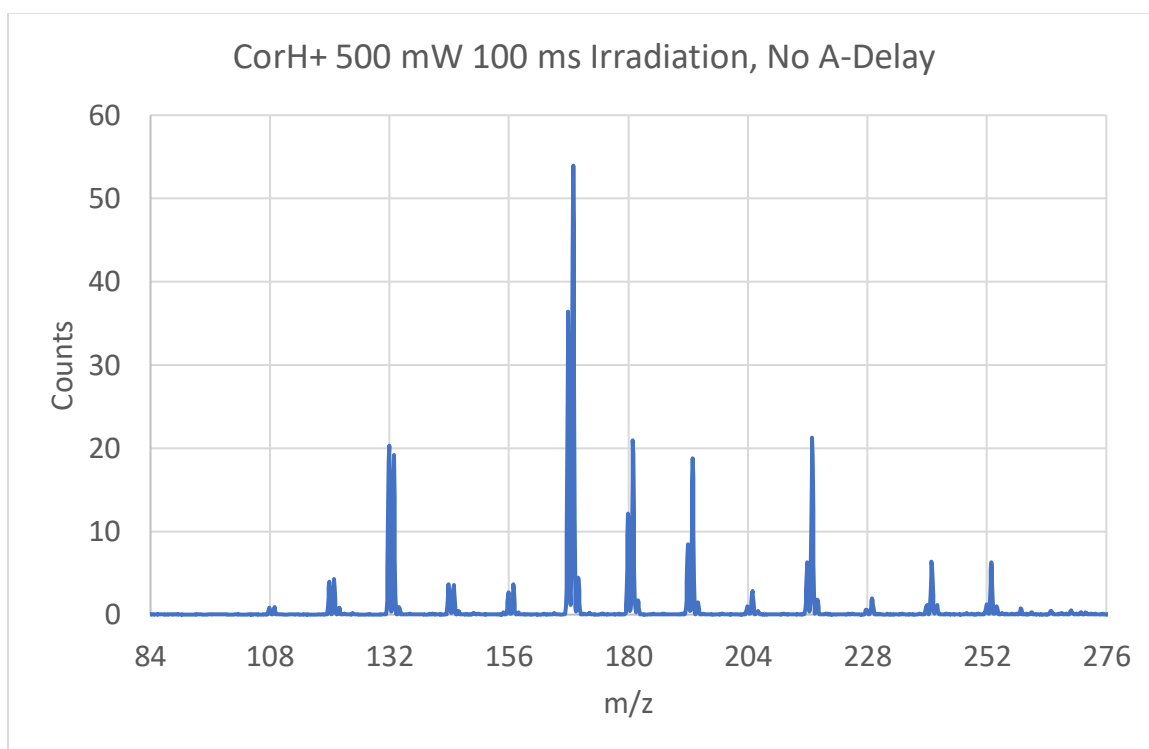


Figure 1.42: $CorH^+$ C-loss region 500 mW 100 ms irradiation, no A-delay.

The ratio between C_n^+ and C_nH^+ changes with carbon number, with C_nH^+ more prominent at larger masses. If there is no energetic penalty for the cation vs the neutral fragment to

have the H, and assuming a single dissociation event occurs creating two fragments, then a naïve model would say the value $n/24$ is the probability the H is still on the cation C_nH^+ , and the value $1 - n/24$ is the probability the H remains on the undetectable neutral fragment, creating a C_n^+ and a neutral $C_{24-n}H$. If only edge C atoms are considered, because that is where H is bonded in $CorH^+$, then both the number of carbons and n would be divided by 2. Thus the predicted ratio is:

$$C_n^+/C_nH^+ \text{ ratio} = \frac{1 - \frac{n}{24}}{\frac{n}{24}} = \frac{24}{n} - 1$$

The modeled ratio is plotted vs the actual ratio. The two are in excellent agreement for such a simple model for $n > 10$, so likely any increased or decreased stability for having an H atom on the cation or neutral fragment is minimal. Interestingly, this model treats every carbon as having identical probability of bonding to the H atom, while in coronene only edge carbon atoms can form bonds under regular conditions.

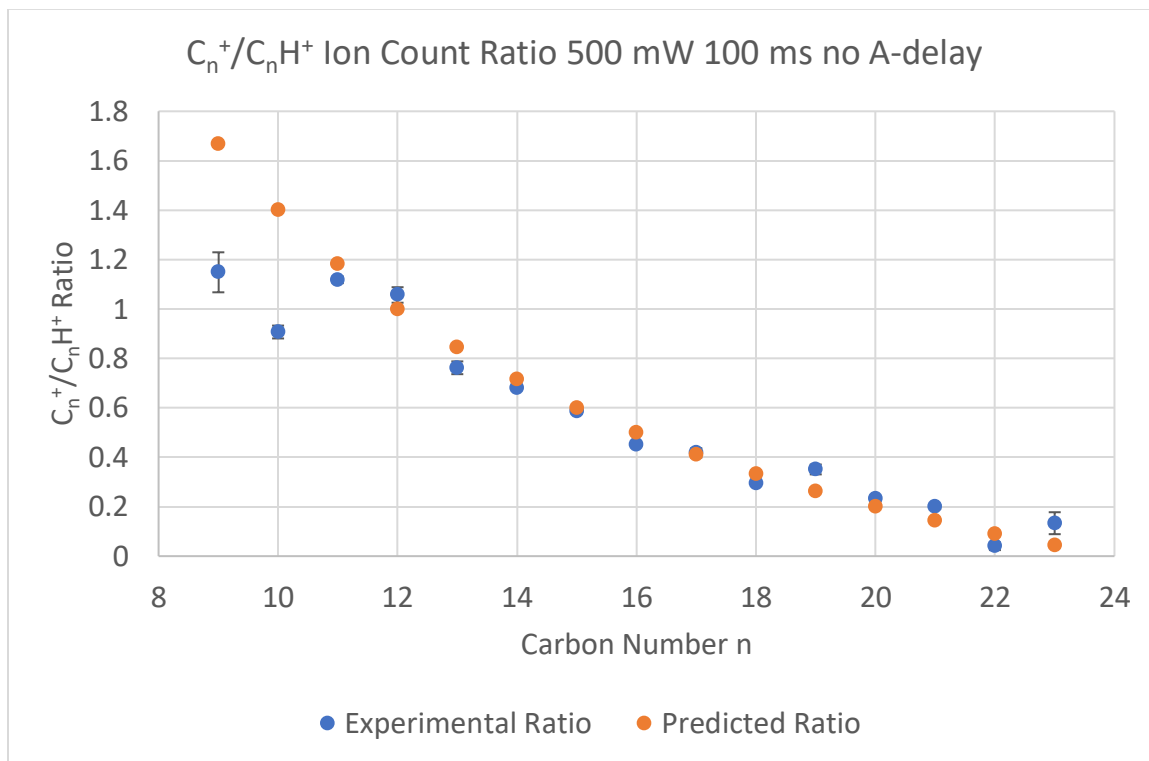


Figure 1.43: Predicted vs experimental C_n^+ / C_nH^+ ratio in C-loss region of $CorH^+$ for 500 mW 100 ms no A-delay

Exploring this dependence of power and irradiation time on the spectrum, it was found higher power and shorter irradiation times produced more fragmentation, likely because there was less time for product ions to thermalize or reach some equilibrium before being photoexcited again. Below is a plot of four scans at high power which all have the same product of power and irradiation time.

Table 1.5: Table of laser power and irradiation time conditions with same total energy delivered

Power (mW)	Irradiation Time (ms)
3200	5
1600	10
320	50
160	100

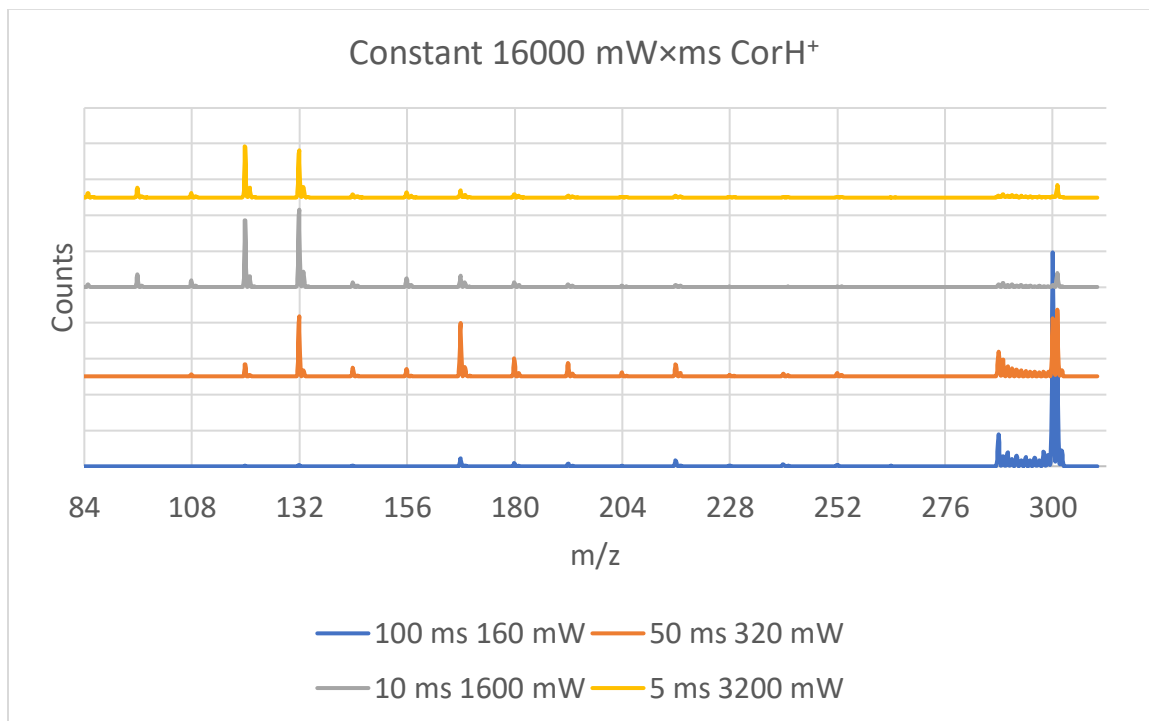


Figure 1.44: Mass spectra of CorH⁺ with same laser power \times irradiation time product. Because energetically two photons of 532 nm light are required to dissociate an H from an aromatic hydrocarbon,³⁰ and approximately two photons are required to remove an H per Castellanos,¹⁵ a relationship of irradiation time \times power² was explored. The absorption however is not a two-photon absorption, since the cross-section for a two-photon absorption at 4.66 eV (2×2.33 eV/532 nm photon) is nearly 0.³¹

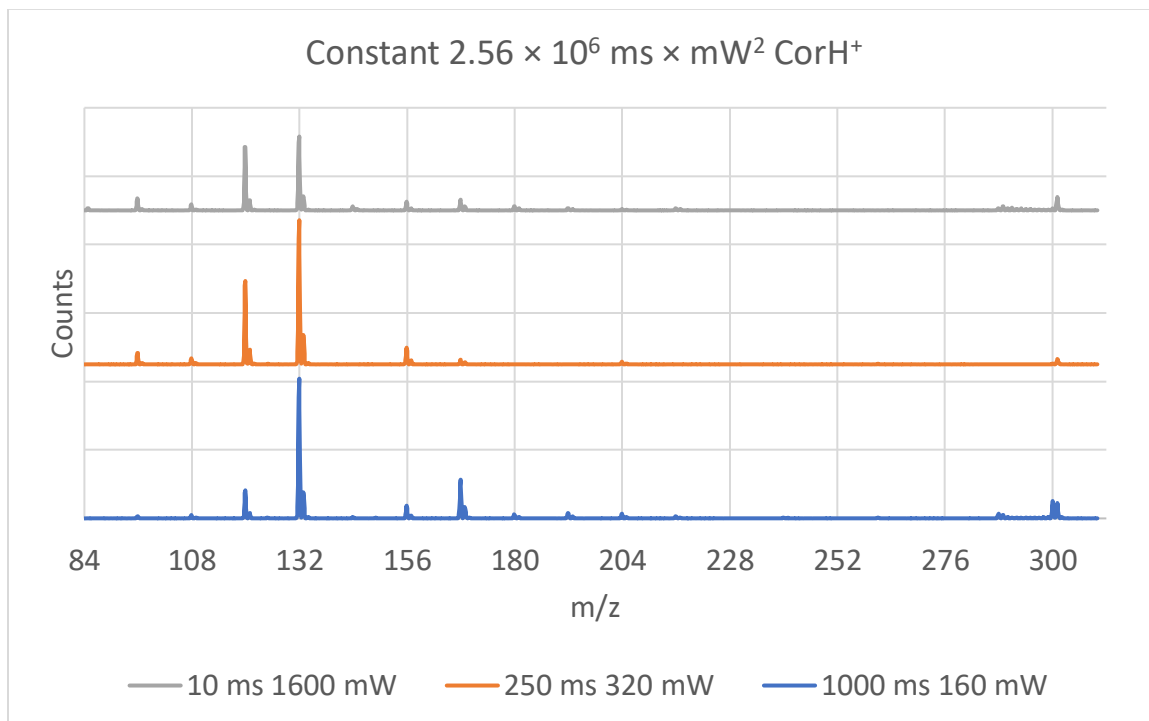


Figure 1.45: Mass spectra of CorH^+ with same $(\text{laser power})^2 \times \text{irradiation time}$ product. While differences exist, these three spectra are qualitatively much more similar than the total energy given to an ion sample. The power and trap times span orders of magnitude; future studies could observe the differences in slight changes to see where bifurcations in the spectrum occur. For example the H-loss region peaks are visible in the 1000 ms 160 mW spectrum and the 10 ms 1600 mW spectrum, but not in the intermediate 250 ms 320 mW spectrum.

One control experiment was looking if an irradiated ion population would continue to react once the laser light ended. A 10 ms or 50 ms exposure to 320 mW light irradiated the CorH^+ ion sample at the beginning, middle, or end of a 500 ms ion trapping period was performed, and the dependence of the spectrum on the location of the irradiation within the ion trapping was noted. The spectra recorded were all the same as the spectra shown above when the laser exposure was as long as the ion trapping, so the

length of time the ions remained non-irradiated had no effect on the spectra. This control experiment was performed on both CorH^+ and $\text{d}_{12}\text{-CorH}^+$, and the conclusion was the same for both molecules.

Perdeuterated Coronene:

The second molecule explored was perdeuterated coronene, motivated by inquiry into whether the first proton removed from CorH^+ was on the sp^3 hybridized protonated carbon. A key difference in $\text{d}_{12}\text{-CorH}^+$ photofragmentation is there is a single H atom which must start on the sp^3 hybridized carbon, thus any odd mass in the H-loss region ($m/z = 288 - 313$ for $\text{d}_{12}\text{-CorH}^+$), must have the H atom attached. Further, once the H atom is lost it is assumed re-addition of an H does not occur, so an odd mass ion must be the photofragment of another odd mass ion. Even mass ions can be the product of either odd (losing H or HD) or even (losing D or D_2) ions, but as reactants can only form other even mass ions.

The same three photofragmentation regimes are seen as for CorH^+ , with substantial differences only in the middle photofragmentation regime (H-loss predominant). A plot of the first H loss from $\text{d}_{12}\text{-CorH}^+$ reveals as a function of power, in the low regime, H loss dominates, but at higher powers, D loss dominates. Even at 0 mW, the $\text{d}_{12}\text{-CorH}^+$ ions have enough internal energy to dehydrogenate H, but at 0 mW no D atoms spontaneously dissociate.

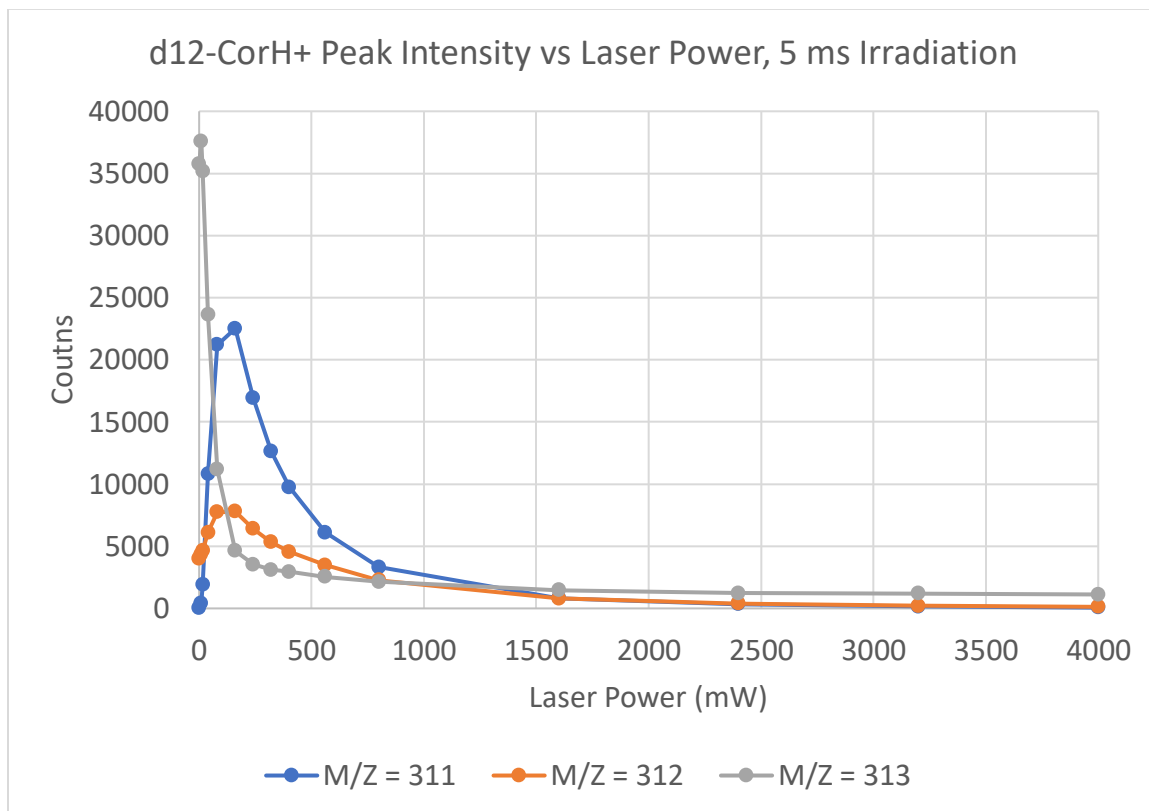


Figure 1.46: d₁₂-CorH⁺ and one-hydrogen loss products vs laser power.

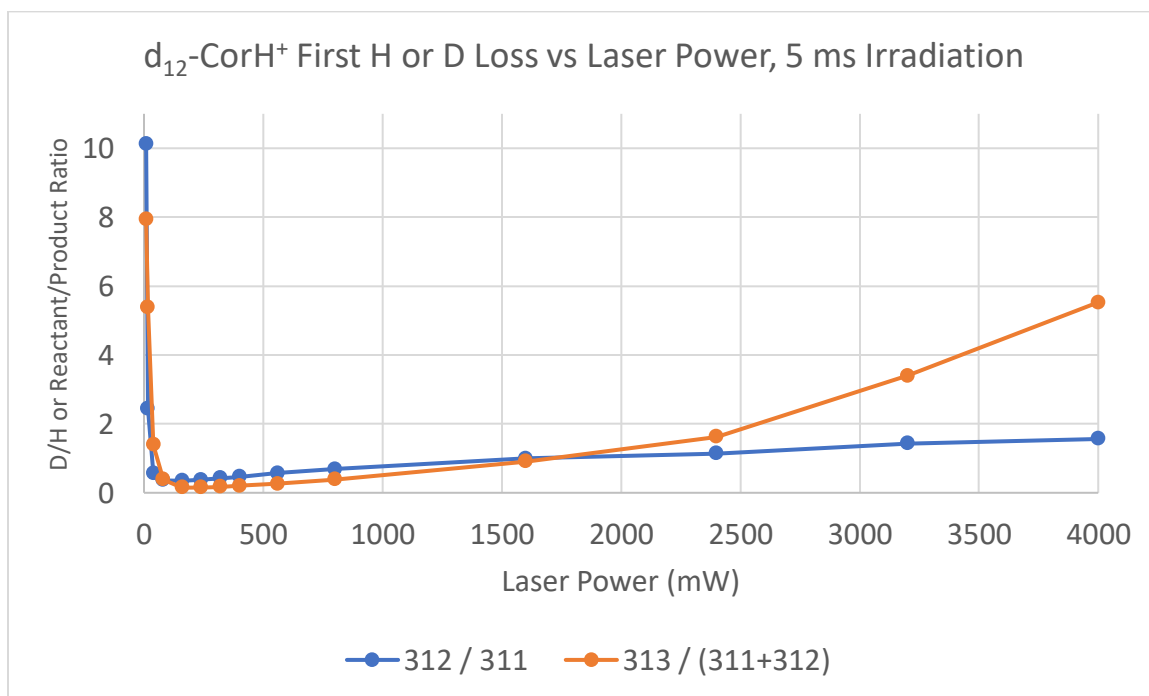


Figure 1.47: d₁₂-CorH⁺ and H vs D loss ratio.

The m/z 312 / 311 ratio reaches a minimum at 160 mW of 0.346, with the 313 / (311+312) reactant to product ratio also near its minimum value 0.153 occurring at 240 mW. If the first dehydrogenation occurs at the aliphatic carbon, without an isotope effect the 312 / 311 ratio is expected to be 1, which would imply a kinetic isotope effect of 2.89 for the rate of H vs D loss. If the first hydrogen lost is assumed to be any hydrogen on $d_{12}\text{-CorH}^+$, then the isotope effect free ratio would be expected to be 1 / 13, implying a kinetic isotope effect of 0.222 for the rate of H vs D loss. However, because 312 and 311 are the precursors to subsequent H and D loss region products, the H and D loss region products begin enriched in H because of entropic effects of $d_{12}\text{-CorH}^+$ having 12 times as many D atoms to lose as H, despite the isotope effect favoring H loss.

The spectrum of $d_{12}\text{-CorH}^+$ is shown below for 560 mW and 4000 mW (full chart in appendix). The portion of the spectrum in the C-loss is not significantly different than the C-loss spectrum for CorH^+ , with almost no C_nD^+ peaks seen, implying C_{24}D^+ is fully photofragmented to C_{24}^+ before C atoms are lost. In contrast, C_nH^+ peaks are seen, indicating $m/z = 289$ will lose C atoms appreciably.

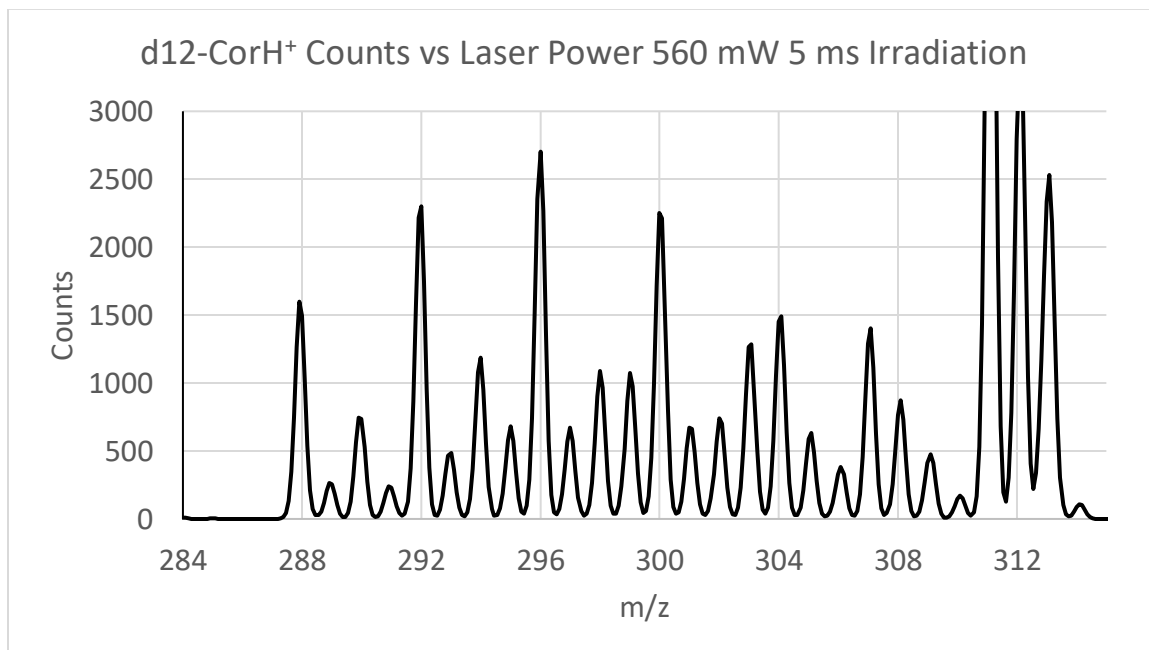


Figure 1.48: Mass spectrum of $d_{12}\text{-CorH}^+$ at 560 mW laser power 5 ms irradiation

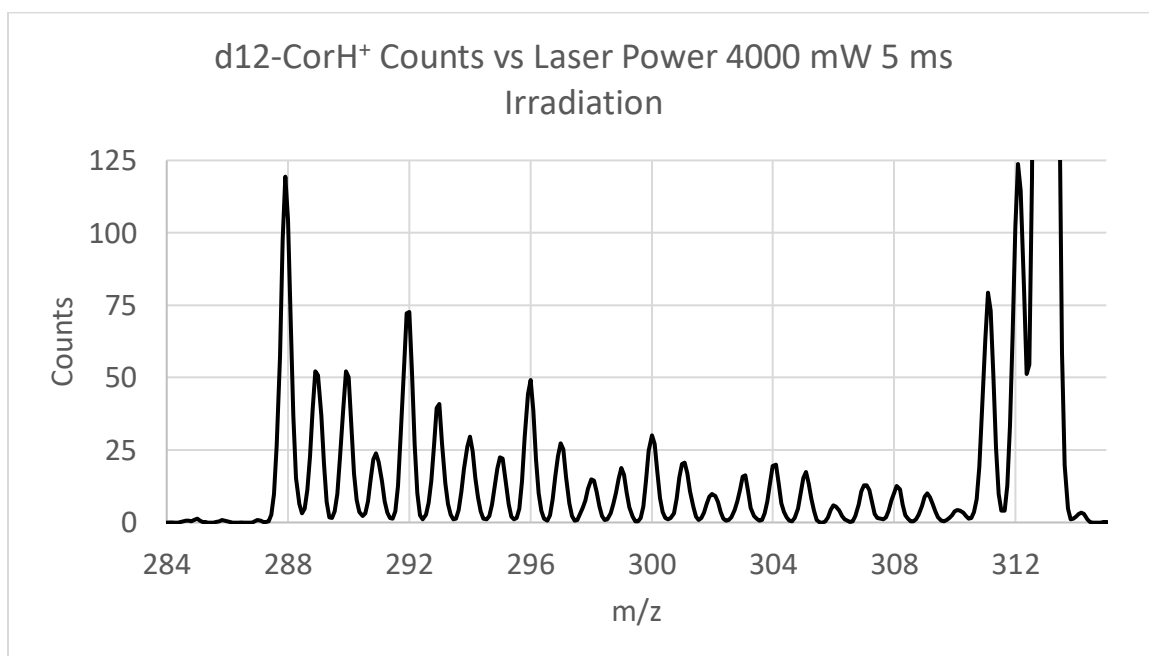


Figure 1.49: Mass spectrum of $d_{12}\text{-CorH}^+$ at 4000 mW laser power 5 ms irradiation

A feature obvious from the highlighted 560 and 4000 laser powers is not only are even masses more abundant compared to odd masses, like for CorH^+ , but masses of the form $\text{C}_{24}\text{H}_m^+$ where m is divisible by 4 (so of the form $4k$ for $0 \leq k \leq 5$) are more prominent

than even masses of the form $4k + 2$. This implies D_2 loss is an important mechanism for conversion of $d_{12}\text{-Cor}^+$ and $d_{11}\text{-CorH}^+$ to C_{24}^+ . For convenience, these types of masses will be abbreviated $4k$ for $C_{24}D_{\text{even}}^+$, $4k + 1$ for $C_{24}D_{\text{even}}H^+$, $4k + 2$ for $C_{24}D_{\text{odd}}^+$, and $4k + 3$ for $C_{24}D_{\text{odd}}H^+$.

Below is a plot of the counts vs laser power, separated by mass type for readability

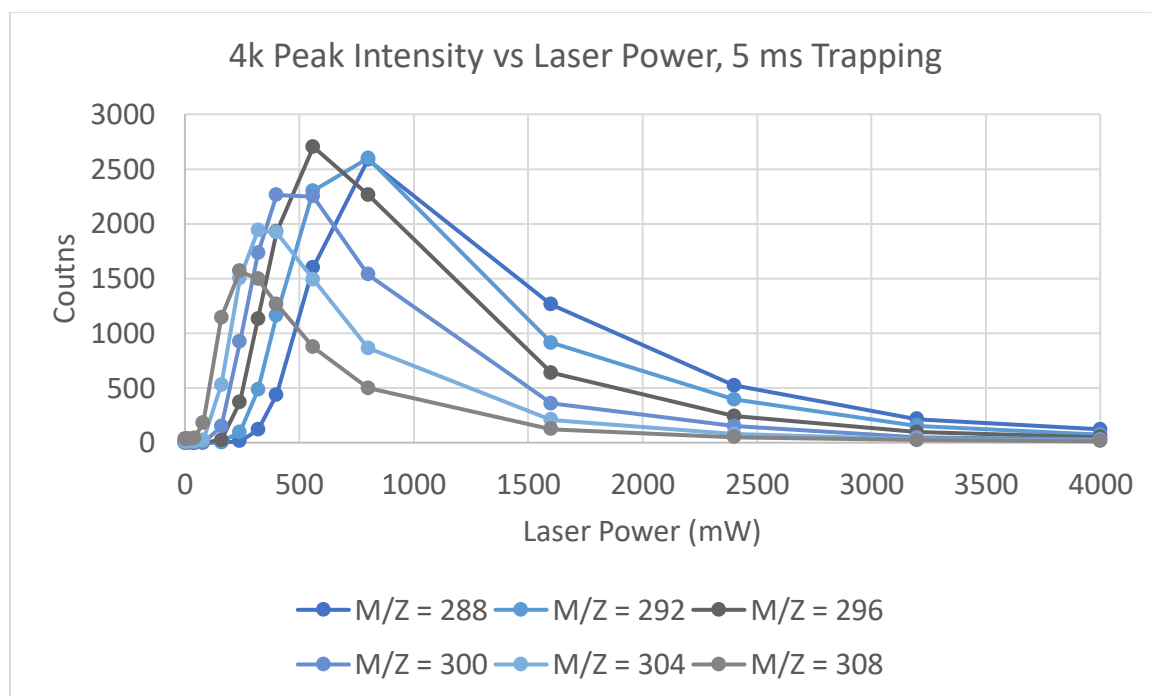


Figure 1.50: Counts vs laser power for $d_{12}\text{-CorH}^+$ 4k peaks 5 ms irradiation

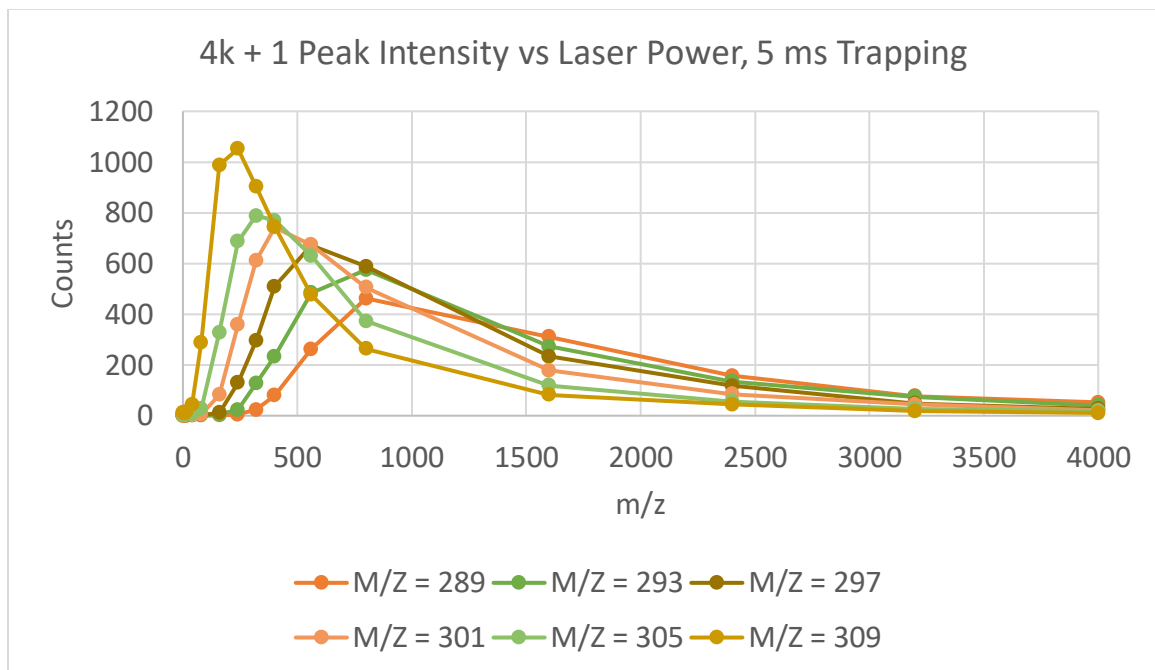


Figure 1.51: Counts vs laser power for $d_{12}\text{-CorH}^+$ 4k + 1 peaks 5 ms irradiation

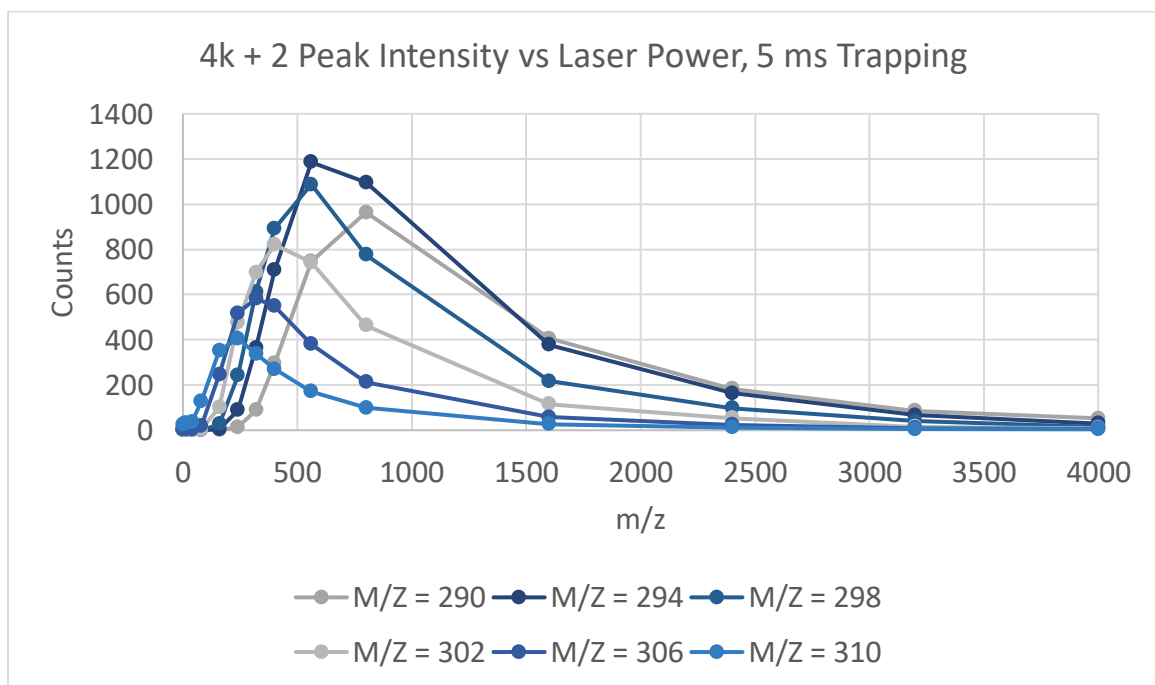


Figure 1.52: Counts vs laser power for $d_{12}\text{-CorH}^+$ 4k + 2 peaks 5 ms irradiation

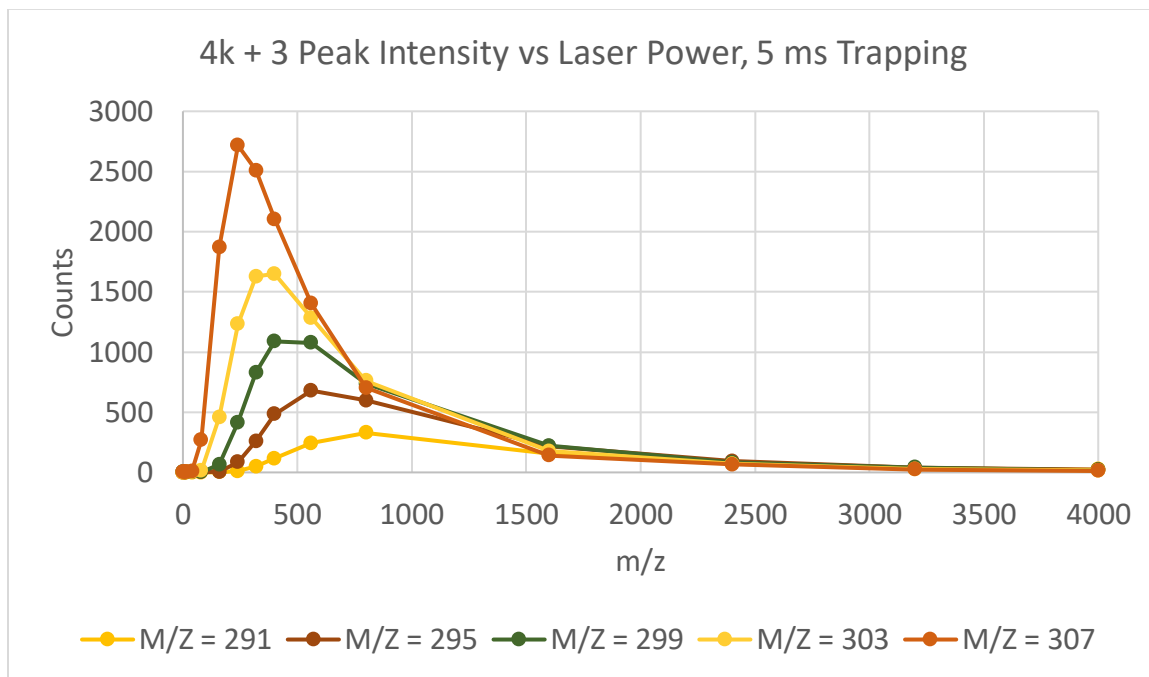


Figure 1.53 Counts vs laser power for $d_{12}\text{-CorH}^+$ 4k + 3 peaks 5 ms irradiation

Each trace's peak value is plotted below with the respective power.

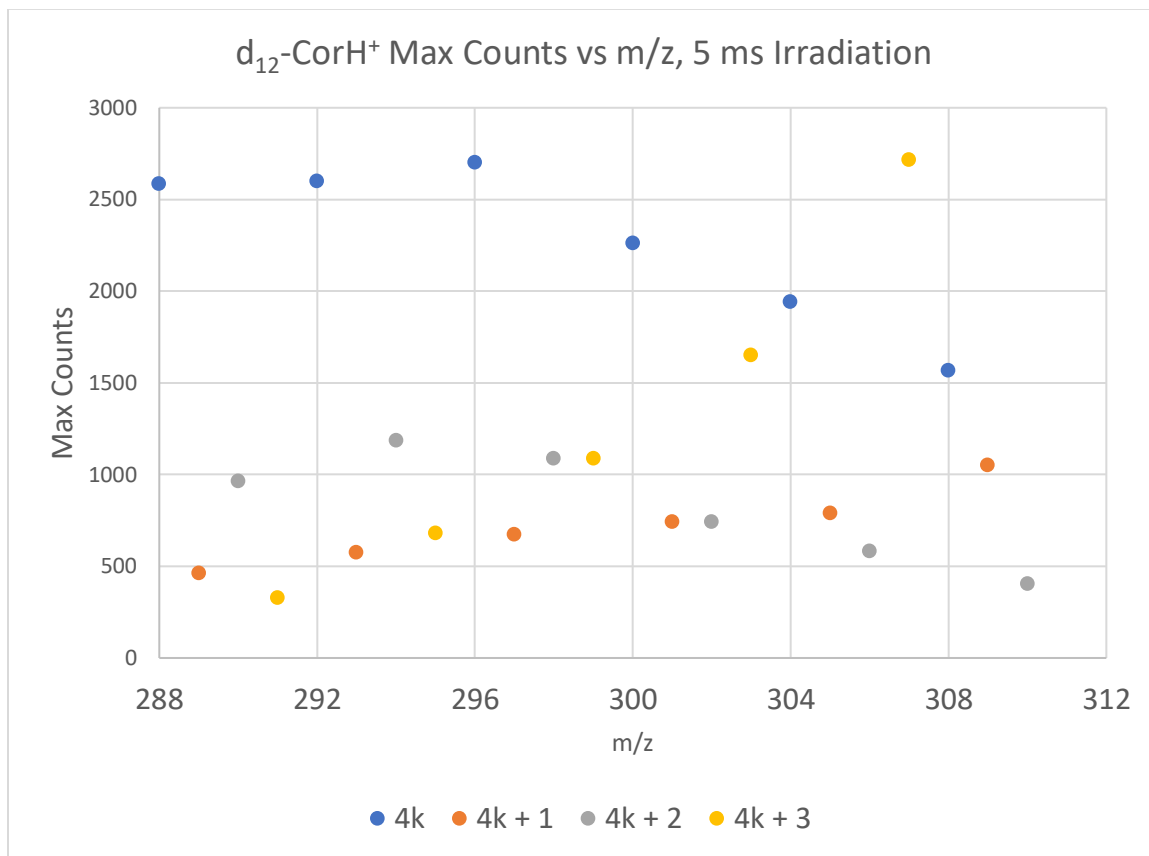


Figure 1.54: Max counts of each H-loss peak of $d_{12}\text{-CorH}^+$ by type.

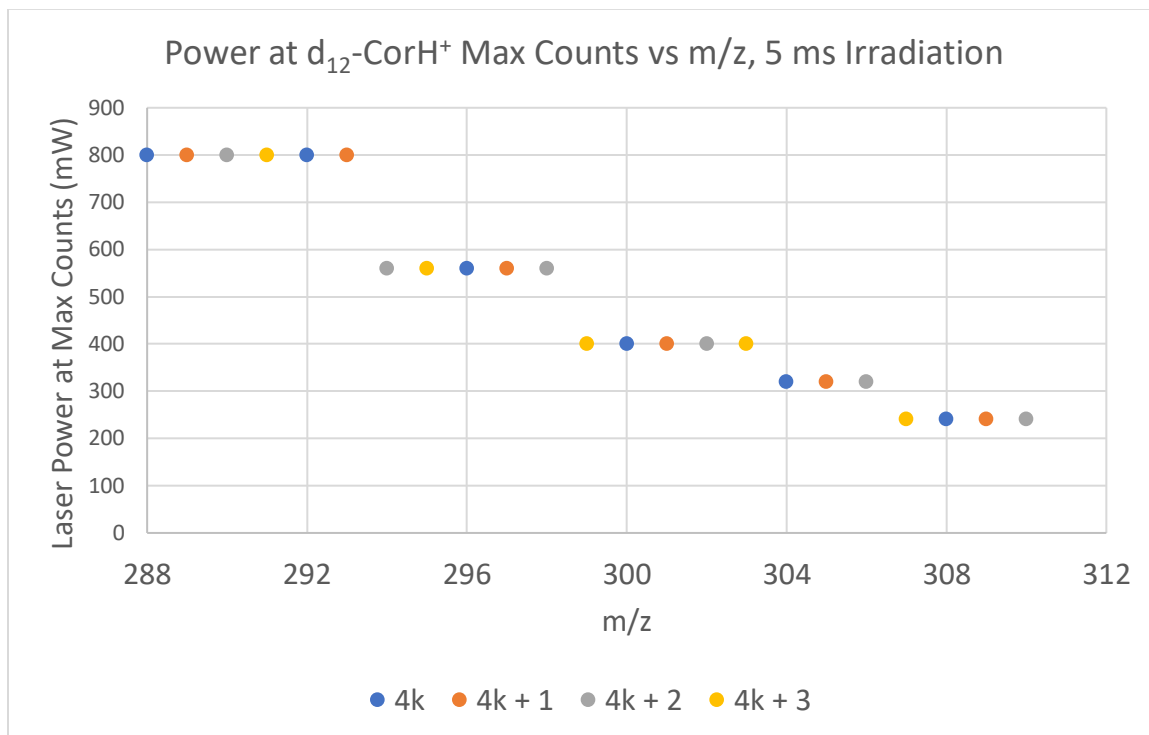


Figure 1.55: Power at which max counts of each H-loss peak of $d_{12}\text{-CorH}^+$ are reached.

The plot of counts vs m/z shows several interesting trends. One trend is at high m/z values in the hydrogen loss range, the maximum peak value increases with decreasing m/z , and these peaks occur at lower laser powers. At these laser powers there is not enough irradiation to remove most hydrogens and the 311 / 312 ratio is near its maximum, so 309 is the result of D loss from 311, and 307 is from D_2 loss from 311. The even peaks 310 are from H loss from 311 or D loss from 312, while 308 and 307 are almost certainly HD or D_2 loss from 311, since there is not enough irradiation for multiple hydrogen loss steps. The odd/even ratio starts high though at large m/z values because the reaction precursors of these masses at 311 and 312 are heavily enriched in H.

At m/z values < 307 , counts of $4k + 3$ masses rapidly fall with decreasing m/z , while $4k$ masses rapidly rise. This contrasts with $4k + 1$ and $4k + 2$ masses, which gradually fall and rise with decreasing m/z . Because the $4k + 3$ and $4k$ peak values nearly

mirror each other, this indicates HD loss is the dominant pathway for creating $4k$ masses, in contrast to H or D loss. Similarly, $4k + 1$ and $4k + 2$ masses peak values nearly mirror each other, again indicating HD loss is the predominant conversion odd to even masses (turning $4k + 1$ into $4(k - 1) + 2$). The $m/z = 288$ and 292 have peak counts less than 296 because by 800 mW irradiation, 288 and 292 are also being appreciably lost to form C-loss region products.

In this H or D loss region, not only does the m/z dependence of the different masses follow a trend, but the power dependence also follows a trend. The $4k + 3$ masses quickly fall off with laser power beyond the power of peak counts, followed by the $4k + 1$ masses and the $4k + 2$ masses which are similar, and the $4k$ masses. This would imply an ion's stability is due to the number of unpaired types of hydrogen atoms, with H and D unpaired less stable than either H or D, and most stable with all D atoms paired. This result is somewhat expected that D atoms lower the vibrational energy of an ion, giving an ion more stability against dissociation, but the stability difference between $4k$ and $4k + 3$ masses is pronounced. Both $4k$ and $4k + 3$ masses have an even number of hydrogen atoms, yet somehow having H and D together is destabilizing compared to having just H or D alone. This could be because the ions are not in thermal equilibrium, being subject to the high voltage ionization process, irradiated with focused light, given kinetic energy to remain in the ion trap, and subject to multiple reactions with potentially non-equilibrium product energy distributions. A potential explanation is based on probability; at higher laser powers multiple atomic and molecular hydrogen loss processes occur, and a $4k + 3$ mass can only lose D_2 to remain a $4k + 3$ product ion, while losing HD results in a much more stable $4k$ ion and HD, which is more stable than losing atomic hydrogen. As

D₂ groups are removed, the remaining H is a greater percentage of all hydrogen atoms remaining. For example, without isotope effects, at $m/z = 307$ the H is 1 of 10 hydrogen atoms and HD loss is 20% of total molecular hydrogen loss, while at $m/z = 295$ the H is 1 of 4 hydrogen atoms, so HD loss is 50%.

In contrast to this though is the minimal difference in rate of losing H vs D. For $4k + 1$ and $4k + 2$ masses, little conversion to $4k$ and $4k + 3$ masses occur, implying losing H for $4k + 1$ is not the dominant reaction pathway, neither is losing D for $4k + 2$ masses, even though $4k$ ions are the most stable. Interestingly, at $m/z = 290$ the $C_{24}D^+$ ions do lose D to form C_{24}^+ instead of undergoing C-loss, because no C_nD^+ ions are seen in the C-loss region. This contrasts to $C_{24}H^+$ ions, which do not only undergo H loss because C_nH^+ ions are seen in the C-loss region. So $C_{24}H^+$ is not a common ion, $C_{24}H^+$ is an usually stable H-containing ion but creating $m/z = 289$ is challenging because the sequential reactions needed to create $m/z = 289$ only allow for D or D₂ reaction products.

Unlike for $CorH^+$, an odd/even ratio does not capture the full extent of reactions possible removing hydrogen atoms. The following plots show the ratio of masses involved in each of the 4 different reaction channels, with ratios being reactants / products.

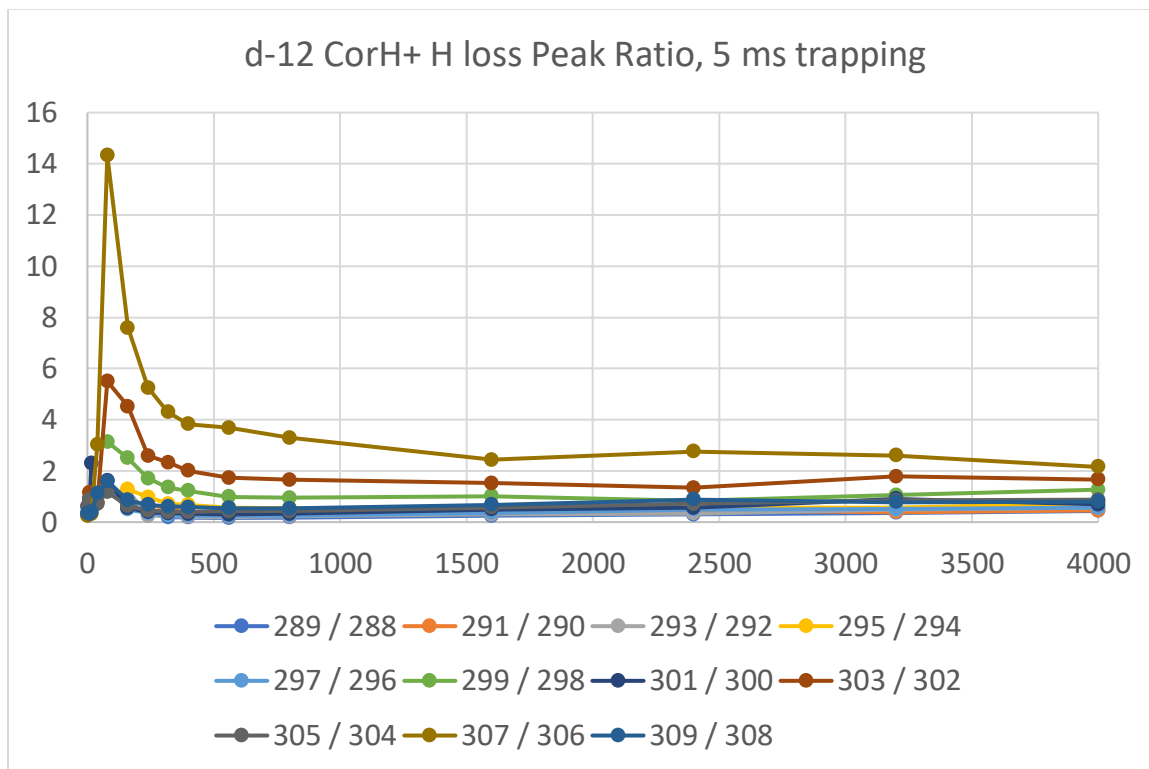


Figure 1.56: d₁₂-CorH⁺ reactant to product ratios of H-loss peaks losing H vs laser power

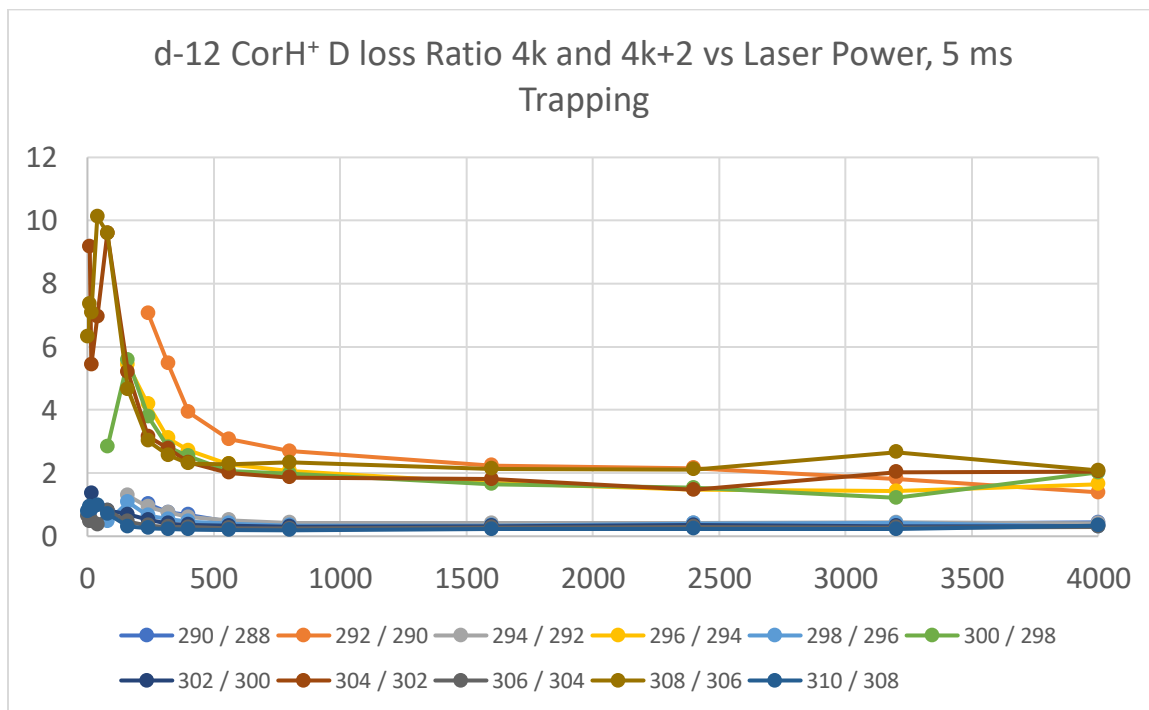


Figure 1.57: d₁₂-CorH⁺ even reactant to product ratios of H-loss peaks losing D vs laser power

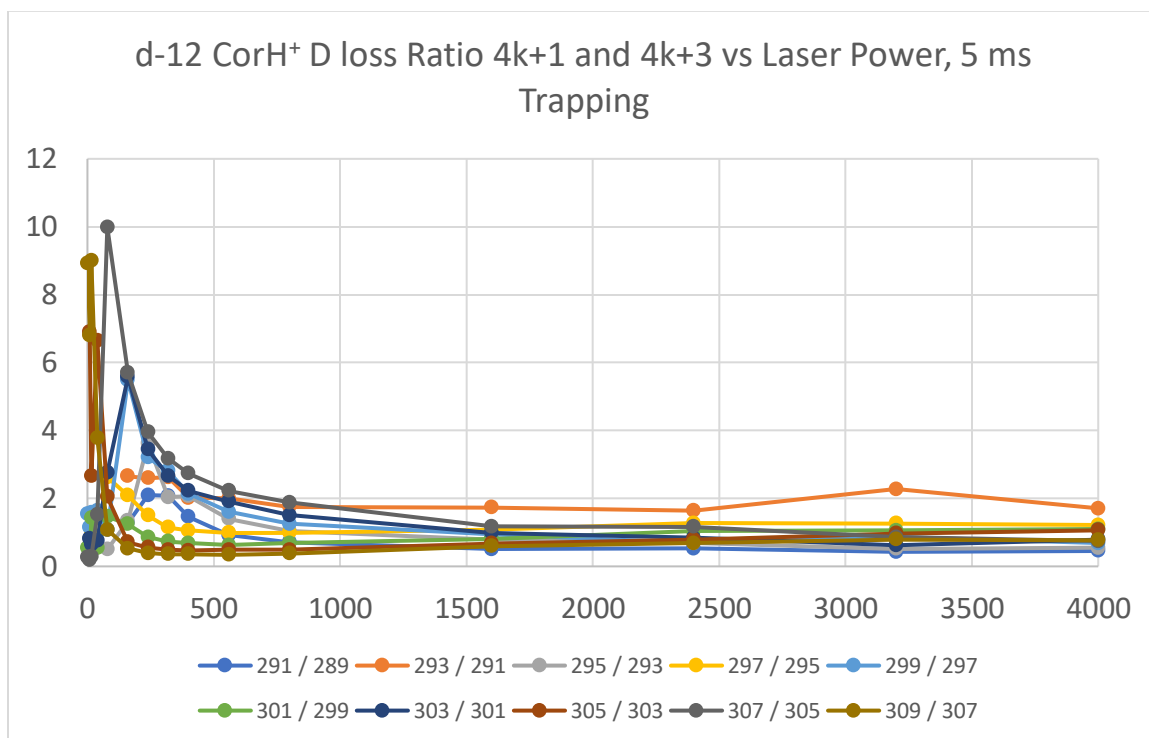


Figure 1.58: d₁₂-CorH⁺ odd reactant to product ratios of H-loss peaks losing D vs laser power

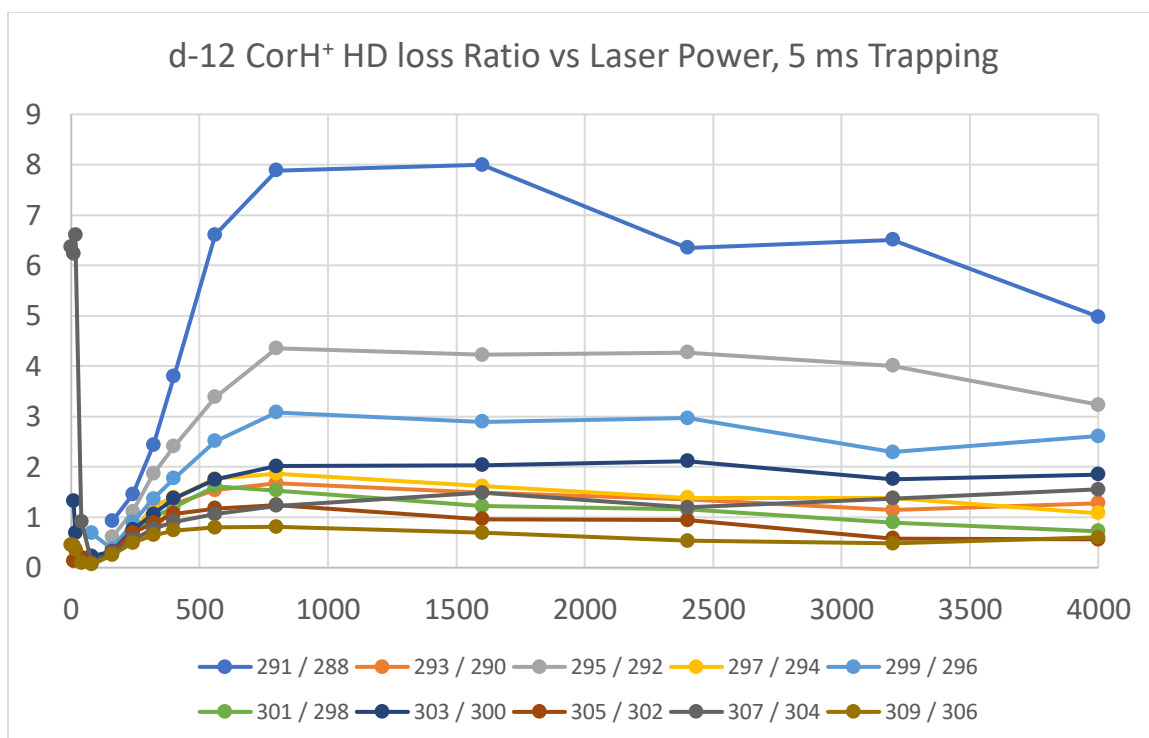


Figure 1.59: d₁₂-CorH⁺ reactant to product ratios of H-loss peaks losing HD vs laser power

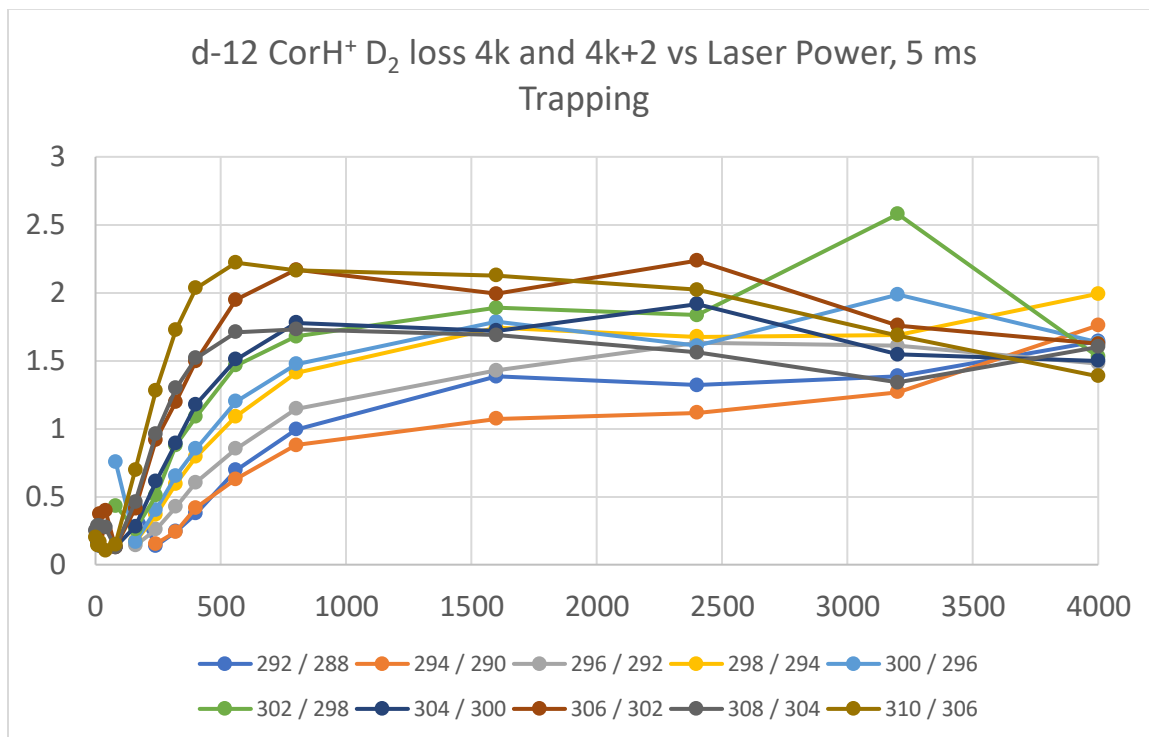


Figure 1.60: d₁₂-CorH⁺ reactant to product ratios of H-loss peaks losing D₂ vs laser power

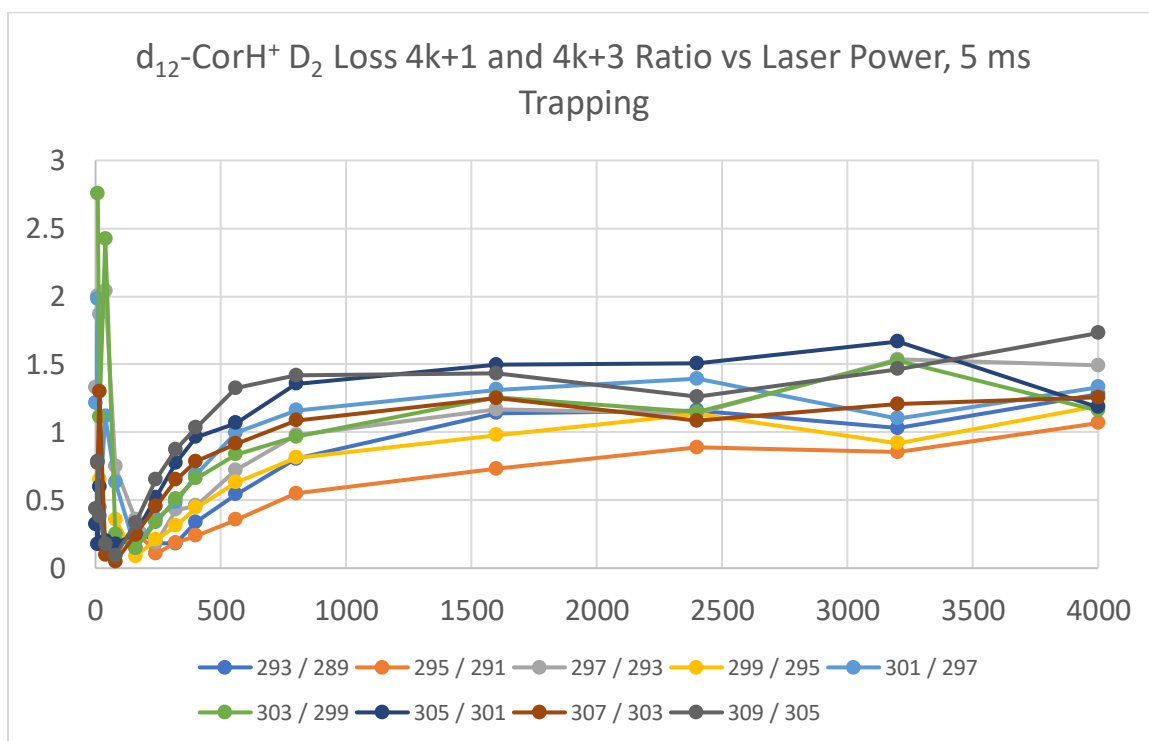


Figure 1.61: d₁₂-CorH⁺ reactant to product ratios of H-loss peaks losing D₂ vs laser power

A general observation is the ratios involving H or D loss are important at high laser powers (less reactant vs products) but are less important at lower laser powers. The ratios involving HD or D₂ loss are the predominant reaction pathway at lower laser powers. This indicates that at high laser powers, there is sufficient energy to cause atomic hydrogen to dissociate in an entropically favored process, while molecular hydrogen formation is entropically less favored but more energetically available at lower laser powers.

Replotting the data as a function of laser power for each reaction channel demonstrates which reaction channels are favorable (lower ratio) or unfavorable (higher ratio) at each laser power.

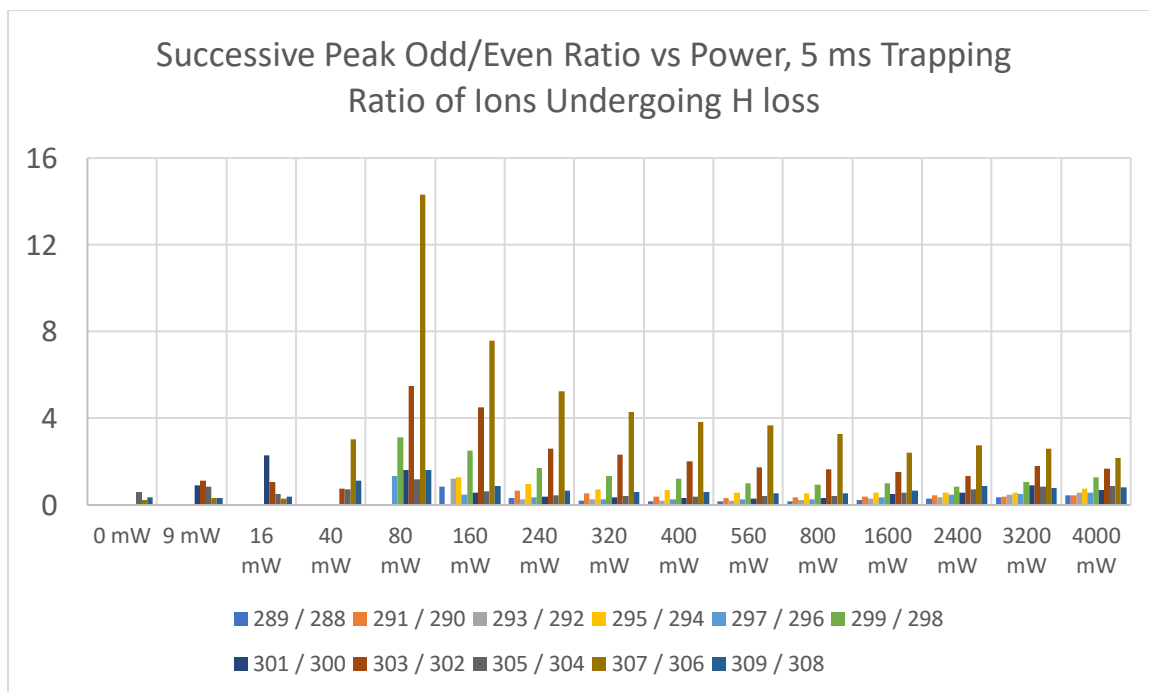


Figure 1.62: d₁₂-CorH⁺ reactant to product ratios of H-loss peaks losing H at each laser power vs m/z

This is also a plot of the odd/even ratio with laser power.

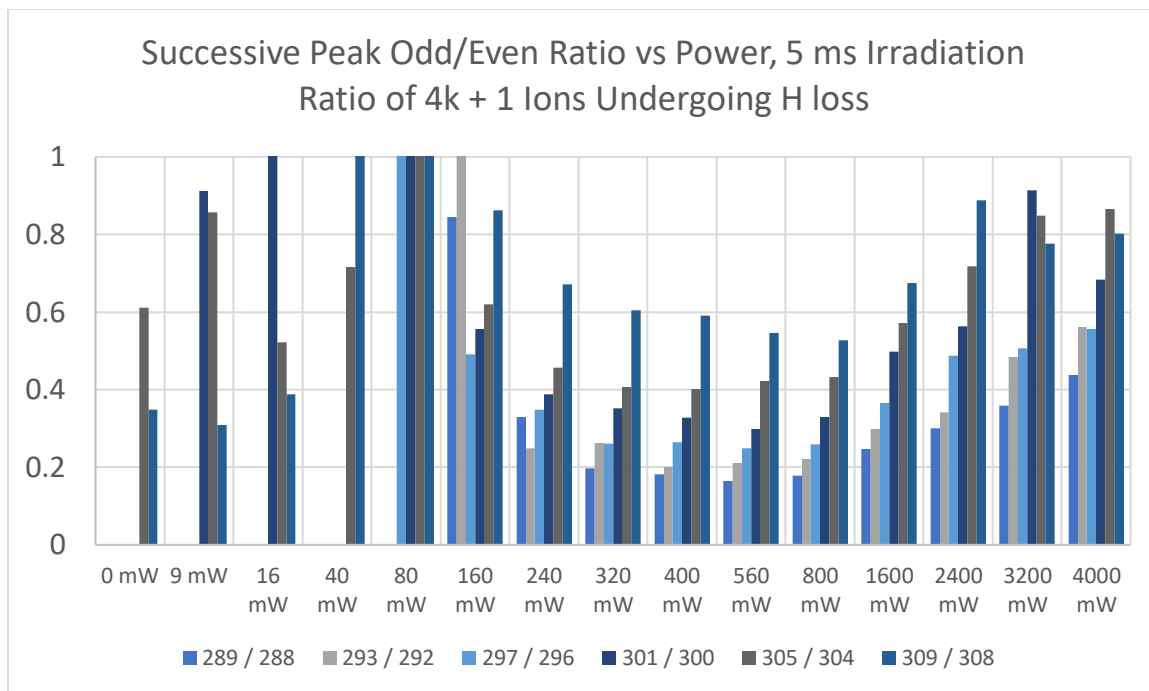


Figure 1.63: $d_{12}\text{-CorH}^+$ odd reactant to product ratios of H-loss peaks losing H at each laser power vs m/z

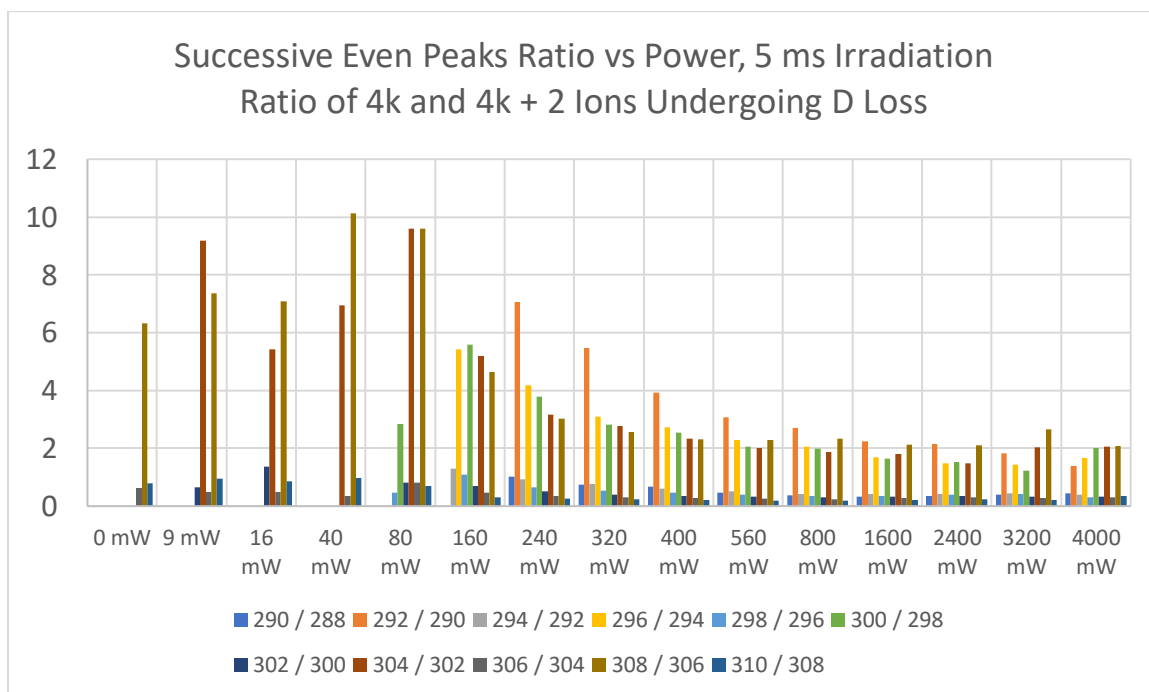


Figure 1.64: $d_{12}\text{-CorH}^+$ even reactant to product ratios of H-loss peaks losing D at each laser power vs m/z

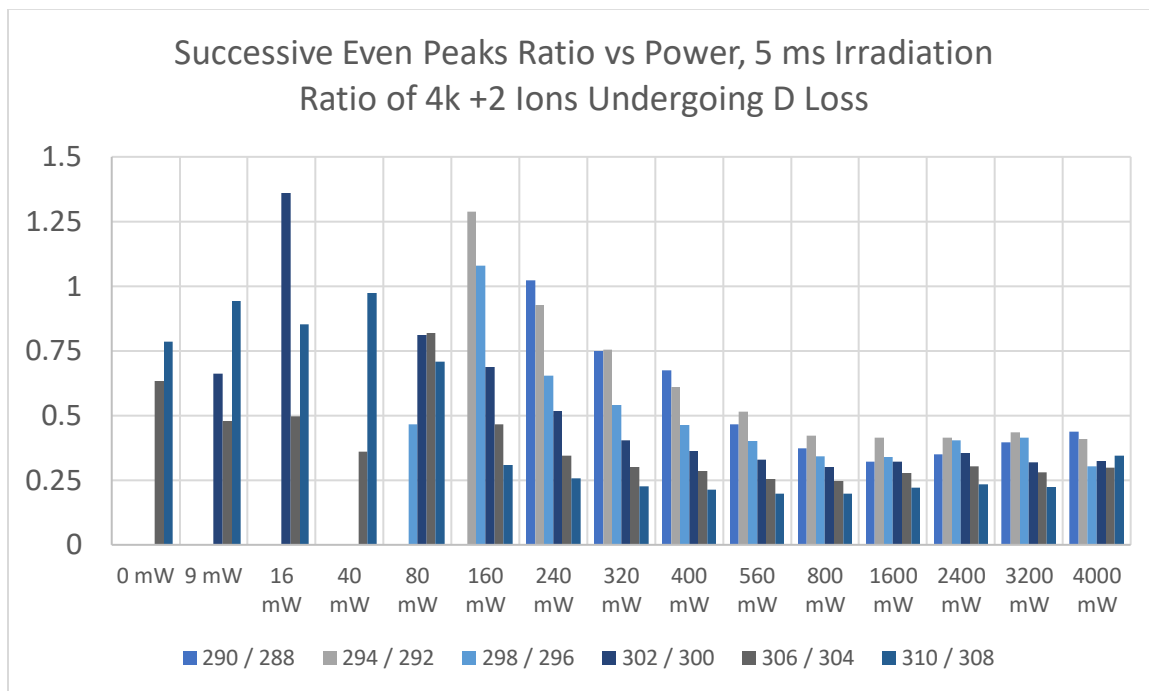


Figure 1.65: $d_{12}\text{-CorH}^+$ 4k+2 reactant to product ratios of H-loss peaks losing D at each laser power vs m/z

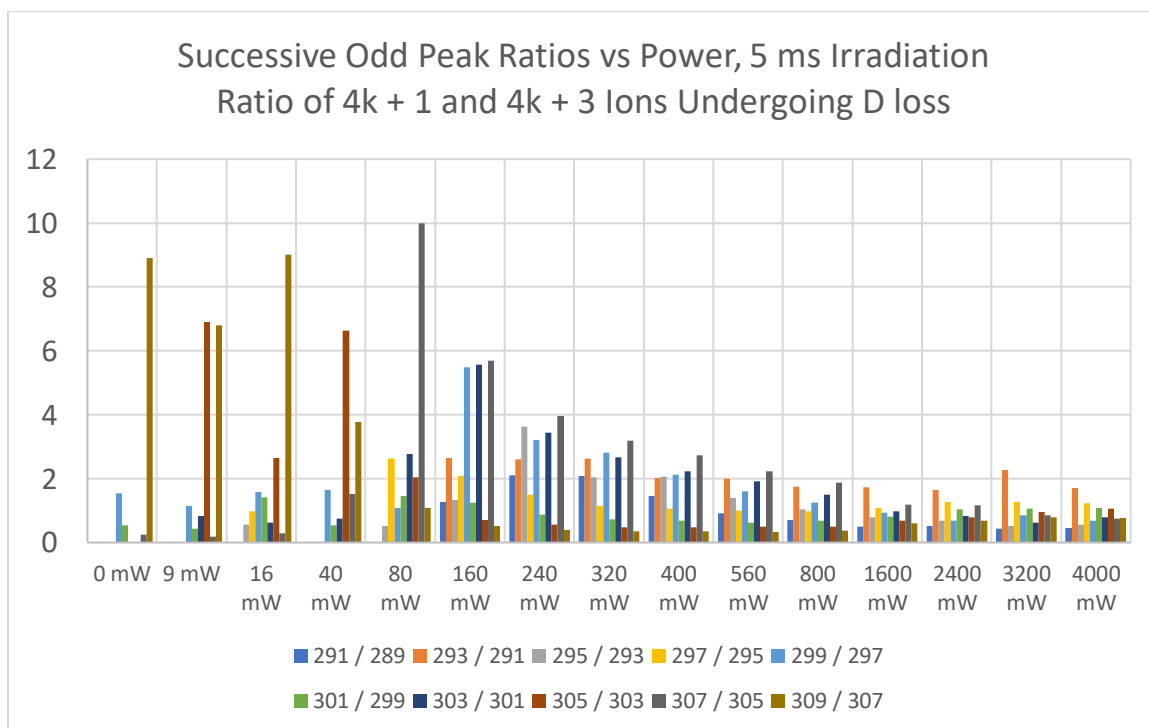


Figure 1.66: $d_{12}\text{-CorH}^+$ odd reactant to product ratios of H-loss peaks losing D at each laser power vs m/z

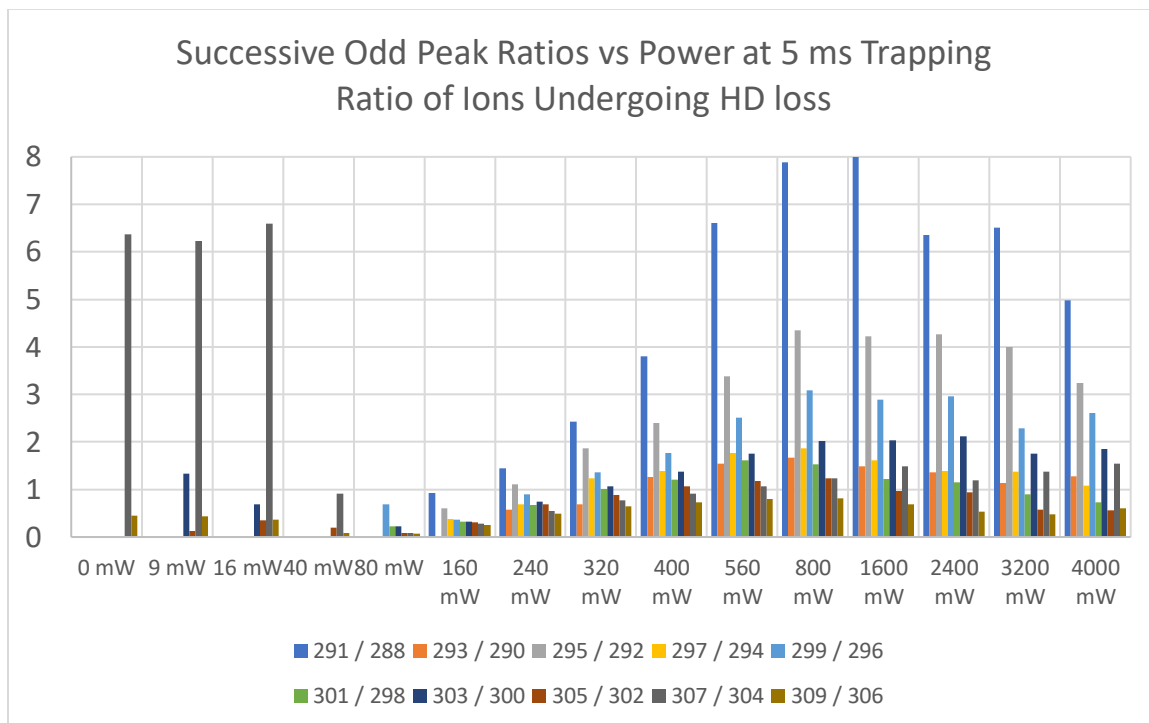


Figure 1.67: $d_{12}\text{-CorH}^+$ reactant to product ratios of H-loss peaks losing HD at each laser power vs m/z

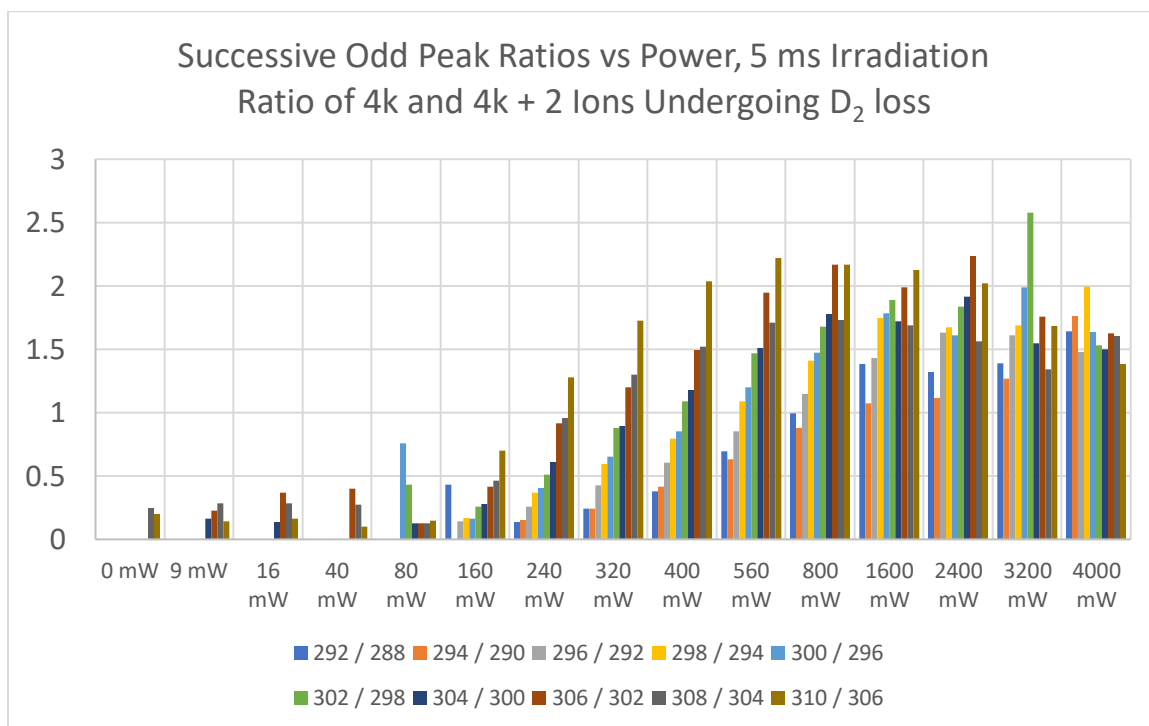


Figure 1.68: $d_{12}\text{-CorH}^+$ even reactant to product ratios of H-loss peaks losing D_2 at each laser power vs m/z

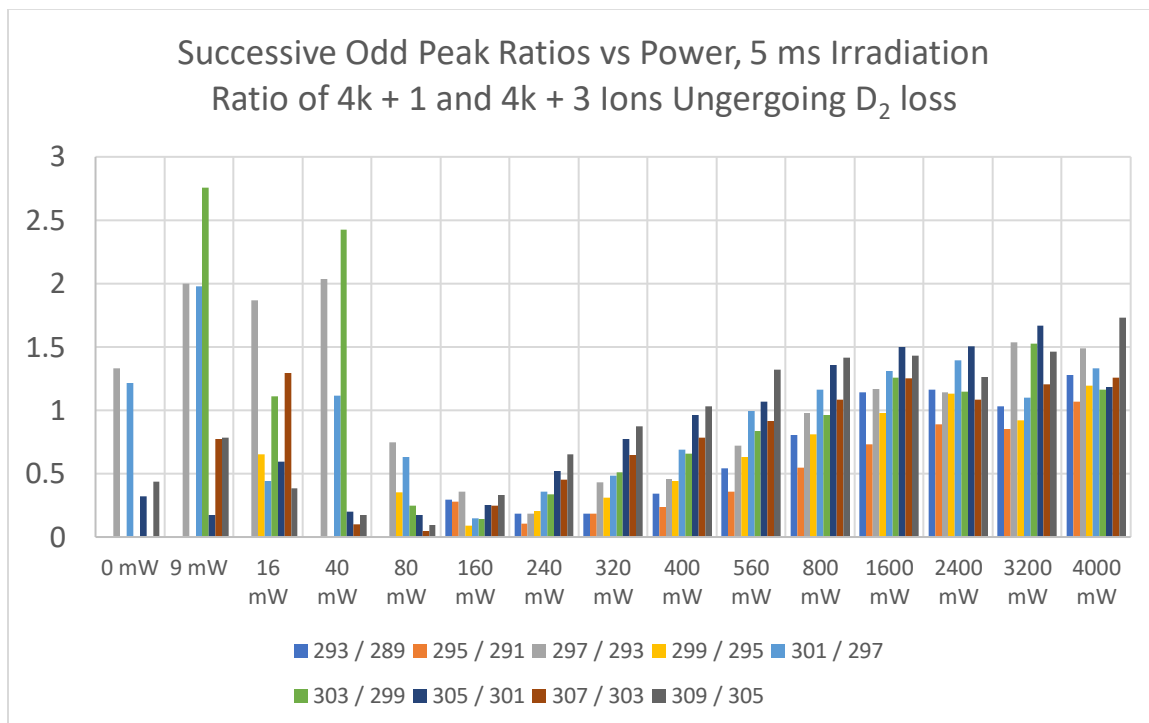


Figure 1.69: d_{12} -CorH⁺ odd reactant to product ratios of H-loss peaks losing D_2 at each laser power vs m/z

As can be seen from the plots above, H loss is more favorable for $4k + 3$ ions, increases with decreasing m/z for both odd ion types, but the increase with m/z is smaller at higher laser powers, and H loss is in general more favorable at higher laser powers. Even ion D loss is favorable for $4k + 2$ ions while very unfavorable for $4k$ ions, but like H loss D loss becomes more favorable as laser power increases. Odd ion D loss is more favorable for $4k + 3$ to $4k + 1$ ions, and becomes more favorable at higher laser powers, with no strong m/z trend within a particular laser power. HD loss is more favorable for $4k + 3$ to $4k$ ions, is strongly favored at larger m/z , and remains similarly favored as a reaction pathway above 400 – 560 mW. Even ion D_2 loss at mid photofragmentation laser powers is much more favorable at lower m/z , but at high laser powers is less important of a reaction channel and loses the m/z dependence. Odd ion D_2 loss at mid

photofragmentation powers shows a strong increase in reaction probability with decreasing m/z , with a more prominent reaction channel for $4k + 1$ ions over $4k + 3$ ions, and at high laser powers is less important of a reaction channel.

Summing taking the ratio of the sum of all possible reactant ions for each product ion with respect to mass and power, the following plots are created.

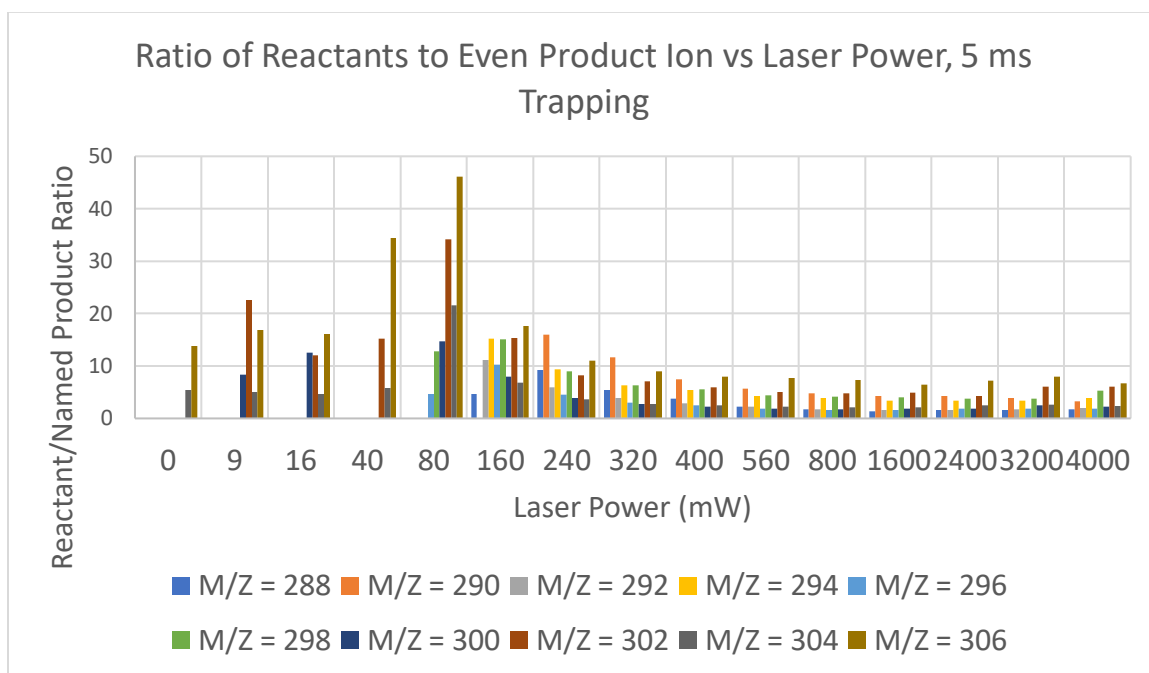


Figure 1.70: $d_{12}\text{-CorH}^+$ all reactant peaks to specific even product peak ratios of H-loss peaks at each laser power vs m/z

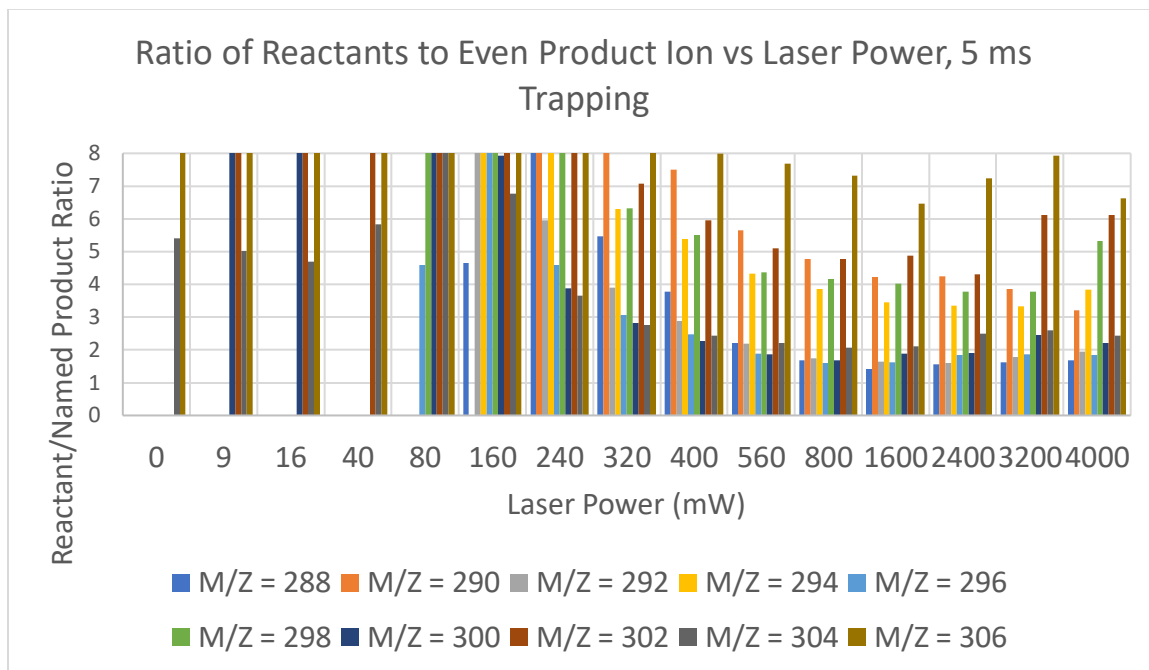


Figure 1.71: $d_{12}\text{-CorH}^+$ all reactant peaks to specific even product peak ratios of H-loss peaks at each laser power vs m/z zoomed in

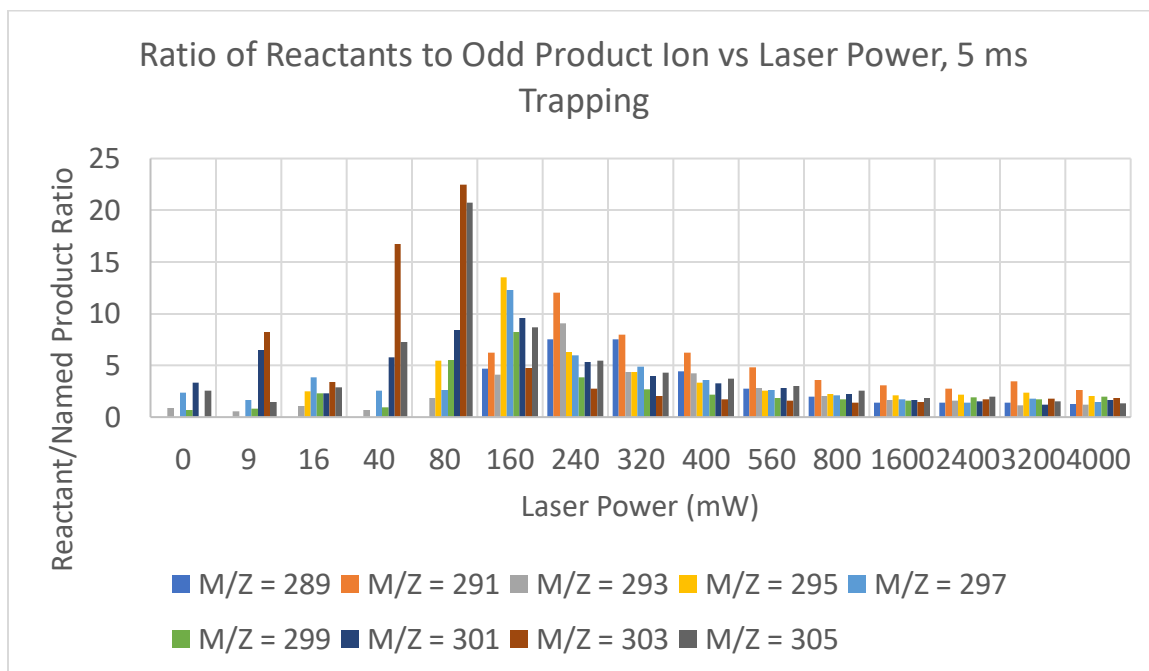


Figure 1.72: $d_{12}\text{-CorH}^+$ all reactant peaks to specific odd product peak ratios of H-loss peaks at each laser power vs m/z

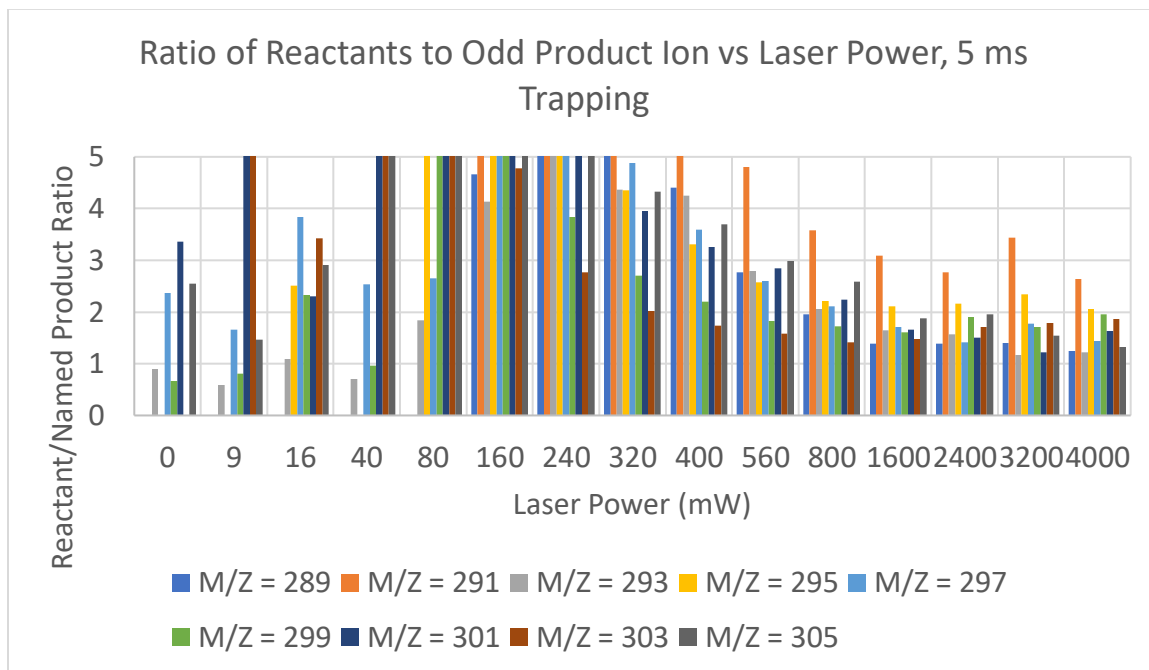


Figure 1.73: $d_{12}\text{-CorH}^+$ all reactant peaks to specific odd product peak ratios of H-loss peaks at each laser power vs m/z zoomed in

Despite being in a non-equilibrium chemical environment, the ion populations display some behaviors typical of a steady state. There are more reactant ions for each product ion, and it is easy to pick-out ions difficult to form, such as $m/z = 291$. This ion may not have a large cross section to 532 nm light but is in low abundance because C_{24}DH^+ is difficult to form from $d_{12}\text{-CorH}^+$ without losing H, and is not favorable as a reaction product from $m/z = 292 - 295$. The stability of 4k ions can be seen, since the ion has high abundance compared to the abundances of the potential reactants. The efficiency of dehydrogenation actually reaches a maximum around 2400 mW, where above this value the reactant to product ratios start to increase again. This would occur if larger m/z ions do not react as fast as smaller m/z ions, potentially indicating an acceleration in the reaction rate as m/z becomes lower due to stored internal energy from each absorption and dissociation.

The odd/even ratio (H vs no H) ratio shown above shows for the $(4k + 1) / 4k$ ratio, the ratio is always above one except for at high laser powers and low m/z . This likely is due to a difference in the C-fragmentation cross section. The ratio of $(4k + 3) / (4k + 2)$ is below 1 for ≥ 160 mW laser power, and the differences in these two types of odd/even ratios indicates again HD loss is the predominant H-removal pathway in d_{12} -CorH⁺.

After this analysis for 5 ms laser irradiation, a summary of 10 ms irradiation time findings are summarized. As discovered earlier looking at the time dependence of CorH⁺, spectra for d_{12} -CorH⁺ at 10 ms irradiation resembled the 5 ms spectra $\sqrt{2}$ times more powerful. The higher laser power H-region spectra at 10 ms showed the H-region peaks growing in then all disappearing from C-atom loss, yet there always remained a population of $m/z = 313$ d_{12} -CorH⁺ ions. It could be these ions evaded photolysis because of the focused laser, where these ions were in a closed trajectory that did not come near the focused 532 nm light.

An overview spectrum is shown below of the 10 ms d_{12} -CorH⁺ H-region.

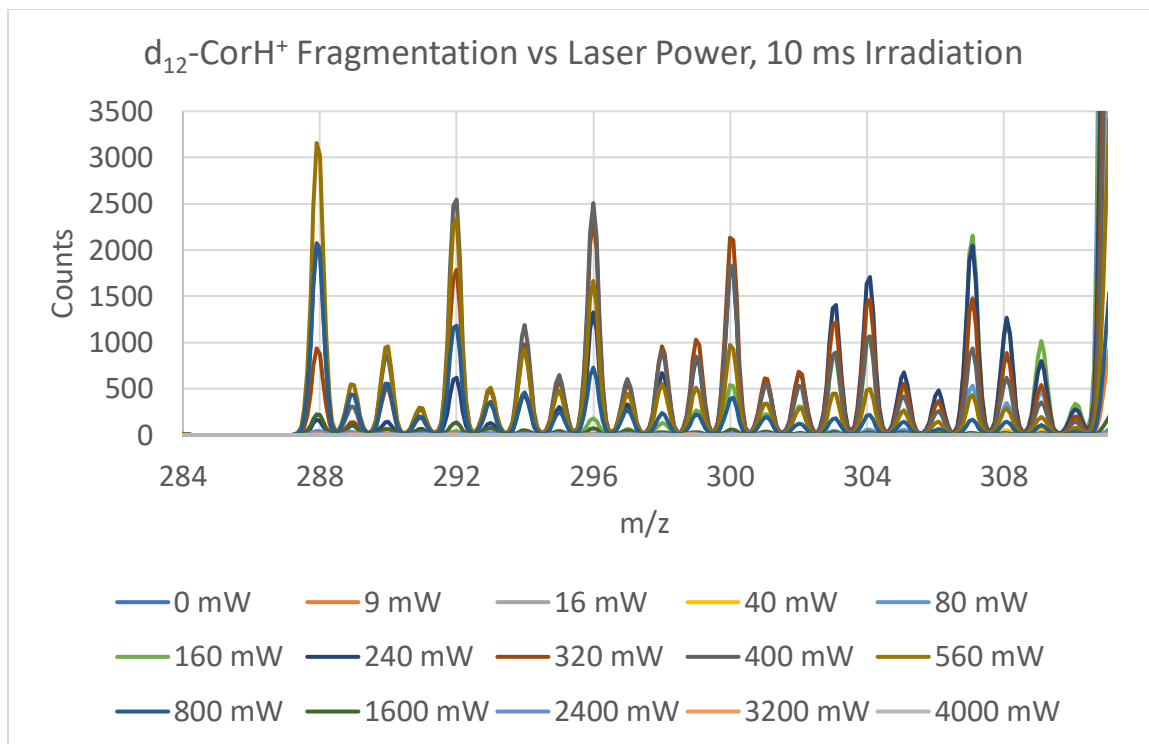


Figure 1.74: d_{12} -CorH⁺ mass spectrum vs laser power, 10 ms irradiation

The time dependence of the d_{12} -CorH⁺ was investigated, with ratio of 311 to 312 investigated.

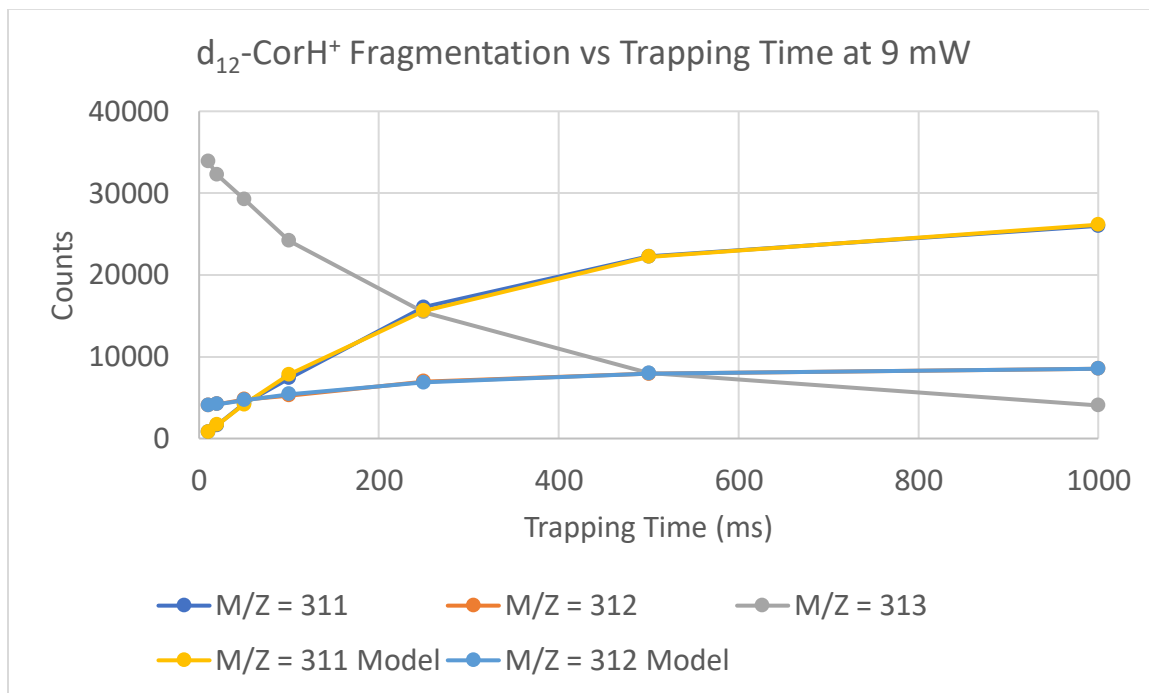


Figure 1.75: d_{12} -CorH⁺ and single H or D loss product counts vs irradiation time at 9 mW

The counts of $m/z = 311$ and 312 fit well to an exponentially-decreasing growth towards a constant.

$$counts_{311}(t) = 27140 \left(1 - \exp \left(-\frac{t}{287} \right) \right) - 170$$

$$counts_{312}(t) = 4780 \left(1 - \exp \left(-\frac{t}{252} \right) \right) + 3840$$

These models indicate that at very short irradiation times with low-power 9 mW light (or 0 mW controls), H will be removed from d_{12} -CorH⁺, which would be expected since the CH bond has a higher zero-point energy than the CD bond attached to the same sp^3 carbon site. Given enough time, the D/H loss ratio will be 5.68, which would be an isotope effect of 5.68 if it is assumed the aliphatic carbon site hydrogen atom dehydrogenates. For any hydrogen to dehydrogenate though, this would indicate an isotope effect of 0.437.

At higher laser power, the decrease in $m/z = 311$ and 312 follows an exponential decay to 0, but $d_{12}\text{-CorH}^+$ exponentially decays to a constant value. Unlike the power dependence which deplete most $d_{12}\text{-CorH}^+$ at high enough laser powers, at 320 mW the population of $d_{12}\text{-CorH}^+$ settles to about 48% of the 0 irradiation time value, and does not decrease further. The non-deuterated CorH^+ only shows this same settling to a value around 1% of the initial ion counts.

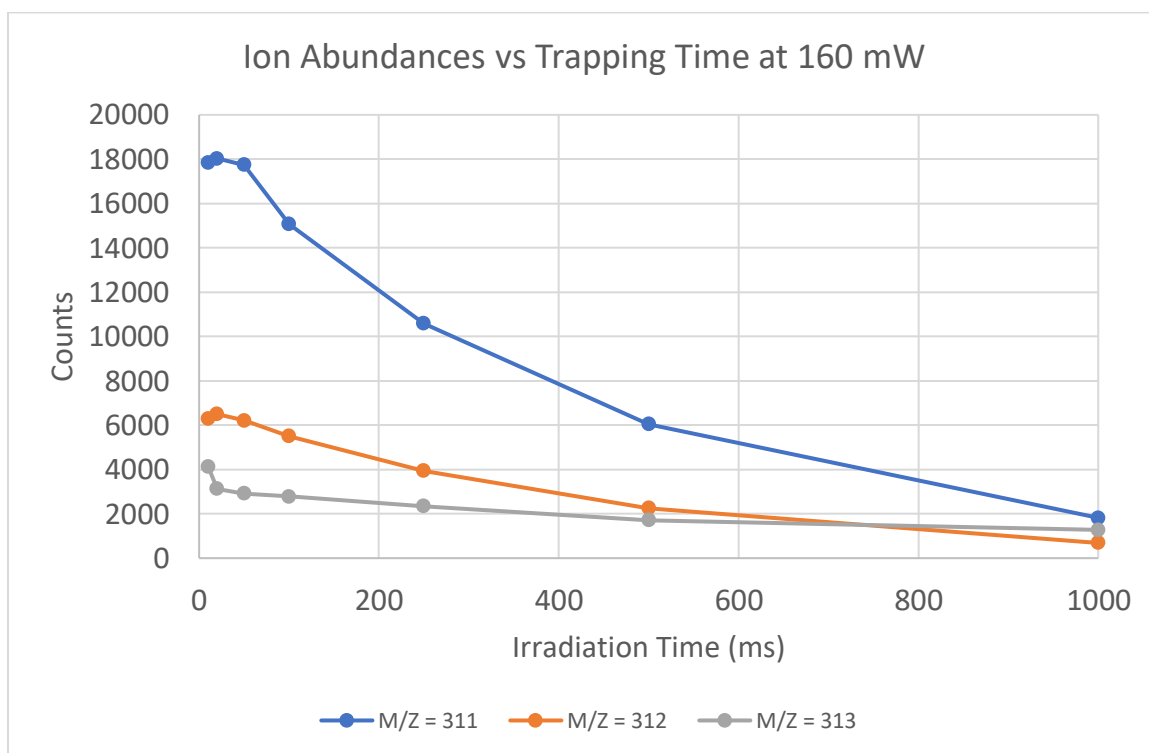


Figure 1.76: $d_{12}\text{-CorH}^+$ and single H or D loss product counts vs irradiation time at 160 mW

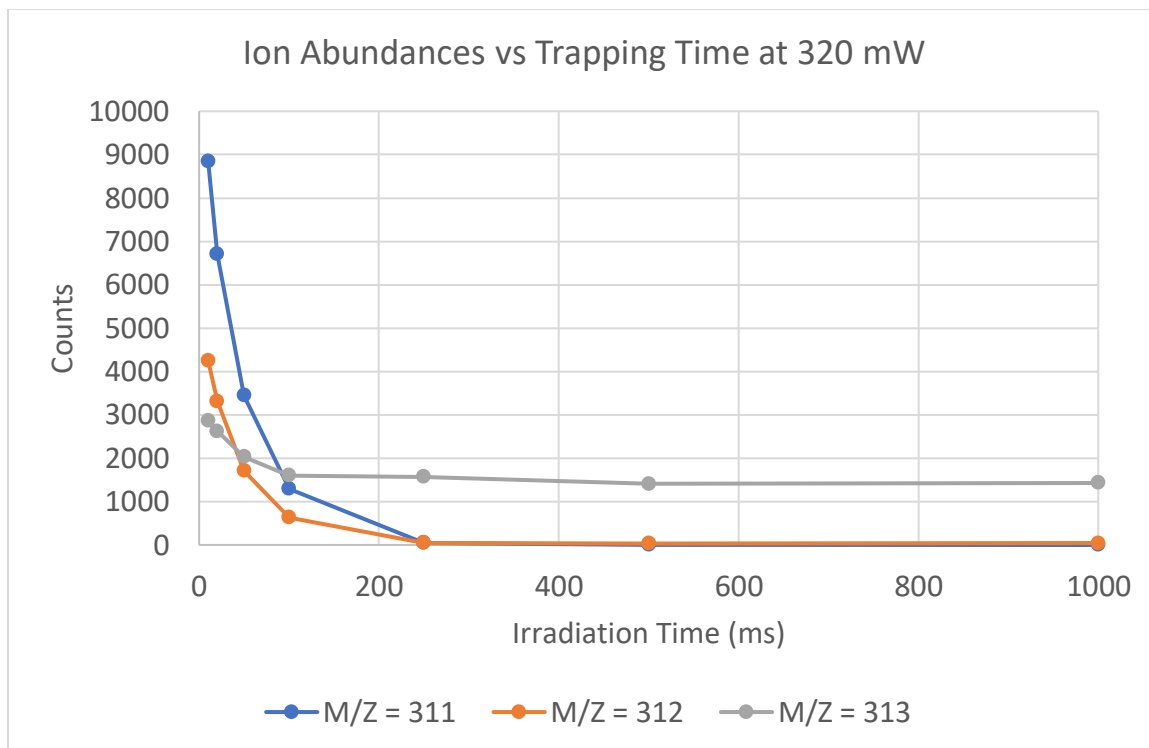


Figure 1.77: d_{12} -CorH⁺ and single H or D loss product counts vs irradiation time at 320 mW

Both 160 and 320 mW show $m/z = 313$ exponentially decaying, but to a non-zero value. All other m/z values in this region decay to 0 with increasing time, but $m/z = 313$ becomes a constant value which is higher at 320 mW than 160 or 9 mW. This potentially means at 320 mW, 48% of d_{12} -CorH⁺ suddenly has a negligible cross-section to 532 nm light, indicating either a photo-induced isomerization or a transition to a long-lived dark state. Likely this long-lived state is an electronic transition, due to the He buffer gas in the ion trap quenching vibrations.

The coronene cation is known to have an S_2 fluorescent state, but a transition to a long-lived triplet state would have to occur for the $m/z = 313$ to survive 1000 ms in appreciable concentration. There is a triplet state also approximately 2.3 eV above the ground state,¹⁹ so 320 mW may provide the perfect optical pump rate to excite coronene

into a dark triplet state without two photon absorption events from either the S_0 or S_2 states dehydrogenating the molecule. However, $m/z = 313$ is the protonated cation, and because of the disruption of the aromatic π system from protonation, this state may not exist at all.

Plots for the abundance of each ion vs trapping time for $d_{12}\text{-CorH}^+$ are shown below.

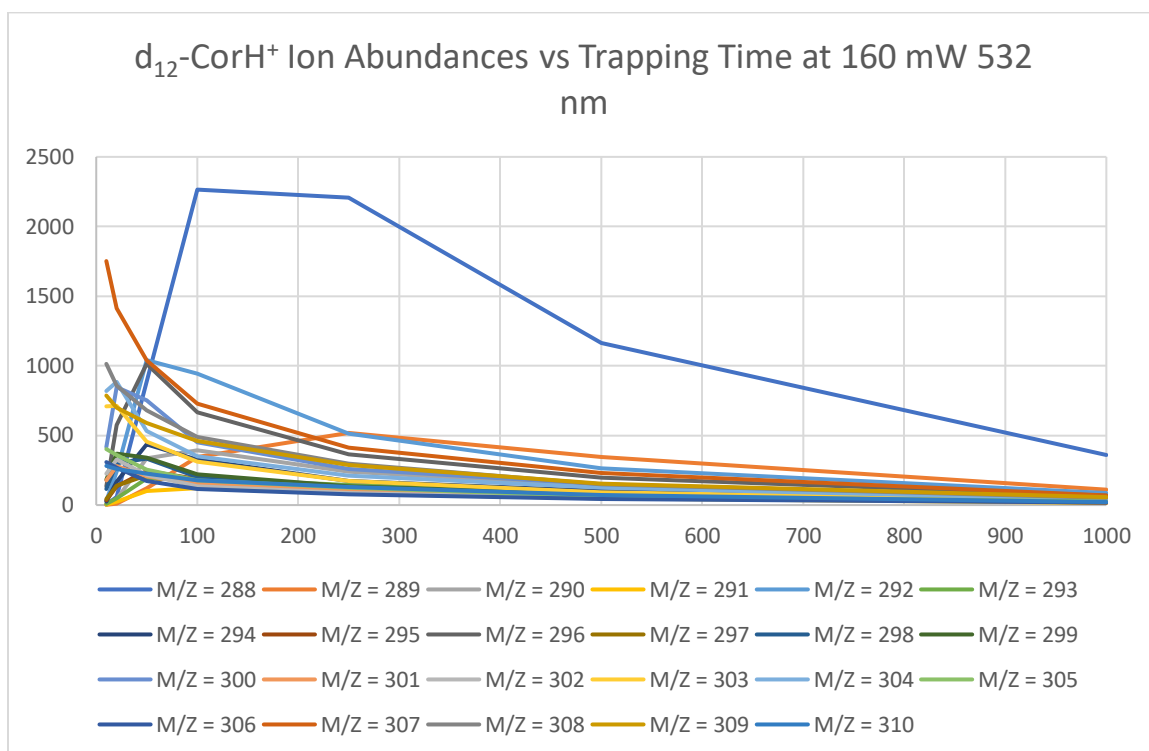


Figure 1.78: $d_{12}\text{-CorH}^+$ H-loss region peaks vs irradiation time at 160 mW

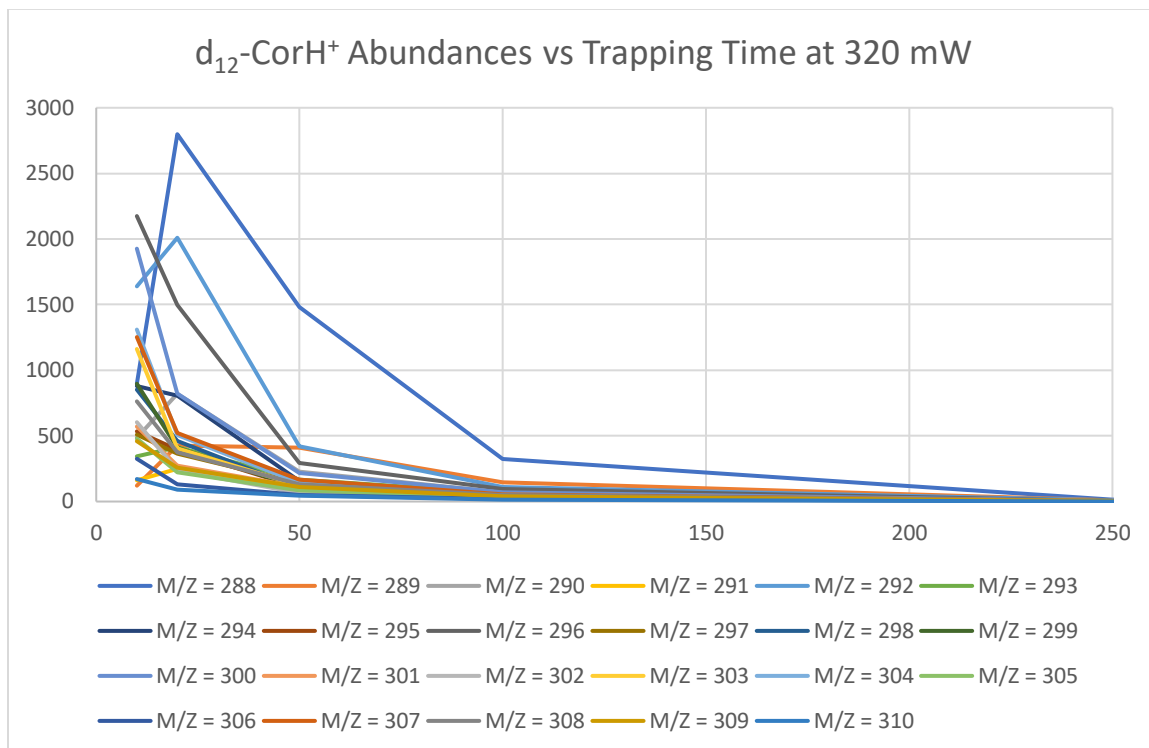
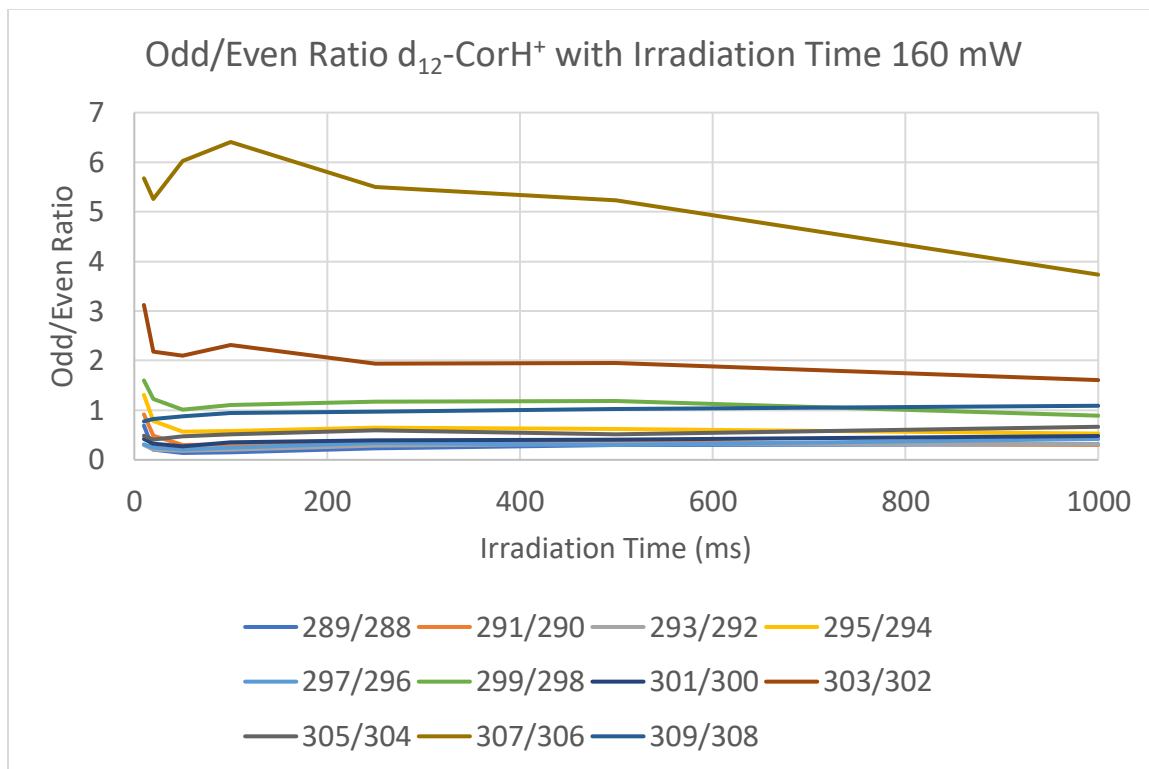
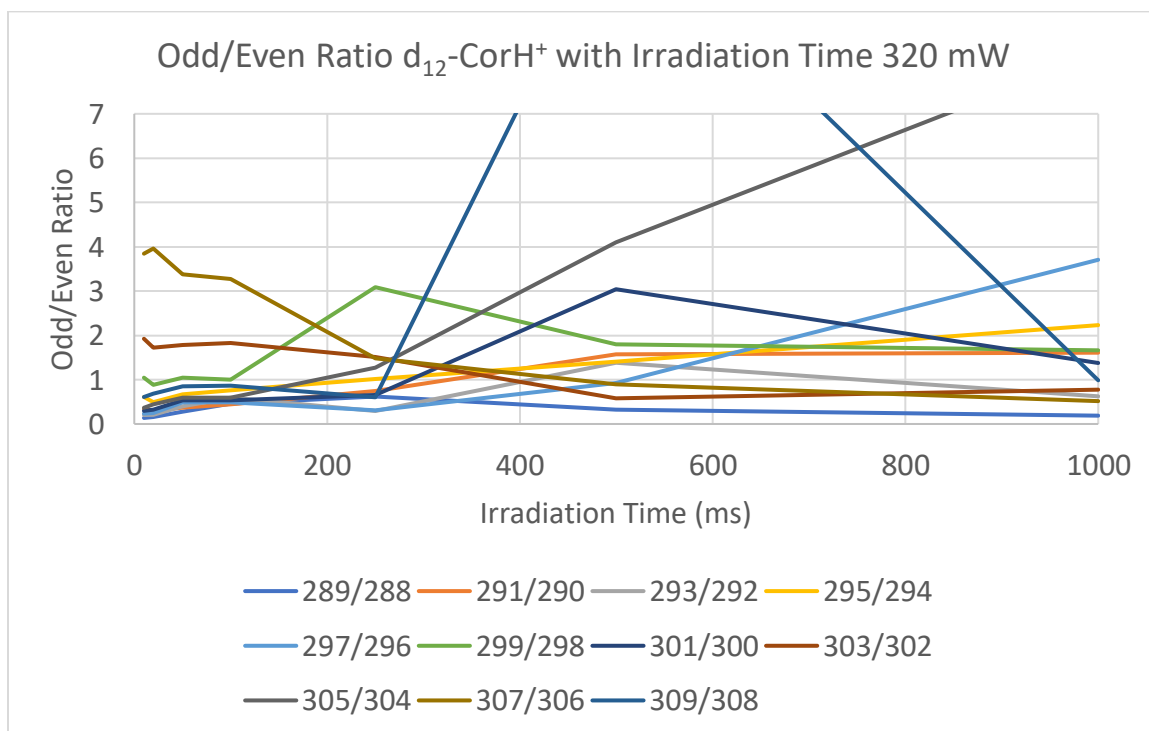


Figure 1.79: $d_{12}\text{-CorH}^+$ H-loss region peaks vs irradiation time at 160 mW

As can be seen, similar trends with power and mass can be seen for $d_{12}\text{-CorH}^+$ as for CorH^+ , in that C_{24}^+ is the most common ion by 50 – 80 ms, and all counts decrease quickly with increasing irradiation time as the C_{24}^+ cation dissociates into smaller carbon cations. Unsurprisingly 160 mW takes over four times longer to reach the same percentage decrease in ion signal as 320 mW. The odd/even ratios were also plotted, which showed some differences between the two laser powers.

Figure 1.80: d_{12} -CorH⁺ H-loss region odd/even ratio vs irradiation time at 160 mWFigure 1.81: d_{12} -CorH⁺ H-loss region odd/even ratio vs irradiation time at 320 mW

As can be seen, the odd/even ratio for 160 mW stays relatively constant over the 1000 ms, with few odd/even ratios changing the relative ordering of greatest to smallest. The ratios for 160 mW also remained more similar to the ratios seen at 5 and 10 ms, with several ratios below 0.5. The ratios for 320 mW suffered from lower ion counts, yielding widely varying odd/even ratios (the value of the 309/308 ratio at 500 ms is 11.57). Additionally, the relative ordering of odd/even ratios changes without a predictable pattern in m/z identity, and is much closer to 1. Therefore the odd/even ion imbalance is less pronounced for H-loss region ions as irradiation times grow beyond approximately 200 ms, since sufficient energy has been added to the system that the system is not energy as energy limited and favoring D₂ or HD loss over H or D loss.

When keeping constant total energy, again the effect of power and laser irradiation time was compared. In the C-loss region, the only condition with appreciable counts was 500 mW for 10 ms.

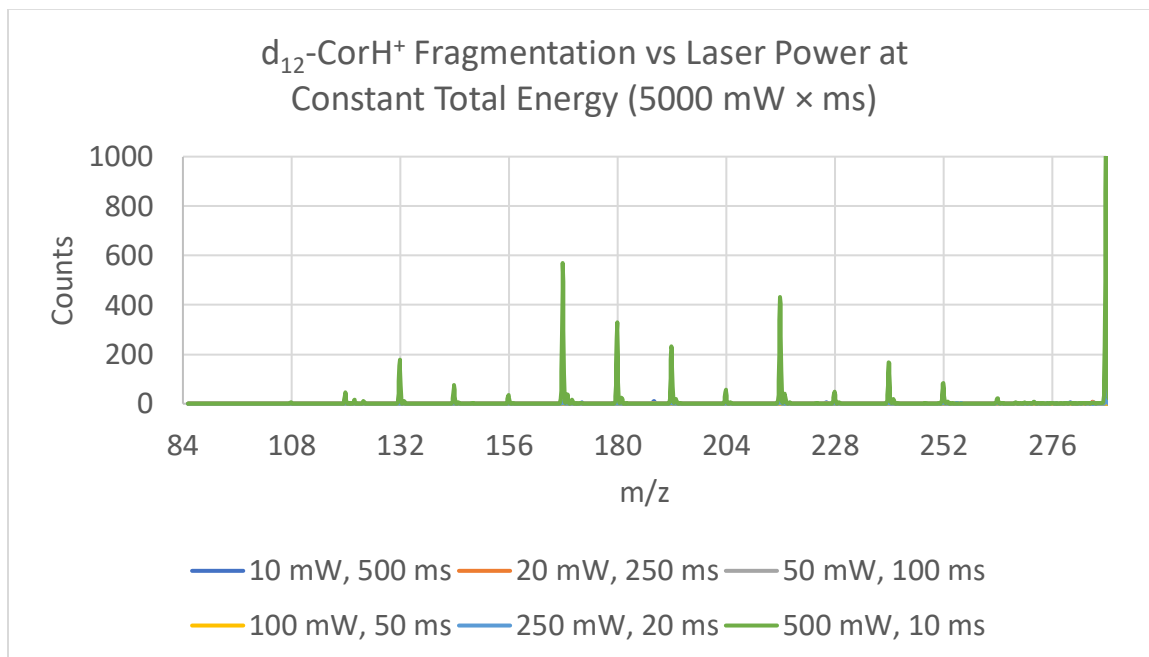


Figure 1.82: d_{12} -CorH⁺ C-loss region mass spectrum vs laser power at constant total energy

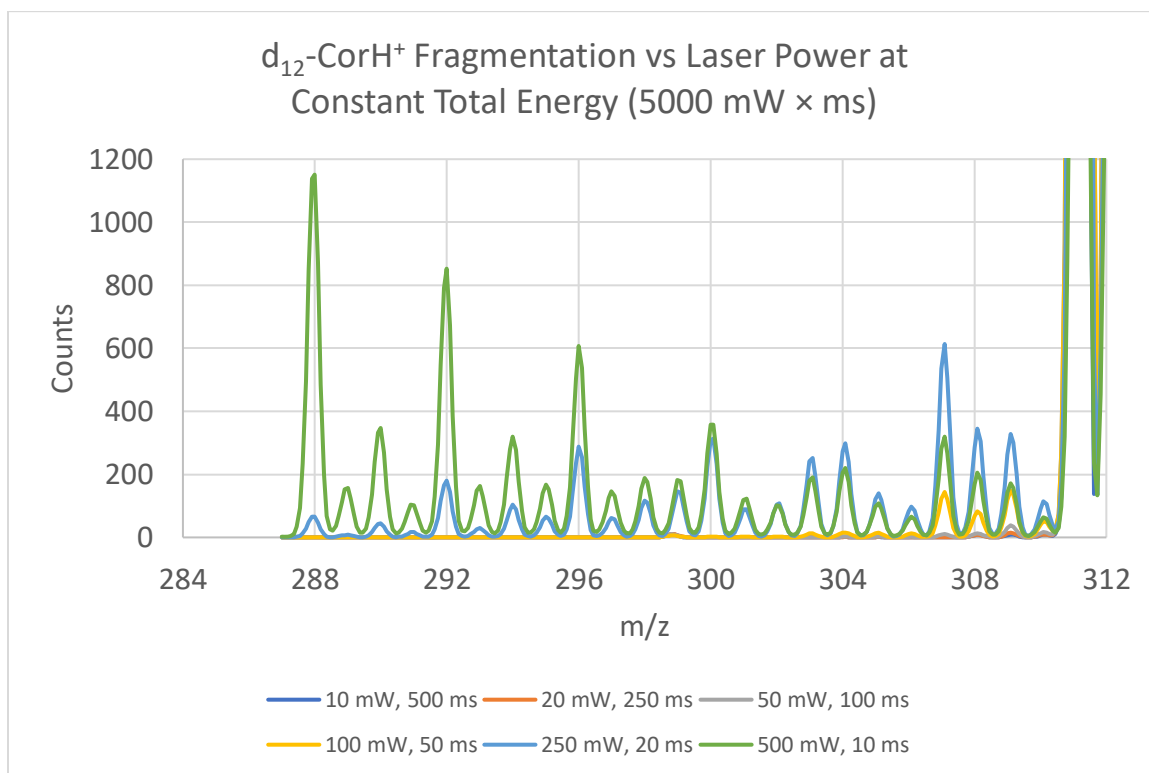


Figure 1.83: d_{12} -CorH⁺ H-loss region mass spectrum vs laser power at constant total energy

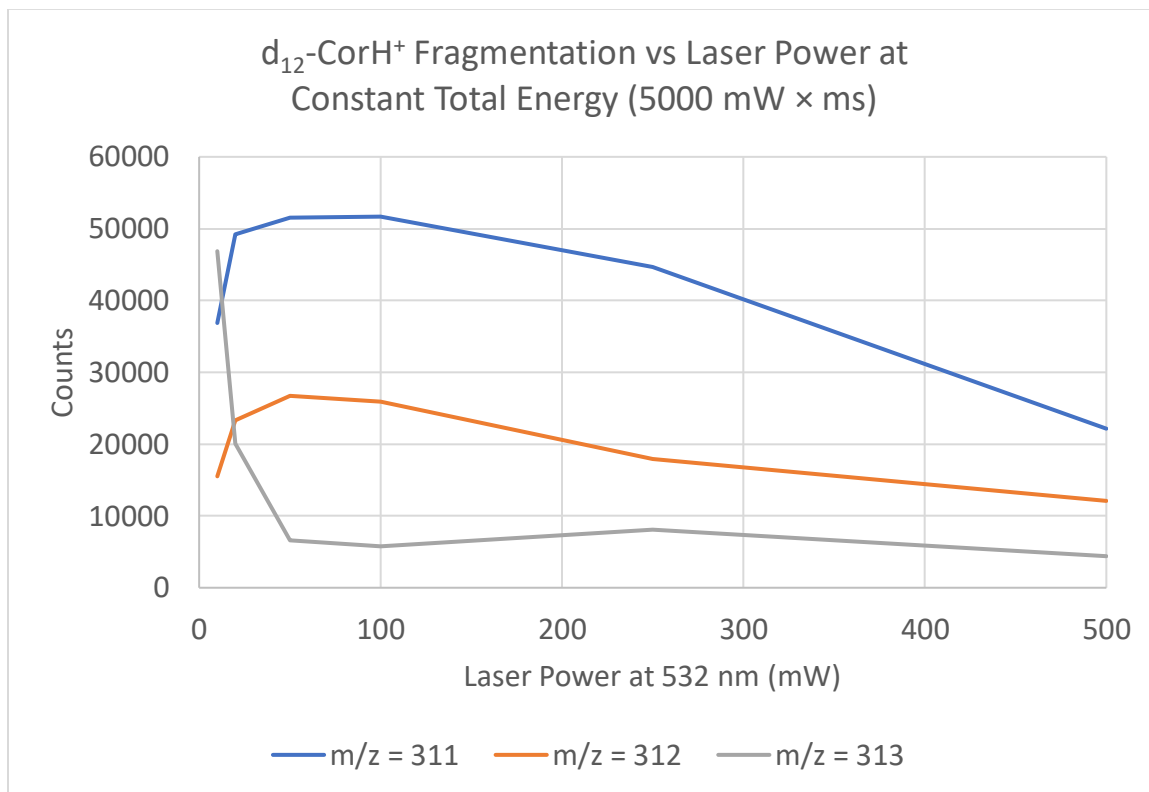


Figure 1.84: d_{12} -CorH⁺ and first H or D counts vs laser power at constant total energy

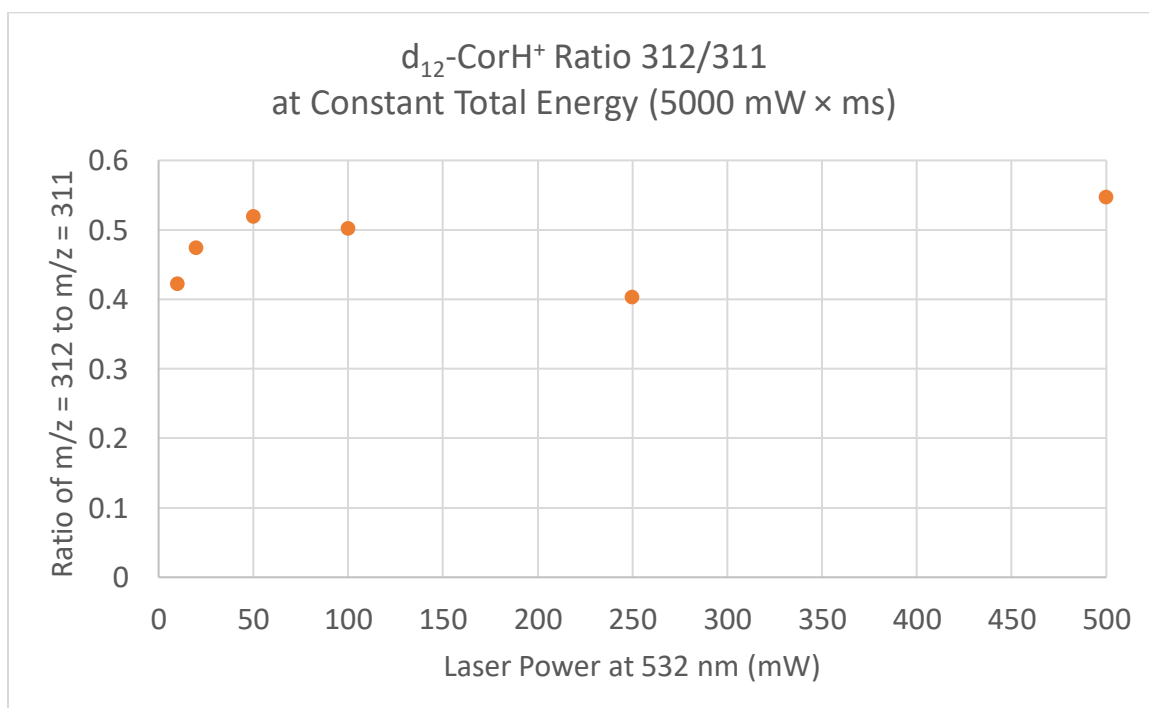


Figure 1.85: d_{12} -CorH⁺ first H or D loss ratio vs laser power at constant total energy

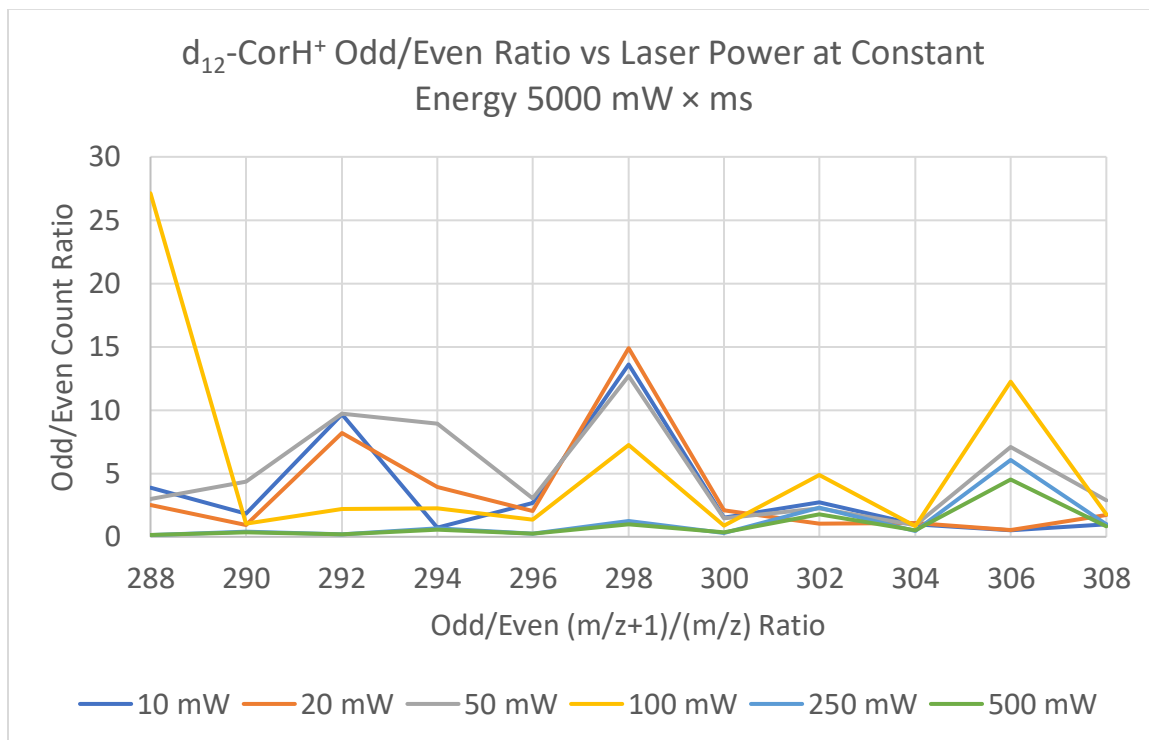


Figure 1.86: d_{12} -CorH⁺ H-loss region odd/even ratio vs laser power at constant total energy

While a nonlinear dependence on power exists for all regions of the d_{12} -CorH⁺ spectrum, the effect in the C-loss region is the same as for CorH⁺. Interesting to note is the pattern of the odd/even ratio between peaks changes around 100 mW and 50 ms of irradiation for a constant 5000 mW × ms spectrum. At low powers, the odd/even ratio is more pronounced at lower m/z , while at higher laser power the odd/even ratio grows larger at larger m/z . In both cases, the region of the H-loss spectrum where the odd/even ratio is highest is the region of the spectrum with the fewest ion counts, likely because the ion populations are more sensitive to production or loss processes which discriminate based on the parity of the ion. Another interesting note is the alternation of the intensity of the odd/even ratio. Above $m/z = 296$, the odd/even ratio is larger when the odd ion is a $4k + 3$ ion and the even ion is $4k + 2$, while the ratio is much closer to 1 for $4k + 1$ and $4k$ ions.

The ions $m/z = 294$ and 295 disturb this trend, possibly because 294 has three D atoms, allowing the D atoms can be spread far enough apart on edge sites to prevent H atoms hopping to an adjacent edge site with a D atom.

Discussion:

To summarize our results, we observed that the photofragmentation of both CorH^+ and $\text{d}_{12}\text{-CorH}^+$ is multistep. The coronene cation (regular or perdeuterated) loses a hydrogen to form CorH^+ (or CorD^+) at low laser powers, then the Cor^+ ion fragments apart to remove all the hydrogens primarily through loss of hydrogen molecules. Once the ion is the bare C_{24}^+ or C_{24}H^+ (but not C_{24}D^+), the carbon cation fragments first to primarily C_{18}^+ and C_{14}^+ , then with more energy C_{11}^+ , then C_{10}^+ , and finally fragments too small for detection.

The CID spectrum of CorH^+ and the 532 nm photodissociation spectra show no similarities. The most common peaks at $m/z = 213, 258, 269,$ and 283 correspond to loss of neutral C_7H_4 , C_3H_7 , C_2H_8 , and CH_6 , though not necessarily all lost in one step. The CID spectrum shows intensity at all masses, indicating the coronene is intact when fragmentation occurs. Masses corresponding to C_n^+ peaks are not more common than other masses. This shows photofragmentation is a complimentary technique to CID, since the fragmentation patterns are different.

The odd/even loss ratio was monitored during hydrogen loss over the full H-loss range for the first time, and found to favor even mass cations at lower laser powers, but to favor odd mass cations at higher laser powers. For $\text{d}_{12}\text{-CorH}^+$, the fragmentation process suggested cations with both an H and an odd number of D atoms were the least stable, while cations with a single H or D were of approximately equal stability, and cations with paired D atoms the most stable.

We also explored the power and irradiation time dependence of the protonated coronene cation and the coronene cation. The spectra were qualitatively dependent on the

product $(532 \text{ nm laser power})^2 \times (\text{irradiation time})$. While more than two photons are expected to be needed to dissociate a partially-dehydrogenated coronene ion, our results suggest two photons is sufficient per dehydrogenation. This could be because the ions are not in thermal equilibrium, being subject to the high voltage ionization process, irradiated with focused light, given kinetic energy to remain in the ion trap, numerous buffer gas collisions, and subject to multiple reactions with potentially non-equilibrium product energy distributions.

Many of our results were consistent with Jochims, Ekern, and Castellanos, in that we saw a preference for the even vs odd H-loss ions. but expanded on their results to describe the process of further H-loss. Our results show no C_2H_2 fragmentation unlike what has been seen for smaller PAHs, despite enough laser irradiation used to substantially decompose Cor^+ . This finding is consistent with Jochims and Ekern, who also did not witness acetylene production, but contrary to Paris's assertion acetylene loss should be an energetically-accessible decomposition pathway.^{7,12,15}

These experiments showed a similar growth in lower m $\text{C}_{24}\text{H}_m^+$ cations with increasing laser power consistent with Ekern's findings. Ekern however could not explore higher irradiation power to see C-loss from the dehydrogenated coronene cation because of limitations in Xe lamp power. At higher laser powers we could observe a decrease in the $\text{C}_{24}\text{H}_m^+$ signal, due to C-loss. Ekern used an unfocused broadband source to photodissociate Cor^+ , which acted as a low-power, very long exposure time source. A long exposure at a laser power around 80 mW likely would have resulted in a similar mass spectrum to Ekern since breaking apart the C_{24}^+ structure requires a certain rate of optical pumping to ensure enough internal energy. Longer exposure time cannot

compensate for energy removal processes, either through radiative de-excitation or collisions with He occurring at a rate of 10^3 sec^{-1} . Castellanos's results show a slowing in lower m $\text{C}_{24}\text{H}_m^+$ fragment growth at higher pulse energies, but this could be due to the laser pulse not filling the entire trapping volume. We did not observe this effect, but our experiment is vulnerable to a similar issue since the 532 nm light is focused to a 91 μm diameter spot. This focusing allowed the $(\text{laser power})^2$ effect to be observed, but our observed chemical reactions could be limited by unequal radiation intensity throughout the trap.

Both Ekern and Castellanos saw the development of the low odd/even ratio in the H-loss region, which is consistent with our findings. However, we saw this ratio fall below 1 with moderate laser powers, but unlike Ekern and Castellanos, we saw the ratio grow to favor odd ions at high laser powers. Ekern did not have enough irradiation available, and Castellanos purposely did not explore processes involving more than 4H atoms dissociating, so could not see the change in the odd/even ratio at high laser power. Castellanos also employed a pulsed set-up at 656 nm, which excites the $S_1 \leftarrow S_0$ transition instead of our 532 nm $S_2 \leftarrow S_0$ transition.

In the C-loss region, some C_n^+ ions were especially abundant, at $n = 10, 11, 14$, and 18. One explanation for these "magic numbers" is the stability of the structure of those cations. Dehydrogenated naphthalene C_{10}^+ is two hexagonal rings, dehydrogenated anthracene or phenanthrene C_{14}^+ is three hexagonal rings in either a line or 120° angle, and dehydrogenated C_{18}^+ is a structure resembling either tetracene, tetraphene, chrysene, benzo[c]phenanthrene, or triphenylene. The most abundant cation is C_{11}^+ , likely because the charge is delocalized in a proposed structure containing adjacent 6- and 7-member

rings (which share 2 carbons), with the positive charge on the 7-member ring to allow for aromaticity.

However, there are two alternate explanations. One is these structures have significantly smaller 532 nm photon cross sections. While Rademacher showed electronic transitions for C_n^+ ring species for even $12 \leq n \leq 28$ showed a linear progression of electronic transition peaks with frequency between $6,000 - 14,000 \text{ cm}^{-1}$ (for reference $532 \text{ nm} = 18,797 \text{ cm}^{-1}$), the transitions are narrow, so a large dip in the intensity across multiple n values would be expected. This explanation does not preclude the stability argument given above; it could be the stable cationic structures described also have no cross section at 532 nm too.

Another explanation is the stability of the neutral fragment plays a role. For $n = 10$ or 14 , the neutral fragment is a magic number too, while $n = 18$ has an $n = 6$ neutral fragment, which would be presumed to be a stable fragment since the carbon backbone of benzene is aromatic and stable.

Our experiments saw potential evidence for C-atom rearrangement, which there was no evidence for or against in previous studies. When our ion trapping procedure removed excess energy from the ions for 29.8 ms prior to irradiation, the C_nH^+/C_n^+ ratio suggested some preference for or against remaining with the cation fragment, while if the 29.8 ms A-delay collisional cooling prior to trapping was eliminated, no preference exists for which fragment the H is bonded to. There are several hypotheses for what could be occurring. One hypothesis is that the C–H BDE is lower than enough to roam around to every carbon in the $C_{24}H^+$ precursor, and the energy to remove the roaming H is high enough for the H to not dissociate from the remaining carbon atoms. Since an aromatic

C–C bond BDE is approximately 5.38 eV,³⁰ and at least two bonds must be broken to form a fragment, this likely indicates the energy to fully dissociate the H is approximately 10.76 eV. Jochims determined the energy required to remove H from the Cor^+ to be 18.7 eV,⁷ so 10.76 eV to remove H is not impossible.

Another explanation is the energy in the C_{24}H^+ fragment is not thermally distributed, and the C–H bond is not vibrationally hot after several photon absorption and H dissociation events, but the internal energy is all contained in the C_{24} network. The He of the trap would only remove about one 532 nm photon's worth of energy in 100 ms, so effectively there is no collisional energy removal from the ion. This hypothesis is possible because PAH fragmentation shows a size dependence on fragmentation probability, with larger PAHs > 40 atoms not dissociating H or H_2 , instead radiatively relaxing. With an IR radiative rate of $\sim 10^2 \text{ sec}^{-1}$ per bond, very high intensity light would be necessary for photofragmentation, larger than the 12 mJ/pulse supplied by Castellanos.¹⁵ All the energy is contained then in the C structure, or H dissociation would also occur in larger PAHs.

A third hypothesis is the H atom appears to have a 1 out of 24 probability of being attached to any C atom upon dissociation because the C_{24} bond network has isomerized. This hypothesis also is potentially valid because coronene has known isomerization pathways to form larger C-rings,³² and the spectroscopy of large C_{24}^+ rings have been studied by Rademacher through 355 nm ablation of a graphite target.³³ Cyclic C_{24}^+ therefore can be produced from a graphene-like surface, and attachment of an H is unlikely to hinder the isomerization process. A single large ring would make every carbon chemically identical, making fragmentation a simple probability that ignores

energy or bonding differences found between C atoms in coronene's carbon network.

This argument assumes characteristic about the neutral fragment though; it could be the neutral fragment also preferentially keeps H atoms, so dissociation can come from $C_{24}H_2^+$ and an H is removed with the neutral.

In coronene, a larger implication of this finding is C_{24}^+ ions could in fact form a catalytic surface for the surface reaction $H + H \rightarrow H_2$. Since the dehydrogenation process was endothermic, a Langumir-Hinshelwood surface reaction for $H + H \rightarrow H_2$ is then possible using C_{24}^+ as a catalyst. In contrast to H, $C_{24}D^+$ was not observed to survive carbon fragmentation with the D still attached to the cation fragment, implying the energy to dissociate D from the remaining carbon atoms is lower than for H. Since the C–D bond has a lower zero-point energy than the C–H bond, the C–D bond is expected to require more energy to dissociate, so the resulting roaming D atom should have less energy to dissociate from the carbon atoms. It is possible though the C–D BDE requires more photons worth of energy than for C–H BDE at 532 nm. This all assumes the D atom has no preference for choosing the neutral vs cation fragment; which if wrong would be a project worthy of further study. Regardless, the formation of an energetic roaming H vs the absence of a roaming D could have significant implications in the H to H_2 ratio vs the D to HD or D_2 ratio in the astrochemistry of regions of space with molecule densities and photon fluxes similar to our experimental conditions..

An alternative hypothesis is the same carbon number n peaks are the most abundant for both methods though, suggesting that the carbon number itself is what is making that C_n^+ cation stable, not any internal cation structure. Ring opening along the edge of coronene would proceed through a mechanism similar to that proposed by

Trinquier,³² but how the center ring is broken has not been studied. This hypothesis suffers from difficulties explaining the stability of $n = 10, 11, 14$, and 18 C_n^+ cations, which as stated earlier would be intuitively stable for a hexagonal patterned C_n^+ ion.

Ring opening would be consistent with the results of von Helden *et al.*,³⁴ who studied carbonaceous C_n^+ ion structure for $6 \leq n \leq 40$ *via* laser desorption, ion chromatography, followed by ion mobility measurements. For $n = 24$, von Helden observed approximately 90% of C_{24}^+ ions adopt a single ring and 10% adopt a propeller or bowtie shaped bicyclic ring system, with a hexagonal ring linking two larger rings. Ions $n < 30$ did not form any cupped open-fullerene fragments, and interestingly found fragmentation for $24 \leq n \leq 30$ to favor ejection of large $n = 10$ and 14 fragments as presumed monocyclic species. Ejection of neutral $n = 10$ and 14 would result in cationic $n = 14$ and 10 , respectively, which are common fragments seen in our data. These species could form from the loss of one bowtie arm from the C_{24}^+ cation. Therefore, the common C-loss ion fragments seen in our mass spectrum may be due to the stability of neutral loss fragments.

An issue affecting all experiment of Cor^+ is whether dissociation is from the excited electronic state or a vibrationally-hot ground electronic state cation. Further, each H or H_2 loss need not happen from the same quantum state at all, only that to be consistent with our findings, more energy is needed to remove more hydrogens from $\text{C}_{24}\text{H}_m^+$. A technique capable of measuring the kinetic energy of the photofragmentation products could answer these question, especially if combined with the ability to trap the intermediate $\text{C}_{24}\text{H}_m^+$ masses.

Another issue that affects both our and previous experiments is the cross-sections for each of the H-loss species is unknown. We assume cross-sections to 532 nm light similar to that of Cor^+ , but further studies should systematically observe the cross-section by using sequential ion traps or MS^2 techniques where first a $\text{C}_{24}\text{H}_m^+$ ion is created, held to de-excite the ion, and the cross-section then carefully measured at low laser powers. Alternatively, these $\text{C}_{24}\text{H}_m^+$ ions could be created by photolysis of a halogenated precursor. Observing the effects of mixed H and D atoms is likely only feasible in theory with the number of potential $\text{C}_{24}\text{H}_m\text{D}_{12-m}^+$ structures.

The presence of the dark state seen on long irradiation times at 320 mW irradiation of $\text{d}_{12}\text{-CorH}^+$ was a surprising find, suggesting nearly half of $\text{d}_{12}\text{-CorH}^+$ ions are entering a long-lived dark state with no 532 nm photon cross-section. This percentage is too large for ions to be missing a focused laser spot in the ion trap, else this dark state would be seen at both 9 and 160 mW. The dark state cannot be rapid collisional de-excitation of the molecule, because then more than half of the population of 9 and 160 mW $\text{d}_{12}\text{-CorH}^+$ cations would be expected to occupy the dark state.

Conclusion:

A custom mass spectrometer capable of laser-induced photodissociation was constructed, which has laser time resolution of 1 ms and has ion count uncertainties ~4%. Trapped protonated coronene exhibited several trends in dissociation with laser power. At low power, a proton is removed to restore aromaticity. At medium power the H atoms dissociate, primarily as H_2 , creating an unbalance in the odd to even mass abundances between 288 – 301 m/z. At high powers C atoms start dissociating from the remaining carbon-only cation to form stable smaller cations. However, depending on the internal

energy of the carbon-only cation, the cation can potentially isomerize, forming a moiety of potential astrochemical catalytic significance. The studies with $\text{d}_{12}\text{-CorH}^+$ reinforce the conclusions with H_2 vs H loss, where HD loss can be seen to predominate. The presence of an excited, yet photostable species $\text{d}_{12}\text{-CorH}^+$ is also of interest, since this species could act as a proton donor in astrochemical environments. Finally, the power and trap time dependences show photofragmentation is greater with higher power than lower trap times, indicating an energy-limited process that can de-excite at rates comparable to photon absorption.

The comparison of our results to other studies is complicated due to the use of continuous vs pulsed lasers, and the different wavelengths used, causing electronic excited states to be accessed. Laser improvements to the experimental design would be to include pulsed lasers, as well as lasers at different wavelengths. The ability to scan wavelength could add an orthogonal data axis to differentiate between various photofragmentation species based on absorption cross section too, and would aid comparison with previous experiments.

Acknowledgments:

The above work was funded by the NASA PICASSO award 80NM0018D0004. A special thanks to fellow graduate student Tyler Nguyen for helping me collect data, as well as Dr. Deacon Nemchick and Dr. Frank Maiwald at JPL. well as Professor Jack Beauchamp and Dr. Rob Hodyss for additional mentorship and advice.

References:

- (1) Cox, N. L. J. The PAH-DIB Hypothesis. In *The PAH-DIB Hypothesis*; EDP Sciences, 2021; pp 349–354. <https://doi.org/10.1051/978-2-7598-2482-3.c038>.
- (2) Allamandola, L. J.; Tielens, A. G. G. M.; Barker, J. R. Polycyclic Aromatic Hydrocarbons and the Unidentified Infrared Emission Bands - Auto Exhaust along the Milky Way. *Astrophys. J.* **1985**, 290, L25. <https://doi.org/10.1086/184435>.
- (3) Boschman, L.; Cazaux, S.; Spaans, M.; Hoekstra, R.; Schlathölter, T. H H_2 Formation on PAHs in Photodissociation Regions: A High-Temperature Pathway to Molecular Hydrogen. *Astron. Astrophys.* **2015**, 579, A72. <https://doi.org/10.1051/0004-6361/201323165>.
- (4) Berné, O.; Montillaud, J.; Joblin, C. Top-down Formation of Fullerenes in the Interstellar Medium. *Astron. Astrophys.* **2015**, 577, A133. <https://doi.org/10.1051/0004-6361/201425338>.
- (5) Berné, O.; Mulas, G.; Joblin, C. Detection of the Buckminsterfullerene Cation (C_{60}^+) in Space. *Proc. Int. Astron. Union* **2013**, 9 (S297), 203–207. <https://doi.org/10.1017/S1743921313015858>.
- (6) Allain, T.; Sedlmayr, E.; Leach, S. Formation and Photodestruction of PAHs. *Astrophys. Space Sci.* **1995**, 224 (1), 417–418. <https://doi.org/10.1007/BF00667884>.
- (7) Jochims, H. W.; Ruhl, E.; Baumgartel, H.; Tobita, S.; Leach, S. Size Effects on Dissociation Rates of Polycyclic Aromatic Hydrocarbon Cations: Laboratory Studies and Astrophysical Implications. *Astrophys. J.* **1994**, 420, 307. <https://doi.org/10.1086/173560>.
- (8) West, B.; Joblin, C.; Blanchet, V.; Bodi, A.; Sztáray, B.; Mayer, P. M. On the Dissociation of the Naphthalene Radical Cation: New IPEPICO and Tandem Mass Spectrometry Results. *J. Phys. Chem. A* **2012**, 116 (45), 10999–11007. <https://doi.org/10.1021/jp3091705>.
- (9) Bouwman, J.; De Haas, A. J.; Oomens, J. Spectroscopic Evidence for the Formation of Pentalene⁺ in the Dissociative Ionization of Naphthalene. *Chem. Commun.* **2016**, 52 (12), 2636–2638. <https://doi.org/10.1039/C5CC10090A>.
- (10) Boissel, P.; de Parseval, P.; Marty, P.; Lefèvre, G. Fragmentation of Isolated Ions by Multiple Photon Absorption: A Quantitative Study. *J. Chem. Phys.* **1997**, 106 (12), 4973–4984. <https://doi.org/10.1063/1.473545>.
- (11) West, B.; Sit, A.; Mohamed, S.; Joblin, C.; Blanchet, V.; Bodi, A.; Mayer, P. M. Dissociation of the Anthracene Radical Cation: A Comparative Look at IPEPICO and Collision-Induced Dissociation Mass Spectrometry Results. *J. Phys. Chem. A* **2014**, 118 (42), 9870–9878. <https://doi.org/10.1021/jp505438f>.

- (12) Ekern, S. P.; Marshall, A. G.; Szczepanski, J.; Vala, M. Photon-Induced Complete Dehydrogenation of Putative Interstellar Polycyclic Aromatic Hydrocarbon Cations: Coronene And Naphtho[2,3-A]Pyrene. *Astrophys. J.* **1997**, No. 488, L39–L41.
- (13) West, B.; Useli-Bacchitta, F.; Sabbah, H.; Blanchet, V.; Bodi, A.; Mayer, P. M.; Joblin, C. Photodissociation of Pyrene Cations: Structure and Energetics from $C_{16}H_{10}^+$ to C_{14}^+ and Almost Everything in Between. *J. Phys. Chem. A* **2014**, *118* (36), 7824–7831. <https://doi.org/10.1021/jp506420u>.
- (14) Jochims, H. W.; Baumgartel, H.; Leach, S. Structure-dependent Photostability of Polycyclic Aromatic Hydrocarbon Cations: Laboratory Studies and Astrophysical Implications. *Astrophys. J.* **1999**, *512* (1), 500–510. <https://doi.org/10.1086/306752>.
- (15) Castellanos, P.; Candian, A.; Zhen, J.; Linnartz, H.; Tielens, A. G. G. M. Photoinduced Polycyclic Aromatic Hydrocarbon Dehydrogenation The Competition between H- and H_2 -Loss. *Astron. Astrophys.* **2018**, *616*, A166. <https://doi.org/10.1051/0004-6361/201833220>.
- (16) Ekern, S. P.; Marshall, A. G.; Szczepanski, J.; Vala, M. Photodissociation of Gas-Phase Polycyclic Aromatic Hydrocarbon Cations. *J. Phys. Chem. A* **1998**, *102* (20), 3498–3504. <https://doi.org/10.1021/jp980488e>.
- (17) Paris, C.; Alcamí, M.; Martín, F.; Díaz-Tendero, S. Multiple Ionization and Hydrogen Loss from Neutral and Positively-Charged Coronene. *J. Chem. Phys.* **2014**, *140* (20), 204307. <https://doi.org/10.1063/1.4875805>.
- (18) Zhen, J.; Castellanos, P.; Paardekooper, D. M.; Ligterink, N.; Linnartz, H.; Nahon, L.; Joblin, C.; Tielens, A. G. G. M. Laboratory Photo-Chemistry of PAHs: Ionization versus Fragmentation. *Astrophys. J. Lett.* **2015**, *804* (1), L7. <https://doi.org/10.1088/2041-8205/804/1/L7>.
- (19) Garkusha, I.; Fulara, J.; Sarre, P. J.; Maier, J. P. Electronic Absorption Spectra of Protonated Pyrene and Coronene in Neon Matrixes. *J. Phys. Chem. A* **2011**, *115* (40), 10972–10978. <https://doi.org/10.1021/jp206188a>.
- (20) Rice, C. A.; Hardy, F.-X.; Gause, O.; Maier, J. P. (1) $^1A' \leftarrow X^1A'$ Electronic Transition of Protonated Coronene at 15 K. *J. Phys. Chem. Lett.* **2014**, *5* (6), 942–945. <https://doi.org/10.1021/jz500068r>.
- (21) Simon, A.; Rapacioli, M.; Rouaut, G.; Trinquier, G.; Gadéa, F. X. Dissociation of Polycyclic Aromatic Hydrocarbons: Molecular Dynamics Studies. *Philos. Transact. A Math. Phys. Eng. Sci.* **2017**, *375* (2092), 20160195. <https://doi.org/10.1098/rsta.2016.0195>.
- (22) West, B.; Rodriguez Castillo, S.; Sit, A.; Mohamad, S.; Lowe, B.; Joblin, C.; Bodi, A.; Mayer, P. M. Unimolecular Reaction Energies for Polycyclic Aromatic

- Hydrocarbon Ions. *Phys. Chem. Chem. Phys. PCCP* **2018**, *20* (10), 7195–7205. <https://doi.org/10.1039/c7cp07369k>.
- (23) Hammonds, M.; Pathak, A.; Sarre, P. J. TD-DFT Calculations of Electronic Spectra of Hydrogenated Protonated Polycyclic Aromatic Hydrocarbon (PAH) Molecules: Implications for the Origin of the Diffuse Interstellar Bands? *Phys. Chem. Chem. Phys.* **2009**, *11* (22), 4458. <https://doi.org/10.1039/b903237a>.
- (24) Mallocci, G.; Mulas, G.; Joblin, C. Electronic Absorption Spectra of PAHs up to Vacuum UV: Towards a Detailed Model of Interstellar PAH Photophysics. *Astron. Astrophys.* **2004**, *426* (1), 105–117. <https://doi.org/10.1051/0004-6361:20040541>.
- (25) Knorke, H.; Langer, J.; Oomens, J.; Dopfer, O. INFRARED SPECTRA OF ISOLATED PROTONATED POLYCYCLIC AROMATIC HYDROCARBON MOLECULES. *Astrophys. J.* **2009**, *706* (1), L66–L70. <https://doi.org/10.1088/0004-637X/706/1/L66>.
- (26) Edward P., H.; Sharon G., L. Proton Affinity Evaluation. In *NIST Chemistry WebBook*; P. J., L., W. G., M., Series Eds.; NIST Standard Reference Database; National Institute of Standards and Technology: Gaithersburg, MD 20899, 2011; Vol. 69.
- (27) Clar, E.; Robertson, J. M.; Schloegl, R.; Schmidt, W. Photoelectron Spectra of Polynuclear Aromatics. 6. Applications to Structural Elucidation: “Circumanthracene.” *J. Am. Chem. Soc.* **1981**, *103* (6), 1320–1328. <https://doi.org/10.1021/ja00396a003>.
- (28) Thermo Electron Corporation. Finnigan LTQ Hardware Manual 97055-97013 Revision B, 2003.
- (29) Franzen, A. GWOptics, 2006.
- (30) Barckholtz, C.; Barckholtz, T. A.; Hadad, C. M. C–H and N–H Bond Dissociation Energies of Small Aromatic Hydrocarbons. *J. Am. Chem. Soc.* **1999**, *121* (3), 491–500. <https://doi.org/10.1021/ja982454q>.
- (31) Aryanpour, K.; Shukla, A.; Mazumdar, S. Electron Correlations and Two-Photon States in Polycyclic Aromatic Hydrocarbon Molecules: A Peculiar Role of Geometry. *J. Chem. Phys.* **2014**, *140* (10), 104301. <https://doi.org/10.1063/1.4867363>.
- (32) Trinquier, G.; Simon, A.; Rapacioli, M.; Gadéa, F. X. PAH Chemistry at EV Internal Energies. 2. Ring Alteration and Dissociation. *Mol. Astrophys.* **2017**, *7*, 37–59. <https://doi.org/10.1016/j.molap.2017.02.002>.

- (33) Rademacher, J.; Reedy, E. S.; Campbell, E. K. Electronic Spectroscopy of Monocyclic Carbon Ring Cations for Astrochemical Consideration. *J. Phys. Chem. A* **2022**, *126* (13), 2127–2133. <https://doi.org/10.1021/acs.jpca.2c00650>.
- (34) Von Helden, G.; Hsu, M. T.; Gotts, N.; Bowers, M. T. Carbon Cluster Cations with up to 84 Atoms: Structures, Formation Mechanism, and Reactivity. *J. Phys. Chem.* **1993**, *97* (31), 8182–8192. <https://doi.org/10.1021/j100133a011>.

Appendix:

5 ms plots CorH^+

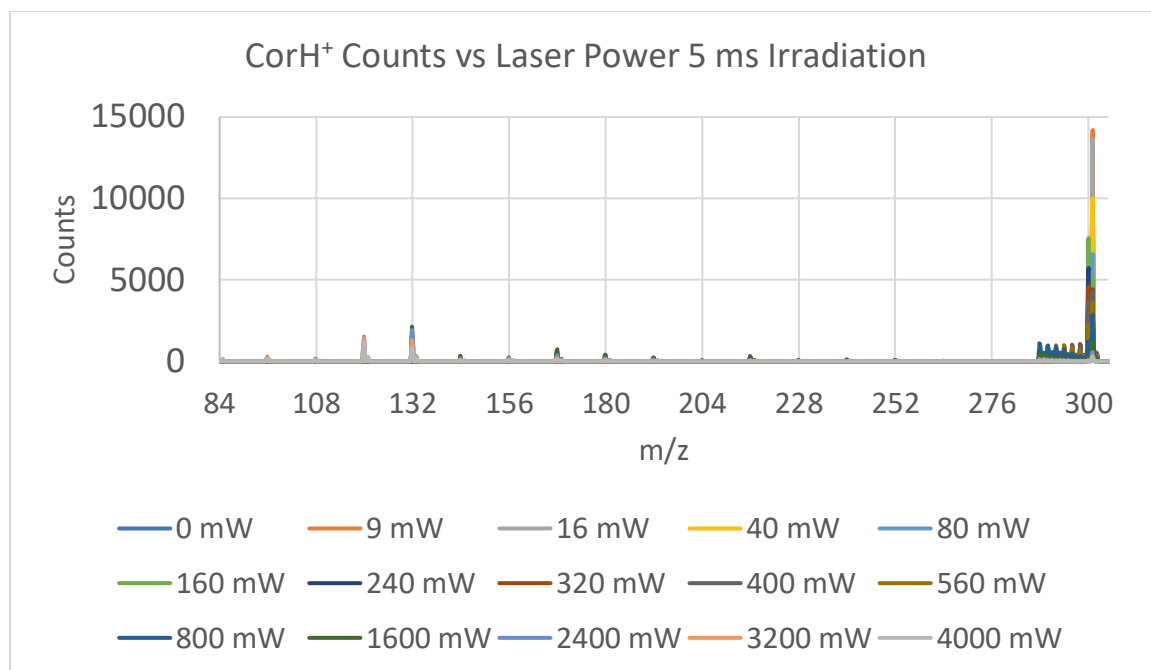


Figure 1.87: CorH^+ mass spectrum vs laser power

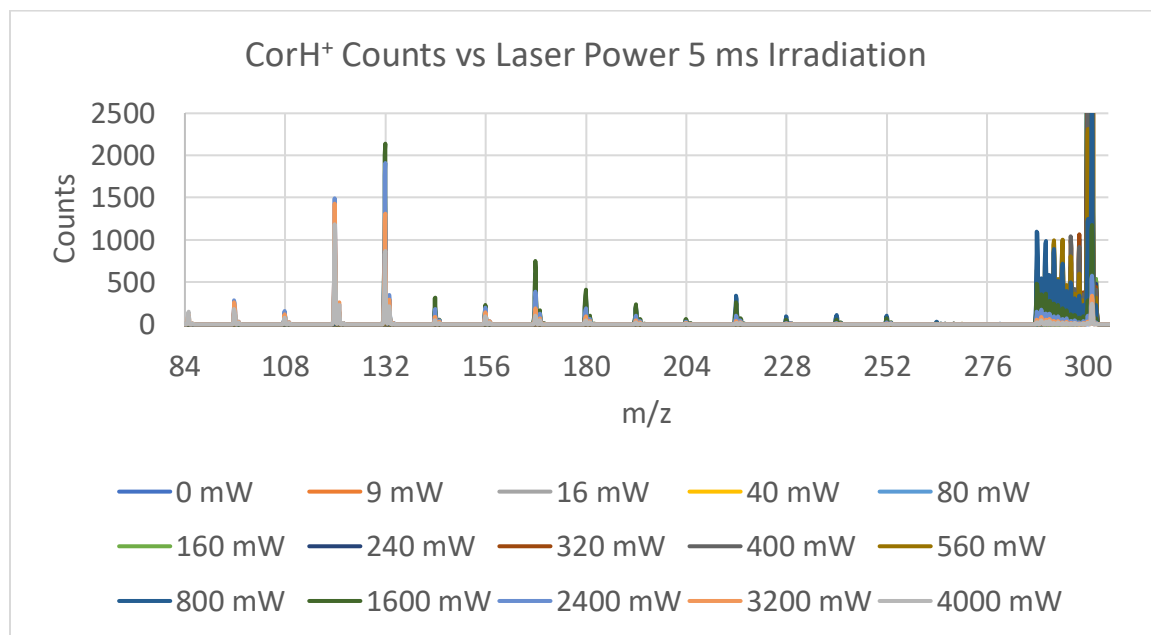


Figure 1.88: CorH^+ mass spectrum vs laser power zoomed in

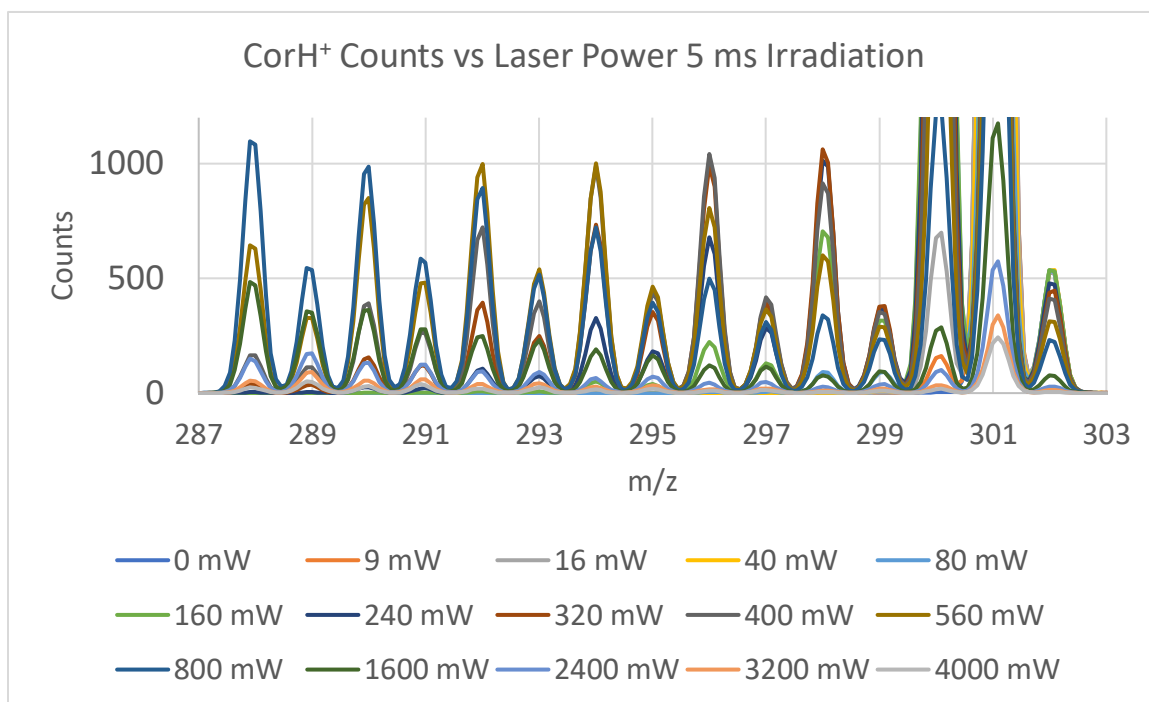


Figure 1.89: CorH⁺ H-loss region mass spectrum vs laser power

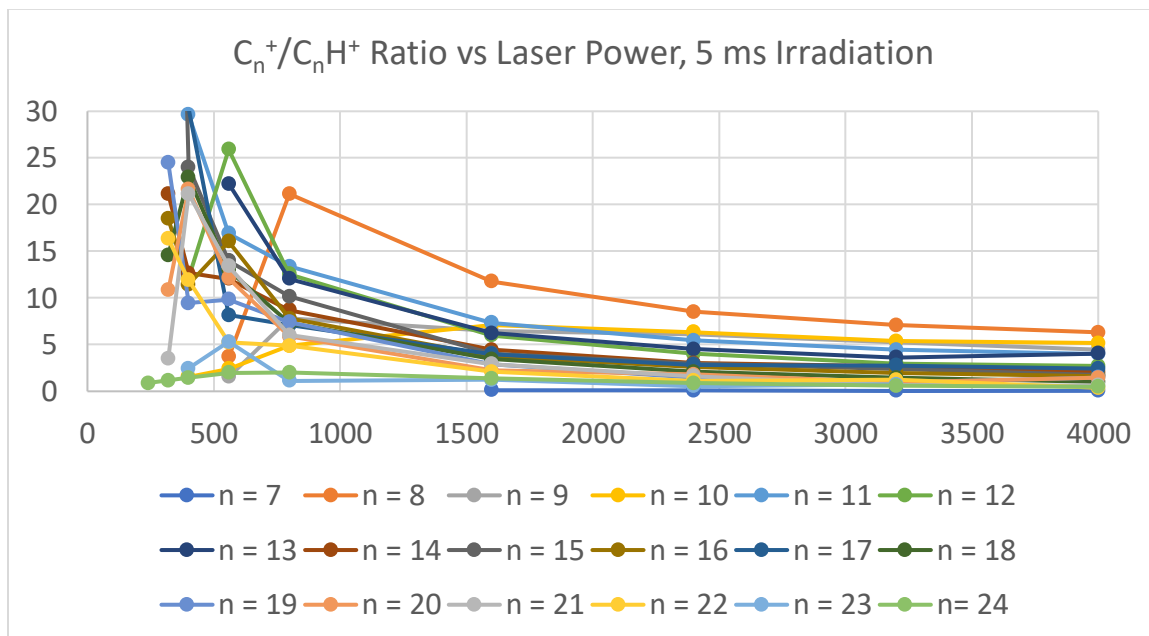


Figure 1.90: CorH⁺ mass spectrum 5 ms irradiation C-loss region $C_n^+ / C_n H^+$ ratio vs laser power

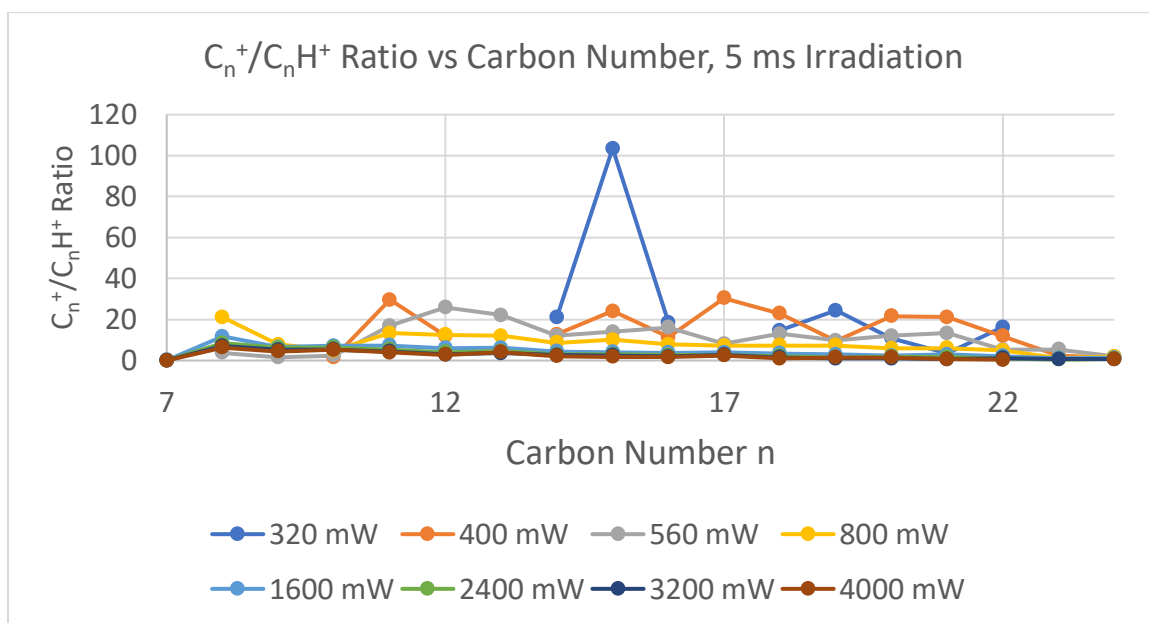


Figure 1.91: CorH⁺ mass spectrum 5 ms irradiation C-loss region $C_n^+ / C_n H^+$ ratio vs carbon number n

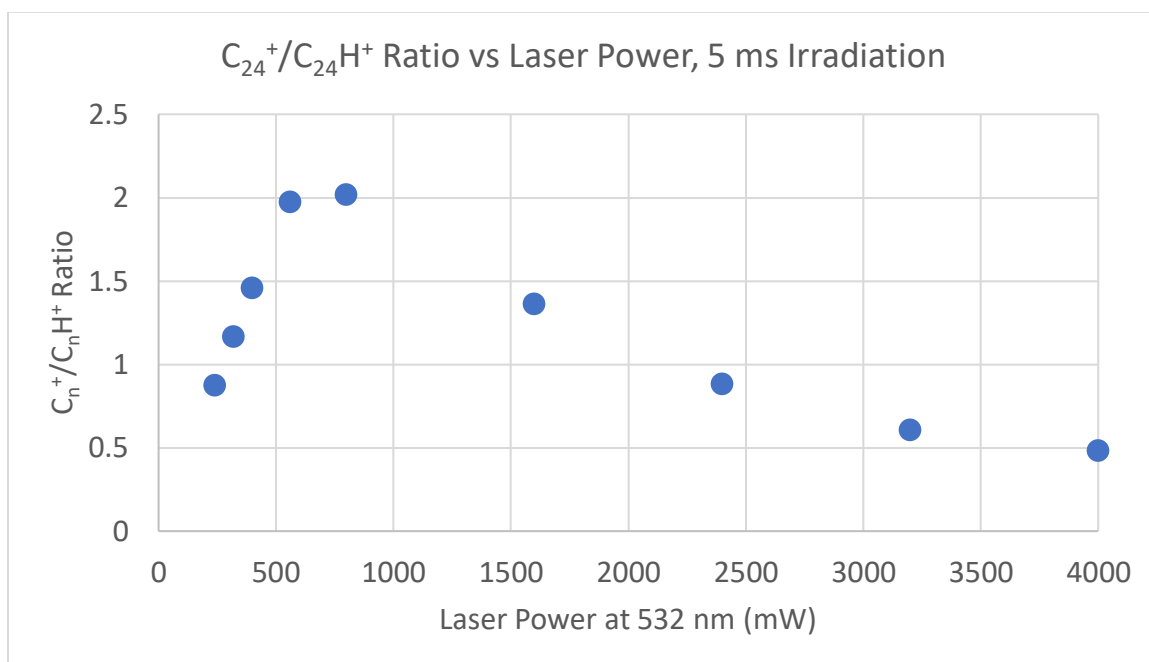


Figure 1.92 Figure 1.93: CorH⁺ 5 ms irradiation $C_{24}^+ / C_{24}H^+$ ratio

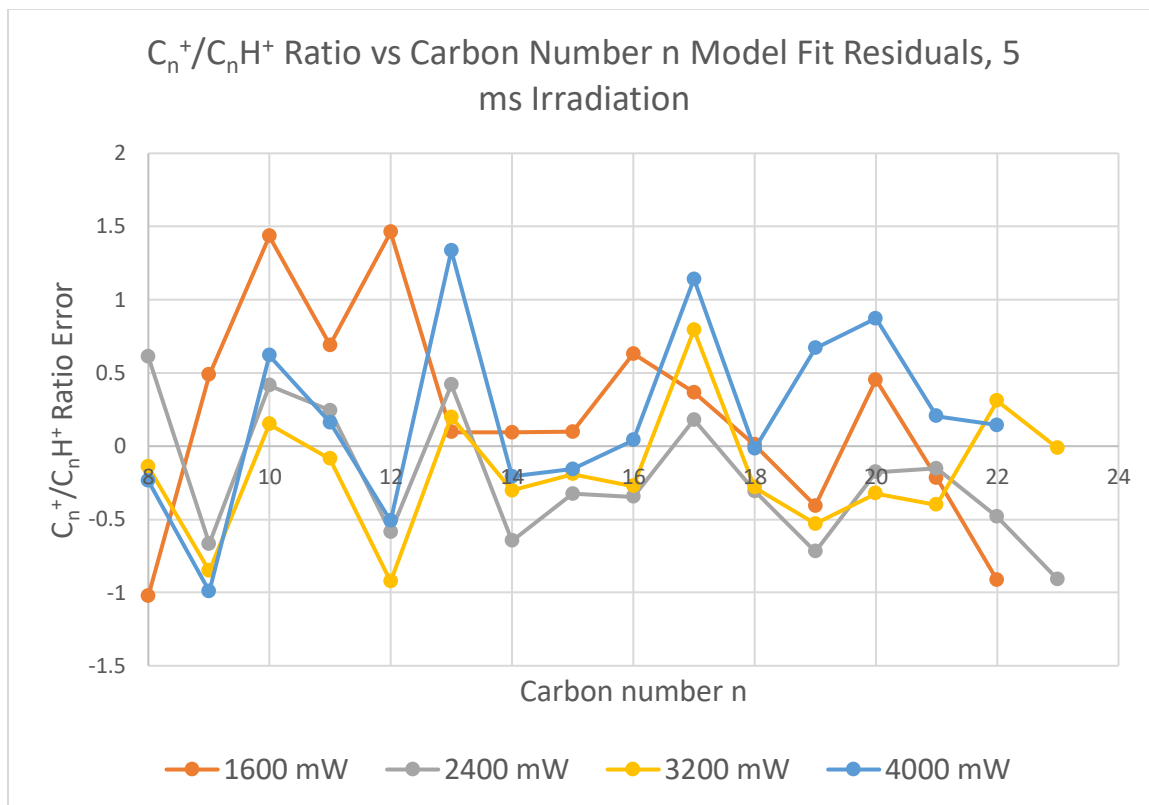
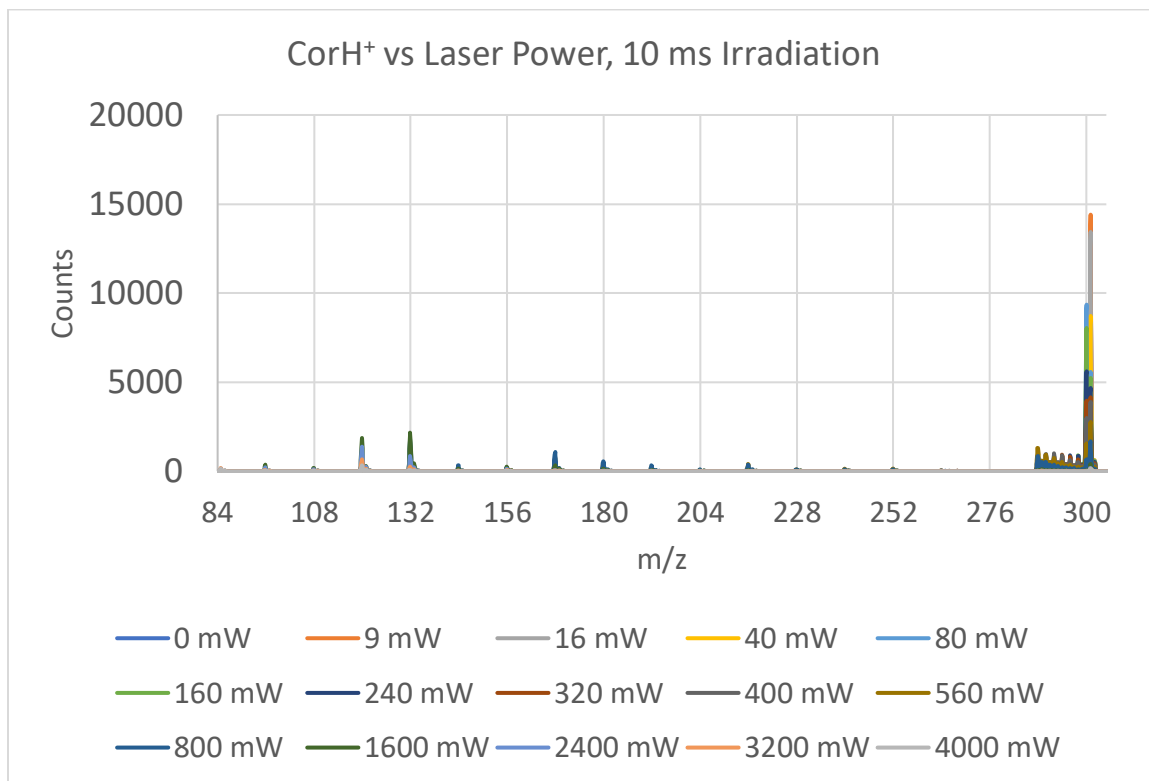
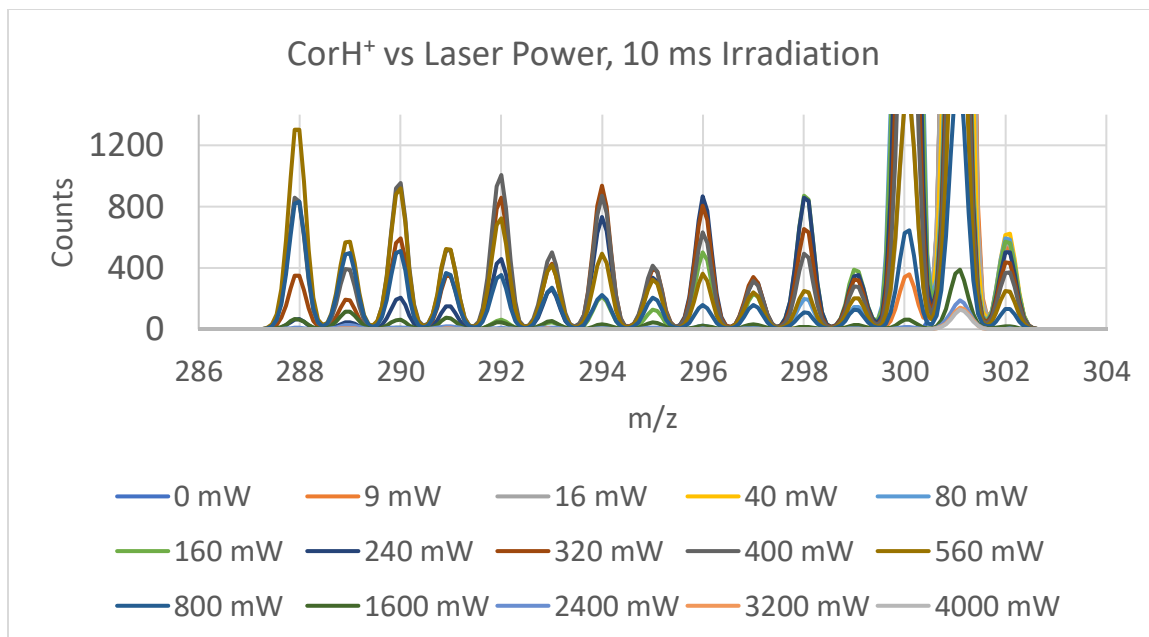


Figure 1.94: CorH⁺ mass spectrum 5 ms irradiation C-loss region C_n^+ / C_nH^+ ratio fit residuals vs carbon number n

10 ms plots CorH⁺Figure 1.95: CorH⁺ mass spectrum 10 ms irradiation vs laser powerFigure 1.96: CorH⁺ mass spectrum H-loss region 10 ms irradiation vs laser power

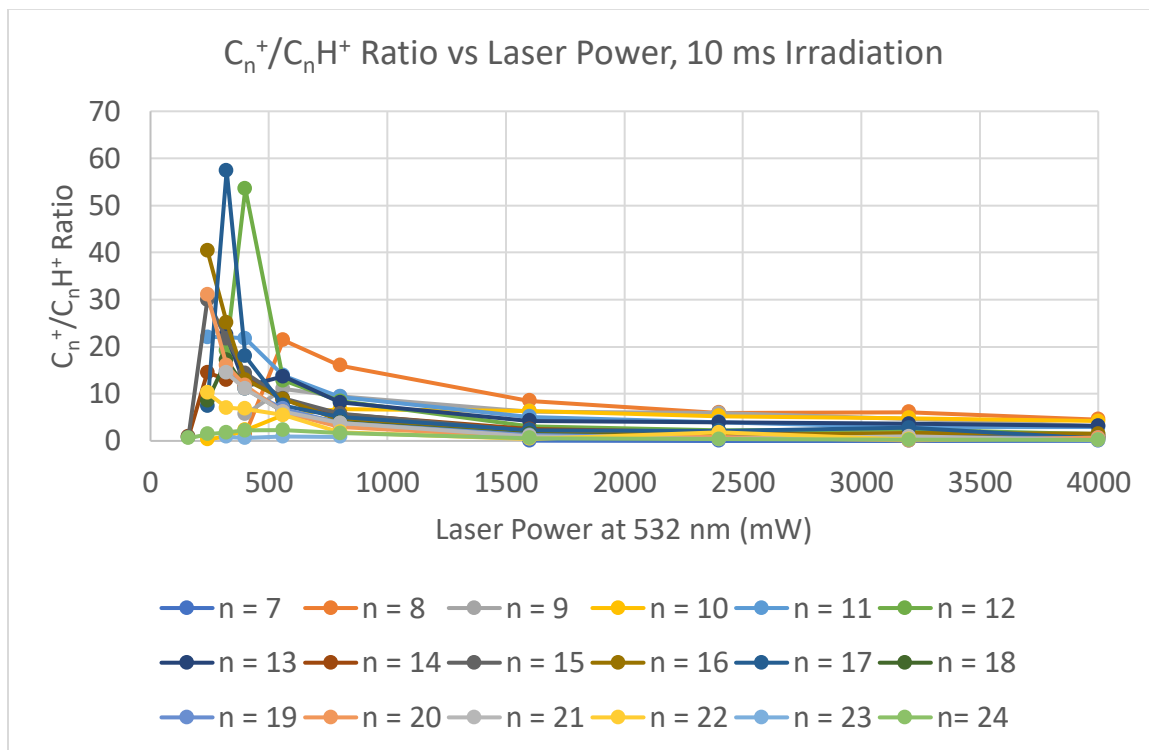


Figure 1.97: CorH⁺ mass spectrum 10 ms irradiation C-loss region C_n^+ / C_nH^+ vs carbon number n

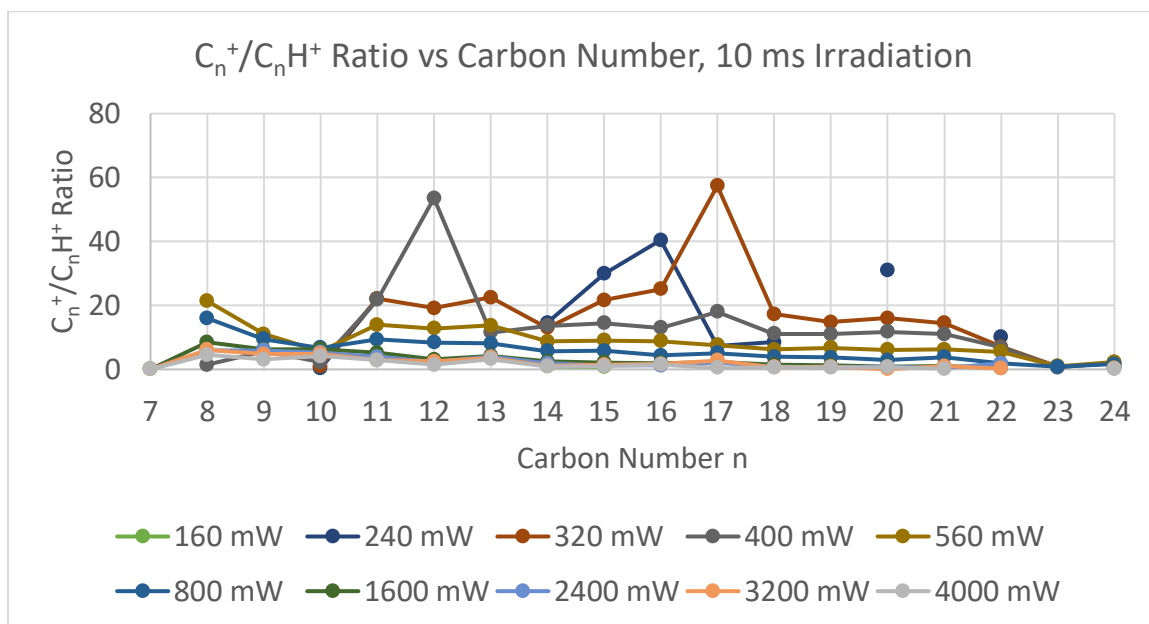


Figure 1.98: CorH⁺ mass spectrum 10 ms irradiation C-loss region C_n^+ / C_nH^+ ratio vs carbon number n

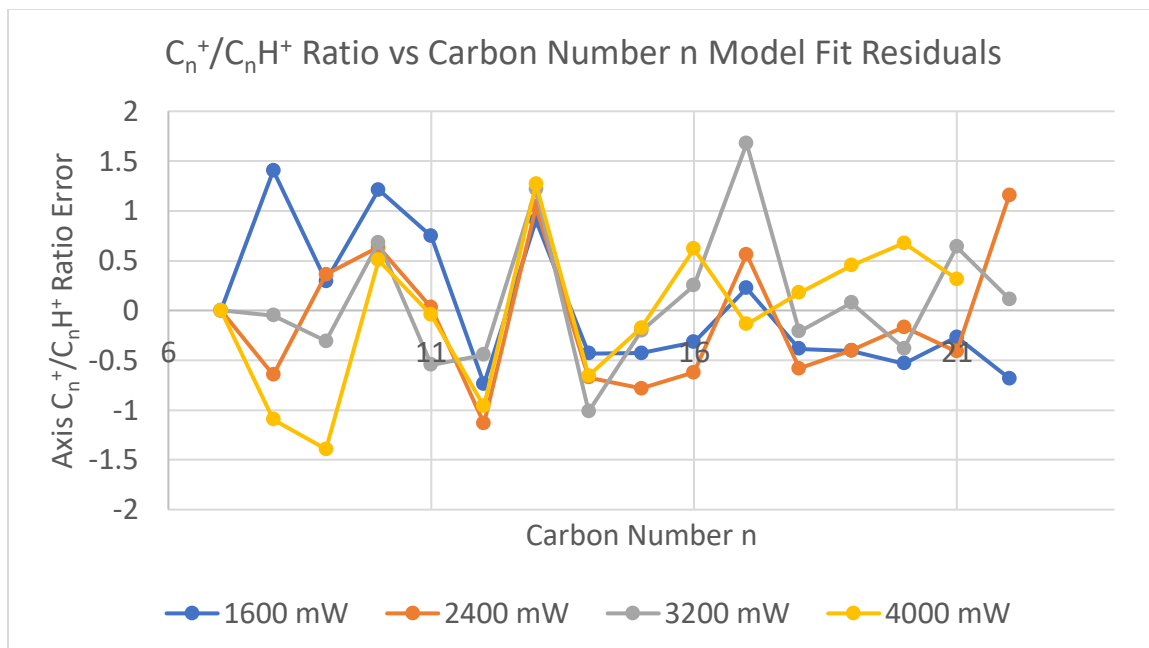


Figure 1.99: CorH⁺ mass spectrum 10 ms irradiation C-loss region C_n^+ / C_nH^+ ratio fit residuals vs carbon number n

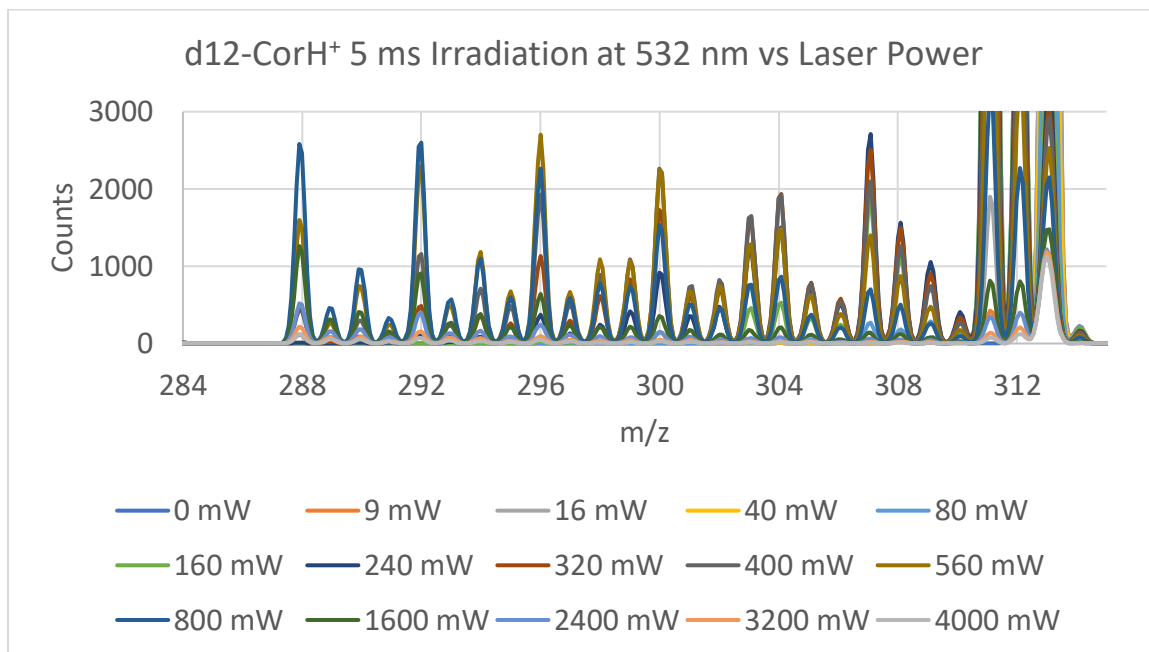
$d_{12}\text{-CorH}^+$ Fragmentation

Figure 1.100: $d_{12}\text{-CorH}^+$ H-loss region mass spectrum 5 ms irradiation vs laser power zoomed in

Feasibility of DART-MS for Remote Detection of Biomolecules

Abstract:

Direct Analysis in Real Time (DART) mass spectra have been measured for a variety of biomolecules using metastable excited He from an arc discharge. Classes of biomolecules were studied for the efficiency of DART ionization and studied for differentiating chemical characteristics. The chemistry of the fragment ions produced via collision-induced dissociation was also discussed. Conditions similar to those on Enceladus were tested for interference with DART-MS of molecules, and the physical design of an efficient DART source is also discussed.

Introduction:

In the search for past or present signs of life in the nearby solar system, mass spectrometers are widely included instruments aboard space flight vehicles. These instruments offer the universal zero-background detection, mechanical reliability, and high sensitivity necessary for the trace levels of biomolecules expected. The biological molecules of greatest interest in the search for extraterrestrial life are building blocks of cells, including lipids for membranes, amino acids for proteins, and nucleotides for encoding genetic information.

While simple ion injection systems without ionization sources can work for satellites, surface probes need an ionization method suited for a wide variety of molecules of interest. Besides existing methods like electron impact ionization and laser ablation ambient ionization,¹ a promising technique is Direct Analysis in Real Time (DART). DART is an ambient atmosphere plasma spray-based mass spectrometry method using a metastable source of neutral electronically-excited gas to produce ions from a condensed sample.² These excited gas molecules can directly ionize a sample, or can engage in proton transfer to H₂O which ionizes a sample. The resulting ions then are analyzed through atmospheric pressure detection methods.

Experimental:

In our helium DART source, a 1.5 L/min flow of UHP He was subjected to a 2.5 kV, 0.154 mA corona discharge in a custom borosilicate tube, exciting the neutral He to the long-lived 2^3S_1 state, with a radiative lifetime of 7870 sec and an energy of 19.8 eV.³ The plasma jet then passed around two 1/8" diameter grounding tungsten electrodes and through a 2 mm diameter, 2.5 cm long tapered glass nozzle. The nozzle could be

resistively heated with a wrapped nichrome wire and the temperature measured via a thermocouple, with the temperature manually varied *via* a constant current power supply. The excited helium jet then blew over the target sample placed approximately 1 mm away from the nozzle outlet, though ideally as close to the nozzle as possible without ingesting sample for maximum ion production.

The analyte was either sprinkled and compacted on a glass microscope slide or if in solution dripped onto the slide. The microscope slide was balanced on a 20 cm copper rod either at room temperature around 20 °C, or the lower 15 cm immersed in liquid nitrogen, reaching a final temperature of –180 °C measured *via* a K-type thermocouple and an Omega 23HH thermocouple reader. This temperature caused frost to condense on the slide in a few minutes, but would not form in the pathway from the He jet to the mass spectrometer inlet.

After ionization, the aspirated ions traveled approximately 1 mm in air to the mass spectrometer inlet. The ions were carried through a 3 cm long 1 mm ID stainless steel capillary extension to the atmospheric pressure inlet (API) of a commercial Thermo-Fisher LTQ-XL linear ion trap mass spectrometer. The ions then passed through an internal 10 cm long 550 μm ID stainless steel capillary heated to 275 °C to break apart molecular clusters. After passing through several ion lenses, the ions are collected in a 5 cm linear ion trap until either 30,000 ions had accumulated or 1 sec had elapsed. For most DART samples, the 1 sec collection time was reached before the ion trap reached approximately 30,000 ions. The trapped ions were either then directly scanned or subjected to collision-induced dissociation (CID) for 30 ms at approximately 3.5 – 4 eV, where 100% CID is approximately 35 – 40 eV. The ions were scanned for intensity vs

m/z ratio with a 0.7 amu FWHM resolution, with a low-mass cutoff (LMCO) of 27% the parent m/z if trapped.

A bag was draped over the instrument set-up, the seams taped, and kept at slight positive pressure with dry nitrogen to try to exclude water vapor from condensing on the system. Below is a picture of the bag.

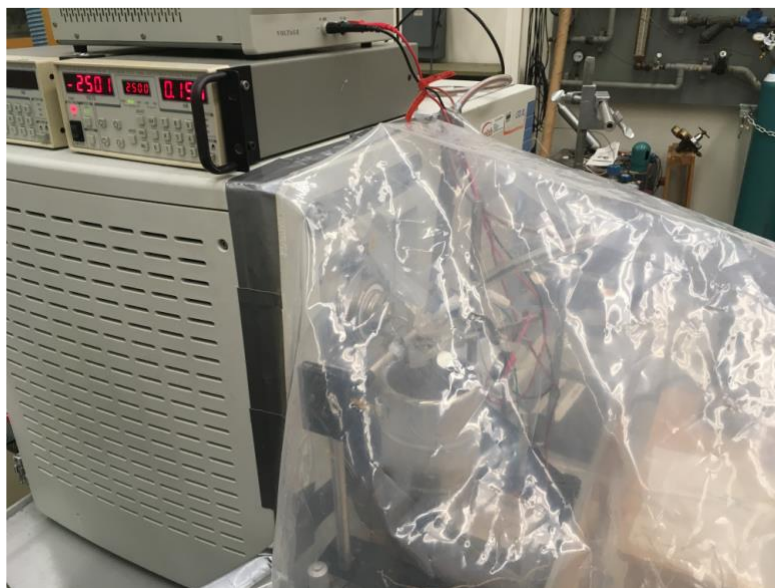


Figure 2.1: Exterior of plastic shroud covering DART inlet. Figure 2.2: DART inlet beneath shroud. Figure 2.3: Close-up of DART ionization source.

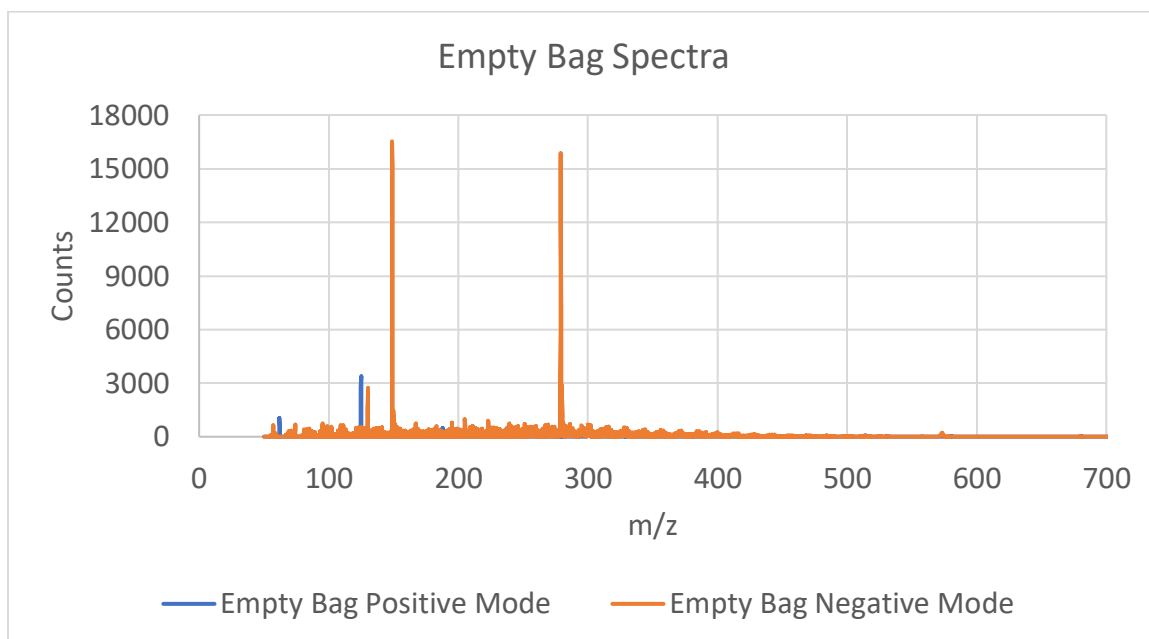


Figure 2.4: Mass spectrum without a bag covering the source apparatus, in positive and negative mode.

Further, an alternate DART Helium nozzle was tested, made from $\frac{1}{4}$ " stainless steel and electrically insulating PTFE Swagelok components.



Figure 2.5: Photograph of stainless steel DART inlet.

Analyte samples were prepared a variety of ways to test the effects of sample preparation on DART analysis. Samples of commercially pure powers were spread onto the surface of fresh glass microscope slides for neat samples and tamped flat, or were either dissolved in water or a simulated Enceladus solution consisting of 0.2 M NaCl and 70 mM NaHCO₃/Na₂CO₃ buffer at pH 11.⁴

To produce ice samples at icy-moon temperatures, two freezing methods were employed. To simulate slow freezing, the sample solution was pipetted onto the glass slide set atop the copper rod which was pre-cooled to -180°C . To simulate flash freezing, the sample solution was dripped from a glass serological pipette into a liquid nitrogen bath, and once the drops fully froze and sank in the liquid nitrogen, the drops were removed and ground with a liquid nitrogen-cooled mortar and pestle. The crushed ice was then sprinkled and tamped down on a liquid nitrogen cooled glass slide, and the slide quickly transferred to the pre-cooled copper rod.

Results:

Several observations were made that improved the sensitivity of the DART apparatus. A 1.5 cm³/min He flow was found to be an optimal balance between He* production and allowing for desorbed ions to be ingested into the mass spectrometer capillary, which was the same flow previously detailed for the glass DART tip.² The stainless steel DART nozzle, while more rugged against breaking from mechanical stress on the electrodes, produced a much weaker intensity signal, likely because of the larger diameter tip, producing a lower ion density in the vicinity of the mass spectrometer inlet tip. A non-transparent DART nozzle also made viewing the quality of the corona

discharge impossible, which is important because a He discharge glows bright pink, but trace quantities of water or O₂ make the discharge glow blue-grey.

The collected signal was very sensitive to the precise orientation of the sample to both the He nozzle jet and the skimmer. The best angle was found to be about 45° above the plane of the sample slide, but with the nozzle and skimmer out of alignment horizontally be ~1 mm. This suggests the lifetime of the ionization source is shorter than the product ions, and the upper velocity limit for the mass spectrometer atmospheric inlet is lower than the velocity of the ionization gas needs to reach the sample.

A heated DART He source improves signal for both room temperature and low temperature samples. The tip was heated to 100 °C, near the current limit of the power supply, though in principle the temperature is arbitrary. Why the heated DART source improves signal speaks to the mechanism of DART ionization. Target molecules are ionized on a surface, either with He* or through atmospheric pressure chemical ionization often with H₃O⁺, which then must enter the gas phase to be analyzed.^{5,6} Thus the signal is vapor-pressure dependent,⁵ the value of which rises exponentially with temperature; however even with a room temperature He jet appreciable DART signal could be detected from cryogenic samples. The samples do not undergo thermal desorption ionization, because when the discharge is off no product signal could be observed.

The ion optic voltages which had the greatest impact on signal were those close to the end of the internal LTQ heated capillary. The ion signal was not sensitive to inlet capillary voltage at 1 atm, likely because the ions are carried by aerodynamic flow into the mass spectrometer capillary, and at 1 atm air is too viscous for the ions to exit with

the allowed tip voltages of 0 – 10 V. The influx for this capillary in a He atmosphere would be 2.2 L/min,^{7,8} thus a sizable fraction of the He and ions emitted should be ingested into the spectrometer. In the low vacuum region the gate lens and simmer voltages had the largest impact on ion collection efficiency, and were optimized for the parent mass of each ion when collecting spectra.

There was no qualitative difference between the two methods of ice production, either by pipetting analyte solution into a puddle which froze slowly on a glass slide, or by flash freezing the solution and grinding the ice. The slow freezing sample looked like a white sheet, which froze from the center outwards, and slowly gathered frost near the center closest to where the slide contacted the copper rod. The flash freezing method resulted in solution drops first floating, but once fully frozen would sink. Water drops would feel crystalline when grinding, but the drops ground finely to less than ~0.5 mm without difficulty. The relative intensities between analyte peaks were similar with both preparation methods, and overall ion counts were similar. This likely is because during slow freezing, solutes are excluded from the ice matrix and are concentrated on the surface, where the DART probe can reach, while in flash freezing, the solute is dispersed throughout the ice, but grinding exposes internal surfaces. For a flash freezing sample, signal may scale with exposed surface area.

The difference between neat samples vs in water or simulated Enceladus ocean solution the relative intensities of the peaks, but all peaks seen in neat samples were observed in both types of solution. For volatile molecules, sodium adducts were not readily observed, potentially from the vapor pressure decrease, however, $M+H_3O^+$ and $2M+H^+$ peaks were seen.

Ibuprofen:

The first molecule analyzed for its mass fragments with DART was ibuprofen ($\text{C}_{13}\text{H}_{18}\text{O}_2$, monoisotopic mass = 206.13 amu), which has the following structure.

Ibuprofen was found to ionize easily, and served as a benchmark molecule for our future DART tests.^{2,9}

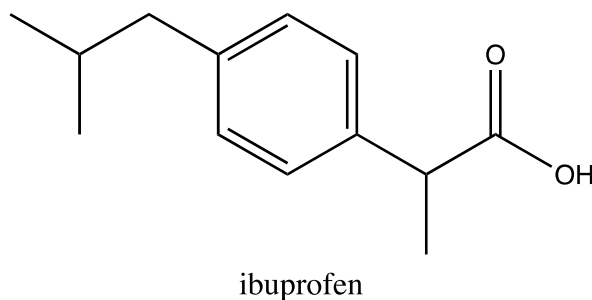


Figure 2.6: Structure of ibuprofen

Shown is a mass spectrum of neat ibuprofen in positive mode.

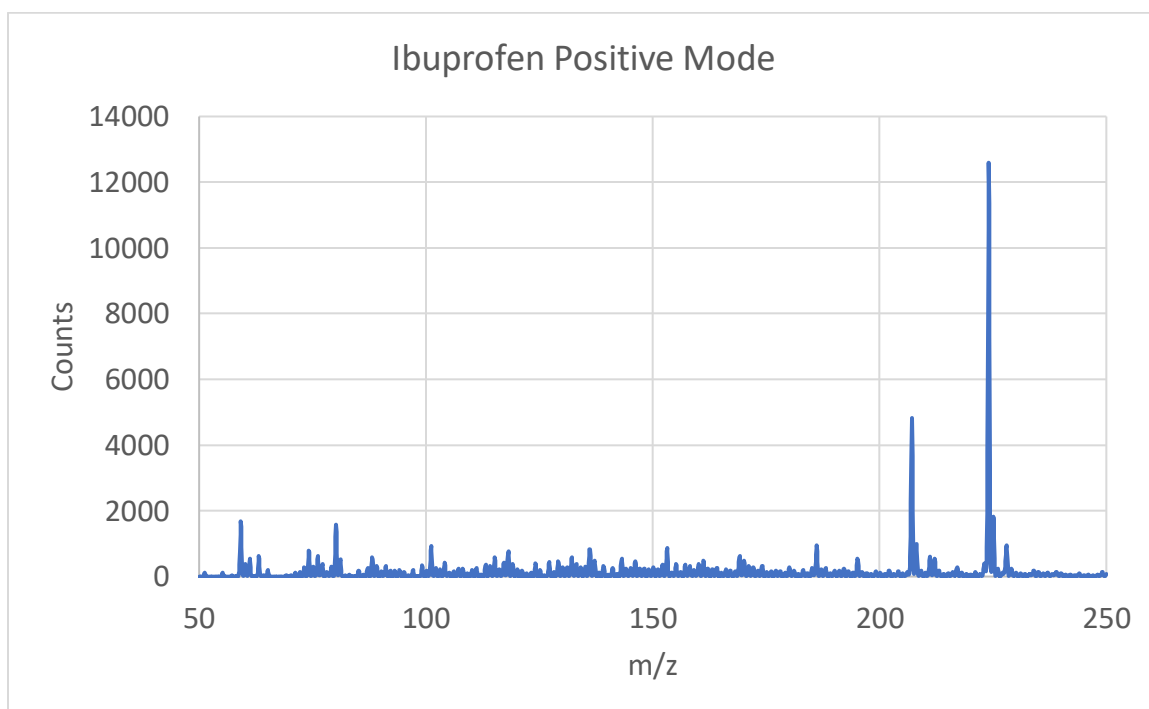


Figure 2.7: Neat Ibuprofen at 20 °C in positive mode.

The major peaks are listed below:

Table 2.1: Neat ibuprofen peaks at room temperature

m/z	Intensity (counts)	Identity
207.1	4755	(M+H) ⁺
208.2	778	(¹³ C-M+H) ⁺
224.1	12593	M+NH ₄ ⁺
225.1	1725	¹³ C-M+NH ₄ ⁺

For a compound where the m/z = 207.1 peak is 85.9% of the summed ion counts between m/z = 207.1 and m/z = 208.8, the abundance is consistent with the formula for M matching the formula for ibuprofen C₁₃H₁₈O₂. From the chemical formula of ibuprofen and average isotopic abundances of the 3 substituent elements, the predicted abundance of the m/z = 207.1 peak is 86.0%, confirming the identity of the m/z = 207.1 peak as ibuprofen.

Adding the bag covering the DART set-up allowed for some contaminants and water to be excluded. However, many smaller peaks are from the plastic shroud.

The major peaks of the positive and negative mode spectra are listed below:

Table 2.2: Neat ibuprofen peaks at room temperature under shroud.

m/z (mode)	Intensity (counts)	Identity
207.1 +	290	(M+H) ⁺
224.1 +	1030	M+NH ₄ ⁺
205.1 -	300	(M-H) ⁻
228.1 -	950	M ²⁻ + Na ⁺ ?

When mass selecting positive mode m/z = 207 and subjecting to 9% CID for 30 ms trapping, a peak at 161.2 appears. This fragment is ibuprofen (M – CO₂H)⁺ having lost a protonated carboxyl group (m/z = 44), which is a common leaving group.

At 12% CID with 30 ms trapping, the negative (M – H)⁻ fragment at m/z = 205 displayed creation of m/z = 161, 177, and 190 fragments in low abundance. The m/z = 161

fragment is 10, corresponding to loss of the CO₂ carboxyl group, the $m/z = 177$ fragment is loss of CO, and the $m/z = 15$ fragment is loss of one of the three CH₃ methyl groups, likely β to the carboxyl group for resonance stabilization from the aryl ring or the carboxyl group.

The following spectra were taken for ibuprofen at $-180\text{ }^{\circ}\text{C}$.

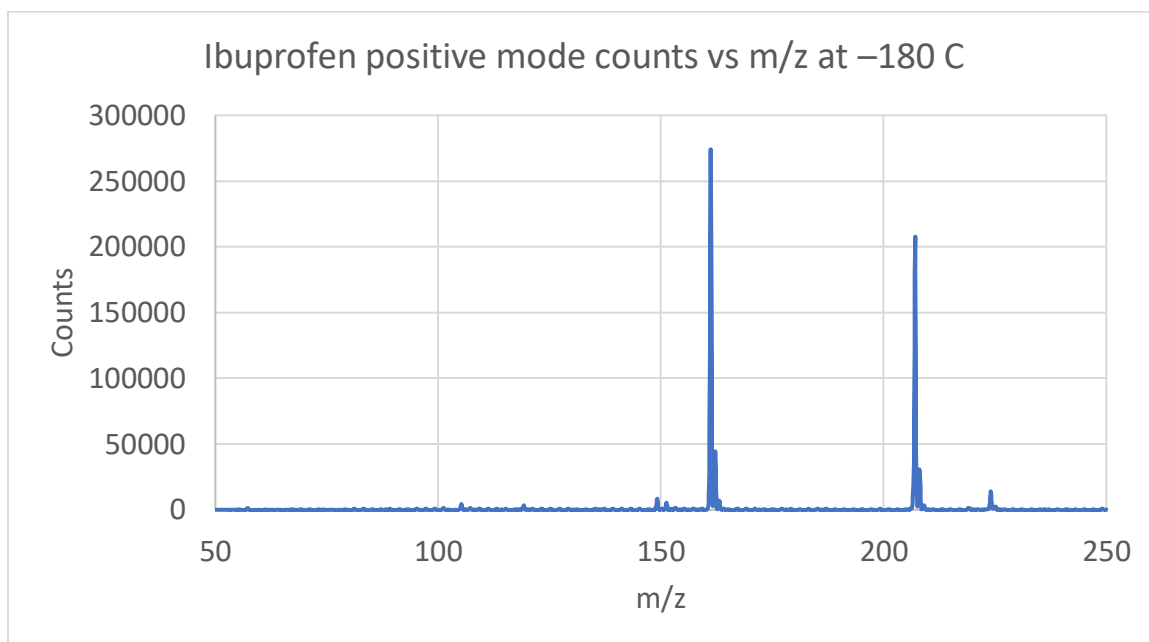


Figure 2.8: Neat ibuprofen mass spectrum at $-180\text{ }^{\circ}\text{C}$ positive mode.

A table of the primary identified masses is presented below.

Table 2.3: Table of neat ibuprofen mass spectrum peaks at $-180\text{ }^{\circ}\text{C}$ positive mode.

m/z	Intensity (counts)	Identity
161.2	274084	$(\text{M} - \text{CO}_2\text{H}_2)^+$
162.2	43605	$(^{13}\text{C}-\text{M} - \text{CO}_2\text{H}_2)^+$
207.1	247949	$(\text{M}+\text{H})^+$
208.2	26420	$(^{13}\text{C}-\text{M}+\text{H})^+$
224.1	11740	$\text{M}+\text{NH}_4^+$
225.1	2407	$^{13}\text{C}-\text{M}+\text{NH}_4^+$

Note the counts are much larger for this sample versus room temperature, but this could be due to inlet geometry. Frost formed across the cooled slide except for where the heated

He DART gas emerged, creating an enclosed area around the DART tip and mass spectrometer inlets.

Also of note is the ratio of $(M+H)^+$ $m/z = 207$ to $M+NH_4^+$ $m/z = 224$ increases significantly at $-180\text{ }^\circ\text{C}$ compared to room temperature, going from 0.38 to 21.1, an increase of 56X. Because volatility is important for successful ionization with DART, this change in the ratio could be because the ammonium complex is less volatile but more abundant in the ibuprofen sample.

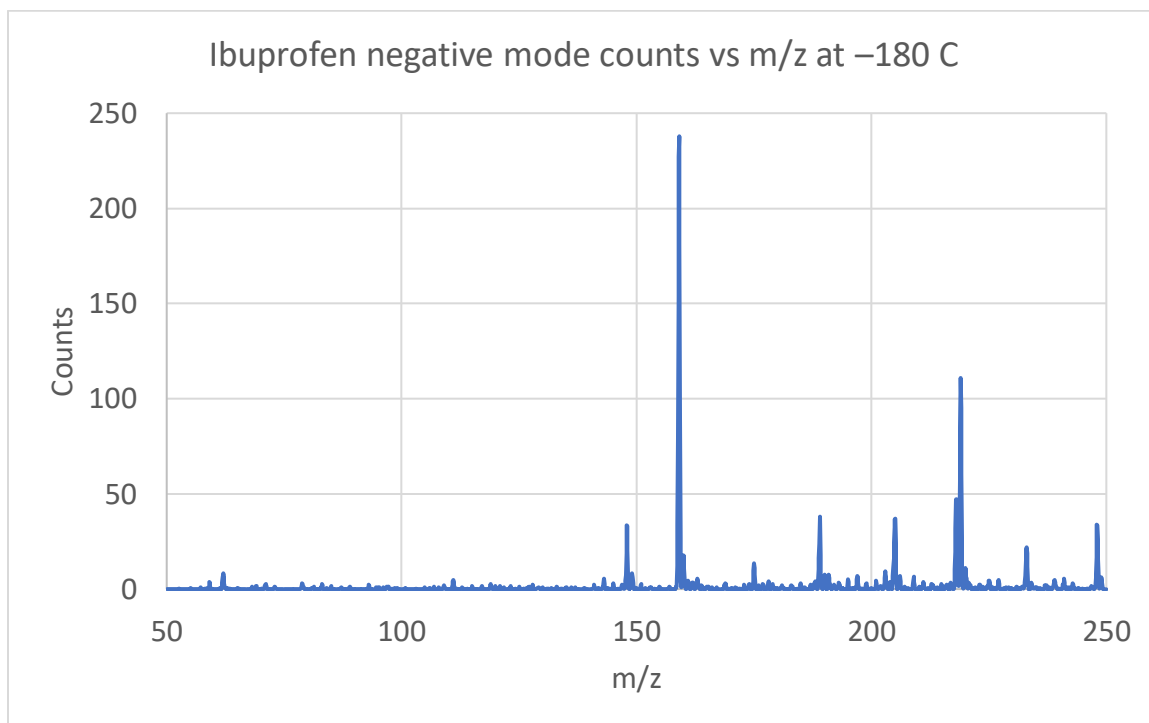


Figure 2.9: Neat ibuprofen mass spectrum at $-180\text{ }^\circ\text{C}$ negative mode.

The negative mode spectrum displays a different mass spectrum at $-180\text{ }^\circ\text{C}$ as at $20\text{ }^\circ\text{C}$, with the peaks listed below.

Table 2.4: Table of neat ibuprofen mass spectrum peaks at $-180\text{ }^\circ\text{C}$ negative mode.

m/z	Intensity (counts)	Identity
147.9	33	$(M-CH(CH_3)^+)^-$
159.1	237	$(M-CO_2H_3^+)^-$
189	38	$(M-OH)^-$

205.2	32	(M-H) ⁻
218.0	27	Contaminant?
219.0	111	Contaminant?
133.2	19	Contaminant?
248.2	26	(M+CO ₂) ⁻

This -180 °C negative mode spectrum looks significantly different than the room temperature spectrum, indicating new decomposition pathways may be taking place with low-temperature samples.

Despite both the positive and negative spectra changing between 20 °C and -180 °C, ibuprofen was detected via DART, establishing that low temperatures are not an impediment to use. Further, while the relative counts between peaks in a mass spectrum are dependent on temperature, the overall counts are highly dependent on inlet geometry, thus comparing between samples will require reproducible geometry in the sampling system.

Glycine

Glycine is a nonpolar amino acid and the prototypical amino acid having only $-H$ as the amino acid R-group. Glycine has been detected on comets¹⁰ and a non-energetic formation mechanism has been described for glycine's formation in the interstellar medium.¹¹ Therefore, glycine is a good target molecule for testing DART's icy moon biomolecule detection capabilities. The chemical formula is $C_2H_5NO_2$ (monoisotopic $M = 75.1$), with the following structure, though at neutral pH values glycine is a zwitterion.

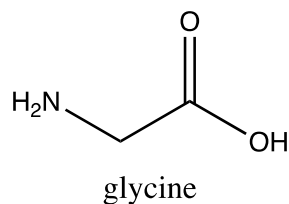


Figure 2.10: Structure of glycine.

The ion intensities are low for all detectable fragments, and no fragments correspond to expected peaks at $m/z = 75.1$ (M^+), 76.1 ($M+H^+$), or 94.1 ($M+H_3O^+$). Dissolving glycine into water at the high concentration of 1 M in the simulated Enceladus solution worked no better.

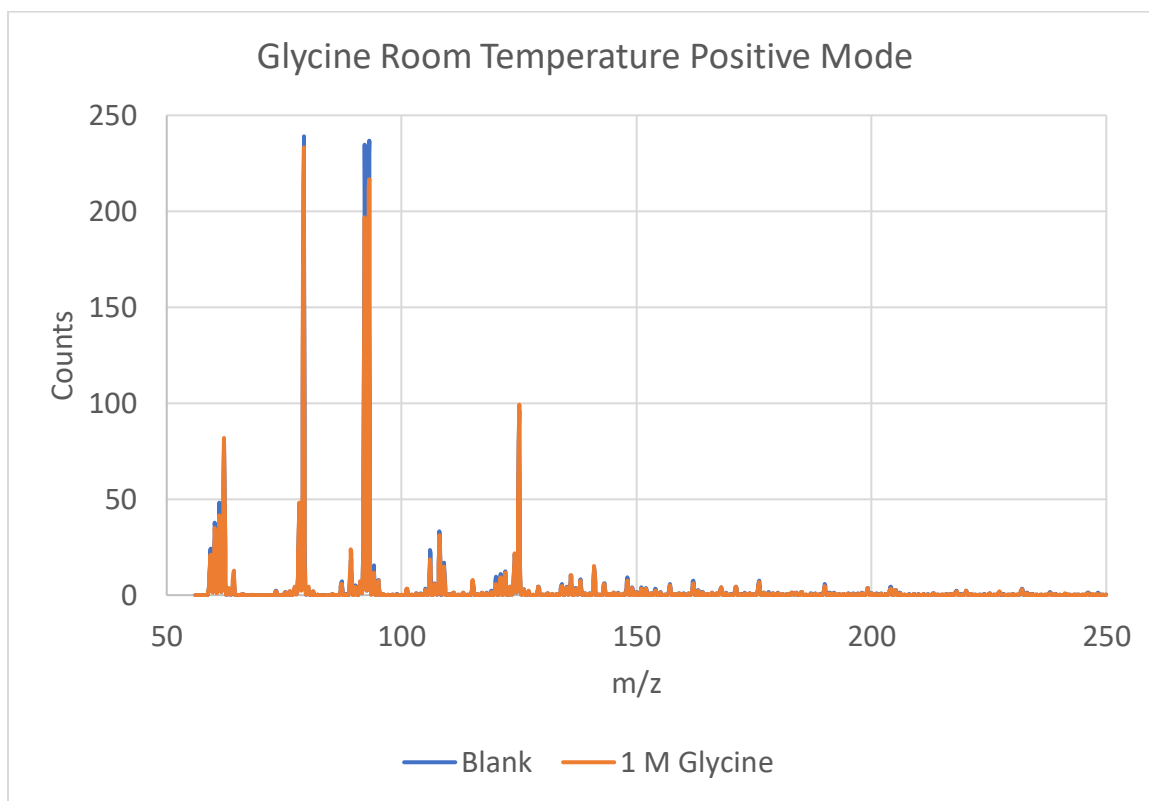


Figure 2.11: 1 M glycine in the simulated Enceladus solution (orange) vs a blank (blue) in positive mode at room temperature.

As can be seen, no 1 M glycine peaks were significantly above the ion count for the blank at any m/z value.

The conclusion is DART is not the right technique to detect glycine.

Arginine

Arginine is a basic amino acid and a good potential candidate for DART, since the amino acid will ionize easily. The chemical formula is $C_6H_{14}N_4O_2$ (monoisotopic $M = 174.2$), with the following structure, though at neutral pH values arginine is a zwitterion.

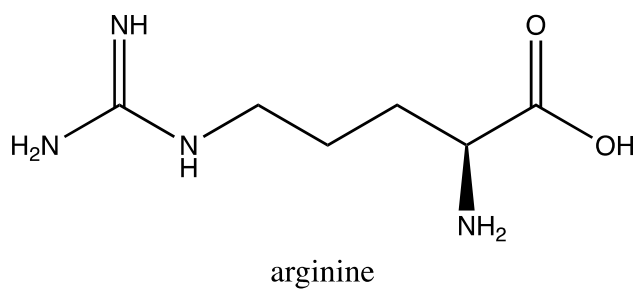


Figure 2.12. Structure of arginine.

While the mass spectrum is noisy due to contamination with fatty acids, no peak at probable masses greater than the baseline ($M + H^+$, $M + H_2O$, $M + H_3O^+$) was seen.

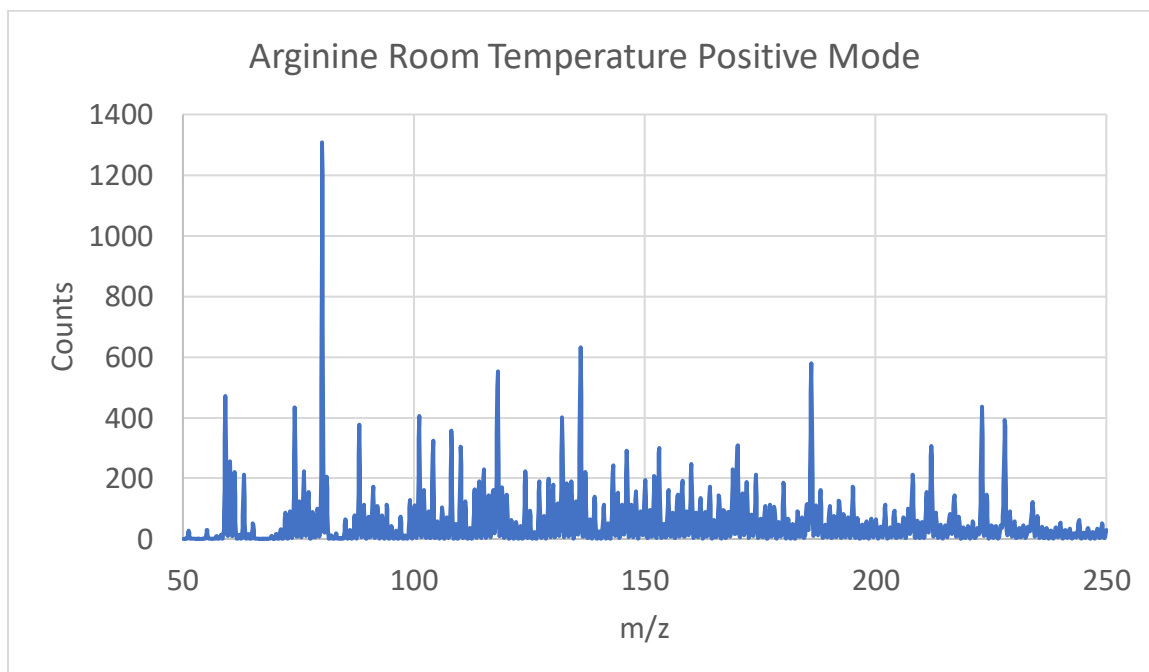


Figure 2.13. Neat arginine at room temperature, positive mode. Despite contamination, no peak above the background was seen near $m/z = 174.2$ which CID could identify as arginine.

The mass spectrum of arginine, despite contamination with fatty acids, has no indication of a peak near $m/z = 174.2$ (M^+), 175.3 ($M + H^+$), or 193.2 ($M + H_3O^+$). The peak at $m/z = 186.2$ is a contaminant, since the CID spectrum does not yield fragments consistent with arginine's structure, nor would an $M + 12$ peak be expected.

Arginine thus is not a good candidate for DART ionization, because despite ease of ionization, arginine's volatility must be low due to its zwitterionic character, likely increasing the energy needed to create a gas-phase sample.

Phenylalanine methyl ester

To try and detect amino acid derivatives, phenylalanine methyl ester was tried. This amino acid methyl ester was chosen because the acidic proton was replaced by a methyl group, preventing the compound from becoming a zwitterion. Phenylalanine methyl ester has the formula $C_{10}H_{13}NO_2$, and (monoisotopic $M = 179.1$) the structure is shown below, though at neutral pH values the methyl ester should be a cation with the amine protonated.

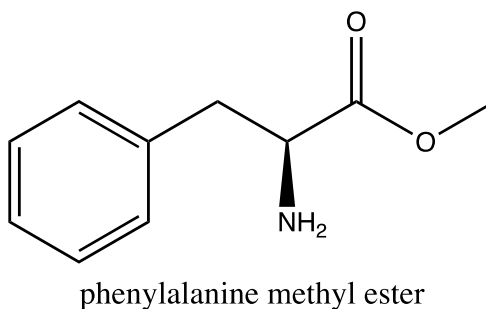


Figure 2.14: Phenylalanine methyl ester structure.

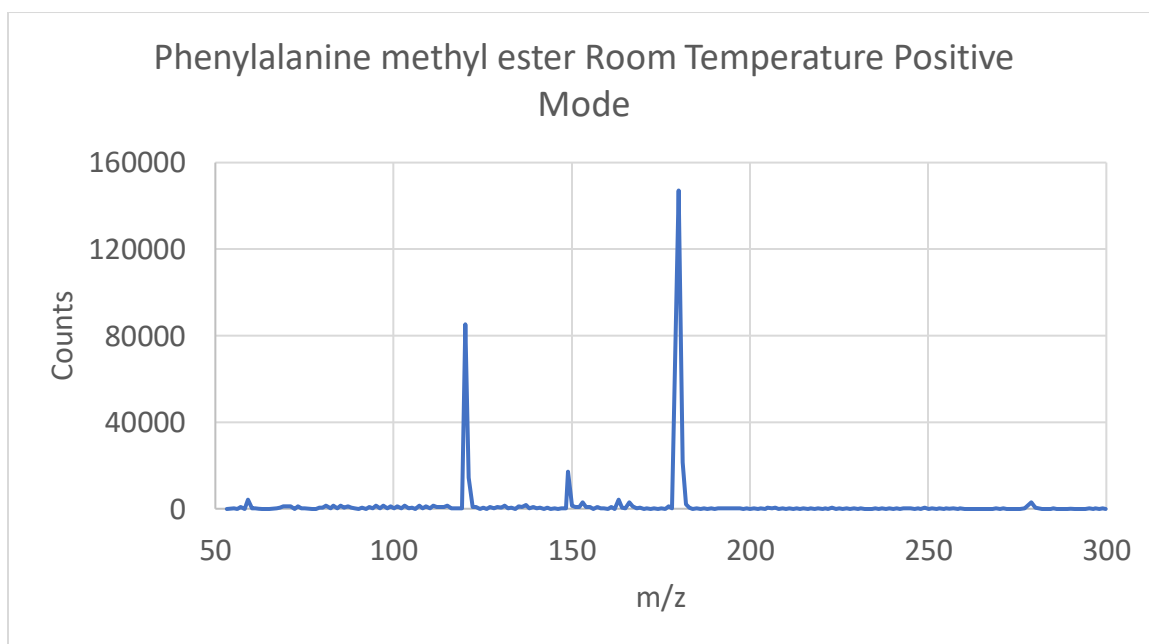
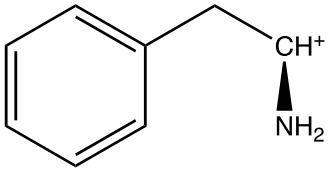
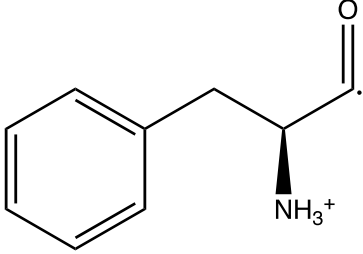


Figure 2.15: Phenylalanine methyl ester room temperature positive mode mass spectrum.

The following table of fragments are seen.

Table 2.5: Phenylalanine methyl ester room temperature positive mode mass peaks.

m/z	Abundance	Identity
120.1	85150	 fragment
149.0	17282	 fragment
180.0	147107	$(M + H)^+$
181.0	21368	$(^{13}C-M + H)^+$

Despite being less biologically relevant, phenylalanine methyl ester shows a clear and identifiable signal, making this molecule a suitable candidate for DART. Regular phenylalanine did not show an identifiable DART mass spectrum, but the substitution of the acid hydrogen for the methyl group and change in ionic character of the molecule was the only change necessary for detection in positive mode with good ion signal.

Bradykinin

Bradykinin is a short 9-amino acid polypeptide which is a mass spectrometry benchmark, which was sampled to gauge DART's ability to detect protein-like molecules in the search for life throughout the solar system. The molecule's structure is $C_{50}H_{73}N_{15}O_{11}$ (monoisotopic molecular $M = 1059.6$), with an amino acid sequence (starting at N-terminus) RPPGFSPFR, or arg – pro – pro – gly – phe – ser – pro – phe – arg. The sequence consists of 2 basic amino acids, 1 hydrophilic uncharged amino acid, 2 hydrophobic aromatic amino acids, and 4 other hydrophobic amino acids. The structure is shown below.

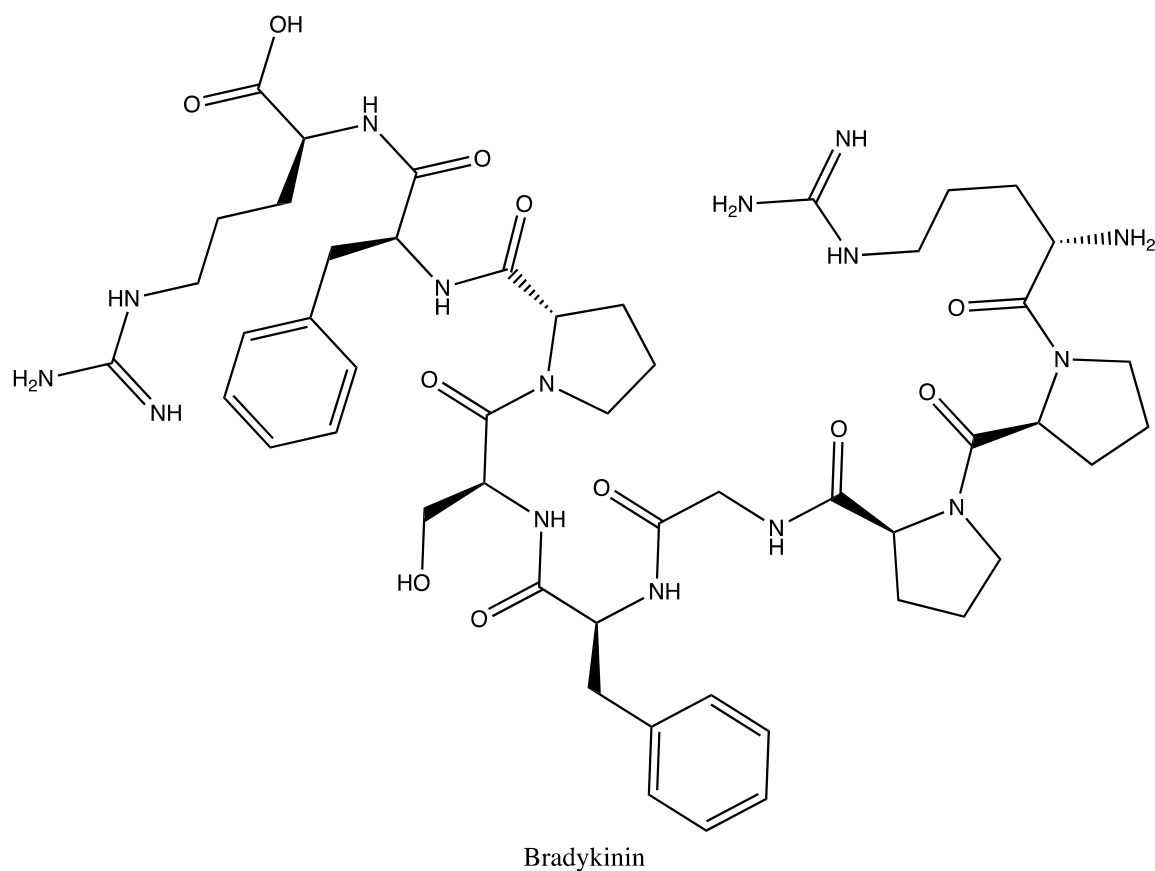


Figure 2.16: Bradykinin structure

Because of the polar and zwitterionic character of bradykinin, the amino acid showed no peaks in its mass spectrum which could be positively assigned to bradykinin. The collection of peaks seen did not correspond to a list of expected peaks. A table of fragments which could correspond to the peaks seen in the experimental DART spectrum is shown below.

Table 2.6: Bradykinin CID fragment ions at CID = 10.

m/z	Abundance	Type	Identity
180.6	95560	Y	$((\text{arg-pro}) + \text{H}_3\text{O})^{2+}$
204.6	20312	B	$((\text{arg-pro-pro-gly}) + \text{H})^{2+}$
279.2	131727	B	$((\text{arg-pro-pro-gly-phe}) + \text{H})^{2+}$
572.3	16679	C	$(\text{arg-pro-pro-gly-phe})^+$

There is no logical reason for these fragments to be more abundant than other predicted fragments, such as the not-observed y-type ion at $m/z = 886.5$, which would be expected to be abundant with the aryl group stabilizing the $m/z = 886.5$ fragment. Further, no parent fragment is seen anywhere near $m/z = 1059.6$ either, making identification of the sample impossible. Several of the peaks seen in the neat bradykinin sample are seen in a blank sample of a plain glass slide, indicating either contamination of the mass spectrometer inlet, or background peaks from the atmosphere.

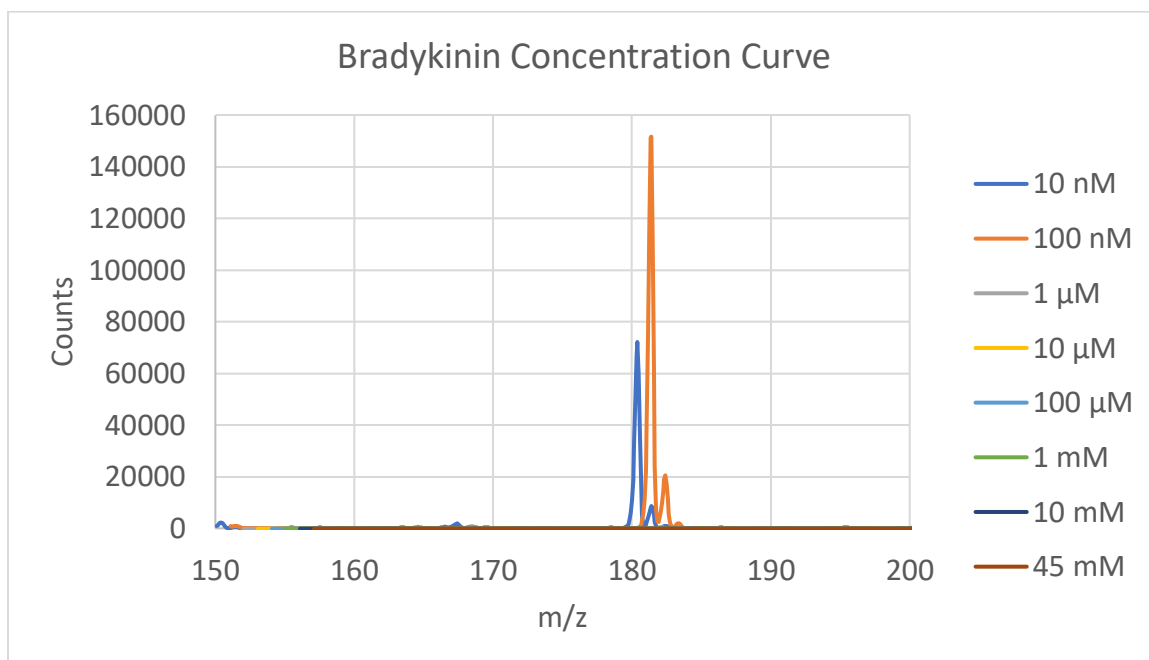


Figure 2.17: Plot of mass spectrum vs bradykinin concentration at room temperature in positive mode. The same plot at -180°C looks similar, with the same qualitative peak shapes and concentration dependence of peak intensity.

There is no correlation between sample concentration and ion signal at room temperature in positive mode. The peak at $m/z = 180$ would correspond to a y-type ion breaking at the first proline in the sequence + H_3O^+ but with a 2+ charge, which is an improbable peak to observe.

Stearic Acid

Fatty acids are key components for cellular membranes, and would likely be found in life on ocean worlds, where a hydrophobic membrane would be needed. Stearic acid was chosen as a prototypical fatty acid as the hydrocarbon chain is of intermediate length for biological amino acids, and was readily available. Stearic acid has the formula $C_{18}H_{36}O_2$ (monoisotopic $M = 284.3$), and the structure is shown below.

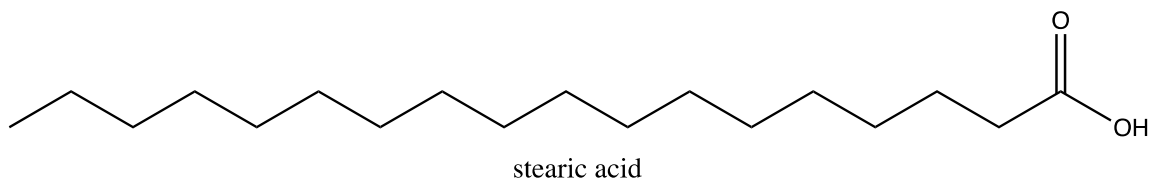


Figure 2.18: Stearic acid structure.

The spectrum of neat stearic acid at room temperature in positive mode is shown below.

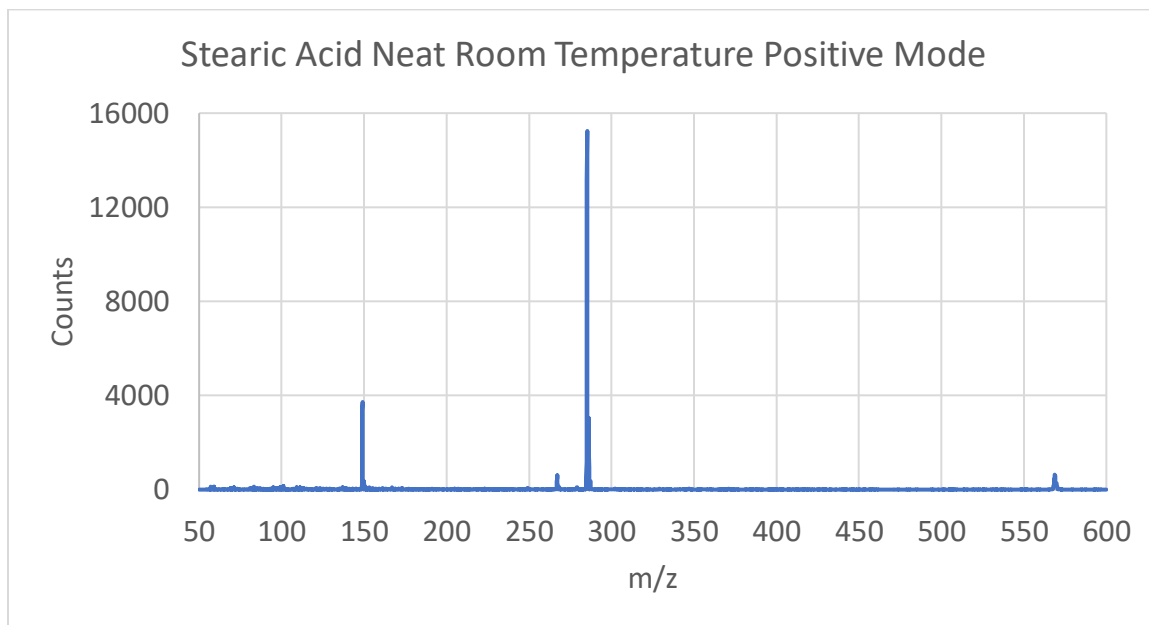


Figure 2.19: Neat stearic acid room temperature positive mode mass spectrum.

A table of the masses of the major peaks is listed below.

Table 2.7: List of stearic acid neat room temperature positive mode mass spectrum peaks.

m/z	Intensity	Identity
149.0	3724	Phthalic anhydride contaminant (in blank)
267.3	287	$(M - OH)^+$
285.2	15241	$(M + H)^+$
286.1	2717	$(^{13}C-M + H)^+$
287.3	244	$(^{13}C_2-M + H)^+$
569.0	476	$(2M + H)^+$

The peaks seen in the neat stearic acid mass spectrum in positive mode clearly identify the sample as stearic acid. When the sample was cooled to -180 C and the spectrum retaken, the sample spectrum appeared nearly identical in the mass and intensities of the peaks.

The isotopic ratios of the isotopically-substituted $(M + H)^+$ species is consistent with substitution with ^{13}C at peak at $m/z = 286.1$ and either $^{13}C_2$ or ^{18}O at $m/z = 287.3$. The experimental ratio is calculated by a particular peak's counts out of the total $(M + H)^+$ counts, while the predicted ratio is the combinatoric combination of the average abundances of the isotopes. The experimental counts have uncertainties of a few percent, so the experimental and predicted isotope ratios for the $(M + H)^+$ agreed well.

Table 2.8: Isotopic Ratios of protonated neat stearic acid at room temperature.

m/z	Counts	Identity	Experimental Ratio	Predicted Ratio
285.2	15241	$(M + H)^+$	83.7%	81.3%
286.1	2717	$(^{13}C-M + H)^+$	14.9%	16.4%
287.3	244	$(^{13}C_2-M + H)^+$	1.3%	1.8%

The only peaks that can be seen in negative mode are the $(M - H)^-$ at $m/z = 283.1$ (1990 counts) and the $(^{13}C-M - H)^-$ peak at $m/z = 284.1$ (413 counts). The presence of these peaks reinforces the identity of M as stearic acid. At -180 C the spectrum looks

nearly identical, thus the DART ionization source is likely viable with many fatty acids at the temperatures found on icy moons.

To more realistically simulate the DART spectrum in conditions found on Enceladus, the stearic acid was dissolved into a simulated Enceladus solution at $-180\text{ }^{\circ}\text{C}$. The resulting mass spectrum was obtained.

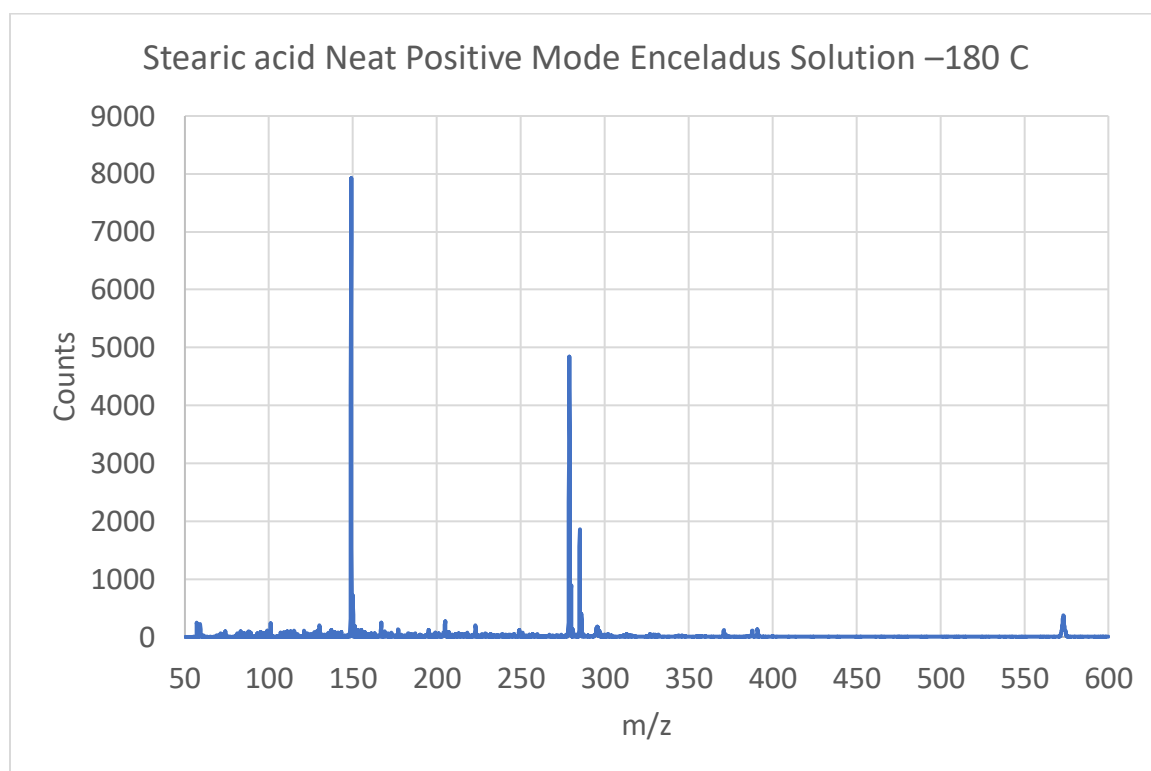


Figure 2.20: Mass spectrum of neat stearic acid positive mode in modeled Enceladus solution at $-180\text{ }^{\circ}\text{C}$.

A table of the common masses is shown below.

Table 2.9: Mass spectrum peaks of neat stearic acid positive mode in modeled Enceladus solution at $-180\text{ }^{\circ}\text{C}$.

Mass	Intensity	Identity
149.0	7926	Phthalic anhydride contaminant (in blank)
279.0	4839	$(\text{M} - \text{C}_2\text{H}_5 + \text{Na})^+$
280.2	586	$(^{13}\text{C}\text{-M} - \text{C}_2\text{H}_5 + \text{Na})^+$
285.3	1680	$(\text{M} + \text{H})^+$
286.4	143	$(^{13}\text{C}\text{-M} + \text{H})^+$

573.3	373	$(2M - OH + Na)^+$
-------	-----	--------------------

The mass spectrum of stearic acid in the Enceladus solution at $-180\text{ }^{\circ}\text{C}$ contained several differences with the neat stearic acid spectrum at $-180\text{ }^{\circ}\text{C}$. The $(M + H)^+$ peak is seen in both spectra, but in the Enceladus solution an $M - 6$ peaks is seen, which due to the isotope abundance at $M - 5$ contains approximately 14 C atoms. A $\Delta m/z = 6$ mass unit difference is challenging to reproduce, but is possible if C_2H_5 is lost and a Na^+ ion is clustered with the remains of the stearic acid molecule. Physically such an ion may develop if during the freezing process, the hydrophobic tails of the stearic acid protrude from the surface of the salty ice into the air, where the He^* can react with the end of the tail and cause a C–C bond breaking. To prevent the terminal carbon, which is primary, from being a radical, the C–C bond which breaks is the second from the end, producing a C_2H_5 radical. The $m/z = 573$ peak is a stearic acid dimer with one monomeric stearic acid's OH removed, and a sodium ion complexed with the dimer.

In the stearic acid negative mode spectrum, the only peak seen is $m/z = 283.2$ at 300 counts besides contaminants seen in the baseline at $m/z = 62$, 125, and 219. This peak corresponds to $(M - H)^-$, which is the form of stearic acid at $pH = 11$. No Cl^- adducts were seen, because chlorine has a 3:1 ratio between ^{35}Cl and ^{37}Cl , which is observed in no pair of peaks separated by $\Delta m/z = 2$.

Since DART source can sufficiently ionize stearic acid, the CID spectrum was taken of the $(M + H)^+$ peak at $m/z = 285$ at room temperature.

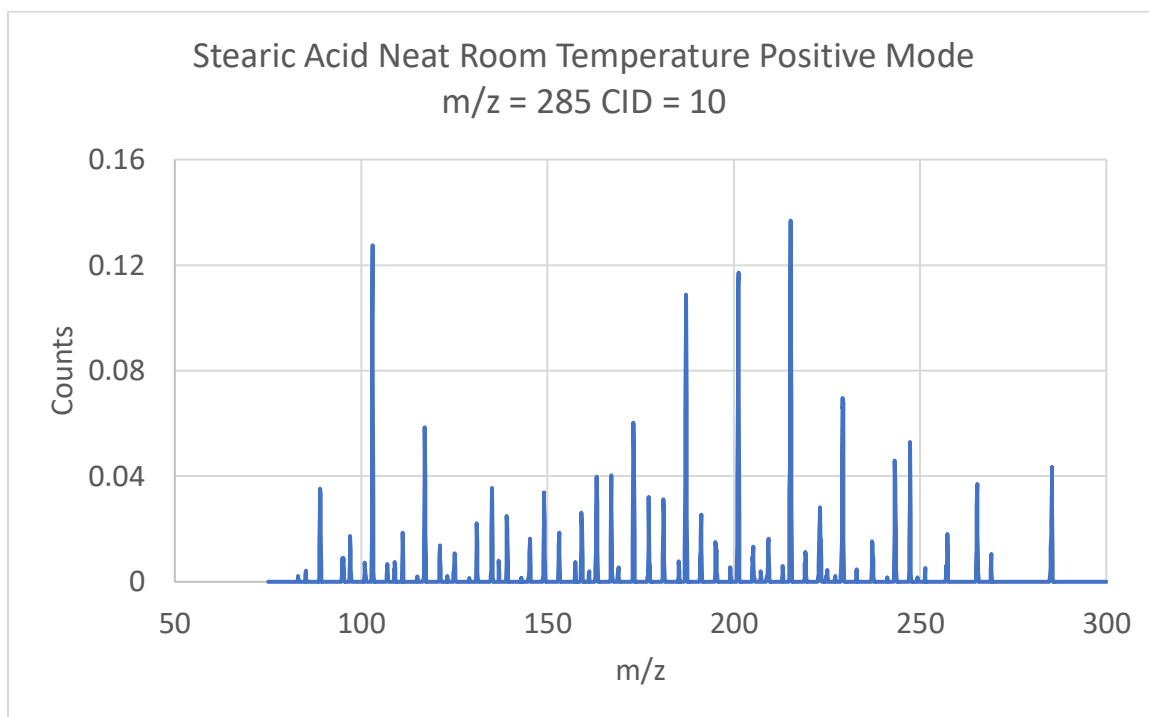


Figure 2.21: Mass spectrum of room temperature neat stearic acid positive mode at CID = 10.

While a forest of peaks is created in the CID spectrum, many of the most intense peaks are spaced 14 m/z units apart, corresponding to fragmentation of the loss of CH₂ units from the long unsaturated hydrocarbon chain. The intermediate peaks differ by 4 m/z units, which corresponds to the shift from a m/z multiple of 12 due to loss of one or two oxygen atoms.

DMPC

Because of the success in using the DART source to detect stearic acid, another class of biomolecules to test is phospholipids. A common membrane phospholipid is dimyristoylphosphatidylcholine (DMPC), which has the molecular formula $C_{36}H_{72}NO_8P$ (monoisotopic $M = 677.5$) and the following structure.

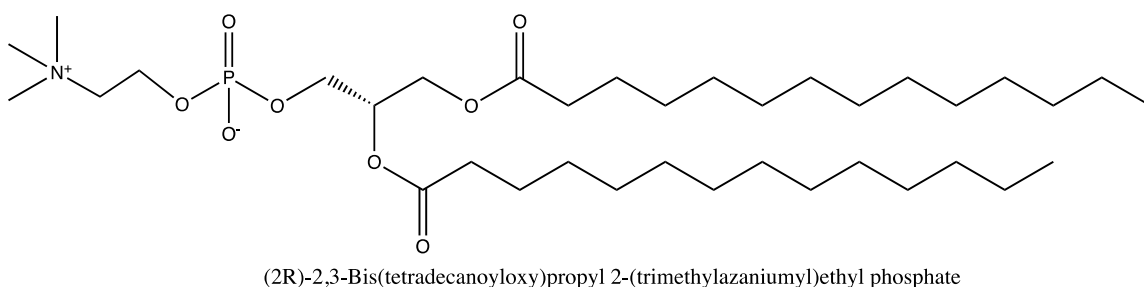


Figure 2.22: DMPC structure.

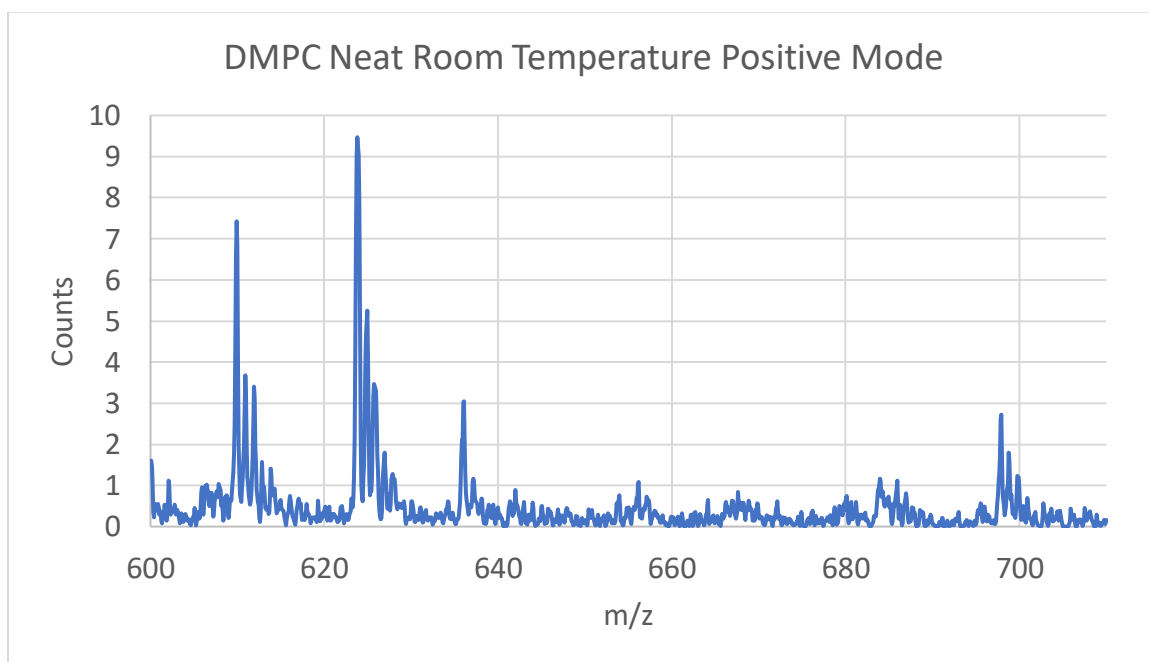
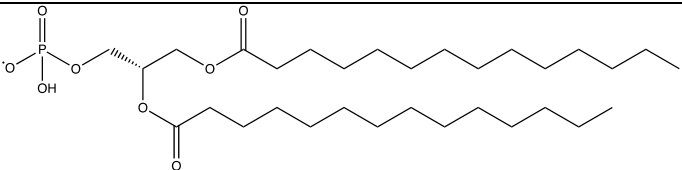
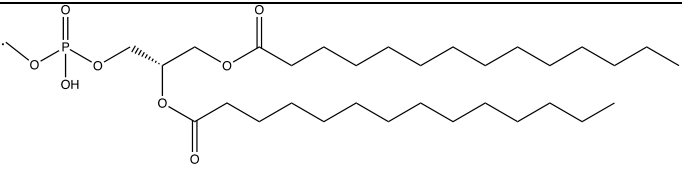
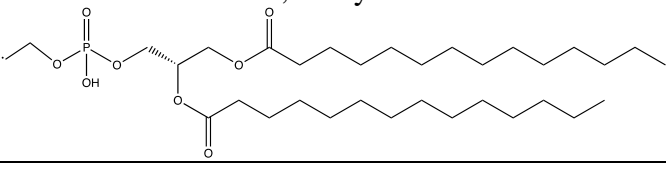


Figure 2.23: Neat DMPC mass spectrum at room temperature positive mode.

Because of the large molecular mass, only 65% of the DMPC sample's molecules will be the lowest-mass isotopologue. Thus a particular ion will appear as a series of peaks of successively more substituted isotopologues. From the peaks given, the phosphate group

was protonated in the mass spectra shown, the parent mass $m/z = 678.5$, explaining the $\Delta m/z = 1$ shift for all the fragment ion peaks. The following is a table of peaks seen.

Table 2.10: DMPC neat positive mode room temperature peaks seen.

m/z (lowest)	Abundance (lowest mass)	Identity
609.9	7.4	 H_3O^+
623.8	9.5	 H_3O^+
636.0	3.0	Unclear, likely involves 
697.8	2.6	$\text{M} + \text{H}_3\text{O}^+$

No substantial peaks that could be linked to DMPC could be seen at less than $m/z = 500$.

A pattern, unlike for stearic acid, is DMPC peaks seen all have breaks between the phosphate and the quaternary amine, cleaving off the nitrogen. The low sensitivity was likely due to poor alignment of the inlet while the data was taken.

At low temperatures, the spectrum of neat DMPC is different than the spectrum of 100 μM DMPC in Enceladus solution both at -180°C .

Table 2.11: DMPC peaks at $-180\text{ }^{\circ}\text{C}$ for neat and $100\text{ }\mu\text{M}$ Enceladus sample.

m/z	Counts Neat	Counts Enceladus	Identity
490.7	1401	54	M – 188
568.4	39	395	M – 109
572.9	446	282	M – 104
685.5	33	15	M + 10

These peaks likely are not from DMPC, because of the lack of isotopologue peaks in a progression at $\Delta m/z = 1$ steps larger than the non-substituted isotopologue peak.

Cholesterol

Another class of molecules likely to be a biosignature on icy moons are steroid-like molecules with multiple hydrocarbon rings. For terrestrial life these molecules stabilize cellular membranes, and chemically-similar hopanoid molecules are among the earliest detectable fossilized molecular remains at 3.5 GYa.¹² For terrestrial life, a common steroid molecule is cholesterol, which has the formula $C_{27}H_{46}O$ (monoisotopic $M = 386.4$) and the following structure.

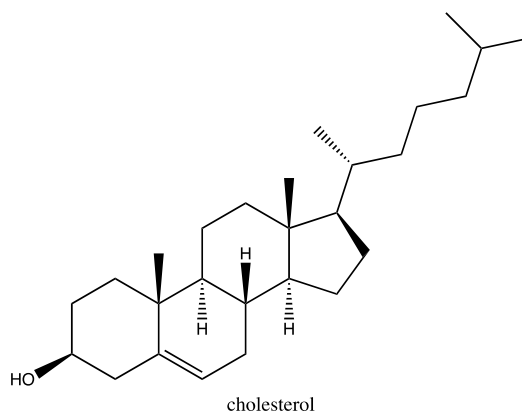


Figure 2.24: Structure of Cholesterol

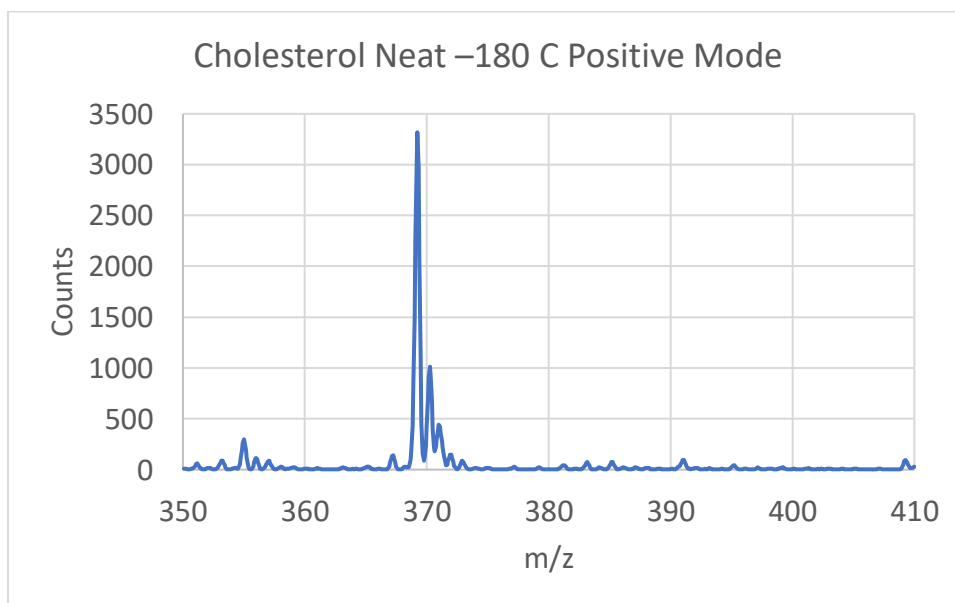


Figure 2.25. Neat cholesterol mass spectrum -180 °C positive mode.

The mass spectrum at $-180\text{ }^{\circ}\text{C}$ has two groups of peaks, one at $m/z = 355.1$ (264 counts), which is $(M - \text{OH} - \text{CH}_2)^+$, and the second at $m/z = 369.3$ (3319 counts), which is $(M - \text{OH})^+$. Cholesterol is challenging to ionize via many methods because the rigid structure and largely aliphatic nature leaves few routes to ionization. DART ionization cannot observe the intact parent or clusters at $M + 1$ or $M + 19$, but can observe loss of the OH group to form $M - 17$. The isotopic ratios of the isotopologue peaks are consistent with a C_{27} compound, further confirming the $m/z = 369$ as being derived from cholesterol. Further dissociation of the $M - 17$ can remove a CH_2 group too, though with lower counts the isotopologue peak ratios are hard to discern.

The negative mode spectrum of neat cholesterol both at room temperature and $-180\text{ }^{\circ}\text{C}$ did not have any ions assignable to cholesterol anions or the dehydroxylated cholesterol anion.

Hopane Mixture

Since hopane molecules are similar to steroids and can remain fossilized as biomolecular signatures of life, DART ionization was conducted on a mixture of hopanes. The hopane mixture was NIST 2266, where the hopanes listed below were suspended in 2,2,4-trimethylpentane (isooctane).

Table 2.12: Hopane mixture composition. From NIST 2266 Reference Analysis, 2 σ deviation uncertainty.¹³

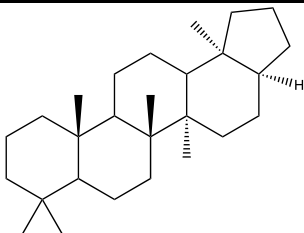
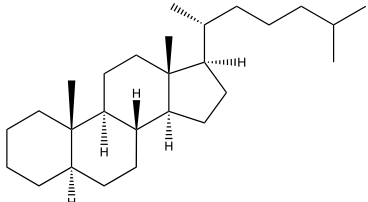
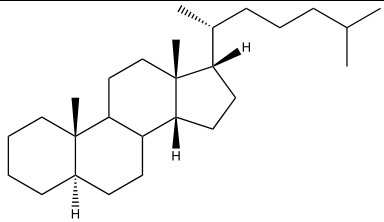
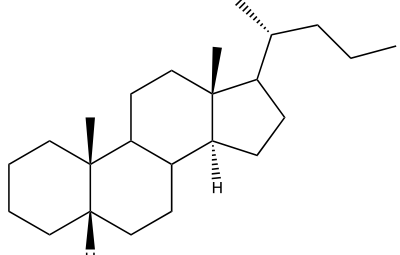
Compound	CAS #	Mass Fraction ($\mu\text{g/g}$)	Mass Concentration ($\mu\text{g/mL}$)
17 α (H)-22,29,30-trisnorhopane	53584-59-1	4.55 \pm 0.23	3.14 \pm 0.16
$\alpha\alpha\alpha$ 20R-cholestane	481-21-0	33.1 \pm 1.0	22.8 \pm 0.7
$\alpha\beta\beta$ 20R-cholestane	69483-47-2	10.61 \pm 0.24	7.32 \pm 0.17
$\alpha\beta\beta$ 20R 24S-methylcholestane	71117-90-3	2.32 \pm 0.10	1.60 \pm 0.07
$\alpha\alpha\alpha$ 20R 24R-ethylcholestane	62446-14-4	8.58 \pm 0.32	5.92 \pm 0.22
17 α (H),21 β (H)-30-norhopane	53584-60-4	1.31 \pm 0.04	0.90 \pm 0.02
$\alpha\beta\beta$ 20R 24R-ethylcholestane	71117-92-5	3.25 \pm 0.15	2.24 \pm 0.11
17 α (H),21 β (H)-hopane	13849-96-2	1.70 \pm 0.12	1.17 \pm 0.08
17 α (H),21 β (H)-22R-homohopane	60305-22-8	0.89 \pm 0.03	0.62 \pm 0.02
17 α (H),21 β (H)- 22S-homohopane	60305-23-9	1.54 \pm 0.09	1.06 \pm 0.06

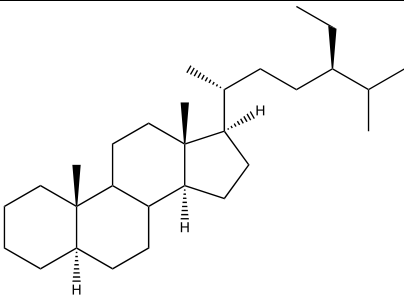
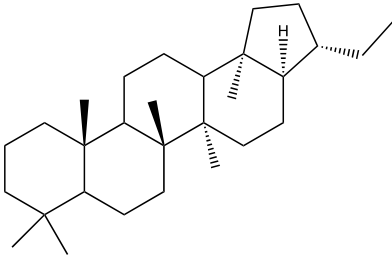
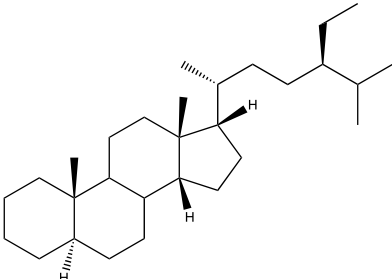
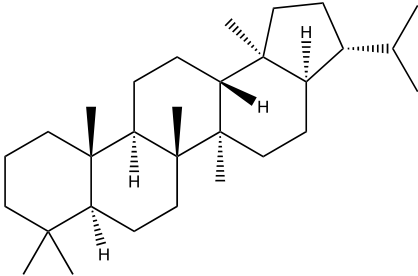
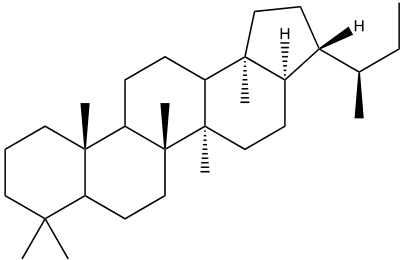
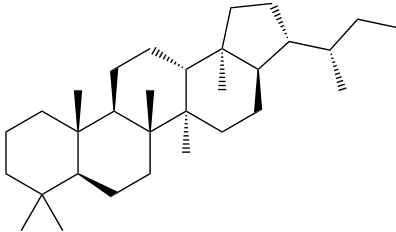
Table 2.13: Hopane mixture expected ion peaks.

Compound	Formula	Mass (Da)	M + H ⁺	M + H ₃ O ⁺
17 α (H)-22,29,30-trisnorhopane	C ₂₇ H ₄₆	370.65	371.65	389.65
$\alpha\alpha\alpha$ 20R-cholestane	C ₂₇ H ₄₈	372.67	373.67	391.67
$\alpha\beta\beta$ 20R-cholestane	C ₂₇ H ₄₈	372.67	373.67	391.67
$\alpha\beta\beta$ 20R 24S-methylcholestane	C ₂₈ H ₅₀	386.70	387.70	405.70

$\alpha\alpha\alpha$ 20R 24R-ethylcholestane	$C_{28}H_{50}$	386.70	387.70	405.70
17 α (H),21 β (H)-30-norhopane	$C_{29}H_{50}$	398.71	399.71	417.71
$\alpha\beta\beta$ 20R 24R-ethylcholestane	$C_{29}H_{52}$	400.70	401.70	419.70
17 α (H),21 β (H)-hopane	$C_{31}H_{54}$	426.76	427.76	445.76
17 α (H),21 β (H)-22R-homohopane	$C_{31}H_{54}$	426.76	427.76	445.76
17 α (H),21 β (H)- 22S-homohopane	$C_{31}H_{54}$	426.76	427.76	445.76

Table 2.14: Hopane mixture chemical structures.

Compound	Structure
17 α (H)-22,29,30-trisnorhopane	
$\alpha\alpha\alpha$ 20R-cholestane	
$\alpha\beta\beta$ 20R-cholestane	
$\alpha\beta\beta$ 20R 24S-methylcholestane	

$\alpha\alpha$ 20R 24R-ethylcholestane	
17 α (H),21 β (H)-30-norhopane	
$\alpha\beta$ 20R 24R-ethylcholestane	
17 α (H),21 β (H)-hopane	
17 α (H),21 β (H)-22R-homohopane	
17 α (H),21 β (H)- 22S-homohopane	

A plot of the positive mode room temperature spectrum of the hopanoid mixture is shown below.

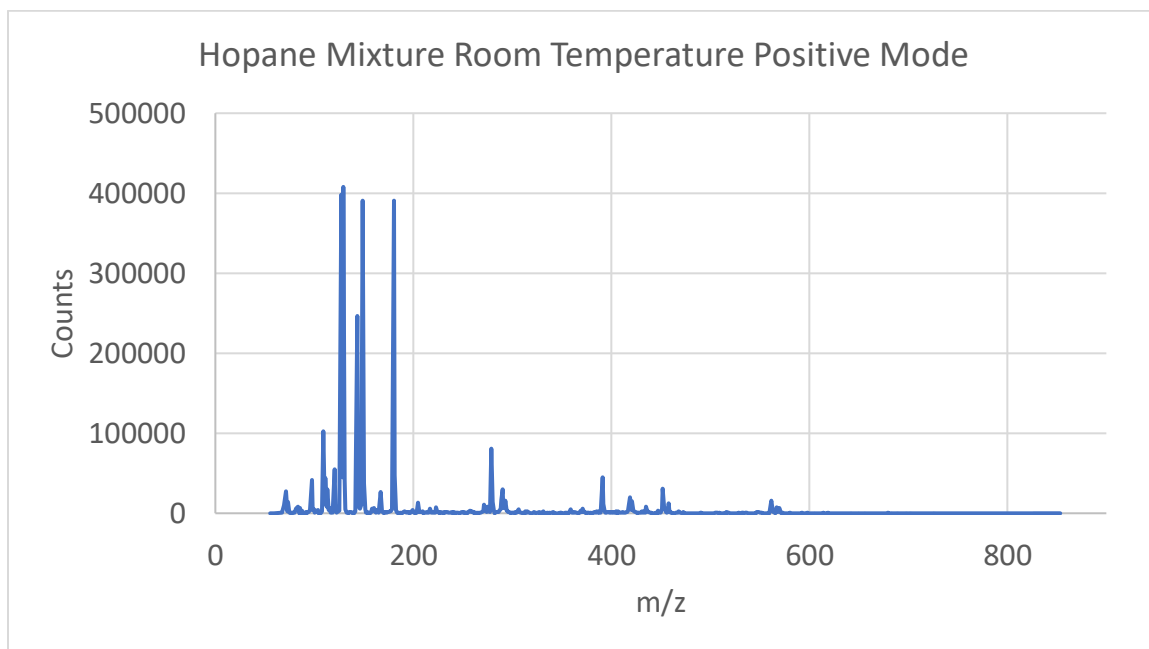


Figure 2.26: Mass Spectrum of hopane mixture at room temperature positive mode

At lower masses the spectrum is dominated by isooctane ($M = 114.2$) and clusters containing isooctane. The hopane molecules have lower volatility and thus less intensity, with the peaks for the hopane mixture appearing in the $m/z = 370 - 450$ range. A plot of that range is shown below.

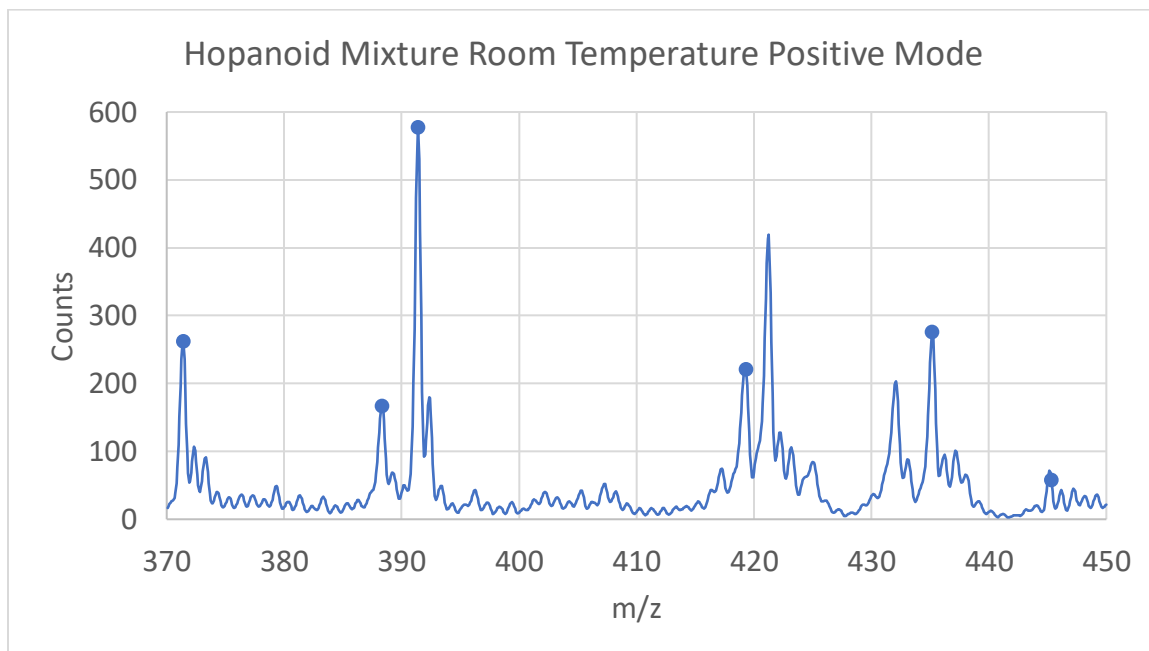


Figure 2.27: Mass Spectrum of hopane mixture at room temperature positive mode

A table of the hopane peaks is shown below.

Table 2.15: Observed peaks in mass spectrum of hopane at room temperature positive mode.

m/z	Intensity	Identity
371.5	236	(17 α (H)-22,29,30-trisnorhopane + H) ⁺
388.3 (peak should be centered at m/z = 387.6)	167	($\alpha\beta\beta$ 20R 24S-methylcholestane + H) ⁺ , ($\alpha\alpha\alpha$ 20R 24S-methylcholestane + H) ⁺
391.4	577	($\alpha\alpha\alpha$ 20R-cholestane + H ₃ O) ⁺ , ($\alpha\beta\beta$ 20R-cholestane + H ₃ O) ⁺
419.3	220	($\alpha\beta\beta$ 20R 24R-ethylcholestane + H ₃ O) ⁺
445.3	58	(17 α (H),21 β (H)-hopane + H ₃ O) ⁺ , (17 α (H),21 β (H)-22R-homohopane + H ₃ O) ⁺ , (17 α (H),21 β (H)- 22S-homohopane + H ₃ O) ⁺

Due to likely drift in the calibration, the observed peaks were approximately $\Delta m/z = 0.2 - 0.3$ less than predicted by the chemical structures.

At $-180\text{ }^{\circ}\text{C}$, no peaks assignable to $(M + 1)^+$ cations could be seen. Ion counts were low, and the peaks visible in the $m/z = 365 - 450$ range did not have enough intensity to identify fragments via CID. For the hopane mixture in negative mode, both room temperature and $-180\text{ }^{\circ}\text{C}$ spectra showed no ions assignable as hopane anions. Similar to cholesterol, ionization efficiency over all is low, since the vapor pressure of the hopanoid compounds is low and there exist few fragmentation pathways available to producing ions.

Discussion:

One of the overall observations is the chemical structure of the sample is predictive if DART ionization will produce a measurable ion signal. Despite a general lack of easy ionization pathways, DART succeeds in ionizing aliphatic groups, and ionizes polar and even charged molecules, as long as the molecules are not zwitterionic.

Aliphatic molecules such as cholesterol and hopanes were ionized and detectable, while amino acids and polypeptides were not detected. However, amino acid methyl esters were detectable, which have a charged NH_4 group but lack the carboxyl group, and fatty acids, which have a carboxyl group but lack an amino group, were both detectable. The fact molecules with charged functional groups can be detected via DART is good for DART's molecular detection versatility, with the caveat that zwitterions cannot be readily detected. Polar groups are also readily detected, with identification of poly-hydroxylated saccharides previously detected.¹⁴

Another observation is the ion signal is strongly dependent on the DART ionization geometry. The exit of the DART gas stream, the sample, and the mass spectrometer vacuum inlet all need to be within a few mm of each other, and slight changes in the geometry can cause order of magnitude changes in ion signal. The set-up employed used micrometer stages to precisely align the inlet and sample, but this is a consideration for potential spaceflight applications, where source positioning systems and sample shrouds for containing gas-phase sample should be engineered carefully.

Preheating the DART He stream and the frost formed on a $-180\text{ }^\circ\text{C}$ sample both helped to increase the signal. A heated DART gas increased a sample's volatility, allowing for more neutral molecules which the DART gas stream can ionize.¹⁵ Future

directions for this work would be to observe the gas temperature dependence of the DART spectrum, giving an orthogonal data axis for identifying analytes. The frost on the $-180\text{ }^{\circ}\text{C}$ sample likely trapped the gas-phase sample and increased the analyte's gas phase concentration at the DART tip. Because the frost was likely warmer than $-180\text{ }^{\circ}\text{C}$, the molecules likely less-readily condensed than had the ions been in a cryogenic chamber, which would be more comparable to conditions on an icy moon like Enceladus. An icy moon also would have little atmospheric pressure guiding the ions into the mass spectrometer. Future versions of the experimental set-up should account for these differences, and test the DART technique's performance in other simulated salt ices, such as the MgSO_4 and NaCl brines predicted in Europa's subsurface ocean.¹⁶

Another upgrade could be the use of different DART gases and secondary chemical ionization (CIMS) to reduce ion fragmentation. The 19.8 eV available from He^* can provide one data set, but recent developments using excited Ar^* gas and chlorobenzene or anisole can produce a complimentary spectrum for species analysis.¹⁷ Aromatic molecules in particular could be detected at ppb level,¹⁷ which are similar to the molecules we discovered produced good mass spectra. Ar DART is dominated by molecular ions and shows less protonation, which could overcome our observed problem of detecting zwitterionic molecules.

Conclusion:

A custom He DART apparatus was improved for better data collection reproducibility, and a variety of terrestrial life biomolecules were tested for compatibility with DART ionization in conditions simulating extraterrestrial icy moons. Molecular characteristics associated with efficient DART ionization were non-polarity (like lipids),

while zwitterions were found to not be detectable with DART (like proteins), even at high concentrations. DART ionization was still efficient with ions, even in simulated salt solutions and decreased temperatures at $-180\text{ }^{\circ}\text{C}$. Molecules without obvious ionization pathways still ionized with the He DART, and many molecules were identifiable from the fragments produced and CID spectra. Sample inlet geometry is a crucial parameter for successful ion collection, which should be carefully optimized for rigidity and fine movement were a DART instrument deployed on an *in situ* sensing mission.

Acknowledgments:

I would like to thank the NASA president's and director's research development fund award 80NM0018D0004W for funding the work herein. I would like to thank my fellow graduate student Tylger Nuygen for help with the data collected in this chapter. I would also like to thank Professor Jack Beauchamp and Dr. Rob Hodyss for their mentorship and advice.

References:

- (1) Yokota, S. Isotope Mass Spectrometry in the Solar System Exploration. *Mass Spectrom.* **2018**, 7 (2), S0076. <https://doi.org/10.5702/massspectrometry.S0076>.
- (2) Upton, K. T.; Schilling, K. A.; Beauchamp, J. L. Easily Fabricated Ion Source for Characterizing Mixtures of Organic Compounds by Direct Analysis in Real Time Mass Spectrometry. *Anal. Methods* **2017**, 9 (34), 5065–5074. <https://doi.org/10.1039/C7AY00971B>.
- (3) Hodgman, S. S.; Dall, R. G.; Byron, L. J.; Baldwin, K. G. H.; Buckman, S. J.; Truscott, A. G. Metastable Helium: A New Determination of the Longest Atomic Excited-State Lifetime. *Phys. Rev. Lett.* **2009**, 103 (5), 053002. <https://doi.org/10.1103/PhysRevLett.103.053002>.
- (4) Glein, C. R.; Baross, J. A.; Waite, J. H. The PH of Enceladus' Ocean. *Geochim. Cosmochim. Acta* **2015**, 162, 202–219. <https://doi.org/10.1016/j.gca.2015.04.017>.
- (5) Gross, J. H. Direct Analysis in Real Time—a Critical Review on DART-MS. *Anal. Bioanal. Chem.* **2014**, 406 (1), 63–80. <https://doi.org/10.1007/s00216-013-7316-0>.
- (6) Cody, R. B.; Laramée, J. A.; Durst, H. D. Versatile New Ion Source for the Analysis of Materials in Open Air under Ambient Conditions. *Anal. Chem.* **2005**, 77 (8), 2297–2302. <https://doi.org/10.1021/ac050162j>.
- (7) Moore, J. H.; Davis, C. C.; Coplan, M. A. Building Scientific Apparatus, Fourth Edition. 663.
- (8) Petersen, H. The Properties of Helium: Density, Specific Heats, Viscosity, and Thermal Conductivity at Pressures from 1 to 100 Bar and from Room Temperature to about 1800 K. 46.
- (9) Williams, J. P.; Patel, V. J.; Holland, R.; Scrivens, J. H. The Use of Recently Described Ionisation Techniques for the Rapid Analysis of Some Common Drugs and Samples of Biological Origin. *Rapid Commun. Mass Spectrom.* **2006**, 20 (9), 1447–1456. <https://doi.org/10.1002/rcm.2470>.
- (10) Elsila, J. E.; Glavin, D. P.; Dworkin, J. P. Cometary Glycine Detected in Samples Returned by Stardust. *Meteorit. Planet. Sci.* **2009**, 44 (9), 1323–1330. <https://doi.org/10.1111/j.1945-5100.2009.tb01224.x>.
- (11) Ioppolo, S.; Fedoseev, G.; Chuang, K.-J.; Cuppen, H. M.; Clements, A. R.; Jin, M.; Garrod, R. T.; Qasim, D.; Kofman, V.; van Dishoeck, E. F.; Linnartz, H. A Non-Energetic Mechanism for Glycine Formation in the Interstellar Medium. *Nat. Astron.* **2021**, 5 (2), 197–205. <https://doi.org/10.1038/s41550-020-01249-0>.

- (12) Waldbauer, J. R.; Newman, D. K.; Summons, R. E. Microaerobic Steroid Biosynthesis and the Molecular Fossil Record of Archean Life. *Proc. Natl. Acad. Sci.* **2011**, *108* (33), 13409–13414. <https://doi.org/10.1073/pnas.1104160108>.
- (13) National Institute of Standards and Technology. Certificate of Analysis: Standard Reference Material 2266, Hopanes and Steranes in 2,2,4-Trimethylpentane, 2016. <https://tsapps.nist.gov/srmext/certificates/2266.pdf> (accessed 2023-05-30).
- (14) Wang, Y.; Liu, L.; Ma, L.; Liu, S. Identification of Saccharides by Using Direct Analysis in Real Time (DART) Mass Spectrometry. *Int. J. Mass Spectrom.* **2014**, *357*, 51–57. <https://doi.org/10.1016/j.ijms.2013.09.008>.
- (15) Huang, M.-Z.; Cheng, S.-C.; Cho, Y.-T.; Shiea, J. Ambient Ionization Mass Spectrometry: A Tutorial. *Anal. Chim. Acta* **2011**, *702* (1), 1–15. <https://doi.org/10.1016/j.aca.2011.06.017>.
- (16) Vu, T. H.; Hodyss, R.; Choukroun, M.; Johnson, P. V. Chemistry of Frozen Sodium-Magnesium-Sulfate-Chloride Brines: Implications for Surface Expression of Europa's Ocean Composition. *Astrophys. J.* **2016**, *816* (2), L26. <https://doi.org/10.3847/2041-8205/816/2/L26>.
- (17) Cody, R. B.; Dane, A. J. Dopant-Assisted Direct Analysis in Real Time Mass Spectrometry with Argon Gas. *Rapid Commun. Mass Spectrom.* **2016**, *30* (10), 1181–1189. <https://doi.org/10.1002/rcm.7552>.

Visible Photodissociation DART Quantification of
Isomeric Naphthalene/Azulene Mixtures

Abstract:

Combining direct analysis in real time (DART) ionization with the custom mass spectrometer described earlier, photodissociation was performed on the cations of structural isomers azulene and naphthalene at 450 and 402 nm with compact continuous-wave laser sources. Trends in laser power, wavelength, and ion trapping time were compared against collision-induced dissociation (CID). A quantitative calibration curve for determining a mixture composed of two isomers was created using the DART ion source with photoionization at both wavelengths, while CID was not found to be quantitative for this isomer pair. The advantage of quantification from the combination of source method and photodissociation expands the potential applications for both DART ionization and photoionization as analytic techniques.

Introduction:

Mass spectrometry has been used quantitatively in a wide variety of fields in routinely hundreds to thousands of laboratories,¹⁻³ with methods spanning brief observation of light m/z ions to long-observations of megadalton ions.^{4,5} Central to mass spectrometry's utility is the wide variety of ion sources and detection methods tailored for individual molecules and chemical problems, as well as ion fragmentation patterns.²

Fragmentation patterns are important for identifying isomers, because isomers have the same m/z ratio. Therefore, the choice of fragmentation method will be important. One such technique is collision-induced dissociation (CID), where trapped ions are accelerated into helium buffer gas, and the fragment distribution analyzed in tandem MS/MS as functions of trapping time and energy.⁶ While effective at fragmenting ions, CID can result in similar fragmentation patterns for similar structure ions, limiting CID's utility when determining isomer mixtures.⁶

Another fragmentation technique is photodissociation, where trapped ions are irradiated to cause dissociation, typically either in the ultraviolet or mid-infrared. Ultraviolet radiation has been used to great effect to study the structure and chemistry of macromolecules such as protein and nucleic acids, as well as higher energy-accessible fundamental chemical processes.⁷⁻¹⁰ Infrared multi-photon dissociation relies on wavelength-specific fragmentation occurring on resonance with an infrared vibrational transition,¹¹ and has been used extensively to observe fundamental chemical interactions as well as dissociation of specific chemical functional groups to create informative MS/MS spectra for biomolecule characterization.¹¹

Because photodissociation is wavelength-dependent, different ion quantum states and reaction channels to be accessed.¹² This makes photodissociation a form of action spectroscopy, where absorption is detected through a chemical change or product. These processes are zero-background, significantly enhancing sensitivity, and mass spectrometry allows detection to be relatively universal.¹³ These advantages make tunable photodissociation mass spectrometry appealing for development as space flight hardware.

Mass spectrometers have flown on a wide variety of remote sensing and *in situ* NASA missions, beginning with Pioneer and Viking missions to Venus and Mars.¹⁴ Laser spectrometers have also been included in mission payloads since the tunable laser spectrometer on the Mars science laboratory.^{15,16} DART ionization is being explored as a candidate for future missions, per this work, so making a combination of techniques would be novel improvement to existing technology.

Quantitative techniques are especially desirable for to measure trace *in situ* constituents, including for isomeric species which cannot be measured by mass spectrometry alone. Photodissociation has very recently been used quantitatively with mass spectrometry by Shi *et al.* looking at chiral isomer ratios,¹⁷ but the technique was not combined with DART nor were different photodissociation wavelengths employed to distinguish between isomers. Marlton and Trevitt have also recently used photodissociation to identify and separate isomers using tunable UV radiation,¹² but in the ultraviolet range and using non-compact OPO light sources.

The polyaromatic hydrocarbons (PAHs) naphthalene and azulene were chosen for ionization to form the naphthalene and azulene cations (abbreviated Nap⁺ and Azu⁺), for

three main reasons. One is the likely presence of at least naphthalene on Saturn's moon Titan,^{18,19} which is the subject of future NASA mission Dragonfly in the search for life in the solar system.^{20,21} Second is the relative ease of DART ionization for both molecules. Third is the absorption spectra differ in the visible region between both molecules, allowing photodissociation rates to vary with wavelength. The chemistry of azulene derivatives is more extensive than that of the Azu^+ cation, but many azulene cation studies and derivatives show an increase in cross section between 400 – 450 nm.^{22,23} Shida and Iwata show an increasing cross section to a maximum near 532 nm.²⁴ In the UV, isomerization rates rise by 6 order of magnitude as energy flows from 115.3 kcal/mol (248 nm) to 287.3 kcal/mol (99.5 nm),²⁵ with the absorbance of substituted species dropping quickly as the photodissociation wavelength passes from the UV into the visible.²³ Naphthalene however shows relatively little absorption in this region, with stronger absorption seen from the $2^2 \text{B}_1 \leftarrow \text{X}$ transition around 532 nm,²⁶ and a steady decrease in absorbance from 400 – 450 nm in an Ar matrix at 12 K.²⁷

The visible wavelength range is relatively unexplored for photodissociation experiments, but allows for compact, inexpensive, and robust continuous-wave (cw) laser diode sources. The goal of this work is to demonstrate mixtures of isomeric species can be quantified using visible photodissociation with DART ionization and compact laser sources.

Experimental:

The experimental apparatus was the same Thermo-Fischer Finnegan Linear quadrupole ion trap mass spectrometer used in the coronene and d₁₂-coronene chapter, except the laser sources were changed to two laser diodes at 450 nm and 402 nm, and the

mass spectrometer source was changed to the same DART source seen in the DART chapter with the same flow rates and voltages. A 100 ms maximum trap filling time and 300 spectrum averages were used per scan.

Sample preparation consisted of weighing azulene (99% Thermo Fisher), azulene (99% Thermo Fisher), or a mixture on an analytical balance in the desired ratio. To ensure a uniform surface, the sample was dissolved in dichloromethane (DCM), dropped onto a cleaned glass microscope slide, and left for the DCM to evaporate. Samples were used promptly after preparation, as both the naphthalene and azulene are volatile; after ~30 min the measured ratio can be seen to change.

Naphthalene and azulene were chosen because these two molecules are isobaric, but ionization proved a challenge. All attempts to use electrospray ionization on naphthalene failed, with electrospray peaks at $m/z = 128$ within the mass spectrum noise, and the peak intensity not changing with increasing concentration. Different solvents and both liquid-phase and gas phase proton sources were tested, but even at 100 mM no naphthalene signal could be seen. Azulene showed a signal with electrospray ionization, but identical ionization methods were needed. Both molecules are volatile and respond well to DART ionization, leading to DART being employed.

The following were the optimized ion guide parameters.

Table 3.1: Optimized Finnegan LTQ Parameters at $m/z = 128$.

Parameter	Value $m/z = 128$
Capillary voltage (V)	5.0
Tube lens voltage (V)	28
Sheath gas flow (arb)	21
Auxiliary gas flow (arb)	15
Sweep gas flow (arb)	8
Multiple RF DAC (V)	740
Multipole 00 offset (V)	-3.6
Lens 0 (V)	-6.1
Multipole 0 offset (V)	-8.2
Lens 1 (V)	-76
Multipole 1 offset (V)	-12.0
Gate lens (V)	-9.0
Front lens (V)	-7.0

Laser light at 402 nm was provided by an 800 mW Panasonic LNC431FS01WW diode and 450 nm light was provided by a 1600 mW Thorlabs L450P1600MM diode. Both diodes were Ø5.6 mm Thorlabs pin-style G and were physically removed from the LDM56 TE-cooled laser diode mount to change wavelengths. The LDM56 was powered by a 1 Amp Thorlabs LDC210C laser diode current controller and a 20 W Thorlabs TEC2000 TE-cooler controller. Both diodes were mounted with laser diode cathode in the photodiode slot (ground pin and square cutout on the mount facing to the left), the LD pin set to cathode ground and the photodiode pin set to anode ground on the LDM56 mount, and the cathode ground mode on the LDC210C current controller. Both diodes were run in cw-operation.

A plot of the Thorlabs L450P1600MM LI curve is given below:

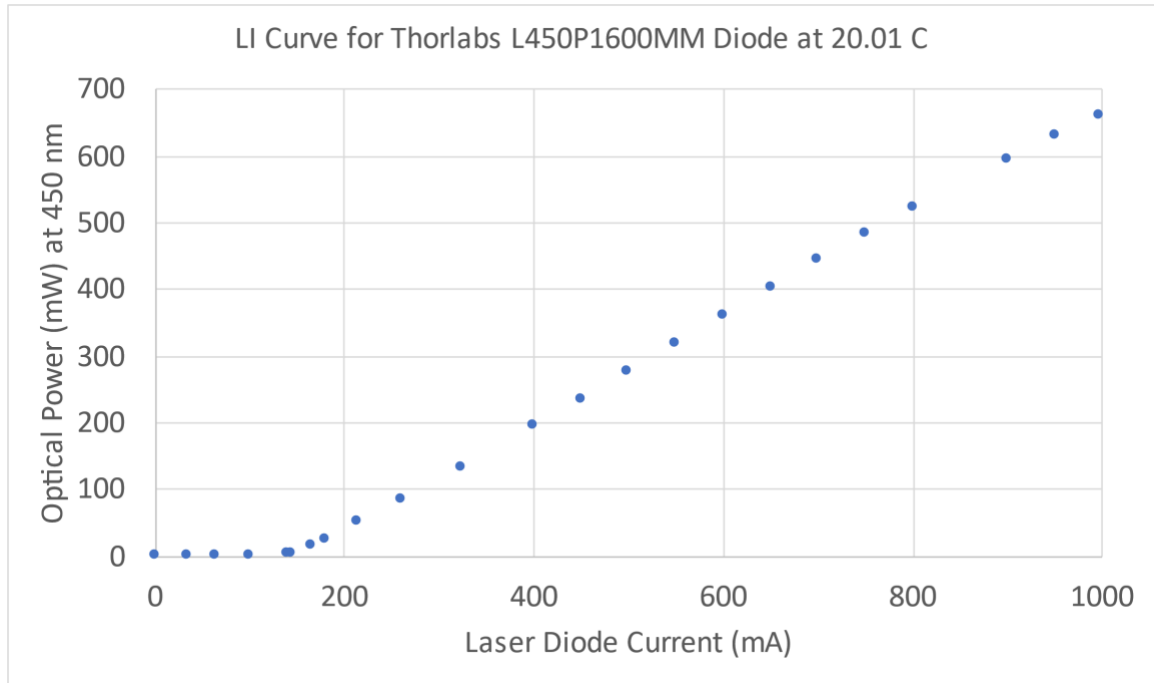


Figure 3.1: Laser power at 450 nm vs laser diode current. Above the 144 mA threshold, a linear trend of optical power = $(0.790 \text{ mW/mA}) \times (\text{current} - 149.3 \text{ mA})$.

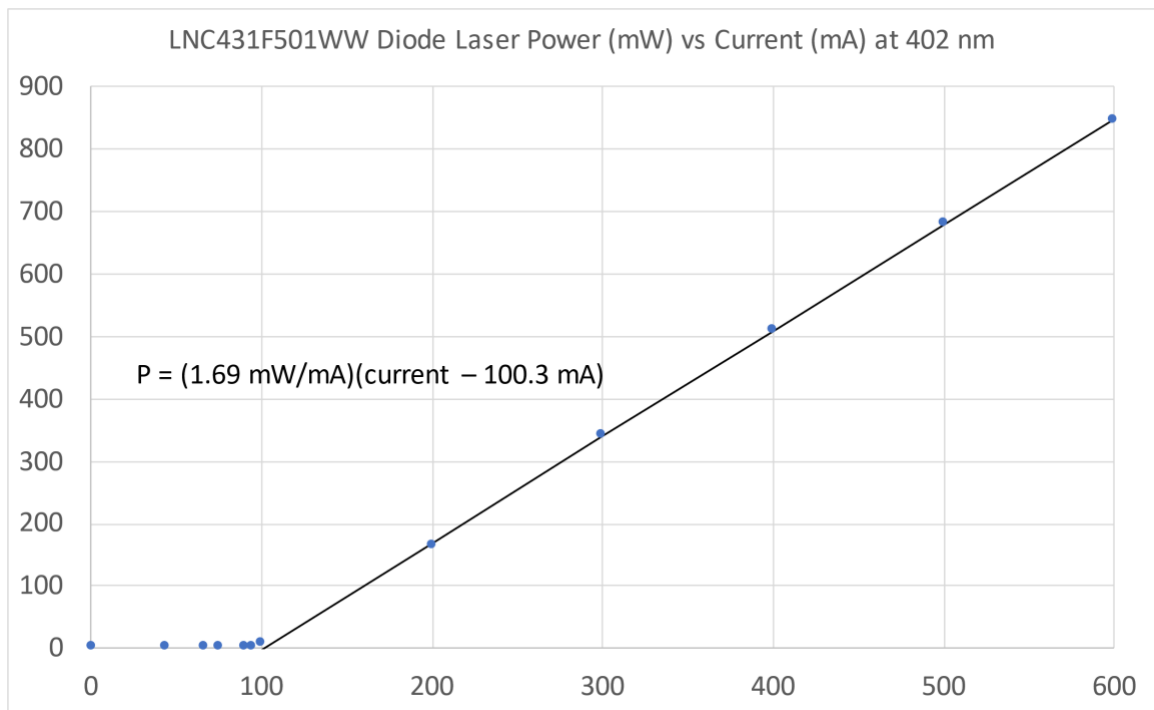


Figure 3.2: Optical power vs current for the LNC431F501WW diode laser at 20.00 °C.

Results:

Naphthalene produced $10^4 - 10^5$ counts at $m/z = 128$ with no other significant peaks when mass selected. Azulene produced $10^5 - 10^6$ counts at $m/z = 129$, comparable to electrospray ion counts of water-soluble ions. Naphthalene was nearly 100% Nap^+ at $m/z = 128$, while azulene was nearly all AzuH^+ at $m/z = 129$, with 2 – 3% intensity as Azu^+ at $m/z = 128$. DART ionized azulene so efficiently that azulene samples had to be placed up to 1 cm from the DART inlet (1 mm is common for other samples). This prevented the ion trap filling too rapidly and making the shuttering filtering circuit ineffective. For all subsequent experiments the Azu^+ ion was trapped.

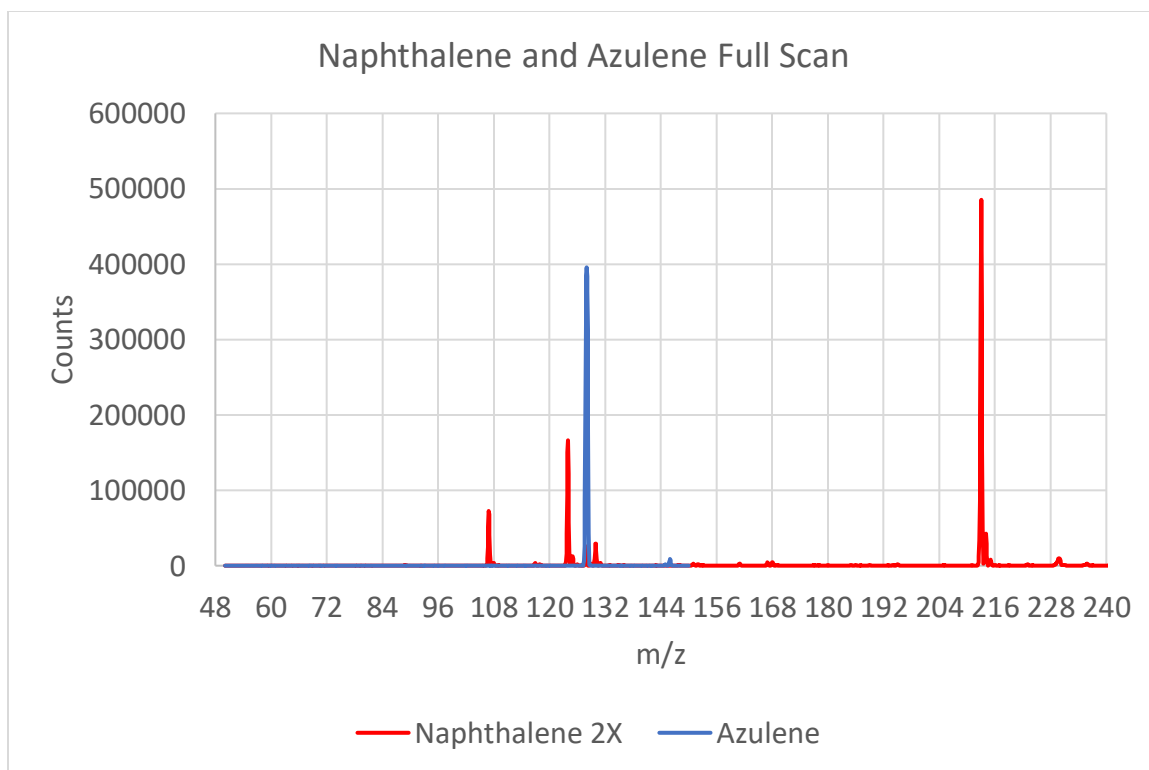


Figure 3.3: Mass spectra of pure naphthalene and azulene in scan mode.

Table 3.2: Masses and potential identities in scan mode spectra.

m/z	Counts Nap⁺	Counts Azu⁺	Identity
107	34085		Likely C ₄ O ₃ H ₁₀ + H ⁺
124	83355		C ₄ O ₃ H ₁₀ + NH ₄ ⁺
128	12037	395722	Nap ⁺ , Azu ⁺
130	14750		Undetermined
213	242660		(C ₄ O ₃ H ₁₀) ₂ + H ⁺
214	21252		¹³ C-(C ₄ O ₃ H ₁₀) ₂ + H ⁺

The photodissociation (PD) yields at both wavelengths varied with laser power and trap time were consistent with results seen for coronene. At low-medium laser powers (100 mW) were < 10% regardless of trapping time, at medium laser powers the PD yields varied with trapping time (20% at 10 ms, 99% at 1000 ms), and at higher laser powers only short trap times still contained appreciable parent ion. Similar trends were seen for both Azu⁺ and Nap⁺ ions.

Compared to collision-induced dissociation (CID), at low energy CID short and medium trap times did not cause significant fragmentation, but long trapping times resulted in nearly 80% fragmentation. At higher energy CID short trap times still produced nearly no dissociation.

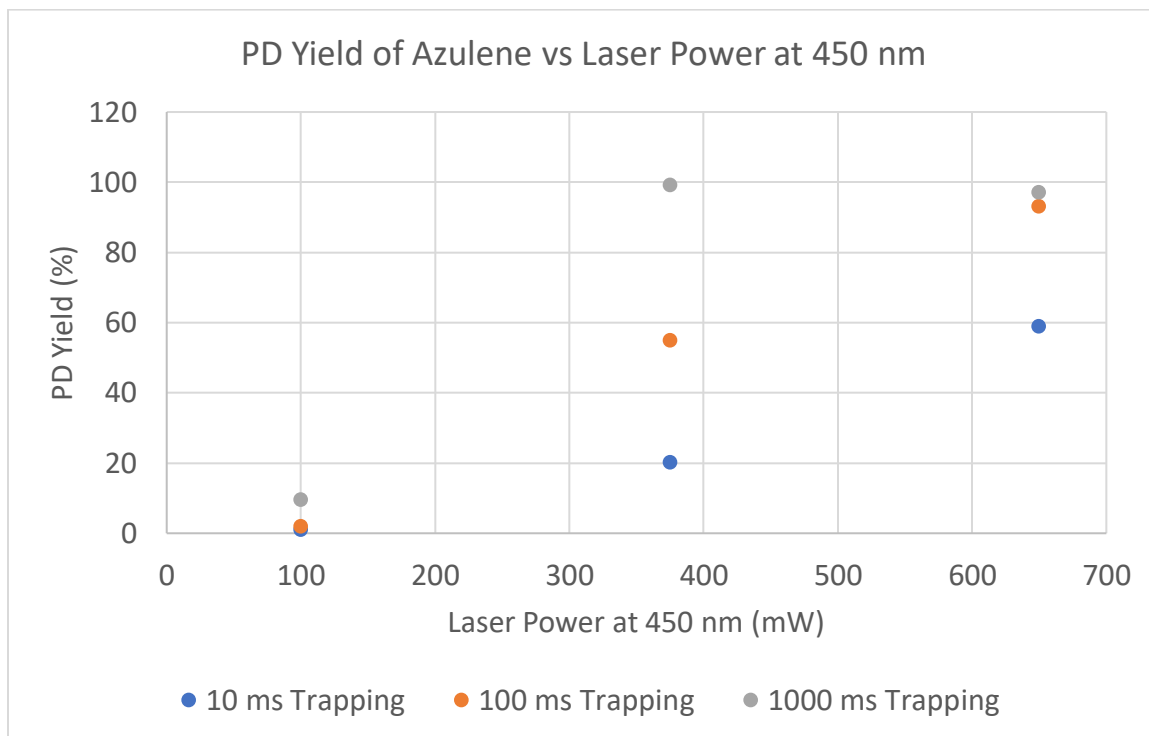


Figure 3.4: PD yield of azulene vs laser power at 450 nm vs different laser powers and trapping times.

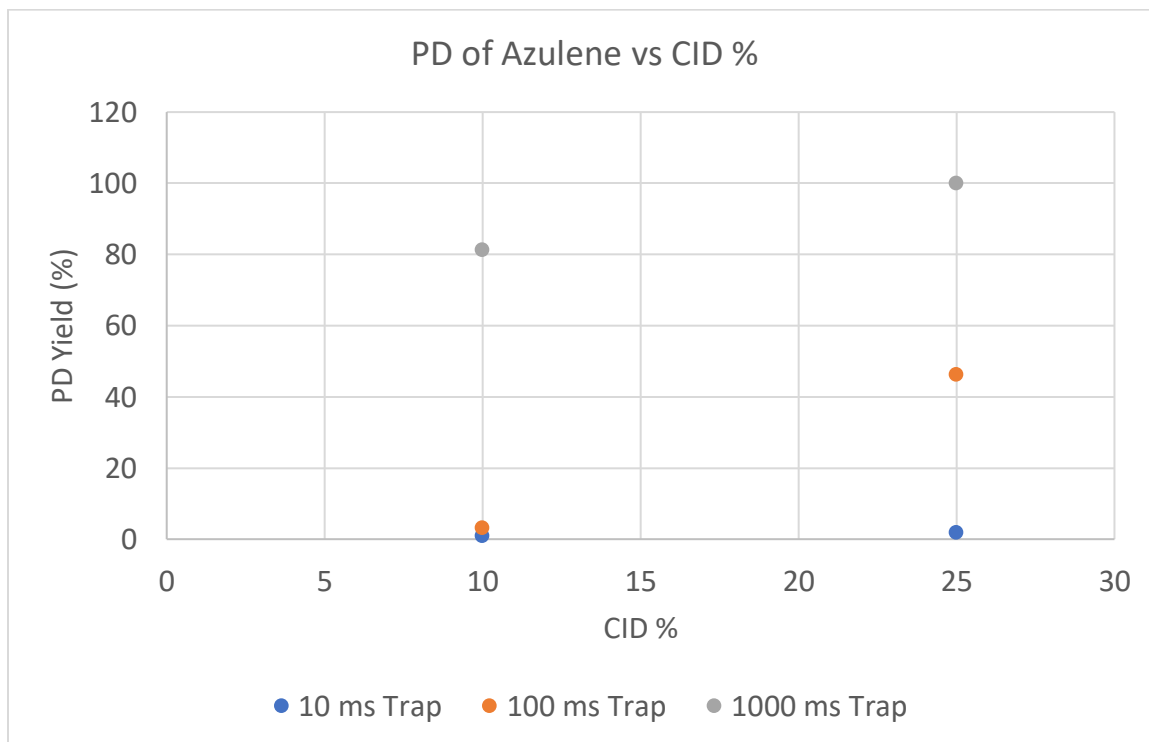


Figure 3.5: Plot of photodissociation yield vs CID % for different trapping times.

The plots for azulene and naphthalene all have the same fragment peaks, but the parent/fragment ratios differ. Below is a spectrum at 450 nm of azulene at higher laser power and varying the irradiation time.

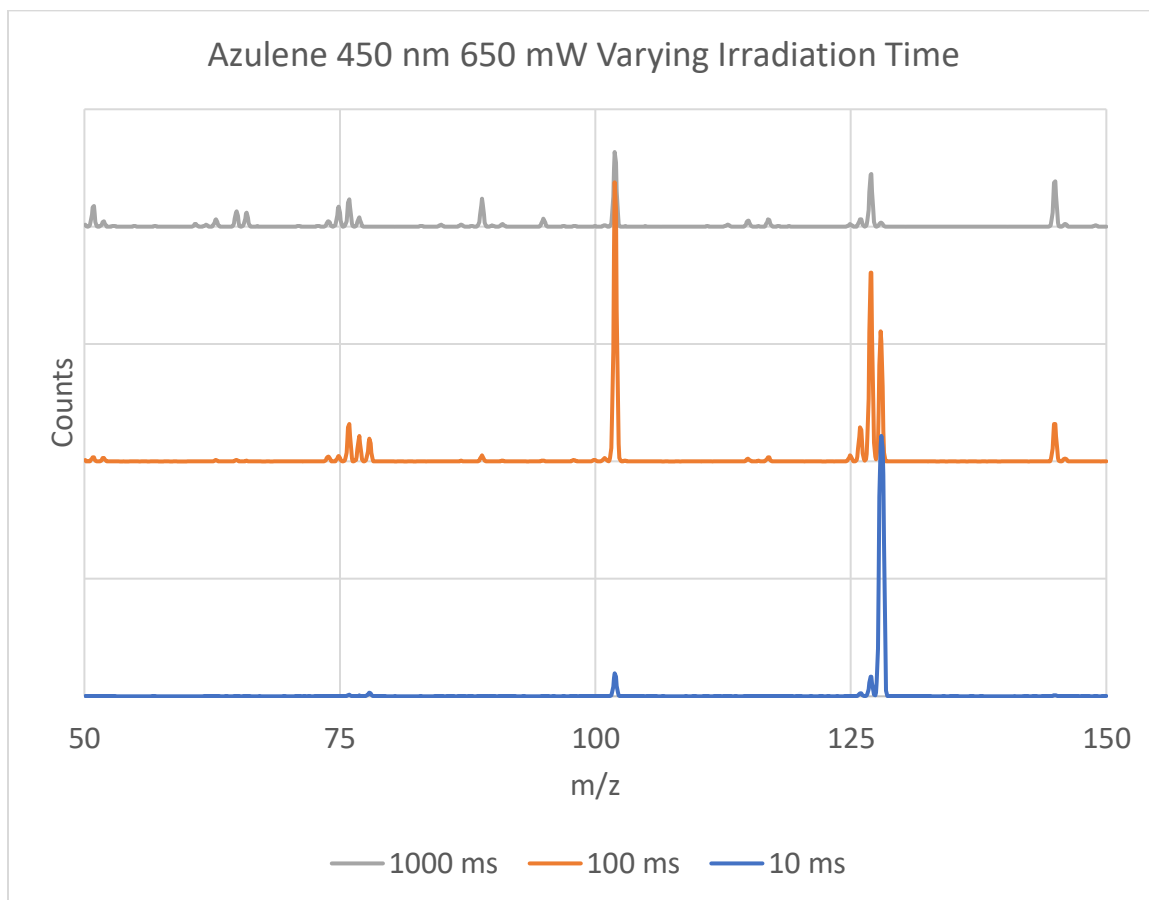


Figure 3.6: Mass spectrum vs different irradiation times to 450 nm 650 mW light. All plots normalized to same value.

The plot of high power 650 mW at 450 nm and a short trap time of 10 ms shows some H atoms are removed in an H loss pathway. This pathway does not result in the complete deprotonation of the Azu^+ cation, but up to -3H loss is seen at medium trap times. A significant decomposition pathway is the formation of $m/z = 102$, which is Azu^+ with a loss of C_2H_2 . A second C_2H_2 loss at $m/z = 76$ (C_6H_6^+) can also be seen to form deprotonated benzene, as well as species corresponding to loss of C_2H and C_2 at $m/z = 77$

(C_6H_5^+) and 78 (C_6H_6^+). The peak at $m/z = 145$ is $M + 17$, which could be a chemical reaction at longer trap times forming hydroxy-azulene from water attaching to the electrophilic azulene pentyl ring.

At high laser powers and long trapping times the parent peak is significantly reduced compared to 127, but with low counts overall. Groups of C_n , $4 \leq n \leq 8$ can be seen, but with little signal seen at C_9 clusters, this suggests a competition between H and C_2H_2 removal. No evidence of concerted H_2 loss is seen, unlike in coronene.

Plotting the spectrum vs laser power yields significantly more fragmentation and variety of species for azulene vs naphthalene. Counts are normalized to $m/z = 128$.

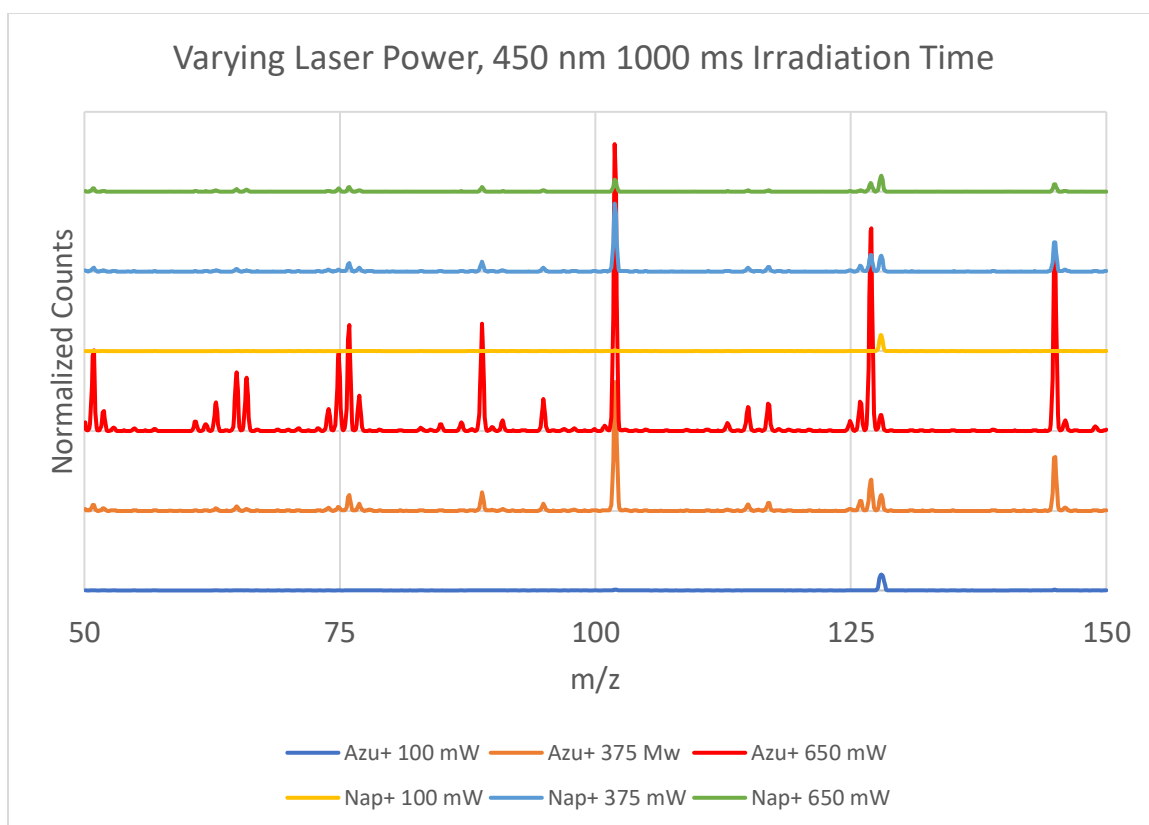


Figure 3.7: Mass spectrum vs varying laser power at 1000 ms trapping time for Azu^+ and Nap^+ . All plots normalized to same value.

A major difference in the fragmentation pattern was seen between the CID and laser irradiation spectra. Similar to coronene, laser irradiation removes specific moieties from a molecule, while CID produces low concentrations of fragments across the mass spectrum.

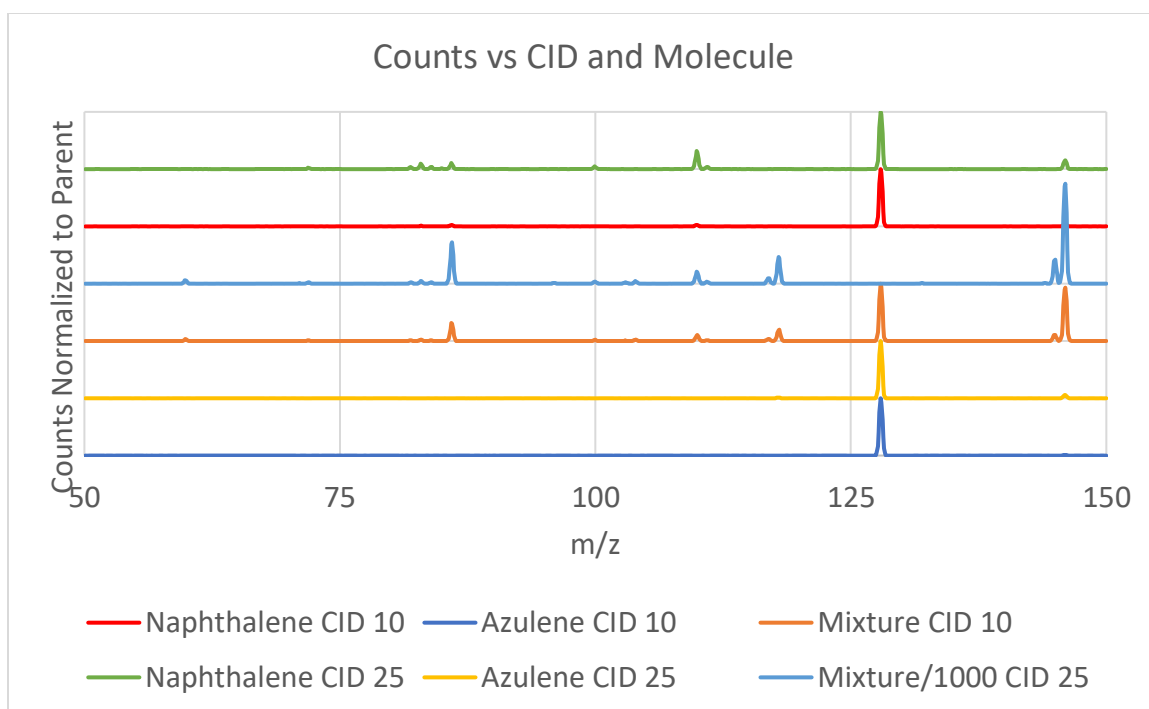


Figure 3.8: Mass spectrum vs CID percentage and molecule.

While the differences are present between the Nap^+ and Azu^+ spectra, the differences are more pronounced using photofragmentation, making photofragmentation a more sensitive technique. The CID spectra of the 50-50 mixture rules out using the spectrum for quantitative component analysis. The peak at $m/z = 86$ and 118 in the mixture is not seen as prominently in either pure compound. The parent peak is depleted in higher CID for the mixture, while neither component's parent peak is depleted as severely. Because of these differences, CID cannot be quantitative for this ion mixture.

Looking at to photofragmentation under the same conditions, the same peaks can be seen for both Azu^+ and Nap^+ , with the primary difference the ratio of the parent to product peaks. Trying to match both peak's intensities yields the following spectrum.

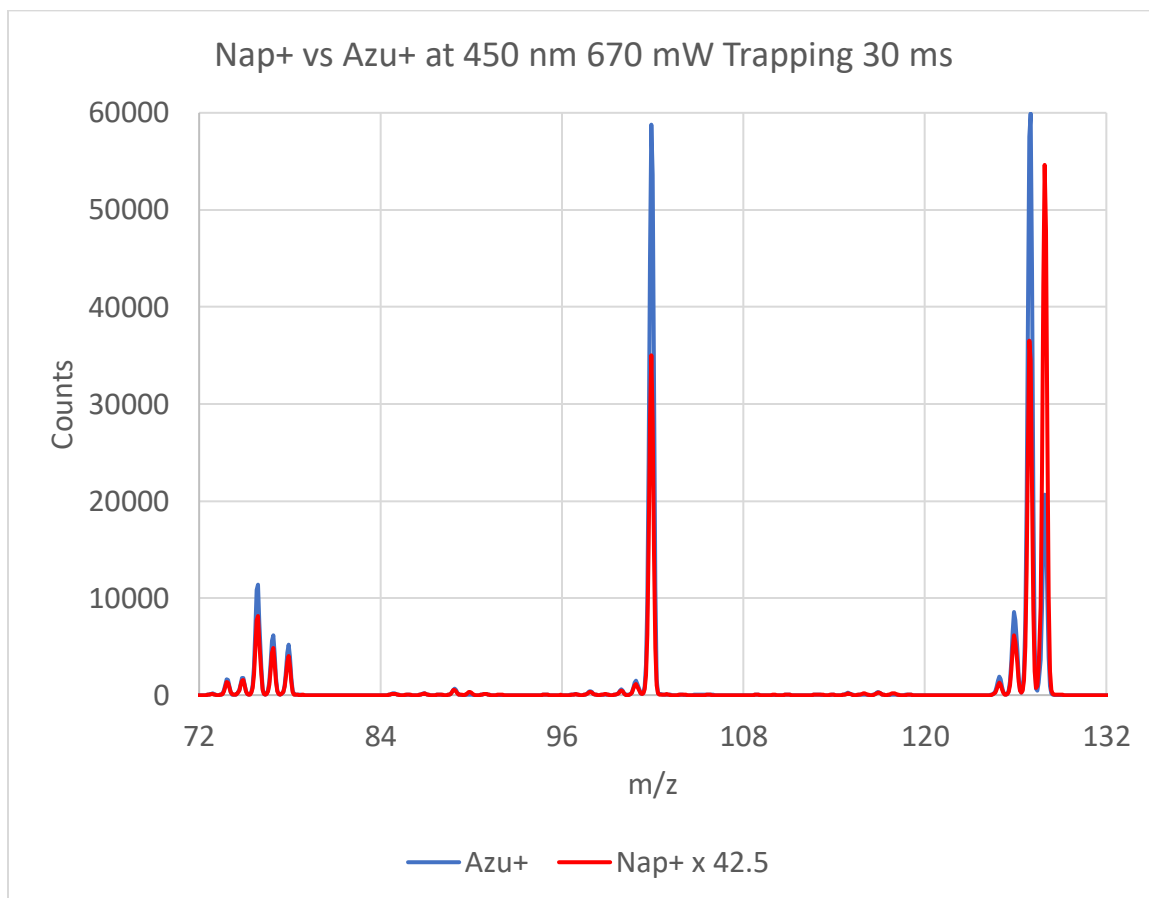


Figure 3.9: Azu^+ and Nap^+ overlayed at scaling value to minimize sum of squares.

A least-squares regression was found the best scaling factor to overlay the Nap^+ and Azu^+ fragmentation spectra. For azulene, the parent is about 1/3 the intensity of the nearly equal $m/z = 102$ and 127 peaks, while for naphthalene, the parent $m/z = 128$ peak is about 1.5X the intensity of the nearly equal $m/z = 102$ and 127 peaks. Two peaks are sufficient to correctly determine a mixture of these two compounds, so the ratio of azulene to naphthalene in a mixture should be obtainable. However, because azulene is

42.5X more sensitive to this method than naphthalene, this technique should have maximum precision when azulene is approximately 2.3% of the total mixture.

A series of isomer mixtures of dilute azulene in naphthalene was prepared. The samples were irradiated for 1000 ms at 300 mW to allow sufficient fragmentation. Mixture and pure compound standards were alternated to reduce instrument drift. The following fit was used.

$$mix^+(m) = f \times Nap^+(m) + (1 - f) \times Azu^+(m)$$

The normalized mixture counts were fit to the algebraic sum of the two pure normalized analyte spectra. The normalization constant for each spectrum was the maximum parent ion counts at $m/z = 128$. All three spectra were a function of m/z value m , and a least-squares fit to determine the optimal value of f was performed. The one-parameter model f is the fraction of the mixture spectrum attributed to Nap^+ . The uncertainty in f is $\sqrt{\chi^2}$, the sum of the squared errors for each value of m for each mixture fit.

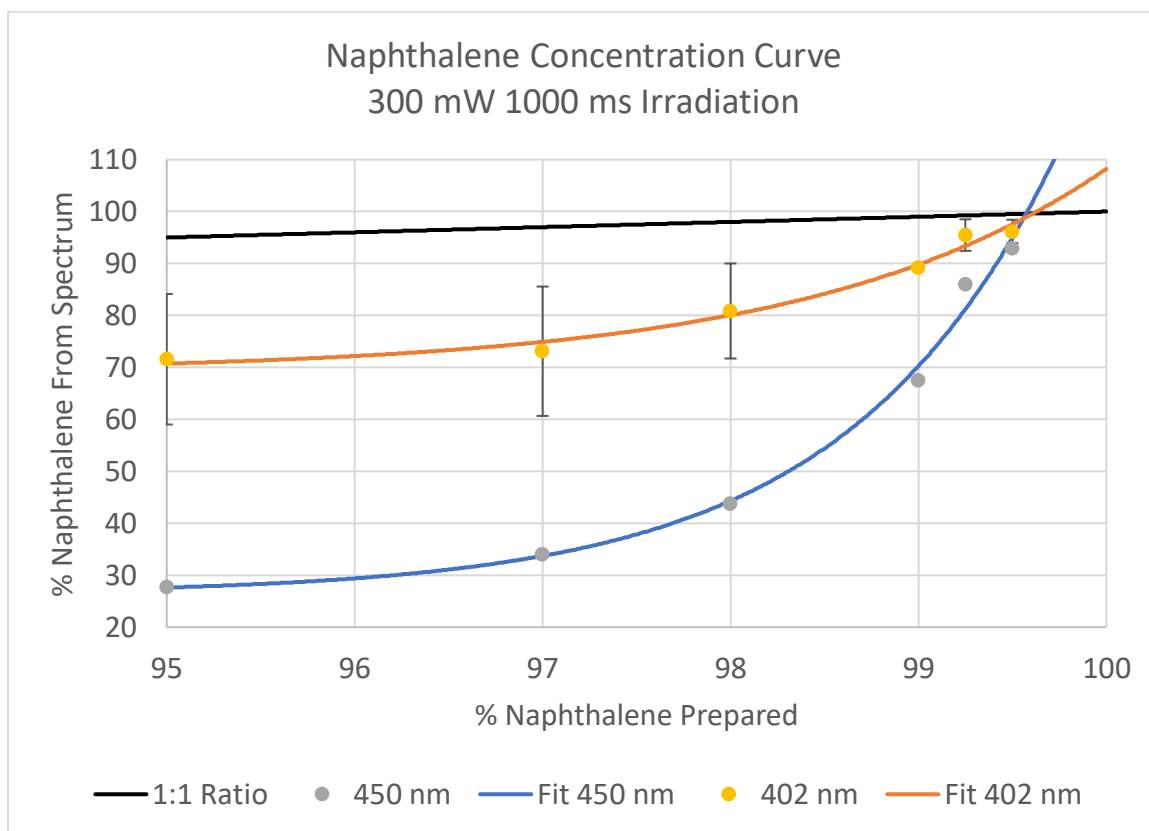


Figure 3.10: Plot of naphthalene concentration derived from spectrum vs naphthalene concentration in the prepared sample.

The data points for both 402 and 450 nm form a monotonically increasing curve, which is well-modeled by an exponential function. Specifically, the following fit of the ratio points was used:

$$f_{fit}(\% \text{ nap measured}) = A \exp\left(\frac{\% \text{ nap prepared} - 95\%}{\tau}\right) + b$$

The offset of 95% was arbitrary but results in the same τ and b values. The fitting constants are given below.

Table 3.3: Fitting constants for exponential fit at both wavelengths.

Parameter (All %)	402 nm	450 nm
A	0.0162	0.0122
τ	1.570	1.117
b	0.691	0.264
χ^2	0.0011	0.0035

These curves show at both wavelengths, the percentage of naphthalene in an unknown sample can be determined against a calibration curve. The uncertainty in the concentration determination is greatest at higher naphthalene concentrations, because the unknown spectrum is dominated by the contribution from azulene. The non-linear dependence between measured and prepared isomer ratios likely is related to the gas-phase ionization and vapor pressure differences between the ions. The measured ion spectrum is likely representative of the ion trap's ion composition. As predicted above, the quantification of these particular isomers is effective around 0 – 2% azulene; an isomer pair with more similar ionization efficiencies likely would allow for a greater dynamic range for quantification.

Discussion:

The choice of naphthalene and azulene as an isomeric pairs was made because both molecules ionize with DART easily and show differing absorption in the visible spectrum, where laser diode sources are inexpensive and robust. The fragmentation patterns and trends with laser power and trap time seen are consistent with the results from the visible photodissociation of coronene, and with results from Jochims and Castellanos.^{28,29} At this low PAH size, C₂H₂ fragmentation is a dominant dissociation pathway, and can be observed to happen twice resulting in the C₆H₄⁺ ion. H loss proceeds through single H loss, not through H₂, because the Nap⁺ and Azu⁺ ions have fewer

degrees of freedom in which to redistribute internal energy. The increased internal energy allows for the entropically-favored H dissociation.

Many of the spectra between the Nap⁺ and Azu⁺ ions contain similar patterns and features; this is likely due to internal isomerization. Isomerization from Azu⁺ to Nap⁺ is energetically favorable with a release of – 18.5 kcal/mol (0.80 eV).²⁵ Dyakov predicts at least 6 isomerization channels and 8 different dissociation pathways are available for Azu⁺, depending on internal energy.²⁵ Not accounting for energy added during ionization, the most probable paths are the so-called bicyclobutane mechanism (47%), the norcaradiene-vinylidene mechanism (47%), and the methylene walk (5%) pathways.²⁵

The quantification method was effective; this is the first use of the combination of DART and photodissociation combined for quantification. While DART has been used quantitatively,^{1,30,31} the technique has more often been used to look at the range of analytes in a sample, from which information can be gleaned. DART has been used analytically to measure the concentration of a particular analyte in a mixture, but has not been used to analyze isomeric compounds.^{1,30,31} Like any other mass-spectrometry technique, requires a standard curve to be made. In the results presented here, the curve is exponential, likely due to different rates of photodissociation of each isomeric ion. The calibration curve is most sensitive in the <1% azulene range, and is ineffective once the azulene concentration is >5%.

The lower exponential decay of 1.41:1 with decreasing naphthalene concentration for 402:450 nm is consistent with a lower cross section of Azu⁺ vs Nap⁺ at 402 vs 450 nm, since less photofragmentation occurs. Given the lower fit b value, another explanation for the greater photodissociation percentage of Azu⁺ at 450 nm is with a

larger cross section, less light and focusing is needed in the ion trap to induce photodissociation. Less intense light allows trapped ions on trajectories not intersecting the laser's focal point to photodissociate. The focused light may have helped achieve a required photon intensity to allow for non-linear photodissociation processes to occur, which occurs regardless at relatively low laser intensities because of cw-operation. The naphthalene cation in this wavelength region has a fairly smooth decrease in cross-section of about 30% as wavelength scans from 402 – 450 nm in matrix isolation experiments,²⁷ therefore scanning from 402 – 450 nm, the cross-section of gas phase Nap⁺ should decrease. However, the azulene to naphthalene cation cross section ratios would also be expected to decrease.

Conclusion:

Photodissociation was successfully performed on the cations of structural isomers azulene and naphthalene at 450 and 402 nm using the DART ion source and compact cw-diode lasers. Trends in laser power, wavelength, and ion trapping time were consistent with previous work in understanding the photodissociation process for small PAH molecules. A quantitative calibration curve for determining a mixture composed of two isomers using photoionization was obtained at both wavelengths, which was found to be both quantitative and exhibit wavelength-dependence. The prospect of a quantifiable photodissociation method with wavelength, power, and temporal tunability expands the potential applications for both DART ionization and photoionization as analytic techniques, allowing another dimension of tunability for isomer mixture determination.

Acknowledgments:

The above work was funded by the NASA PICASSO award 80NM0018D0004. A special thanks to fellow graduate student Tyler Nguyen for helping me collect data, as well as Dr. Deacon Nemchick and Dr. Frank Maiwald at JPL. well as Professor Jack Beauchamp and Dr. Rob Hodyss for additional mentorship and advice.

References:

- (1) Gross, J. H. Direct Analysis in Real Time—a Critical Review on DART-MS. *Anal Bioanal Chem* **2014**, 406 (1), 63–80. <https://doi.org/10.1007/s00216-013-7316-0>.
- (2) Urban, P. L. Quantitative Mass Spectrometry: An Overview. *Philos Trans A Math Phys Eng Sci* **2016**, 374 (2079), 20150382. <https://doi.org/10.1098/rsta.2015.0382>.
- (3) Cody, R. B.; Laramée, J. A.; Nilles, J. M.; Durst, H. D. Direct Analysis in Real Time (DARTtm) Mass Spectrometry. *JEOL News* **2005**, 40 (1), 8–12.
- (4) Wörner, T. P.; Aizikov, K.; Snijder, J.; Fort, K. L.; Makarov, A. A.; Heck, A. J. R. Frequency Chasing of Individual Megadalton Ions in an Orbitrap Analyser Improves Precision of Analysis in Single-Molecule Mass Spectrometry. *Nat. Chem.* **2022**, 14 (5), 515–522. <https://doi.org/10.1038/s41557-022-00897-1>.
- (5) Glish, G. L.; Vachet, R. W. The Basics of Mass Spectrometry in the Twenty-First Century. *Nat Rev Drug Discov* **2003**, 2 (2), 140–150. <https://doi.org/10.1038/nrd1011>.
- (6) Johnson, A. R.; Carlson, E. E. Collision-Induced Dissociation Mass Spectrometry: A Powerful Tool for Natural Product Structure Elucidation. *Anal. Chem.* **2015**, 87 (21), 10668–10678. <https://doi.org/10.1021/acs.analchem.5b01543>.
- (7) Brodbelt, J. S. Photodissociation Mass Spectrometry: New Tools for Characterization of Biological Molecules. *Chem Soc Rev* **2014**, 43 (8), 2757–2783. <https://doi.org/10.1039/c3cs60444f>.
- (8) R Julian, R. The Mechanism Behind Top-Down UVPD Experiments: Making Sense of Apparent Contradictions. *J Am Soc Mass Spectrom* **2017**, 28 (9), 1823–1826. <https://doi.org/10.1007/s13361-017-1721-0>.
- (9) Bonner, J.; Lyon, Y. A.; Nellessen, C.; Julian, R. R. Photoelectron Transfer Dissociation Reveals Surprising Favorability of Zwitterionic States in Large Gaseous Peptides and Proteins. *J. Am. Chem. Soc.* **2017**, 139 (30), 10286–10293. <https://doi.org/10.1021/jacs.7b02428>.
- (10) Freiser, B. S.; Beauchamp, J. L. *Acid-base properties of molecules in excited electronic states utilizing ion cyclotron resonance spectroscopy*. ACS Publications. <https://doi.org/10.1021/ja00452a003>.
- (11) Maitre, P.; Scuderi, D.; Corinti, D.; Chiavarino, B.; Crestoni, M. E.; Fornarini, S. Applications of Infrared Multiple Photon Dissociation (IRMPD) to the Detection of Posttranslational Modifications. *Chem. Rev.* **2020**, 120 (7), 3261–3295. <https://doi.org/10.1021/acs.chemrev.9b00395>.

- (12) Marlton, S. J. P.; Trevitt, A. J. The Combination of Laser Photodissociation, Action Spectroscopy, and Mass Spectrometry to Identify and Separate Isomers. *Chem. Commun.* **2022**, 58 (68), 9451–9467. <https://doi.org/10.1039/D2CC02101C>.
- (13) Baer, T.; Dunbar, R. C. Ion Spectroscopy: Where Did It Come From; Where Is It Now; and Where Is It Going? *Journal of the American Society for Mass Spectrometry* **2010**, 21 (5), 681–693. <https://doi.org/10.1016/j.jasms.2010.01.028>.
- (14) Palmer, P. T.; Limero, T. F. Mass Spectrometry in the U.S. Space Program: Past, Present, and Future. *Journal of the American Society for Mass Spectrometry* **2001**, 12 (6), 656–675. [https://doi.org/10.1016/S1044-0305\(01\)00249-5](https://doi.org/10.1016/S1044-0305(01)00249-5).
- (15) Cabane, M.; Coll, P.; Szopa, C.; Israël, G.; Raulin, F.; Sternberg, R.; Mahaffy, P.; Person, A.; Rodier, C.; Navarro-González, R.; Niemann, H.; Harpold, D.; Brinckerhoff, W. Did Life Exist on Mars? Search for Organic and Inorganic Signatures, One of the Goals for “SAM” (Sample Analysis at Mars). *Advances in Space Research* **2004**, 33 (12), 2240–2245. [https://doi.org/10.1016/S0273-1177\(03\)00523-4](https://doi.org/10.1016/S0273-1177(03)00523-4).
- (16) Vasavada, A. R. Mission Overview and Scientific Contributions from the Mars Science Laboratory Curiosity Rover After Eight Years of Surface Operations. *Space Sci Rev* **2022**, 218 (3), 14. <https://doi.org/10.1007/s11214-022-00882-7>.
- (17) Shi, Y.; Zhou, M.; Kou, M.; Zhang, K.; Zhang, X.; Kong, X. Simultaneous Quantitative Chiral Analysis of Four Isomers by Ultraviolet Photodissociation Mass Spectrometry and Artificial Neural Network. *Front Chem* **2023**, 11, 1129671. <https://doi.org/10.3389/fchem.2023.1129671>.
- (18) Malaska, M. J.; Hodyss, R. Dissolution of Benzene, Naphthalene, and Biphenyl in a Simulated Titan Lake. *Icarus* **2014**, 242, 74–81. <https://doi.org/10.1016/j.icarus.2014.07.022>.
- (19) Zhao, L.; Kaiser, R. I.; Xu, B.; Ablikim, U.; Ahmed, M.; Evseev, M. M.; Bashkurov, E. K.; Azyazov, V. N.; Mebel, A. M. Low-Temperature Formation of Polycyclic Aromatic Hydrocarbons in Titan’s Atmosphere. *Nature Astronomy* **2018**, 2 (12), 973–979. <https://doi.org/10.1038/s41550-018-0585-y>.
- (20) Northon, K. *NASA’s Dragonfly Mission to Titan Will Look for Origins, Signs of Life*. NASA. <http://www.nasa.gov/press-release/nasas-dragonfly-will-fly-around-titan-looking-for-origins-signs-of-life> (accessed 2023-05-26).
- (21) Scott, C. J.; Ozimek, M. T.; Adams, D. S.; Lorenz, R. D.; Bhaskaran, S.; Ionasescu, R.; Jesick, M.; Laipert, F. E. Preliminary Interplanetary Mission Design and Navigation for the Dragonfly New Frontiers Mission Concept. 21.
- (22) Tao, T.; Fan, Y.; Zhao, J.; Yu, J.; Chen, M.; Huang, W. Reversible Alteration of Spectral Properties for Azulene Decorated Multiphenyl-Ethylenes by Simple Acid-

- Base and Redox Processes. *Dyes and Pigments* **2019**, *164*, 346–354. <https://doi.org/10.1016/j.dyepig.2019.01.054>.
- (23) Lewis, J. W.; Nauman, R. V. Azulenium Cations. An Experimental and Theoretical Study of the Cations Derived from Hydrocarbon Derivatives of Azulene. *Can. J. Chem.* **1985**, *63* (7), 2081–2085. <https://doi.org/10.1139/v85-343>.
- (24) Shida, Tadamasa.; Iwata, Suehiro. Electronic Spectra of Ion Radicals and Their Molecular Orbital Interpretation. III. Aromatic Hydrocarbons. *J. Am. Chem. Soc.* **1973**, *95* (11), 3473–3483. <https://doi.org/10.1021/ja00792a005>.
- (25) Dyakov, Yu. A.; Ni, C.-K.; Lin, S. H.; Lee, Y. T.; Mebel, A. M. Ab Initio and RRKM Study of Photodissociation of Azulene Cation. *Phys. Chem. Chem. Phys.* **2006**, *8* (12), 1404. <https://doi.org/10.1039/b516437k>.
- (26) Bally, T.; Carra, C.; Fülcher, M. P.; Zhu, Z. Electronic Structure of the Naphthalene Radical Cation and Some Simple Alkylated Derivatives. *J. Chem. Soc., Perkin Trans. 2* **1998**, No. 8, 1759–1766. <https://doi.org/10.1039/a802861c>.
- (27) Szczepanski, J.; Roser, D.; Personette, W.; Eyring, M.; Pellow, R.; Vala, M. Infrared Spectrum of Matrix-Isolated Naphthalene Radical Cation. *J. Phys. Chem.* **1992**, *96* (20), 7876–7881. <https://doi.org/10.1021/j100199a010>.
- (28) Jochims, H. W.; Ruhl, E.; Baumgartel, H.; Tobita, S.; Leach, S. Size Effects on Dissociation Rates of Polycyclic Aromatic Hydrocarbon Cations: Laboratory Studies and Astrophysical Implications. *ApJ* **1994**, *420*, 307. <https://doi.org/10.1086/173560>.
- (29) Castellanos, P.; Candian, A.; Zhen, J.; Linnartz, H.; Tielens, A. G. G. M. Photoinduced Polycyclic Aromatic Hydrocarbon Dehydrogenation The Competition between H- and H₂-Loss. *A&A* **2018**, *616*, A166. <https://doi.org/10.1051/0004-6361/201833220>.
- (30) Hajslova, J.; Cajka, T.; Vaclavik, L. Challenging Applications Offered by Direct Analysis in Real Time (DART) in Food-Quality and Safety Analysis. *TrAC Trends in Analytical Chemistry* **2011**, *30* (2), 204–218. <https://doi.org/10.1016/j.trac.2010.11.001>.
- (31) Cody, R. B.; Dane, A. J. Dopant-Assisted Direct Analysis in Real Time Mass Spectrometry with Argon Gas. *Rapid Communications in Mass Spectrometry* **2016**, *30* (10), 1181–1189. <https://doi.org/10.1002/rcm.7552>.

Kinetic Isotope Effect of O(¹D) and Methane

Abstract:

In this chapter, we introduce upgrades to an existing near-IR cavity ring-down spectroscopic instrument and standardize sample preparation to avoid unwanted isotope separation. The KIE of CH₂D₂ was measured for the first time via flash photolysis, as well as the remeasurement of ¹³CH₄ and CH₃D + O(¹D). Spectroscopic parameters of unlisted molecules to improve line shape fitting could be determined, as well as absorption profiles for molecules not recorded as having transitions in the 5996 – 6014 cm⁻¹ and 6450 – 6248 cm⁻¹ regions.

Introduction:

Atmospheric methane is the second most important greenhouse gas to radiative forcing in Earth's atmosphere,¹ and has nearly 20 times the warming power compared to CO₂.¹ Atmospheric methane has also more than doubled from preindustrial levels of 0.7 ppm to over 1.8 ppm.² Methane plays an important role in both stratospheric and tropospheric chemistry. In the troposphere, CH₄ is the most abundant hydrocarbon, and is an important precursor to carbon monoxide, formaldehyde, and ozone.³ In the stratosphere methane oxidation is the main source of water which increases at higher altitudes,⁴ and impacts stratospheric HO_x (OH and HO₂) abundances.

Sources of methane are either natural or anthropogenic, and the budgets of these different types of sources and their respective sinks, both globally and locally, have high uncertainty.² Each source and sink processes imparts a distinct isotopic signature onto the existing isotopic ratio,^{5,6} typically indicative of the chemical mechanism of formation or destruction. One such mechanism is destruction by the O(¹D) radical in earth's stratosphere,⁷ occurring when tropospheric air mixes with the lower stratosphere. This isotopic signature can superimpose on other aging signatures, complicating source attribution and carbon cycling studies.^{2,6}

Besides the terrestrial atmosphere, *in situ* measurement of Martian methane by NASA's mobile space laboratory have prompted questions about the sources and sinks of methane on Mars.⁸⁻¹⁰ Methane (CH₄) has been detected in the Martian atmosphere, with a measured upper range of 5 – 19 ppbv for observations in the nighttime surface boundary layer,¹¹ but <0.05 ppbv for remote sensing observations a few km above the surface.¹² Methane is thus being created and either destroyed or reabsorbed into the regolith on

timescales of weeks, rather than hundreds of years predicted from atmospheric chemical destruction.¹³ Proposed mechanisms have been adsorption to weathered silica,¹⁴ adsorption into the regolith,^{15,16} or oxidation on UV-activated perchlorate salts.¹³ Each would leave a distinct methane isotopic signature to be further changed via oxidation with atmospheric oxidants, among them O(¹D) produced from O₃. With a maximum of 0.45 ppmv O₃ in the Martian atmosphere,^{17,18} O(¹D) could be a significant source of methane oxidation, especially considering the reaction with OH, the main methane oxidant on Earth, is much slower at Martian temperatures.¹⁹

To provide data for modelling and field studies, the oxidation of methane with O(¹D) and the imparted isotope effect (KIE) is carried out in this study. The reactions of the most common substituted isotopologues, ¹³CH₄ and ¹²CH₃D, were remeasured via flash photolysis to provide confirmation to previously-measured but incompatible KIE values using simple and low reactant-depletion chemistry. Detection was performed using near-infrared frequency-stabilized cavity ring-down spectroscopy (FS-CRDS), a sensitive direct absorption technique using a high-finesse optical cavity.²⁰ Experimental results will provide a first estimate for the KIE of the rare CH₂D₂ isotopologue, allowing its potential future use for isotopic signatures of field samples.

Experimental:

A typical kinetic isotope effect (KIE) experiment seeks to measure the ratio of the kinetic rates of reaction of the predominant ¹²CH₄ isotopologue versus a substituted methane isotopologue, doing so by measuring the initial and final concentrations of both isotopologues. The reaction takes place in a temperature-controlled static cell undergoing

flash photolysis, with methane depletion kept low to suppress secondary chemistry. The KIE value for say $^{12}\text{CH}_3\text{D} + \text{O}(^1\text{D})$ is as follows:

$$\text{KIE} = \frac{k(^{12}\text{CH}_4)}{k(^{12}\text{CH}_3\text{D})} = \frac{\ln([^{12}\text{CH}_4]_{\text{rxn}}/[^{12}\text{CH}_4]_{\text{ref}})}{\ln([^{12}\text{CH}_3\text{D}]_{\text{rxn}}/[^{12}\text{CH}_3\text{D}]_{\text{ref}})}$$

First, a mixture of methane isotopologues, the $\text{O}(^1\text{D})$ photolytic precursor N_2O , and He is made which has to simultaneously fulfill several requirements. First is the methane isotopologue concentrations, which for the FS-CRDS apparatus should have a loss of ideally 100 – 200 ppm. Because isotopically pure methane samples are available, mixtures enriched in the rare isotopologue allows both isotopologues to show appreciable absorption within the bandwidth of our two available lasers between 5996 – 6011 cm^{-1} and 6251 – 6467 cm^{-1} . Both methane isotopologue absorption peaks should ideally be singlet peaks without any overlapping peaks from the same molecule, the other methane isotopologue, or N_2O . This endeavor is complicated by the fact the HITRAN database does not have a published list of N_2O absorption lines in our lasers' wavelength bandwidths. The N_2O concentration should ideally be 10X the total methane concentration, to ensure that the ~1% photolysis of N_2O per 193 nm ArF excimer pulse produces 10X less $\text{O}(^1\text{D})$ than methane. Further, N_2O reacts with $\text{O}(^1\text{D})$ to produce NO, which scavenges any OH formed as a product of $\text{CH}_4/\text{CH}_3\text{D} + \text{O}(^1\text{D}) \rightarrow \text{CH}_3 + \text{OH}$, the most common reaction pathway with a branching ratio of 0.75.

The total pressure must also be greater than approximately 20 torr in the photolysis cells to allow for the $\text{O}(^1\text{D})$ to translationally cool to the reaction temperature efficiently, and the concentration of He must be approximately 10X greater than the rest of the reactants. He is chosen as the balancing gas because the reaction $\text{O}(^1\text{D}) + \text{He} \rightarrow$

$O(^3P) + He^*$ is not efficient, unlike most other balancing gases, but a downside is the HITRAN air-broadening and self-broadening pressure parameters are no longer valid for the methane absorption peaks. Further, the concentration of He should be low enough so that after transferring the gases from the reaction cells to the CRDS measurement apparatus, the pressure is not so high to cause pressure broadening to be the dominant line broadening effect.

Weighing these parameters, a kinetic model of the reaction was built using KINTECUS (see appendix) to ensure a low but measurable per-pulse reaction rate of methane with $O(^1D)$ while suppressing secondary reactions between CH_4 and OH .²¹ Typical concentrations are shown below for looking at the KIE of $CH_3D + O(^1D)$.

Table 4.1: Table of conditions for $CH_3D + O(^1D)$ experiment.

Gas	Partial Pressure at 293 K in quartz cells	Total Pressure at 293 K in quartz cells
CH_3D	230 mtorr	230 mtorr
CH_4	200 mtorr	430 mtorr
N_2O	3.30 torr	3.73 torr
He	46.3 torr	50 torr

The above mixture has a lower N_2O :total methane ratio than desired because an N_2O absorption peak not in the HITRAN database slightly overlaps our chosen CH_4 absorption line. A plot of these modeled concentrations is shown below.

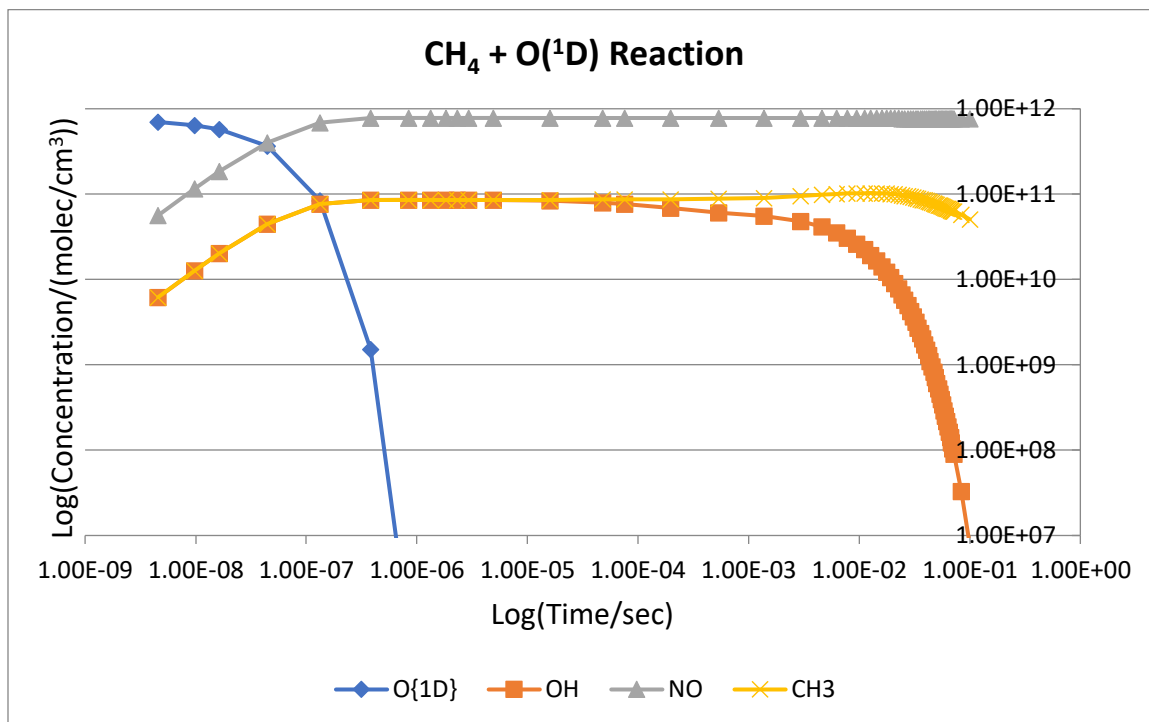


Figure 4.1: Kintecus plot of key species concentration vs time for $\text{CH}_4 + \text{O}(^1\text{D})$ reaction.²¹

While difficult to see on this scale, there are two time regimes in these experiments. First is the reaction of $\text{O}(^1\text{D})$, which occurs $< 1 \mu\text{s}$. The $[\text{NO}]$ concentration grows in while CH_3 and OH depletion effectively drop to 0 in 100 – 200 ms. The fraction of the OH product reacting with NO , OH , and CH_3 (OH does not react with N_2O) vs CH_4 at maximum $[\text{OH}]$ after the first laser pulse is:

$$\frac{k_{\text{NO}+\text{OH}}[\text{NO}] + k_{\text{CH}_3+\text{OH}}[\text{CH}_3] + \frac{1}{2}k_{\text{OH}+\text{OH}}[\text{OH}]}{k_{\text{CH}_4+\text{OH}}[\text{CH}_4]} = 46$$

Initially, most of the OH created reacts with molecules other than CH_4 , and over time the ratio grows larger because $[\text{NO}]$ increases, while $[\text{OH}]$ and $[\text{CH}_3]$ are created and fully reacted before the subsequent laser pulse fires.

To measure the methane concentrations before and after a reaction, FS-CRDS technique will be employed. CRDS uses two highly-reflective mirrors ($R=99.997\%$) to

create an etalon, and once optical power builds beyond a certain threshold, the incoming light from the laser to the cavity is disrupted, allowing the light emanating from the cavity to exponentially decay. The decay rate τ is inversely proportional to the absorption with the following formula.

$$A \pm \Delta A = \frac{1-R}{c} \left(\frac{n_{abs}}{\tau_{abs}} - \frac{1}{\tau_{vac}} \right) \pm \frac{1-R}{c} \sqrt{\frac{n_{abs}^2 \Delta \tau_{abs}^2}{\tau_{abs}^4} + \frac{\Delta \tau_{vac}^2}{\tau_{vac}^4}}$$

Advantages of the technique are sensitivity, being a direct absorption technique, and insensitivity to fluctuations in source intensity noise and to some extent frequency noise, since off-resonant frequencies are filtered by the optical cavity.²² Disadvantages are poor dynamic range and poor coupling efficiency of commonly-available laser sources at high reflectivity. Frequency-stabilization is added to provide a reproducible frequency axis, allowing for better averaging and lower fitting uncertainty.

Mixture creation:

A custom mixing manifold was created to pre-mix the gases prior to introduction into the two static cells, with one cell serving as the photolysis reaction volume and the other as the unreacted reference cell. First, the two quartz cells with compression valves are connected to the manifold via a port not containing a flow-constricting needle valve, which can cause the isotope ratio to change as gas passes through, since heavier isotopologues diffuse more slowly through openings than lighter isotopologues. The cells are evacuated to 1 μ torr, after which the cells are closed off to the manifold. The gases are then added from least to most concentrated, and allowed to mix for 2 min after He is added to homogenize the mixture. The valve to the evacuated cells are then opened, whereby the pressure drops by a factor of 2.02. The valve to the manifold and the

individual cells are left open for at least 5 min to allow the two cells to fully equilibrate, an essential step for the validity of the KIE measurement.

Reaction:

The photolysis cell is then added to a custom temperature-controlled evacuated photolysis chamber, as described in Dr. Think Bui's thesis,²⁰ where the photolysis cell is supported by a liquid nitrogen-cooled copper jacket which is heated by a resistor to maintain a desired temperature. The copper jacket assembly is suspended in a vacuum chamber pumped to < 1 mtorr to suppress condensation. The photolysis cell is then subjected to pulses of 193 nm light from an excimer laser through a quartz window. The reference cell is stored for later use.

First, the excimer is turned on, the lasing mix refilled if necessary, and is allowed to fire for 10 min for the pulse power to stabilize. The laser is not turned off until after the experiment is over but is shuttered to prevent the laser gas from cooling. The power is measured using a Coherent FieldMaxII power meter before the quartz laser window and after the cell to establish the per-pulse power and transmission percentage.

Approximately 10 – 20 data points are collected, with powers of approximately 40 – 80 mJ/pulse typical, with pulse-to-pulse variations of $\pm 1 - 2$ mJ/pulse. The per-pulse power is converted into a methane and N₂O depletion percentage per pulse, which is empirically derived by estimating a 0.017% depletion/pulse for N₂O. Ideally there should be cumulatively 10 – 20% methane depletion.

Next the laser is shuttered, the photolysis cell is added, the chamber closed, evacuated, and allowed to reach temperature, which takes approximately 1 hour. With the quartz window blocked, the power is re-recorded and the number of pulses necessary for

10 – 20% photolysis is verified. The photolysis mixture is then exposed to the laser at high power (26 kV laser discharge voltage) but low repetition rate. At 293 K, 1 second between pulses is sufficient to allow the bleached reacted volume to diffuse and homogenize with the rest of the sample, but at low temperatures around 193 K, 5 seconds is necessary, which requires triggering the excimer laser using an SRS 535 TTL-pulse generator. Once enough photolysis pulses have been recorded, the quartz window is blocked and the pulse power is re-recorded and verified to match the per-pulse power measurement taken before photolysis. Finally, the chamber is opened, allowed to warm-up to room temperature, and the cell removed.

The cell was added to a manifold connected to the CRDS spectrometer, as depicted in Chen *et al.* and seen below.²³ When adding a sample to the spectrometer, the quartz cell is connected via a compression connection. With the vial compression connection closed, the vacuum connection to the manifold is opened and the manifold is allowed to evacuate via an oil-free scroll pump, then the valves to the CRDS cell are opened and the CRDS cavity is allowed to evacuate. Once the pressure reaches 0.5 torr, the CRDS cavity was filled via the needle valve and UHP N₂ or He to 10 torr (measured on a 10 torr capacitance manometer), which was then evacuated and refilled three times. After the last evacuation, the turbomolecular pump was activated, bringing the CRDS cavity to 10 μ torr, after which the valves to the turbomolecular pump were closed.

The cell was then opened and allowed to equilibrate for 5+ minutes to allow for diffusion between the cell and the CRDS cavity. The ring-down time was then measured with the cavity length stabilized to the frequency-stabilization laser (see below). Both the reference and photolysis cells are measured at room temperature. The temperature was

measured at each scan point using a Thorlabs 10k Ω thermistor in thermal contact with the ring-down cavity.

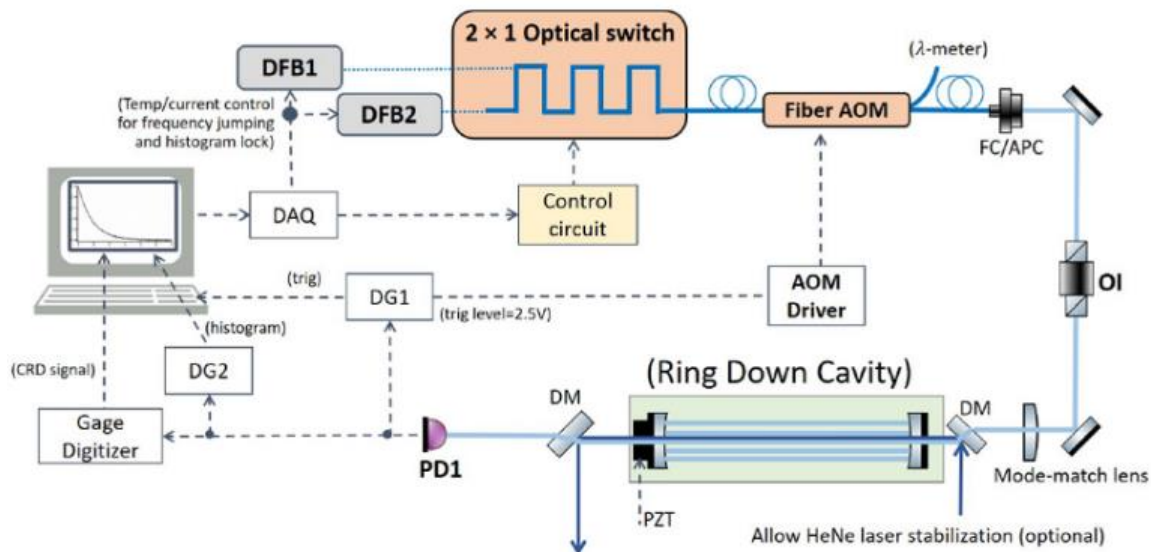


Figure 4.2: The FS-CRDS alignment set-up, from Chen *et al.*²³ with FS laser in dark blue, near-IR in light grey. Abbreviations: (DFB) distributed feedback laser, (AOM) acousto-optic modulator, (OI) optical isolator, (FP/APC) fiber connector/angle polished connector, (DG) delay generator. DFB1 is 5996 – 6014 cm⁻¹, DFB2 is 6450 – 6468 cm⁻¹. The cavity free spectral range (FSR) was measured to be 158.86 ± 0.30 MHz, corresponding to a length of 94.36 ± 0.18 cm.

$$FSR = \frac{c}{2nL}$$

The cavity length is actively stabilized via a frequency-stabilized HeNe laser (in earlier versions) or an iodine-stabilized DFB, which is shown below. The design was inspired by Schuldt *et al.*²⁴ A 633 nm NEK diode is temperature and current tuned (ILX Lightwave LDC-3724B), is split into two counter-propagating beams to act as both pump and probe beams through an iodine vapor cell (Precision Glassblowing TG-ABI-Q). The light is frequency modulated by an AOM, light is focused onto a 2051 New Focus detector, which then demodulated via a SRS SR830 lock-in detector to create an error signal. A New Focus LB1005 servo then current-modulates the 633 nm diode to keep the

error zero. Lock to a single I_2 line in the 33P(6-3) in $B \leftarrow X$ system of I_2 could be maintained for approximately 1 day, and had error comparable to the long-term error of the HeNe previously for frequency-stabilization of the CRDS cavity (Micro-g-LaCoste ML-1) at < 800 kHz (2×10^{-9}) per day.

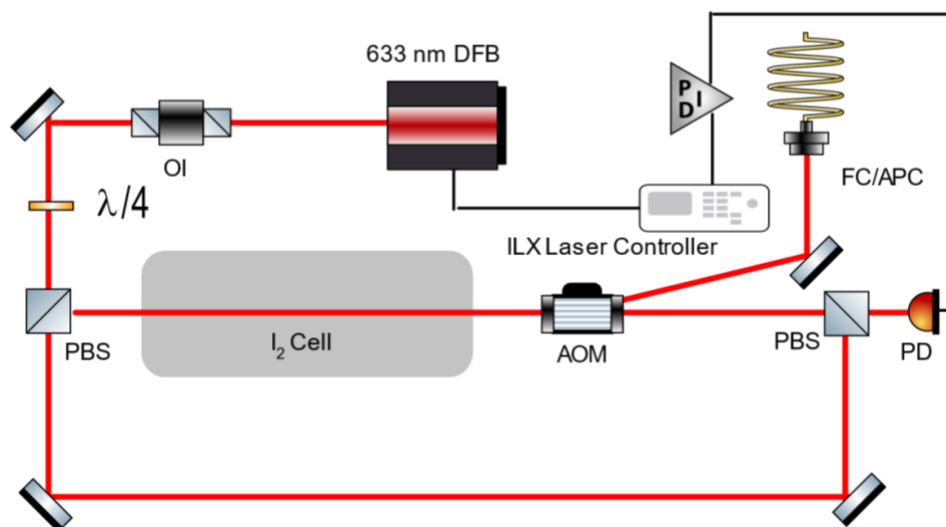


Figure 4.3: Diagram of the I_2 stabilized DFB laser, inspired by Schuldt *et al.*²⁴ (PBS) polarizing beam splitter, other abbreviations same as above. The fiber is attached to a fiber collimator to produce the frequency-stabilization light. Created with Inkscape using optics package by Alexander Franzen.²⁵

The frequency-stabilized light maintains the cavity length through a piezoelectric motor PDH locked using 20.1 MHz sidebands added by an electro-optic modulator (Thorlabs EO-PM-NR-C3). A New Focus 125 MHz heterodyne detector detects the beat signal between the light incident on the optical cavity with the reflected light. An SRS 830 lock-in amplifier extracts the error signal, which is fed to a servo (Vescent) and piezo controller (Thorlabs MDT 693-B). A schematic is shown below.

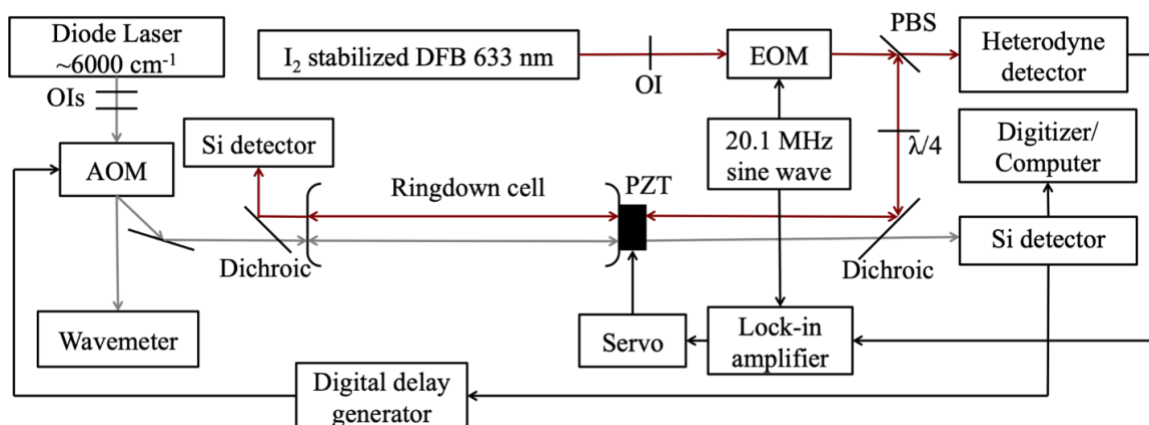
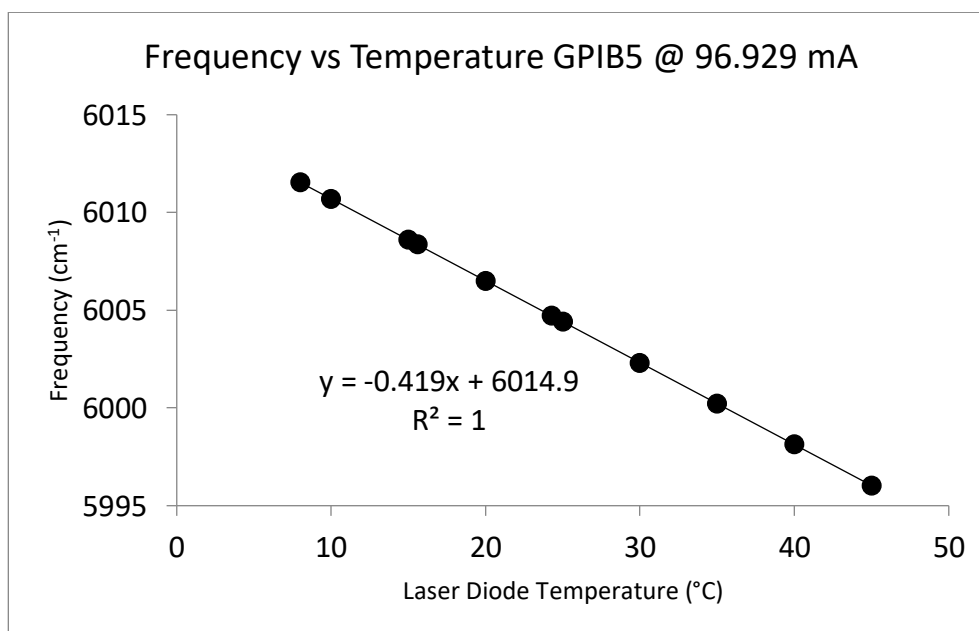


Figure 4.4: Frequency-stabilized 633 nm light in red, near-IR light in grey.

The near-IR probe laser was locked to a cavity mode via a transmission lock. The laser was stepped between cavity modes via temperature tuning the diode (approximately 0.02 °C/FSR), and transmission locking achieved by current tuning the diode (4 mA/FSR). Because of frequency stabilization, future scans could reliably begin at the same frequency and couple to the same cavity mode. Below is a plot of diode temperature vs frequency, taken on a Bristol 621A wavemeter.



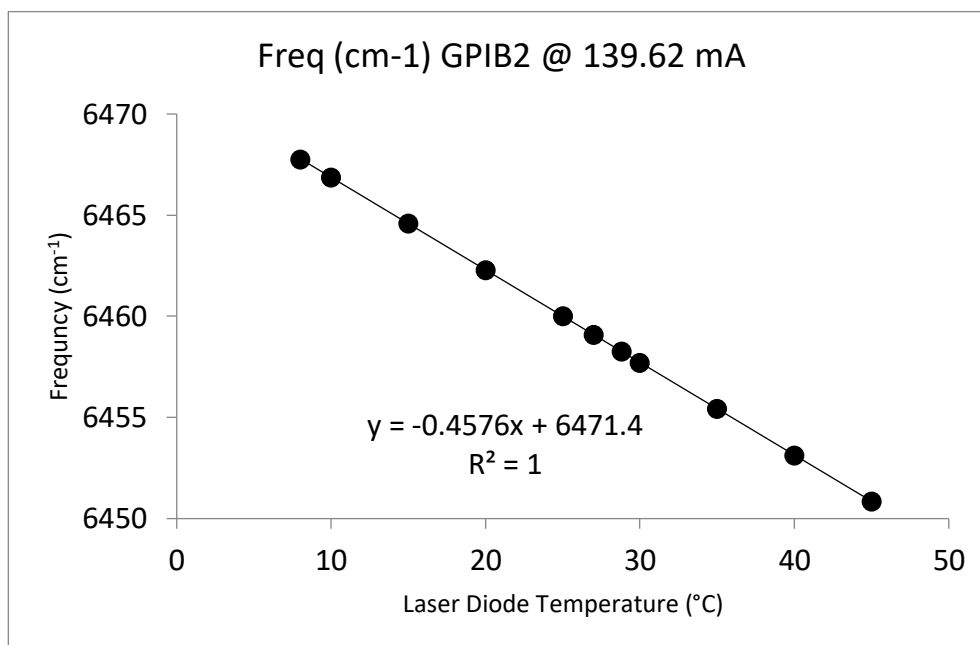


Figure 4.5 and Figure 4.6: Frequency vs laser diode temperature for DFB1 and DFB2.

Data Processing:

For the conditions modeled above, $[\text{CH}_4]$ experiences a 5.8 ppm depletion/(laser pulse power in $\text{mJ} \times \# \text{ pulses}$), equating to a 15% total depletion of CH_4 and 18% depletion of N_2O after 375 laser pulses at 75 mJ/pulse. The greatest experimental difficulty with the experiment lay in finding the isolated absorption features of both CH_4 and CH_3D with 100 – 200 ppm absorption.

The piezoelectric motor on the back of a piezomechanic motor (Piezomechanik) maintains a stable cavity length by correction with an error signal generated by the 633 I_2 -stabilized DFB light reflecting and interfering with light from the optical cavity.

For the different KIE studies, different combinations of absorption peaks were used. The line strength values S , natural abundances, and line centers were taken from the HITRAN 2020 database for those listed ($^{12}\text{CH}_4$, $^{13}\text{CH}_4$, $^{12}\text{CH}_3\text{D}$).²⁶ Line centers and strengths for CH_2D_2 were measured (see Appendix). Line strengths were normalized for

abundance to give a per-molecule S , since isotopically enriched samples were being generated.

Table 4.2: Line center and line strength divided by HITRAN abundance for lines used.

Isotopologue	Line Center (cm^{-1})	S / Abundance ($\text{cm}^{-1} / (\text{molec} \times \text{cm}^{-2})$)
$^{12}\text{CH}_4$	6006.067 (for $^{13}\text{CH}_4$ and $^{12}\text{CH}_3\text{D}$)	6.585×10^{-24}
	6004.863 (for $^{13}\text{CH}_4$)	3.193×10^{-22}
	5995.913 (for $^{12}\text{CH}_2\text{D}_2$)	3.568×10^{-24}
$^{13}\text{CH}_4$	6008.465	5.33×10^{-22}
$^{12}\text{CH}_3\text{D}$	6458.327	1.756×10^{-23}
$^{12}\text{CH}_2\text{D}_2$	5996.835	3.53×10^{-24}

Empirical line strengths are calculated as a ratio of nearby known CH_4 line strengths and the corresponding measured absorption, accounting for difference in sample concentration, molecular mass, and frequency center. Lines were fit with both Voigt and Galatry profiles, but with four peak parameters (center, height, Doppler width, Lorentzian width) to fit with 9 data points across the 550 MHz FWHM CH_4 peaks, no structure in the residuals could be seen. A Galatry profile incorporates an additional Dicke narrowing fit parameter,²⁷ but does not improve signal-to-noise significantly and reduces the fit's degrees of freedom.

Below is an image of a sample fit for the $\text{CH}_2\text{D}_2 + \text{O}(^1\text{D})$ kinetic isotope effect with an 18% depletion in methane concentration.

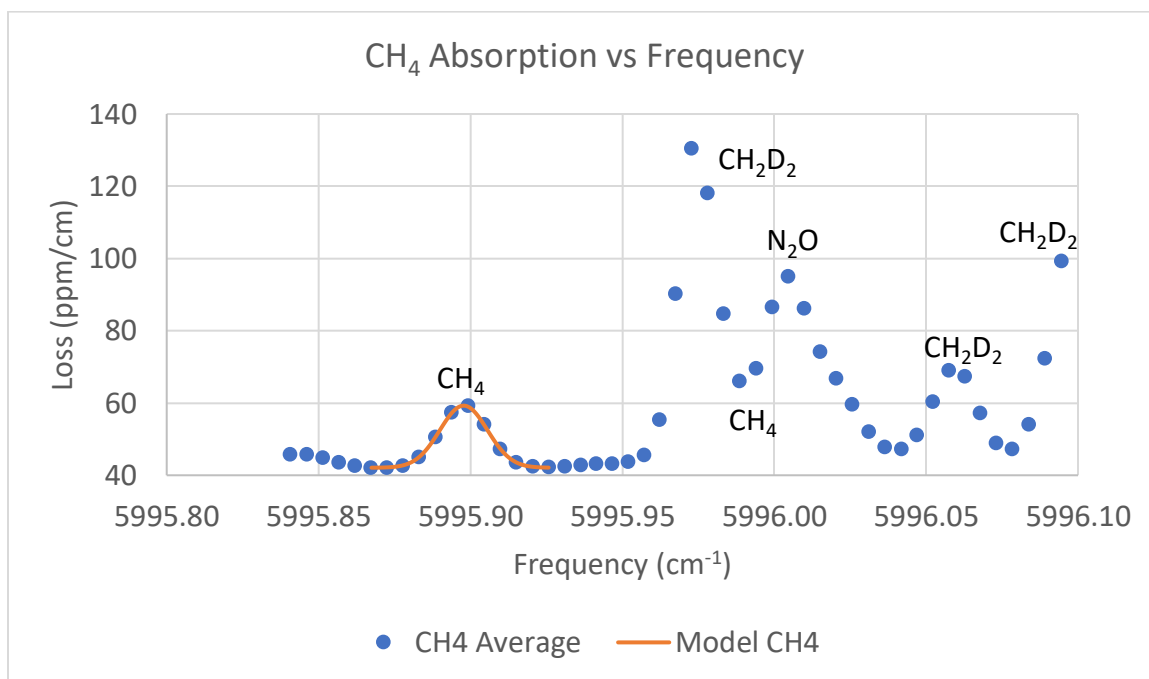


Figure 4.7: CH₄ peak used to fit the CH₂D₂ + O(¹D) data. Fit peak is 50.1 mtorr CH₄ in 9.69 torr total pressure. Nearby peaks are marked.

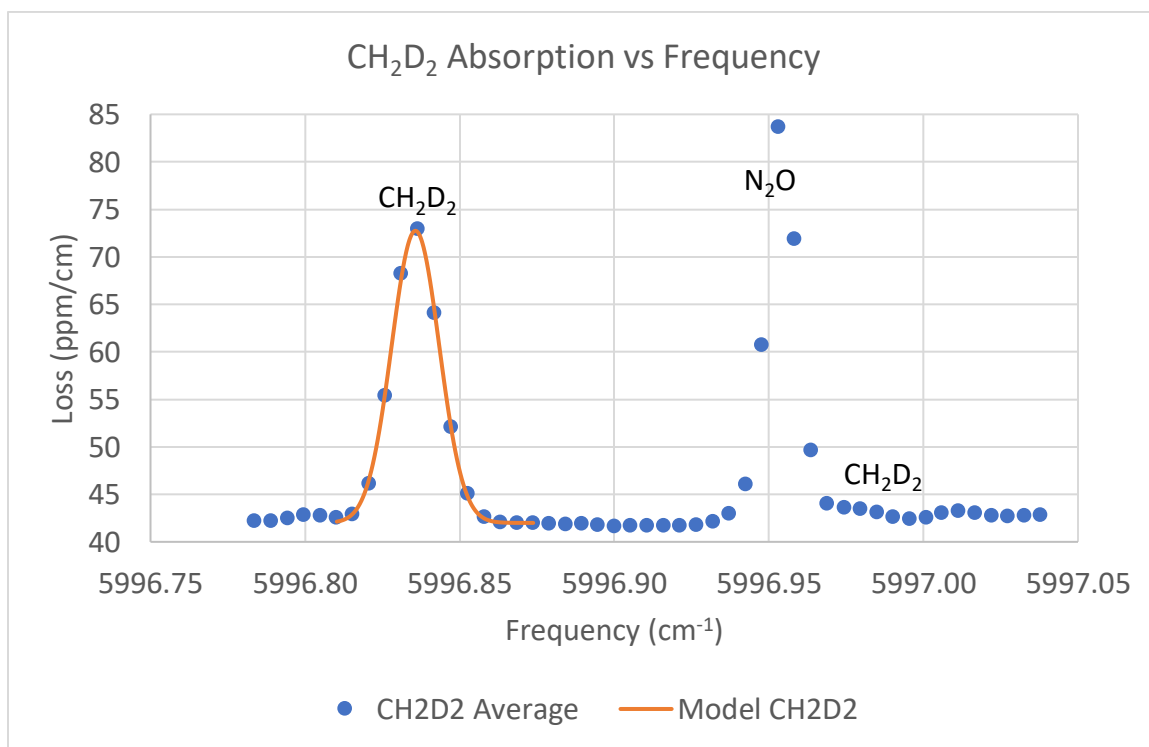


Figure 4.8: CH₂D₂ peak used to fit the CH₂D₂ + O(¹D) KIE. Fit peak is 85.5 mtorr CH₂D₂, 9.69 torr total pressure. Nearby lines are marked.

The two peaks are alternately measured to avoid systematic error in sample measurement temperature. After both peaks for the reacted samples and measurement samples were recorded each 5 – 10 times, the absorption peaks for CH₂D₂ and CH₄ were integrated for both the reference and photolysis samples. These values were the concentrations used for the KIE formula above, since the integrated areas are proportional to the concentration \times line strength, which algebraically cancels.

The peaks are fit with a Voigt line shape, which is a convolution of a Gaussian and Lorentzian pressure-broadening line profiles. The Gaussian linewidth using the measured temperature, molecular mass, and center frequency in the following formula:²⁸

$$\text{FWHM } \Delta\nu_D = 2\nu_0 \sqrt{\frac{2k_B T \ln(2)}{mc^2}} \rightarrow \text{FWHM } \Delta\tilde{\nu}_D = 7.154 \times 10^{-7} \tilde{\nu}_0 \sqrt{\frac{T}{M}}$$

For T in K, M in amu, $\tilde{\nu}_0$ in cm⁻¹, and $\Delta\tilde{\nu}_0$ in cm⁻¹. At 294 K the resulting FWHM for CH₄ is 551 MHz, while the FWHM for CH₂D₂ is 519 MHz.

The Lorentzian linewidth is proportional to pressure, but pressure-broadening coefficients are transition and buffer-gas dependent. Coefficients recorded in the literature are either for self-broadening or air-broadening in the HITRAN spectral database,²⁶ or are for visible or mid-IR transitions when He is the buffer gas.^{29–33} Assuming an estimated 0.05 cm⁻¹/atm for He-induced CH₄ broadening from Keffer and HITRAN,^{26,29} a FWHM of 2 MHz is expected, or a >0.4% correction to the width.

To understand for example the pressure-dependence of the CH₂D₂ peak in He at 5996.83 cm⁻¹ seen in the image above, 141.1 torr CH₂D₂ was mixed with increasing concentrations of He, and the FWHM and peak center frequency plotted vs total pressure. He was chosen because ~90% of a sample is He, though ideally increasing pressure of an

identical reaction mixture would be introduced because line broadening due to a mixture is not necessarily additive.³⁴ The linear trend of FWHM vs total pressure should have a slope of the Lorentzian pressure broadening parameter γ_{He} and a 0-pressure intercept of the Doppler FWHM. The peak center frequency trend should have a slope of the pressure shift parameter δ_{He} and a 0-pressure intercept of the vacuum line position.

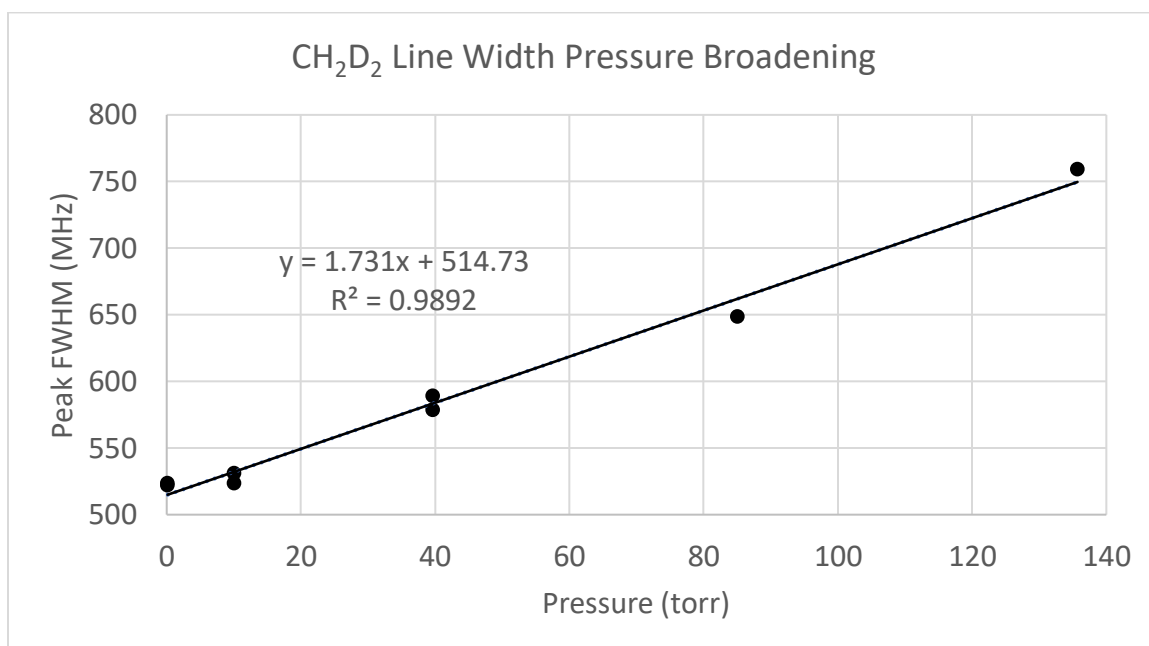


Figure 4.9: Change in the CH₂D₂ peak width at 5993.83 cm⁻¹ vs pressure.

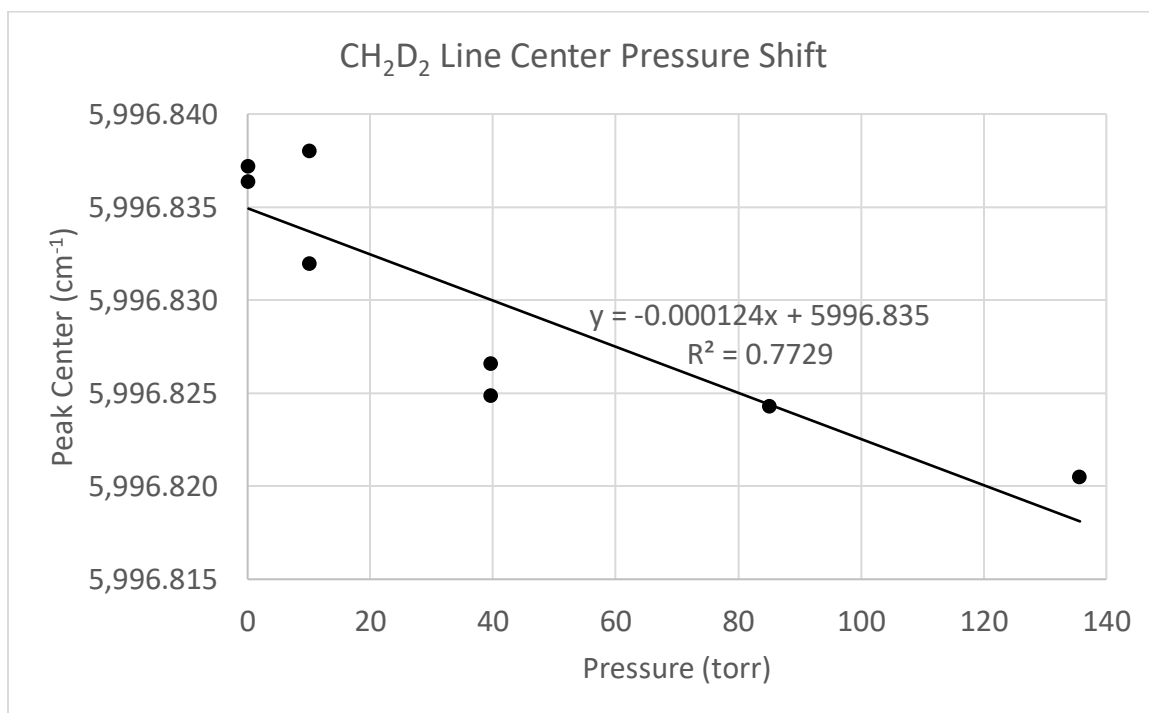


Figure 4.10: Change in the CH₂D₂ peak center frequency at 5993.83 cm⁻¹ vs pressure.

Theoretically neither plot need have a linear trendline, but in the still (relatively) low pressure range scanned and the limited number of points, higher-order effects should be minimal and more fitting parameters would have allowed for overfitting.

Converting the values γ_{He} and δ_{He} to HITRAN units, the CH₂D₂ peak was determined to have line fitting parameters of $\gamma_{He} = 0.0439 \pm 0.0019$ cm⁻¹ / atm, a $\delta_{He} = -0.094 \pm 0.021$ cm⁻¹ / atm, and a center $\nu_{p=0} = 5996.8349 \pm 0.0017$ cm⁻¹. These values are entirely reasonable compared with HITRAN and Keffer.^{26,29} The FWHM of the 141.1 mtorr value was 522.38 ± 0.85 MHz, consistent with the predicted value of 519 MHz, with the difference in the sample and in the fit's y-intercept likely due to temperature drift of the sample. Because these studies were only carried out at a single temperature, no temperature-dependence to the line could be assigned.

After integrating all the peaks, the KIE value can be determined. The uncertainty of a KIE value is given below. If we define L and H as the ratios of the before and after reaction abundances for the light and heavy isotopologue respectively (here using CH₃D as the example heavy isotopologue), then

$$L \pm \Delta L = \frac{[CH_4]_{rxn}}{[CH_4]_{ref}} \left(1 \pm \sqrt{\left(\frac{\Delta[CH_4]_{rxn}}{[CH_4]_{rxn}} \right)^2 + \left(\frac{\Delta[CH_4]_{ref}}{[CH_4]_{ref}} \right)^2} \right)$$

$$H \pm \Delta H = \frac{[CH_3D]_{rxn}}{[CH_3D]_{ref}} \left(1 \pm \sqrt{\left(\frac{\Delta[CH_3D]_{rxn}}{[CH_3D]_{rxn}} \right)^2 + \left(\frac{\Delta[CH_3D]_{ref}}{[CH_3D]_{ref}} \right)^2} \right)$$

And overall

$$KIE \pm \Delta KIE = \left(\frac{\ln(L)}{\ln(H)} \right) \left(1 \pm \sqrt{\left(\frac{\Delta L}{L \ln(L)} \right)^2 + \left(\frac{\Delta H}{H \ln(H)} \right)^2} \right)$$

Results:

A table of the KIE results are shown below:

Table 4.3: KIE Results

Reaction	KIE
¹³ CH ₄ + O(¹ D)	1.069 ± 0.028
CH ₃ D + O(¹ D)	1.09 ± 0.03
CH ₃ D + O(¹ D) @ - 116 °C	1.08 ± 0.22
CH ₂ D ₂ + O(¹ D)	1.102 ± 0.022

The KIE values derived were overall larger than previous literature studies, with previous measurements of the ¹³CH₄ + O(¹D) reaction measured to be 1.001 by Davidson,³⁵ 1.0054 by Cantrell,³⁶ and 1.013 from Saueressig,^{35,37} with stratospheric sample retrieval and modelling favoring Saueressig's larger value.³⁸ The unusually high KIE for a barrierless reaction is likely due to rotational coupling within the transition

state, known to occur in $\text{CH} + \text{CH}_4$.³⁹ Recent work from Bui and Shen point to a higher value of 1.042 ± 0.018 (2σ) using the same instrumentation,²⁰ and the value derived in this work overlaps barely with Bui. The implications of a higher value are additional constraints on the seasonal and interhemispheric methane variability, because correlation between the seasonal methane concentration and isotope ratio changes (both $\delta^{13}\text{C}$ and δD) are due to changes in both source and sink reactions.^{7,40–42}

Potential sources of error between the work here and literature results relates to the percentage methane depleted. Our aim was for a 10 – 20% depletion of CH_4 and N_2O to avoid secondary chemistry, while Saueressig's experiments had 11 – 47% depletion,³⁷ while Davidson has 31 – 92% depletion,³⁵ and an earlier study by Cantrell had 30 – 95% depletion,³⁶ all using Hg arc lamps to photolyze O_3 to form $\text{O}(^1\text{D})$. Our own attempts to use O_3 as a photolytic precursor were stymied due to the incompatible cross-sections at our excimer wavelengths, since the quartz photolysis cells would attenuate nearly all light until the O_3 was almost fully depleted.

Previous studies' heavy-depletion conditions may have allowed secondary radical reactions to deplete methane and obscuring the KIE solely from $\text{O}(^1\text{D})$. Another reason to avoid high methane depletion is potential methane reformation, which would convolve the methane + $\text{O}(^1\text{D})$ KIE with the KIE of reformation reactions. Key to preventing reformation is keeping the CH_3 and H density low, since the reaction $\text{CH}_3 + \text{H} \rightarrow \text{CH}_4$ has a rate constant 1.8X larger than $\text{CH}_4 + \text{O}(^1\text{D})$.⁴³ Potential wall reactions with CH_3 could also reform methane too with an unknown KIE.

The value for $\text{CH}_3\text{D} + \text{O}(^1\text{D})$ was measured to be 1.09 ± 0.03 , which is higher than the literature value from Saueressig of 1.06,³⁷ though Saueressig's value is within

range of the value measured here. Since the abstraction reaction does not have a transition state, it is unlikely to be temperature-dependent, which is consistent with the 1.08 ± 0.22 value seen here at $-166\text{ }^{\circ}\text{C}$. However, the error is large enough most measured and literature values fall within the error.

The $\text{CH}_2\text{D}_2 + \text{O}(^1\text{D})$ KIE was measured for the first time, and the value found to be 1.102 ± 0.022 . This is within error of being 2X the literature value of 1.06 for $\text{CH}_3\text{D} + \text{O}(^1\text{D})$ given by Saueressig, and at a ± 0.022 uncertainty it is not possible to detect if there is additional stabilization from two deuterium atoms being present. This KIE is also not expected to have a noticeable temperature dependence.

Systematic sources of error in our experiment largely are related to both the temperature stability of our apparatus, and the temperature dependence of the absorption lines used. Better temperature stabilization would improve the sampling error in the integrated line strengths by keeping the line strength S constant. Improving scanning times would greatly help reduce this systematic issue; currently measurement occupies at most 10% of a scan's real time; most is spent temperature tuning and stabilizing the laser diode between frequency points.

Another source of error is in the transitions picked for observation. The error in the ratio in an isotope measurement is given by Bergamanschi *et al.*⁴⁴

$$\frac{\Delta\delta_{\text{isotope}}}{\Delta T} = \frac{\Delta E''}{kT^2}$$

Where $\Delta E''$ is the difference in ground state energies between a heavy isotopologue and $^{12}\text{CH}_4$. If the temperature dependence and E'' parameters were known for each transition, this problem could be mitigated. Fortunately, because the KIE is a ratio, the value is insensitive to errors in the listed line strengths, which is the dominant source of error

when measuring $\delta^{13}\text{C}$ or δD changes in isotope abundance with this instrumentation.²³

Therefore improvements to the existing apparatus are all that are needed, not more accurate reference data.

Conclusion:

In this chapter, we introduce upgrades to an existing cavity ring-down spectroscopic instrument, namely the frequency-stabilized DFB laser, the PDH frequency-stabilization, the optical switching between wavelengths, and increased precision for sample preparation and transfer. We are able to measure for the first time the KIE of $\text{CH}_2\text{D}_2 + \text{O}(^1\text{D}) = 1.102 \pm 0.022$ as well as remeasure $^{13}\text{CH}_4$ and $\text{CH}_3\text{D} + \text{O}(^1\text{D})$ via flash photolysis, and we can determine spectroscopic parameters of the measured transitions to improve line shape fitting.

Future upgrades to the system would be to systematically study all lines for broadening parameters and ground state energies, and to implement a technique to collect cavity-ring down data at a higher duty cycle. Frequency-agile rapid scanning is a technique which would eliminate temperature tuning a diode, allowing for near-maximum data collection to be achieved. Allowing the cavity piezoelectric motor to move would allow interleaving of data points, reducing fitting uncertainty, and allow for more accurate measurements of these isotope effects.

Acknowledgments:

I would like to thank NASA Solar System Workings award 80NSSC18K0263 for funding the included work. I would also like to thank Dr. Linhan Shen for her mentorship starting this project, and the help of Professor Tzu-Ling Chen for helping collect the data.

References

- (1) Arias, P. A.; Bellouin, N.; Coppola, E.; Jones, R. G.; Krinner, G.; Marotzke, J.; Naik, V.; Palmer, M. D.; Plattner, G.-K.; Rogelj, J.; Rojas, M.; Sillmann, J.; Storelvmo, T.; Thorne, P. W.; Trewin, B.; Achuta Rao, K.; Adhikary, B.; Allan, R. P.; Armour, K.; Bala, G.; Barimalala, R.; Berger, S.; Canadell, J. G.; Cassou, C.; Cherchi, A.; Collins, W.; Collins, W. D.; Connors, S. L.; Corti, S.; Cruz, F.; Dentener, F. J.; Dereczynski, C.; Di Luca, A.; Diongue Niang, A.; Doblas-Reyes, F. J.; Dosio, A.; Douville, H.; Engelbrecht, F.; Eyring, V.; Fischer, E.; Forster, P.; Fox-Kemper, B.; Fuglestad, J. S.; Fyfe, J. C.; Gillett, N. P.; Goldfarb, L.; Gorodetskaya, I.; Gutierrez, J. M.; Hamdi, R.; Hawkins, E.; Hewitt, H. T.; Hope, P.; Islam, A. S.; Jones, C.; Kaufman, D. S.; Kopp, R. E.; Kosaka, Y.; Kossin, J.; Krakovska, S.; Lee, J.-Y.; Li, J.; Mauritsen, T.; Maycock, T. K.; Meinshausen, M.; Min, S.-K.; Monteiro, P. M. S.; Ngo-Duc, T.; Otto, F.; Pinto, I.; Pirani, A.; Raghavan, K.; Ranasinghe, R.; Ruane, A. C.; Ruiz, L.; Sallée, J.-B.; Samset, B. H.; Sathyendranath, S.; Seneviratne, S. I.; Sörensson, A. A.; Szopa, S.; Takayabu, I.; Tréguier, A.-M.; van den Hurk, B.; Vautard, R.; von Schuckmann, K.; Zaehle, S.; Zhang, X.; Zickfeld, K. Technical Summary. *Climate Change 2021: The Physical Science Basis. Contribution of Working Group I to the Sixth Assessment Report of the Intergovernmental Panel on Climate Change*, 2021, 33–144. <https://doi.org/10.1017/9781009157896.002>.
- (2) Kirschke, S.; Bousquet, P.; Ciais, P.; Saunoy, M.; Canadell, J. G.; Dlugokencky, E. J.; Bergamaschi, P.; Bergmann, D.; Blake, D. R.; Bruhwiler, L.; Cameron-Smith, P.; Castaldi, S.; Chevallier, F.; Feng, L.; Fraser, A.; Heimann, M.; Hodson, E. L.; Houweling, S.; Josse, B.; Fraser, P. J.; Krummel, P. B.; Lamarque, J.-F.; Langenfelds, R. L.; Le Quéré, C.; Naik, V.; O'Doherty, S.; Palmer, P. I.; Pison, I.; Plummer, D.; Poulter, B.; Prinn, R. G.; Rigby, M.; Ringeval, B.; Santini, M.; Schmidt, M.; Shindell, D. T.; Simpson, I. J.; Spahni, R.; Steele, L. P.; Strode, S. A.; Sudo, K.; Szopa, S.; van der Werf, G. R.; Voulgarakis, A.; van Weele, M.; Weiss, R. F.; Williams, J. E.; Zeng, G. Three Decades of Global Methane Sources and Sinks. *Nat. Geosci.* **2013**, 6 (10), 813–823. <https://doi.org/10.1038/ngeo1955>.
- (3) Harnung, S. E.; Johnson, M. S. *Chemistry and the Environment*; Cambridge University Press, 2012.
- (4) Noël, S.; Weigel, K.; Bramstedt, K.; Rozanov, A.; Weber, M.; Bovensmann, H.; Burrows, J. P. Water Vapour and Methane Coupling in the Stratosphere Observed Using SCIAMACHY Solar Occultation Measurements. *Atmospheric Chem. Phys.* **2018**, 18 (7), 4463–4476. <https://doi.org/10.5194/acp-18-4463-2018>.

- (5) Stolper, D. A.; Martini, A. M.; Clog, M.; Douglas, P. M.; Shusta, S. S.; Valentine, D. L.; Sessions, A. L.; Eiler, J. M. Distinguishing and Understanding Thermogenic and Biogenic Sources of Methane Using Multiply Substituted Isotopologues. *Geochim. Cosmochim. Acta* **2015**, *161*, 219–247. <https://doi.org/10.1016/j.gca.2015.04.015>.
- (6) Douglas, P. M. J.; Stolper, D. A.; Eiler, J. M.; Sessions, A. L.; Lawson, M.; Shuai, Y.; Bishop, A.; Podlaha, O. G.; Ferreira, A. A.; Santos Neto, E. V.; Niemann, M.; Steen, A. S.; Huang, L.; Chimiak, L.; Valentine, D. L.; Fiebig, J.; Luhmann, A. J.; Seyfried, W. E.; Etiope, G.; Schoell, M.; Inskeep, W. P.; Moran, J. J.; Kitchen, N. Methane Clumped Isotopes: Progress and Potential for a New Isotopic Tracer. *Org. Geochem.* **2017**, *113*, 262–282. <https://doi.org/10.1016/j.orggeochem.2017.07.016>.
- (7) Whitehill, A. R.; Joelsson, L. M. T.; Schmidt, J. A.; Wang, D. T.; Johnson, M. S.; Ono, S. Clumped Isotope Effects during OH and Cl Oxidation of Methane. *Geochim. Cosmochim. Acta* **2017**, *196*, 307–325. <https://doi.org/10.1016/j.gca.2016.09.012>.
- (8) Webster, C. R.; Mahaffy, P. R.; Atreya, S. K.; Flesch, G. J.; Farley, K. A.; Team, the M. S. Low Upper Limit to Methane Abundance on Mars. *Science* **2013**, 1242902. <https://doi.org/10.1126/science.1242902>.
- (9) Webster, C. R.; Mahaffy, P. R.; Atreya, S. K.; Flesch, G. J.; Mischna, M. A.; Meslin, P.-Y.; Farley, K. A.; Conrad, P. G.; Christensen, L. E.; Pavlov, A. A.; Martín-Torres, J.; Zorzano, M.-P.; McConnochie, T. H.; Owen, T.; Eigenbrode, J. L.; Glavin, D. P.; Steele, A.; Malespin, C. A.; Archer, P. D.; Sutter, B.; Coll, P.; Freissinet, C.; McKay, C. P.; Moores, J. E.; Schwenzer, S. P.; Bridges, J. C.; Navarro-Gonzalez, R.; Gellert, R.; Lemmon, M. T.; Team, the M. S. Mars Methane Detection and Variability at Gale Crater. *Science* **2015**, *347* (6220), 415–417. <https://doi.org/10.1126/science.1261713>.
- (10) Webster, C. R.; Mahaffy, P. R.; Atreya, S. K.; Moores, J. E.; Flesch, G. J.; Malespin, C.; McKay, C. P.; Martinez, G.; Smith, C. L.; Martin-Torres, J.; Gomez-Elvira, J.; Zorzano, M.-P.; Wong, M. H.; Trainer, M. G.; Steele, A.; Archer, D.; Sutter, B.; Coll, P. J.; Freissinet, C.; Meslin, P.-Y.; Gough, R. V.; House, C. H.; Pavlov, A.; Eigenbrode, J. L.; Glavin, D. P.; Pearson, J. C.; Keymeulen, D.; Christensen, L. E.; Schwenzer, S. P.; Navarro-Gonzalez, R.; Pla-García, J.; Rafkin, S. C. R.; Vicente-Retortillo, Á.; Kahanpää, H.; Viudez-Moreiras, D.; Smith, M. D.; Harri, A.-M.; Genzer, M.; Hassler, D. M.; Lemmon, M.; Crisp, J.; Sander, S. P.; Zurek, R. W.; Vasavada, A. R. Background Levels of Methane in Mars'

- Atmosphere Show Strong Seasonal Variations. *Science* **2018**, 360 (6393), 1093–1096. <https://doi.org/10.1126/science.aaq0131>.
- (11) Mumma, M. J.; Villanueva, G. L.; Novak, R. E.; Hewagama, T.; Bonev, B. P.; DiSanti, M. A.; Mandell, A. M.; Smith, M. D. Strong Release of Methane on Mars in Northern Summer 2003. *Science* **2009**, 323 (5917), 1041–1045. <https://doi.org/10.1126/science.1165243>.
- (12) Korablev, O.; Vandaale, A. C.; Montmessin, F.; Fedorova, A. A.; Trokhimovskiy, A.; Forget, F.; Lefèvre, F.; Daerden, F.; Thomas, I. R.; Trompet, L.; Erwin, J. T.; Aoki, S.; Robert, S.; Neary, L.; Viscardy, S.; Grigoriev, A. V.; Ignatiev, N. I.; Shakun, A.; Patrakeeve, A.; Belyaev, D. A.; Bertaux, J.-L.; Olsen, K. S.; Baggio, L.; Alday, J.; Ivanov, Y. S.; Ristic, B.; Mason, J.; Willame, Y.; Depiesse, C.; Hetey, L.; Berkenbosch, S.; Clairquin, R.; Queirolo, C.; Beeckman, B.; Neefs, E.; Patel, M. R.; Bellucci, G.; López-Moreno, J.-J.; Wilson, C. F.; Etiope, G.; Zelenyi, L.; Svedhem, H.; Vago, J. L. No Detection of Methane on Mars from Early ExoMars Trace Gas Orbiter Observations. *Nature* **2019**, 568 (7753), 517–520. <https://doi.org/10.1038/s41586-019-1096-4>.
- (13) Zhang, X.; Berkinsky, D.; Markus, C. R.; Chitturi, S. R.; Grieman, F. J.; Okumura, M.; Luo, Y.; Yung, Y. L.; Sander, S. P. Reaction of Methane and UV-Activated Perchlorate: Relevance to Heterogeneous Loss of Methane in the Atmosphere of Mars. *Icarus* **2022**, 376, 114832. <https://doi.org/10.1016/j.icarus.2021.114832>.
- (14) Knak Jensen, S. J.; Skibsted, J.; Jakobsen, H. J.; ten Kate, I. L.; Gunnlaugsson, H. P.; Merrison, J. P.; Finster, K.; Bak, E.; Iversen, J. J.; Kondrup, J. C.; Nørnberg, P. A Sink for Methane on Mars? The Answer Is Blowing in the Wind. *Icarus* **2014**, 236, 24–27. <https://doi.org/10.1016/j.icarus.2014.03.036>.
- (15) Gough, R. V.; Turley, J. J.; Ferrell, G. R.; Cordova, K. E.; Wood, S. E.; DeHaan, D. O.; McKay, C. P.; Toon, O. B.; Tolbert, M. A. Can Rapid Loss and High Variability of Martian Methane Be Explained by Surface H₂O₂? *Planet. Space Sci.* **2011**, 59 (2), 238–246. <https://doi.org/10.1016/j.pss.2010.09.018>.
- (16) Gough, R. V.; Tolbert, M. A.; McKay, C. P.; Toon, O. B. Methane Adsorption on a Martian Soil Analog: An Abiogenic Explanation for Methane Variability in the Martian Atmosphere. *Icarus* **2010**, 207 (1), 165–174. <https://doi.org/10.1016/j.icarus.2009.11.030>.

- (17) Olsen, K. S.; Lefèvre, F.; Montmessin, F.; Trokhimovskiy, A.; Baggio, L.; Fedorova, A.; Alday, J.; Lomakin, A.; Belyaev, D. A.; Patrakeeve, A.; Shakun, A.; Korablev, O. First Detection of Ozone in the Mid-Infrared at Mars: Implications for Methane Detection. *Astron. Astrophys.* **2020**. <https://doi.org/10.1051/0004-6361/202038125>.
- (18) Brown, M. a. J.; Patel, M. R.; Lewis, S. R.; Holmes, J. A.; Sellers, G. J.; Streeter, P. M.; Bennaceur, A.; Liuzzi, G.; Villanueva, G. L.; Vandaele, A. C. Impacts of Heterogeneous Chemistry on Vertical Profiles of Martian Ozone. *J. Geophys. Res. Planets* **2022**, *127* (11), e2022JE007346. <https://doi.org/10.1029/2022JE007346>.
- (19) Dlugokencky, E. J.; Nisbet, E. G.; Fisher, R.; Lowry, D. Global Atmospheric Methane: Budget, Changes and Dangers. *Philos. Trans. R. Soc. Math. Phys. Eng. Sci.* **2011**. <https://doi.org/10.1098/rsta.2010.0341>.
- (20) Bui, T. Q. Cavity Enhanced Spectroscopies for Applications of Remote Sensing, Chemical Kinetics and Detection of Radical Species, California Institute of Technology, Pasadena, CA, 2015.
<http://resolver.caltech.edu/CaltechTHESIS:06032015-151007228>.
- (21) Ianni, J. C. Kintecus, 2021. www.kintecus.com.
- (22) Maity, A.; Maithani, S.; Pradhan, M. Chapter 3 - Cavity Ring-down Spectroscopy: Recent Technological Advances and Applications. In *Molecular and Laser Spectroscopy*; Gupta, V. P., Ozaki, Y., Eds.; Elsevier, 2020; pp 83–120.
<https://doi.org/10.1016/B978-0-12-818870-5.00003-4>.
- (23) Chen, T.-L.; Ober, D. C.; Miri, R.; Bui, T. Q.; Shen, L.; Okumura, M. Optically Switched Dual-Wavelength Cavity Ring-Down Spectrometer for High-Precision Isotope Ratio Measurements of Methane ΔD in the Near Infrared. *Anal. Chem.* **2021**, *93* (16), 6375–6384. <https://doi.org/10.1021/acs.analchem.0c05090>.
- (24) Schuldt, T.; Döringshoff, K.; Reggentin, M.; Kovalchuk, E. V.; Gohlke, M.; Weise, D.; Johann, U.; Peters, A.; Braxmaier, C. A High-Performance Iodine-Based Frequency Reference for Space Applications. In *International Conference on Space Optics — ICSO 2012*; SPIE, 2017; Vol. 10564, pp 425–430.
<https://doi.org/10.1117/12.2309085>.

- (25) Franzen, A. GWOptics, 2006.
- (26) Gordon, I. E.; Rothman, L. S.; Hargreaves, R. J.; Hashemi, R.; Karlovets, E. V.; Skinner, F. M.; Conway, E. K.; Hill, C.; Kochanov, R. V.; Tan, Y.; Weislo, P.; Finenko, A. A.; Nelson, K.; Bernath, P. F.; Birk, M.; Boudon, V.; Campargue, A.; Chance, K. V.; Coustenis, A.; Drouin, B. J.; Flaud, J. –M.; Gamache, R. R.; Hodges, J. T.; Jacquemart, D.; Mlawer, E. J.; Nikitin, A. V.; Perevalov, V. I.; Rotger, M.; Tennyson, J.; Toon, G. C.; Tran, H.; Tyuterev, V. G.; Adkins, E. M.; Baker, A.; Barbe, A.; Canè, E.; Császár, A. G.; Dudaryonok, A.; Egorov, O.; Fleisher, A. J.; Fleurbaey, H.; Foltynowicz, A.; Furtenbacher, T.; Harrison, J. J.; Hartmann, J. –M.; Horneman, V. –M.; Huang, X.; Karman, T.; Karns, J.; Kassi, S.; Kleiner, I.; Kofman, V.; Kwabia–Tchana, F.; Lavrentieva, N. N.; Lee, T. J.; Long, D. A.; Lukashevskaya, A. A.; Lyulin, O. M.; Makhnev, V. Yu.; Matt, W.; Massie, S. T.; Melosso, M.; Mikhailenko, S. N.; Mondelain, D.; Müller, H. S. P.; Naumenko, O. V.; Perrin, A.; Polyansky, O. L.; Raddaoui, E.; Raston, P. L.; Reed, Z. D.; Rey, M.; Richard, C.; Tóbiás, R.; Sadiek, I.; Schwenke, D. W.; Starikova, E.; Sung, K.; Tamassia, F.; Tashkun, S. A.; Vander Auwera, J.; Vasilenko, I. A.; Vigasin, A. A.; Villanueva, G. L.; Vispoel, B.; Wagner, G.; Yachmenev, A.; Yurchenko, S. N. The HITRAN2020 Molecular Spectroscopic Database. *J. Quant. Spectrosc. Radiat. Transf.* **2022**, 277, 107949. <https://doi.org/10.1016/j.jqsrt.2021.107949>.
- (27) Ouyang, X.; Varghese, P. L. Reliable and Efficient Program for Fitting Galatry and Voigt Profiles to Spectral Data on Multiple Lines. *Appl. Opt.* **1989**, 28 (8), 1538. <https://doi.org/10.1364/AO.28.001538>.
- (28) Bernath, P. F. *Spectra of Atoms and Molecules*; Oxford University Press, Inc., 1995.
- (29) Keffer, C. E.; Conner, C. P.; Smith, W. H. Pressure Broadening of Methane Lines in the 6190 Å And 6825 Å Bands at Room and Low Temperatures.
- (30) Serdyukov, V. I.; Sinitsa, L. N.; Bykov, A. D.; Shcherbakov, A. P. Broadening and Shift of the Methane Absorption Lines in the 11000–11400 Cm⁻¹ Region. *Atmospheric Ocean. Opt.* **2018**, 31 (2), 153–156. <https://doi.org/10.1134/S1024856018020136>.
- (31) Millot, G.; Lavorel, B.; Steinfeld, J. I. Collisional Broadening, Line Shifting, and Line Mixing in the Stimulated Raman 2v₂ Q Branch of CH₄. *J. Chem. Phys.* **1991**, 95 (11), 7938–7946. <https://doi.org/10.1063/1.461322>.

- (32) Singh, K.; O'Brien, J. J. Measurement of Pressure-Broadening and Lineshift Coefficients at 77 and 296 K of Methane Lines in the 727 NM Band Using Intracavity Laser Spectroscopy. *J. Quant. Spectrosc. Radiat. Transf.* **1994**, 52 (1), 75–87. [https://doi.org/10.1016/0022-4073\(94\)90140-6](https://doi.org/10.1016/0022-4073(94)90140-6).
- (33) Margolis, J. S. Hydrogen and Helium Broadening and Pressure Induced Line Shifts of $^{13}\text{CH}_4$ in the N4 Band. *J. Quant. Spectrosc. Radiat. Transf.* **1996**, 55 (6), 823–836. [https://doi.org/10.1016/0022-4073\(95\)00185-9](https://doi.org/10.1016/0022-4073(95)00185-9).
- (34) Giesen, T.; Schieder, R.; Winnewisser, G.; Yamada, K. M. T. Precise Measurements of Pressure Broadening and Shift for Several H_2O Lines in the N2 Band by Argon, Nitrogen, Oxygen, and Air. *J. Mol. Spectrosc.* **1992**, 153 (1), 406–418. [https://doi.org/10.1016/0022-2852\(92\)90485-7](https://doi.org/10.1016/0022-2852(92)90485-7).
- (35) Davidson, J. A.; Cantrell, C. A.; Tyler, S. C.; Shetter, R. E.; Cicerone, R. J.; Calvert, J. G. Carbon Kinetic Isotope Effect in the Reaction of CH_4 with HO. *J. Geophys. Res. Atmospheres* **1987**, 92 (D2), 2195–2199. <https://doi.org/10.1029/JD092iD02p02195>.
- (36) Cantrell, C. A.; Shetter, R. E.; McDaniel, A. H.; Calvert, J. G.; Davidson, J. A.; Lowe, D. C.; Tyler, S. C.; Cicerone, R. J.; Greenberg, J. P. Carbon Kinetic Isotope Effect in the Oxidation of Methane by the Hydroxyl Radical. *J. Geophys. Res. Atmospheres* **1990**, 95 (D13), 22455–22462. <https://doi.org/10.1029/JD095iD13p22455>.
- (37) Saueressig, G.; Crowley, J. N.; Bergamaschi, P.; Brühl, C.; Brenninkmeijer, C. A. M.; Fischer, H. Carbon 13 and D Kinetic Isotope Effects in the Reactions of CH_4 with O(1 D) and OH: New Laboratory Measurements and Their Implications for the Isotopic Composition of Stratospheric Methane. *J. Geophys. Res. Atmospheres* **2001**, 106 (D19), 23127–23138. <https://doi.org/10.1029/2000JD000120>.
- (38) McCarthy, M. C.; Connell, P.; Boering, K. A. Isotopic Fractionation of Methane in the Stratosphere and Its Effect on Free Tropospheric Isotopic Compositions. *Geophys. Res. Lett.* **2001**, 28 (19), 3657–3660. <https://doi.org/10.1029/2001GL013159>.

- (39) Taatjes, C. A.; Klippenstein, S. J. Kinetic Isotope Effects and Variable Reaction Coordinates in Barrierless Recombination Reactions. *J. Phys. Chem. A* **2001**, *105* (37), 8567–8578. <https://doi.org/10.1021/jp011632q>.
- (40) Brownlow, R.; Lowry, D.; Fisher, R. E.; France, J. L.; Lanoisellé, M.; White, B.; Wooster, M. J.; Zhang, T.; Nisbet, E. G. Isotopic Ratios of Tropical Methane Emissions by Atmospheric Measurement. *Glob. Biogeochem. Cycles* **2017**, *31* (9), 1408–1419. <https://doi.org/10.1002/2017GB005689>.
- (41) Allen, H. M. Constraining the Formation and Fate of Hydroperoxides in the Remote Atmosphere.
- (42) Strode, S. A.; Wang, J. S.; Manyin, M.; Duncan, B.; Hossaini, R.; Keller, C. A.; Michel, S. E.; White, J. W. C. *Strong Sensitivity of the Isotopic Composition of Methane to the Plausible Range of Tropospheric Chlorine*; preprint; Isotopes/Atmospheric Modelling/Troposphere/Chemistry (chemical composition and reactions), 2019. <https://doi.org/10.5194/acp-2019-1047>.
- (43) Klippenstein, S. J.; Georgievskii, Y.; Harding, L. B. A Theoretical Analysis of the CH₃+H Reaction: Isotope Effects, the High-Pressure Limit, and Transition State Recrossing. *Proc. Combust. Inst.* **2002**, *29* (1), 1229–1236. [https://doi.org/10.1016/S1540-7489\(02\)80152-3](https://doi.org/10.1016/S1540-7489(02)80152-3).
- (44) Bergamaschi, P.; Bräunlich, M.; Marik, T.; Brenninkmeijer, C. A. M. Measurements of the Carbon and Hydrogen Isotopes of Atmospheric Methane at Izaña, Tenerife: Seasonal Cycles and Synoptic-Scale Variations. *J. Geophys. Res. Atmospheres* **2000**, *105* (D11), 14531–14546. <https://doi.org/10.1029/1999JD901176>.

Appendix: KINTECUS CH₄ model²¹

Model Description Spreadsheet				
# Reactions can be entered in as				
# k	Reaction	Comments		
# 1.2345	A+B=C	A sample reaction with rate constant		
# OR		Multiply E/R by 8.3145		
#	When naming species, write OH(v=0) as: OH{v0}			
# A	T^m	Ea	Reaction	Comments
# Ox Reactions				
1.00E+00	0	0	O+O2+M[JPL1;6.1E-34;2.4;1;0.0;He(0.6);H2O(2.5)]=>O3	JPL Publication 19-5 p. 2-5
8.00E-12	0	17128	O+O3==>2O2	JPL Publication 19-5 p. 1-6
# O{1D} Chemistry				
3.30E-11	0	-457	O{1D}+O2==>O+O2	JPL Publication 19-5 p. 1-7, makes 80% O2{1Sigma} 20% O2{1Delta}
2.40E-10	0	0	O{1D}+O3==>2O2	JPL Publication 19-5 p. 1-7
2.40E-10	0	0	O{1D}+O3==>O2+2O	JPL Publication 19-5 p. 1-7
3.36E-11	0	0	O{1D}+H2==>OH+H	JPL Publication 19-5 p. 1-7 total of O{1D}+H2, Huang Y. et al. 1986 for branching ratio

#=0.22*0.00000 000012	0	0	$\text{O}\{1\text{D}\} + \text{H}_2 \rightleftharpoons \text{OH}\{v1\} + \text{H}$	JPL Publication 19-5 p. 1-7 total of $\text{O}\{1\text{D}\} + \text{H}_2$, Huang Y. et al. 1986 for branching ratio
#=0.22*0.00000 000012	0	0	$\text{O}\{1\text{D}\} + \text{H}_2 \rightleftharpoons \text{OH}\{v2\} + \text{H}$	JPL Publication 19-5 p. 1-7 total of $\text{O}\{1\text{D}\} + \text{H}_2$, Huang Y. et al. 1986 for branching ratio
#=0.19*0.00000 000012	0	0	$\text{O}\{1\text{D}\} + \text{H}_2 \rightleftharpoons \text{OH}\{v3\} + \text{H}$	JPL Publication 19-5 p. 1-7 total of $\text{O}\{1\text{D}\} + \text{H}_2$, Huang Y. et al. 1986 for branching ratio
#=0.09*0.00000 000012	0	0	$\text{O}\{1\text{D}\} + \text{H}_2 \rightleftharpoons \text{OH}\{v4\} + \text{H}$	JPL Publication 19-5 p. 1-7 total of $\text{O}\{1\text{D}\} + \text{H}_2$, Huang Y. et al. 1986 for branching ratio
1.63E-10	0	-499	$\text{O}\{1\text{D}\} + \text{H}_2\text{O} \rightleftharpoons 2\text{OH}$	JPL Publication 19-5 p. 1-7
2.15E-11	0	-915	$\text{O}\{1\text{D}\} + \text{N}_2 \rightleftharpoons \text{O} + \text{N}_2$	JPL Publication 19-5 p. 1-7
1.00E+00	0	0	$\text{O}\{1\text{D}\} + \text{N}_2 + \text{M}[\text{JPL}1; 2.8\text{E}-36; 0.9; 1; 0; \text{He}(0.6); \text{H}_2\text{O}(2.5)] \rightleftharpoons \text{N}_2\text{O}$	JPL Publication 19-5 p. 2-5
4.00E-11	0	-500	$\text{O}\{1\text{D}\} + \text{NO} \rightleftharpoons \text{O} + \text{NO}$	Estimated from similar $\text{O}\{1\text{D}\}$ rates
4.64E-11	0	-166	$\text{O}\{1\text{D}\} + \text{N}_2\text{O} \rightleftharpoons \text{N}_2 + \text{O}_2$	JPL Publication 19-5 p. 1-7
7.26E-11	0	-166	$\text{O}\{1\text{D}\} + \text{N}_2\text{O} \rightleftharpoons 2\text{NO}$	JPL Publication 19-5 p. 1-7

4.70E-11	0	-527	$\text{O}\{1\text{D}\} + \text{CO} \Rightarrow \text{O} + \text{CO}$	Davidson et al. 1978, T=113-333 K
7.50E-11	0	-956	$\text{O}\{1\text{D}\} + \text{CO}_2 \Rightarrow \text{O} + \text{CO}_2$	JPL Publication 19-5 p. 1-8
1.31E-10	0	0	$\text{O}\{1\text{D}\} + \text{CH}_4 \Rightarrow \text{CH}_3 + \text{OH}$	JPL Publication 19-5 p. 1-8
3.50E-11	0	0	$\text{O}\{1\text{D}\} + \text{CH}_4 \Rightarrow \text{CH}_3\text{O} + \text{H}$	JPL Publication 19-5 p. 1-8
8.75E-12	0	0	$\text{O}\{1\text{D}\} + \text{CH}_4 \Rightarrow \text{CH}_2\text{O} + \text{H}_2$	JPL Publication 19-5 p. 1-8
3.01E-10	0	-166	$\text{O}\{1\text{D}\} + \text{CH}_3\text{OH} \Rightarrow \text{CH}_3\text{O} + \text{OH}$	Osif 1975 J. Photochem.
3.53E-10	0	-166	$\text{O}\{1\text{D}\} + \text{CH}_3\text{OH} \Rightarrow \text{CH}_2\text{O} + \text{H}_2\text{O}$	Osif 1975 J. Photochem.
7.00E-16	0	0	$\text{O}\{1\text{D}\} + \text{He} \Rightarrow \text{O} + \text{He}$	Heidner & Husain 1974175
# HOx Chemistry				
1.80E-11	0	-1497	$\text{O} + \text{OH} \Rightarrow \text{O}_2 + \text{H}$	JPL Publication 19-5 p. 1-53
3.00E-11	0	-1663	$\text{O} + \text{HO}_2 \Rightarrow \text{OH} + \text{O}_2$	JPL Publication 19-5 p. 1-53
1.40E-12	0	16629	$\text{O} + \text{H}_2\text{O}_2 \Rightarrow \text{OH} + \text{HO}_2$	JPL Publication 19-5 p. 1-53
1.00E+00	0	0	$\text{H} + \text{O}_2 + \text{M} [\text{JPL}1; 5.3\text{E}-32; 1.8; 9.5\text{E}-11; -0.4; \text{He}(0.6); \text{H}_2\text{O}(2.5); \text{CO}_2(2.4)] \Rightarrow \text{HO}_2$	JPL Publication 19-5 p. 2-5, Ashman 1998 Proc. Combust. Inst. CO ₂ enhancement
6.00E-31	2	0	$\text{H} + \text{OH} + \text{M} \Rightarrow \text{H}_2\text{O}$	Baulch et al. 1992 J Phys Chem Ref Data
1.40E-10	0	3908	$\text{H} + \text{O}_3 \Rightarrow \text{OH} + \text{O}_2$	JPL Publication 19-5 p. 1-53
7.20E-11	0	0	$\text{H} + \text{HO}_2 \Rightarrow 2\text{OH}$	JPL Publication 19-5 p. 1-53

1.60E-12	0	0	$\text{H} + \text{HO}_2 \rightleftharpoons \text{O} + \text{H}_2\text{O}$	JPL Publication 19-5 p. 1-53
6.90E-12	0	0	$\text{H} + \text{HO}_2 \rightleftharpoons \text{H}_2 + \text{O}_2$	JPL Publication 19-5 p. 1-53
4.05E-18	0	0	$\text{H} + \text{N}_2\text{O} \rightleftharpoons \text{OH} + \text{N}_2$	Arthur et al. 1997
1.70E-12	0	7816	$\text{OH} + \text{O}_3 \rightleftharpoons \text{HO}_2 + \text{O}_2$	JPL Publication 19-5 p. 1-53
2.80E-12	0	1496 6	$\text{OH} + \text{H}_2 \rightleftharpoons \text{H}_2\text{O} + \text{H}$	JPL Publication 19-5 p. 1-53
1.80E-12	0	0	$2\text{OH} \rightleftharpoons \text{H}_2\text{O} + \text{O}$	JPL Publication 19-5 p. 1-53
1.00E+00	0	0	$2\text{OH} + \text{M}[\text{JPL}1; 6.9\text{E}-31; 1.0; 2.6\text{E}-11; 0; \text{He}(0.6); \text{H}_2\text{O}(2.5)] \rightleftharpoons \text{H}_2\text{O}_2$	JPL Publication 19-5 p. 2-5
4.80E-11	0	- 2079	$\text{OH} + \text{HO}_2 \rightleftharpoons \text{H}_2\text{O} + \text{O}_2$	JPL Publication 19-5 p. 1-53
1.80E-12	0	0	$\text{OH} + \text{H}_2\text{O}_2 \rightleftharpoons \text{H}_2\text{O} + \text{HO}_2$	JPL Publication 19-5 p. 1-53
1.00E-14	0	4074	$\text{HO}_2 + \text{O}_3 \rightleftharpoons \text{OH} + 2\text{O}_2$	JPL Publication 19-5 p. 1-53
3.00E-13	0	- 3825	$2\text{HO}_2 \rightleftharpoons \text{H}_2\text{O}_2 + \text{O}_2$	JPL Publication 19-5 p. 1-53
1.00E+00	0	0	$2\text{HO}_2 + \text{S}[\text{USER}; \text{T}, \text{M}, \text{cHe}, \text{cH}_2\text{O} : (2.10\text{E}-33 * \exp(7649 / (8.3145 * \text{T}))) * (\text{M}-\text{cHe} + 0.6 * \text{cHe}) * (1 + 1.4\text{E}-21 * \text{cH}_2\text{O} * \exp(2200 / \text{T}))] \rightleftharpoons \text{H}_2\text{O}_2 + \text{O}_2$	JPL Publication 19-5 p. 1-53 and 1-61
5.40E-11	0	3409	$\text{HO}_2 + \text{HO}_2 \rightleftharpoons \text{H}_2\text{O}_2 + \text{O}_2 + \text{H}_2\text{O}$	JPL Publication 19-5 p. 1-53
1.00E-12	0	2270	$\text{HO}_2 + \text{H}_2\text{O} \rightleftharpoons \text{HO}_2\text{H}_2\text{O}$	JPL Publication 19-5 p. 3-3. Assumed E_a/R = 273 K and A = 1.0×10^{-12} . $K_{eq} = 2.4\text{E}-25$ * $\exp(4350/T)$

4.17E+12	0	4091 6	HO2H2O+S[MCM4;0;- 298;]==>HO2+H2O	JPL Publication 19-5 p. 3-3. Calculated from reverse rate. Keq = 2.4E-25 * exp(4350/T)
# Keyser				
2.81E-12	0	1571 0	H+H2O2==>HO2+H2	Baulch et al. 1992 J Phys Chem Ref Data
3.00E-14	0	1663 0	H+H2O2==>OH+H2O	Baulch et al. 1992 J Phys Chem Ref Data
6.10E-26	-2	0	H+OH+M==>H2O+M	Baulch et al. 1992 J Phys Chem Ref Data
8.10E-21	2.8	1621 0	H+OH==>O+H2	Tsang 1986 J Phys Chem Ref Data
7.70E-12	0	1746 0	OH+H2==>H+H2O	Atkinson 2004 Atmos Chem Phys
#10	0	0	OH==>OH{wall}	
#5	0	0	HO2==>HO2{wall}	
#5	0	0	O==>O{wall}	
2.00E-32	0	0	H+NO+M==>HNO+M	
1.00E-13	0	0	H+HNO==>H2+NO	
1.00E-15	0	0	O+HONO==>OH+NO2	
7.00E-11	0	0	OH+HNO==>H2O+NO	
1.50E-14	0	0	NO+F2==>F+FNO	
# NOx Chemistry				
1.00E+00	0	0	O+NO+M[JPL1; 9.1E- 32;1.5;3.0E- 11;0.0;He(0.6);H2O(2.5)]==>N O2	JPL Publication 19-5 p. 2-5

1.00E+00	0	0	$\text{O} + \text{NO}_2 + \text{M}[\text{JPL2}; 3.4\text{E}-31; 1.6; 2.3\text{E}-11; 0.2; \text{He}(0.6); \text{H}_2\text{O}(2.5)] \Rightarrow \text{NO}_3$	JPL Publication 19-5 p. 2-55
5.30E-12	0	- 1663	$\text{O} + \text{NO}_2 + \text{M}[\text{JPL2}; 3.4\text{E}-31; 1.6; 2.3\text{E}-11; 0.2; \text{He}(0.6); \text{H}_2\text{O}(2.5)] \Rightarrow \text{NO} + \text{O}_2$	JPL Publication 19-5 p. 2-55
1.30E-11	0	0	$\text{O} + \text{NO}_3 \Rightarrow \text{O}_2 + \text{NO}_2$	JPL Publication 19-5 p. 1-69
7.80E-11	0	2826 9	$\text{O} + \text{HO}_2\text{NO}_2 \Rightarrow \text{NO}_2 + \text{OH} + \text{O}_2$	JPL Publication 19-5 p. 1-69, products conjectured
1.35E-10	0	0	$\text{H} + \text{NO}_2 \Rightarrow \text{OH} + \text{NO}$	JPL Publication 19-5 p. 1-69
1.00E+00	0	0	$\text{OH} + \text{NO} + \text{M}[\text{JPL1}; 7.1\text{E}-31; 2.6; 3.6\text{E}-11; 0.1; \text{He}(0.6); \text{H}_2\text{O}(2.5)] \Rightarrow \text{HONO}$	JPL Publication 19-5 p. 2-5
1.00E+00	0	0	$\text{OH} + \text{NO}_2 + \text{M}[\text{JPL1}; 1.8\text{E}-30; 3.0; 2.8\text{E}-11; 0.0; \text{He}(0.6); \text{H}_2\text{O}(2.5)] \Rightarrow \text{HONO}_2$	JPL Publication 19-5 p. 2-5
1.00E+00	0	0	$\text{OH} + \text{NO}_2 + \text{M}[\text{JPL1}; 9.3\text{E}-32; 3.9; 4.2\text{E}-11; 0.5; \text{He}(0.6); \text{H}_2\text{O}(2.5)] \Rightarrow \text{HOONO}$	JPL Publication 19-5 p. 2-5
3.00E-12	0	- 2079	$\text{OH} + \text{HONO} \Rightarrow \text{H}_2\text{O} + \text{NO}_2$	JPL Publication 19-5 p. 1-69
3.70E-14	0	- 1995	$\text{OH} + \text{HONO}_2 + \text{M}[\text{JPL2}; 3.9\text{E}-31; 7.2; 1.5\text{E}-13; 4.8; \text{He}(0.6); \text{H}_2\text{O}(2.5)] \Rightarrow \text{H}_2\text{O} + \text{NO}_3$	JPL Publication 19-5 p. 2-55
8.80E-19	2	- 9395	$\text{OH} + \text{HO}_2\text{NO}_2 \Rightarrow \text{H}_2\text{O} + \text{O}_2 + \text{NO}_2$	JPL Publication 19-5 p. 1-69 and 1-72
3.44E-12	0	- 2162	$\text{HO}_2 + \text{NO} \Rightarrow \text{NO}_2 + \text{OH}$	JPL Publication 19-5 p. 1-69

1.00E+00	0	0	HO2+NO+S[USER;T,M,cHe,cH2O:(3.44E-12*exp(2162/(8.3145*T)))*(530/T+6.4E-4*(M-cHe+0.6*cHe)/((3.29573E16)*(293/T))-1.73)*(1+2E-17*cH2O)]=>HONO2	JPL Publication 19-5 p. 2-5 and 2-16, 3.29E16 converts from molec/cc to torr
1.00E+00	0	0	HO2+NO2+M[JPL1;1.9E-31;3.4;4.0E-12;0.3;He(0.6);H2O(2.5)]=>HO2NO2	JPL Publication 19-5 p. 2-5
3.50E-12	0	0	HO2+NO3=>OH+NO2+O2	JPL Publication 19-5 p. 1-69 and 1-75, branching ratio between 0.57 and 1.0. No temp data
3.30E-39	0	-4410	2NO+O2=>2NO2	NIST Search 2004ATK/BA U1461-1738
9.00E-19	2.25	7067	NO+O3=>NO2+O2	JPL Publication 19-5 p. 1-70 and 1-77
1.70E-11	0	-1039	NO+NO3=>2NO2	JPL Publication 19-5 p. 1-70
1.20E-13	0	20370	NO2+O3=>NO3+O2	JPL Publication 19-5 p. 1-70
1.00E+00	0	0	NO2+NO3+M[JPL1;2.4E-30;3.0;1.6E-12;-0.1;He(0.6);H2O(2.5)]=>N2O5	JPL Publication 19-5 p. 2-5
3.80E-11	0	0	HNO+O=>NO+OH	Inomata and Washida J Phys Chem A 1999
3.65E-14	0	38250	HNO+O2=>NO+HO2	Bryukov et al. Chem Phys Lett 1993
3.00E-11	0	4160	HNO+H=>NO+H2	Tsang et al. J Phys Chem Ref Data 1991

8.00E-11	0	4160	$\text{HNO} + \text{OH} \rightleftharpoons \text{NO} + \text{H}_2\text{O}$	Tsang et al. J Phys Chem Ref Data 1991
5.00E-11	0	0	$\text{HNO} + \text{HO}_2 \rightleftharpoons \text{NO} + \text{H}_2\text{O}_2$	Estimated from rate of $\text{HCO} + \text{HO}_2 = 5\text{E-11}$
5.00E-11	0	0	$\text{HNO} + \text{CH}_3\text{O} \rightleftharpoons \text{NO} + \text{CH}_3\text{OH}$	He et al. J Phys Chem 1988
1.40E-15	0	12970	$\text{HNO} + \text{HNO} \rightleftharpoons \text{H}_2\text{O} + \text{N}_2\text{O}$	Tsang et al. J Phys Chem Ref Data 1991
# Organic Compound Reactions				
1.10E-10	0	0	$\text{O} + \text{CH}_3 \rightleftharpoons \text{CH}_2\text{O} + \text{H}$	JPL Publication 19-5 p. 1-92
3.40E-11	0	13303	$\text{O} + \text{CH}_2\text{O} \rightleftharpoons \text{OH} + \text{HCO}$	JPL Publication 19-5 p. 1-96 and 1-98. Channel H + HCO ₂ may exist in <30% yield
2.00E-12	0	0	$\text{O}_2 + \text{HOCO} \rightleftharpoons \text{HO}_2 + \text{CO}_2$	JPL Publication 19-5 p. 1-92
7.00E-15	0	0	$\text{OH} + \text{CO} + \text{M}[\text{JPL2}; 6.9\text{E-33}; 2.1; 1.1\text{E-12}; -1.3; \text{He}(0.6); \text{H}_2\text{O}(2.5)] \rightleftharpoons \text{HOCO}$	JPL Publication 19-5 p. 2-55
2.00E-12	0	0	$\text{HOCO} + \text{O}_2 \rightleftharpoons \text{HO}_2 + \text{CO}_2$	JPL Publication 19-5 p. 2-58, believed to be T independent
1.85E-13	0	540	$\text{OH} + \text{CO} + \text{M}[\text{JPL2}; 6.9\text{E-33}; 2.1; 1.1\text{E-12}; -1.3; \text{He}(0.6); \text{H}_2\text{O}(2.5)] \rightleftharpoons \text{H} + \text{CO}_2$	JPL Publication 19-5 p. 2-55
#0.000000000000000086	0	0	$\text{OH}\{\text{v}4\} + \text{CH}_4 \rightleftharpoons \text{OH}\{\text{v}3\} + \text{CH}_4$	Yamasaki et al. 1999160

#0.000000000000 48	0	0	$\text{OH}\{\text{v}3\} + \text{CH}_4 \Rightarrow \text{OH}\{\text{v}2\} + \text{CH}_4$	Yamasaki et al. 1999160
#0.000000000000 11	0	0	$\text{OH}\{\text{v}2\} + \text{CH}_4 \Rightarrow \text{OH}\{\text{v}1\} + \text{CH}_4$	Yamasaki et al. 1999160
#0.000000000000 035	0	0	$\text{OH}\{\text{v}1\} + \text{CH}_4 \Rightarrow \text{OH} + \text{CH}_4$	Yamasaki et al. 1999160
2.80E-14	0.667	1309 5	$\text{OH} + \text{CH}_4 \Rightarrow \text{CH}_3 + \text{H}_2\text{O}$	JPL Publication 19-5 p. 1-92 and 1-103
#0.000000000000 021	0	1475 8	$\text{OH}\{\text{v}1\} + \text{CH}_4 \Rightarrow \text{CH}_3 + \text{H}_2\text{O}$	Yamasaki et al. 1999160
#0.000000000000 09	0	1475 8	$\text{OH}\{\text{v}2\} + \text{CH}_4 \Rightarrow \text{CH}_3 + \text{H}_2\text{O}$	Yamasaki et al. 1999160
#0.000000000000 0181	0	1475 8	$\text{OH}\{\text{v}3\} + \text{CH}_4 \Rightarrow \text{CH}_3 + \text{H}_2\text{O}$	Yamasaki et al. 1999160
#0.000000000000 0294	0	1475 8	$\text{OH}\{\text{v}4\} + \text{CH}_4 \Rightarrow \text{CH}_3 + \text{H}_2\text{O}$	Yamasaki et al. 1999160
#0.000000000000 06	0	0	$\text{OH}\{\text{v}1\} + \text{H}_2 \Rightarrow \text{OH} + \text{H}_2$	Light & Matsumoto, 1978161
5.50E-12	0	- 1039	$\text{OH} + \text{CH}_2\text{O} \Rightarrow \text{H}_2\text{O} + \text{HCO}$	JPL Publication 19-5 p. 1-92
2.00E-12	0	0	$\text{OH} + \text{CH}_3\text{O} \Rightarrow \text{H}_2\text{O} + \text{CH}_2\text{O}$	Tsang 1986 J Phys Chem Ref Data
2.47E-12	0	2869	$\text{OH} + \text{CH}_3\text{OH} \Rightarrow \text{CH}_2\text{OH} + \text{H}_2\text{O}$	JPL Publication 19-5 p. 1-92 and 1-105
4.35E-13	0	2869	$\text{OH} + \text{CH}_3\text{OH} \Rightarrow \text{CH}_3\text{O} + \text{H}_2\text{O}$	JPL Publication 19-5 p. 1-92 and 1-105
2.66E-12	0	- 1663	$\text{OH} + \text{CH}_3\text{OOH} \Rightarrow \text{CH}_3\text{O}_2 + \text{H}_2\text{O}$	JPL Publication 19-5 p. 1-92 and 1-106
1.14E-12	0	- 1663	$\text{OH} + \text{CH}_3\text{OOH} \Rightarrow \text{CH}_2\text{O} + \text{OH} + \text{H}_2\text{O}$	JPL Publication 19-5 p. 1-92 and 1-106
7.66E-12	0	8481	$\text{OH} + \text{C}_2\text{H}_6 \Rightarrow \text{H}_2\text{O} + \text{C}_2\text{H}_5$	JPL Publication 19-5 p. 1-93

8.00E-13	0	8315	$\text{OH} + \text{CH}_3\text{ONO}_2 \rightleftharpoons \text{CH}_3\text{ONO} + \text{HO}_2$	JPL Publication 19-5 p. 1-93, products conjectured
6.70E-15	0	- 4989	$\text{HO}_2 + \text{CH}_2\text{O} \rightleftharpoons \text{CH}_2\text{OHO}_2$	JPL Publication 19-5 p. 1-94
4.10E-13	0	- 6236	$\text{HO}_2 + \text{CH}_3\text{O}_2 \rightleftharpoons \text{CH}_3\text{OOH} + \text{O}_2$	JPL Publication 19-5 p. 1-94
7.50E-13	0	- 5820	$\text{HO}_2 + \text{C}_2\text{H}_5\text{O}_2 \rightleftharpoons \text{C}_2\text{H}_5\text{OOH} + \text{O}_2$	JPL Publication 19-5 p. 1-94
1.40E-10	0	0	$\text{CH}_3 + \text{O} \rightleftharpoons \text{CH}_3\text{O}$	Seakins J Phys Chem 1992
1.00E-11	0	1072 57	$\text{CH}_3 + \text{O}_2 \rightleftharpoons \text{CH}_3\text{O}_2$	JPL Publication 19-5 p. 1-94 and 1-132
1.00E+00	0	0	$\text{CH}_3 + \text{O}_2 + \text{M}[\text{JPL}1; 4.1\text{E}-31; 3.6; 1.2\text{E}-12; -1.1; \text{He}(0.6); \text{H}_2\text{O}(2.5)] \rightleftharpoons \text{CH}_3\text{O}_2$	JPL Publication 19-5 p. 2-5
5.40E-12	0	1829	$\text{CH}_3 + \text{O}_3 \rightleftharpoons \text{CH}_3\text{O} + \text{O}_2$	JPL Publication 19-5 p. 1-94, products conjectured
4.00E-10	-0.34	0	$2\text{CH}_3 \rightleftharpoons \text{C}_2\text{H}_6$	Wang et al. 2003=4.8E-11, Sangwan 2014 near high P limit, T=292-714, 4.55E-10 T ^{-0.37} , Blitz 2015 used
1.32E-10	0.153	69	$\text{CH}_3 + \text{H} \rightleftharpoons \text{CH}_4\{\text{newH}\}$	Klippenstein 2002
1.00E-10	0	0	$\text{CH}_3 + \text{OH} \rightleftharpoons \text{CH}_3\text{OH}$	Baulch J Phys Chem Ref Data 1994
1.20E-10	0	1164 0	$\text{CH}_3 + \text{OH} \rightleftharpoons \text{H}_2\text{O} + \text{CH}_2$	Baulch J Phys Chem Ref Data 1994
6.70E-22	2.9	6219 0	$\text{CH}_3 + \text{H}_2\text{O} \rightleftharpoons \text{CH}_4\{\text{newH}_2\text{O}\} + \text{OH}$	Tsang 1986 J Phys Chem Ref Data

6.67E-22	0	- 2494	CH ₃ +H ₂ O ₂ ==>CH ₄ {newH ₂ O ₂ }+HO ₂	Tsang 1986 J Phys Chem Ref Data
1.00E-30	0	0	CH ₃ +NO+M[He(0.6);H ₂ O(2.5)] ==>CH ₃ NO	NIST Search 1993KAI11681 -11688
2.30E-11	0	0	CH ₃ +NO ₂ ==>CH ₃ O+NO	Srinivasan J Phys Chem A 2005
4.00E-11	0	0	CH ₃ +CH ₃ O==>CH ₄ {newCH ₃ O}+CH ₂ O	Tsang 1986 J Phys Chem Ref Data
2.00E-11	0	0	CH ₃ +CH ₃ O==>CH ₃ OCH ₃	Tsang 1986 J Phys Chem Ref Data
5.00E-11	0	0	CH ₃ +CH ₃ O ₂ ==>2CH ₃ O	NIST Search 1985PIL/SMI4 713
5.20E-12	0	0	HCO+O ₂ ==>CO+HO ₂	JPL Publication 19-5 p. 1-94
9.10E-12	0	0	CH ₂ OH+O ₂ ==>CH ₂ O+HO ₂	JPL Publication 19-5 p. 1-94
2.50E-11	0	0	CH ₃ O+O==>CH ₃ +O ₂	Baulch et al. J Phys Chem Ref Data 1992
1.00E-11	0	0	CH ₃ O+O==>CH ₂ O + OH	Tsang 1986 J Phys Chem Ref Data
3.90E-14	0	7483	CH ₃ O+O ₂ ==>CH ₂ O+HO ₂	JPL Publication 19-5 p. 1-94
8.00E-12	0	0	CH ₃ O+NO==>CH ₂ O+HNO	JPL Publication 19-5 p. 1-94 and 1-135
1.00E+00	0	0	CH ₃ O+NO+M[JPL1;2.3E- 29;2.8;3.8E- 11;0.6;He(0.6);H ₂ O(2.5)]==>C H ₃ ONO	JPL Publication 19-5 p. 2-6
1.00E+00	0	0	C ₂ H ₅ +O ₂ +M[JPL2;1.3E- 28;4.2;7.6E- 12;1.4;He(0.6);H ₂ O(2.5)]==>C ₂ H ₅ O ₂	JPL Publication 19-5 p. 2-55

1.80E-13	0	0	C2H5+O2+M[JPL2;1.3E-28;4.2;7.6E-12;1.4;He(0.6);H2O(2.5)]==>C2H4+HO2	JPL Publication 19-5 p. 2-55
1.00E+00	0	0	C2H5O+NO+M[JPL1;2.9E-27;4.0;5.0E-11;0.2;He(0.6);H2O(2.5)]==>C2H5ONO	JPL Publication 19-5 p. 2-6
1.00E+00	0	0	C2H5O+NO2+M[JPL1;2.1E-27;4.0;2.8E-11;1.0;He(0.6);H2O(2.5)]==>C2H5ONO2	JPL Publication 19-5 p. 2-6
1.00E+00	0	0	CH3O2+NO2+M[JPL1;1.0E-30;4.8;7.3E-12;2.1;He(0.6);H2O(2.5)]==>C H3O2NO2	JPL Publication 19-5 p. 2-6
1.00E+00	0	0	C2H5O2+NO2+M[JPL1;1.2E-29;4.0;9.0E-12;0.0;He(0.6);H2O(2.5)]==>C2H5O2NO2	JPL Publication 19-5 p. 2-6
# do not remove this END				
END				

All spectra taken at 20 °C.

P = 142.7 mtorr except for 5993.75 – 5996 cm^{-1} where P = 31 mtorr.

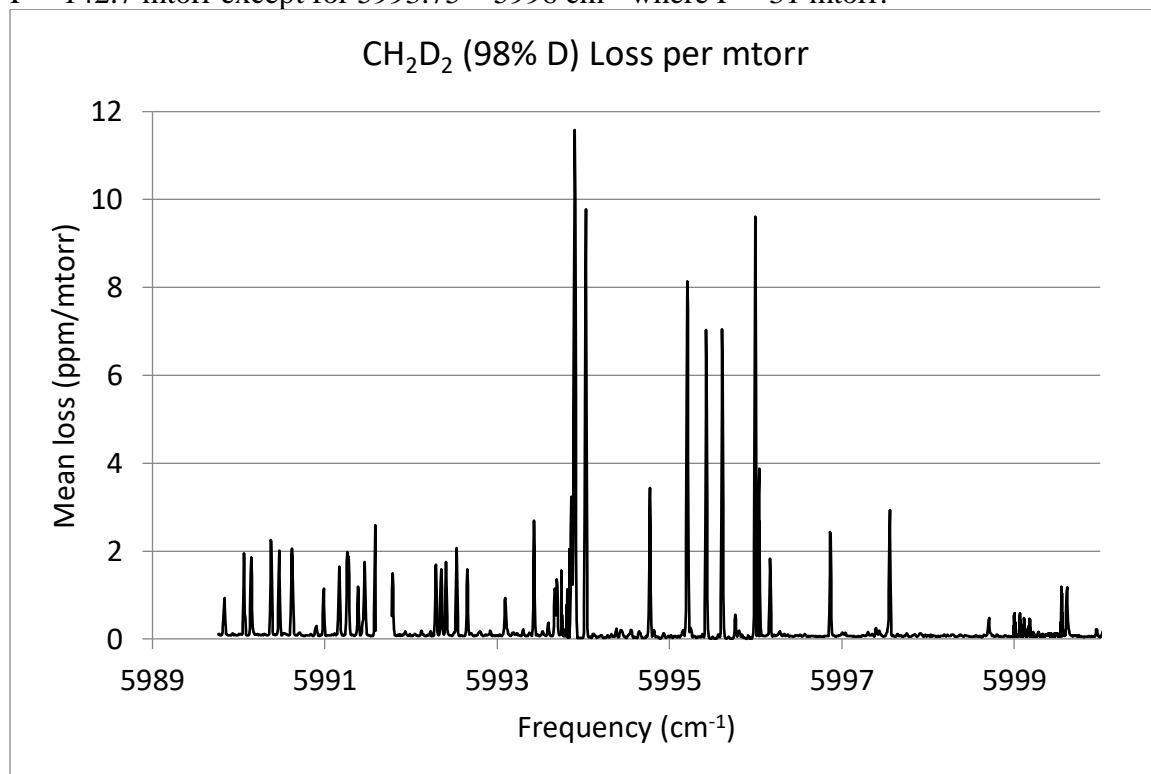


Figure 4.11: Spectrum of CH₂D₂ loss vs frequency 5989.75 – 6000 cm^{-1}

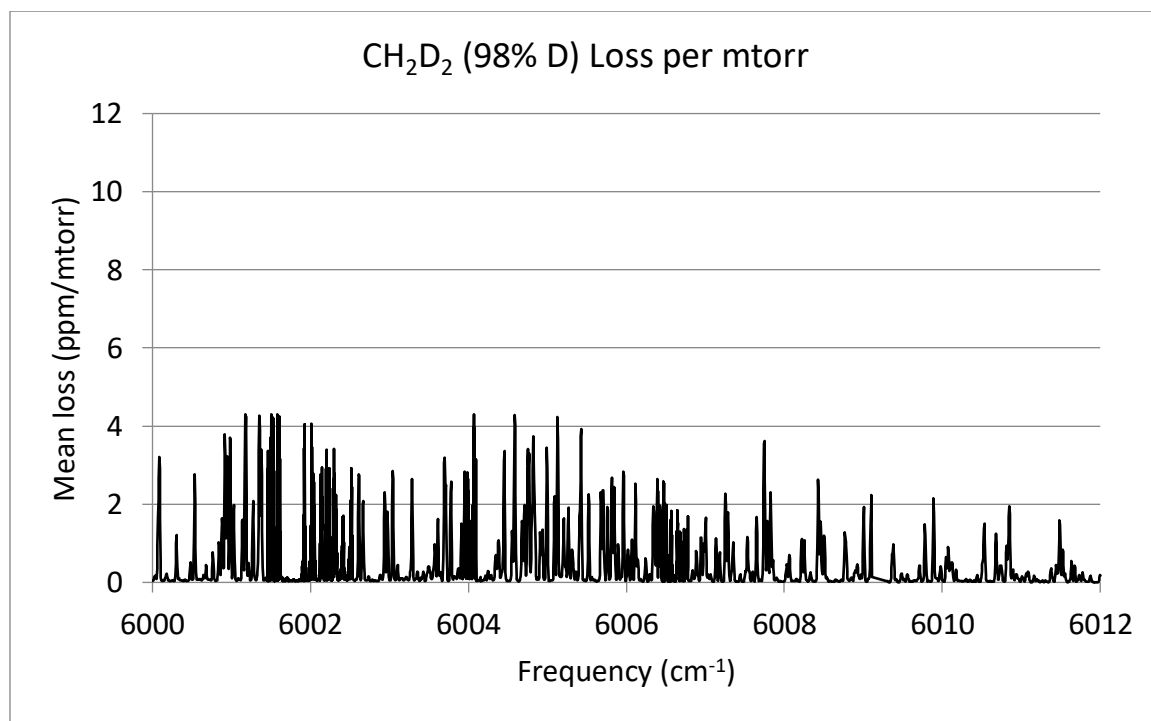


Figure 4.12: Spectrum of CH₂D₂ loss vs frequency 6000 – 6012 cm^{-1}

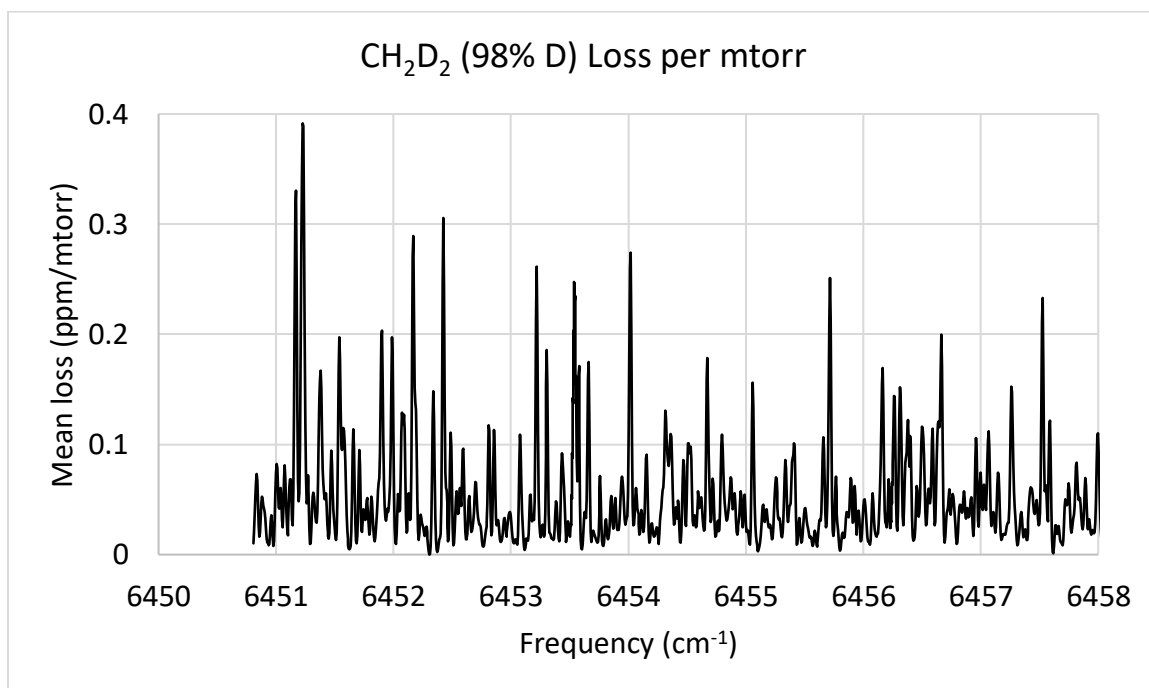


Figure 4.13: Spectrum of CH_2D_2 loss vs frequency $6450.8\text{ cm}^{-1} - 6468\text{ cm}^{-1}$